Influence of Microstructure on the Mechanical Properties of Thermally Sprayed NiCoCrAlY Coatings Determined by Small Punch Testing

George Jackson, MEng

Thesis submitted to the University of Nottingham

for the degree of Doctor of Philosophy

Faculty of Engineering
University of Nottingham

December 2017

Preface

This thesis is submitted for the degree of Doctor of Philosophy at the University of Nottingham.

The research work was carried out under the supervision of Professor D.G. McCartney and Professor W. Sun in the Faculty of Engineering.

It hereby certify that the work presented in this thesis is original, and suitable references are made to any work cited from the literature.

Signed: _____

Date: _____

The list of publications from the work presented in this thesis is presented here:

i G.A. Jackson, H. Chen, W. Sun, D.G. McCartney. The High Temperature Creep Properties of a Thermally Sprayed CoNiCrAlY Coating via Small Punch Creep Testing, *Key Engineering Materials*, Vol. 734, pp. 37-48, 2017

ii G.A. Jackson, W. Sun, D.G. McCartney. The Application of the Small Punch Tensile Test to Evaluate the Ductile to Brittle Transition of a Thermally Sprayed CoNiCrAlY Coating, *Key Engineering Materials*, Vol. 734, pp. 144-155, 2017

Abstract

The development of new thermal barrier coatings (TBCs) capable of increasing the efficiency of gas powered turbines requires an understanding of the time-dependent and time-independent properties of MCrAlY bond coats. High velocity oxy-fuel (HVOF) thermal spraying was used to manufacture free-standing coatings from one commercially available CoNiCrAlY bond coat alloy powder and three experimental NiCoCrAlY powders with potential application as new bond coat alloys. All coatings were subsequently heat treated at 1100 °C for 2 h to simulate a high temperature heat treatment stage used in manufacturing coated components. X-ray diffraction (XRD), scanning electron microscopy (SEM), energy dispersive X-ray analysis (EDX) and electron back-scatter diffraction (EBSD) were used to characterise the microstructure of powders and coatings and characterise crack growth and fracture behaviour following mechanical testing.

Microstructural characterisation revealed that the CoNiCrAlY coating exhibited a two-phase microstructure consisting of a FCC γ-Ni matrix with BCC B2 β-NiAl as a secondary phase. After the same heat treatment, all three NiCoCrAlY coatings exhibited a β-NiAl matrix with γ-Ni as a secondary phase. The TCP phase σ-Cr_2Co was also observed in the NiCoCrAlY coatings as well as the ordered $L1_2$ γ'-Ni_3(Al,Ta) phase in two of the NiCoCrAlY coatings. All the coatings exhibited a fine scale microstructure with grain sizes typically in the range 1 - 5 μm. All coatings formed the desired protective Al_2O_3 scale after an accelerated oxidation test of 96 hours at 1100 °C in air, but the scale thickness in NiCoCrAlY coatings ranged from $\sim$ 5 to 7.5 μm compared to $\sim$ 2.5 μm in the CoNiCrAlY.

CALPHAD methods were employed, using ThermoCalc and the TTNi7 database, to model the phase equilibria of each of the MCrAlY alloys as a function of temperature. A comparison was made with the experimental observations for the novel alloys for the first time. Agreement was found to be surprisingly good using this database which was originally designed for compositions used in the manufacture of single crystal turbine blades.

Small punch tensile (SPT) tests were conducted on the CoNiCrAlY coating and two of the NiCoCrAlY coatings between room temperature (RT) and

750 °C in order to evaluate the influence of coating microstructure on their time-independent mechanical properties; specifically strength, ductility and brittle to ductile transition. The SPT tests demonstrated the ductile to brittle transition temperatures (DBTTs) of the CoNiCrAlY coating and two NiCoCrAlY coatings were 500-700 °C, 600-700 °C and 650-750 °C respectively. One NiCoCrAlY coating exhibited superior yield strength above 650 °C compared to the CoNiCrAlY coating, but both NiCoCrAlY coatings exhibited lower ductility and lower fracture strengths below 600 °C. Increasing the phase fraction of β-NiAl was shown to increase the DBTT and also increase the yield strength above 650 °C, but also caused lower ductility and lower fracture strength below 600 °C. The TCP phase σ-Cr_2Co was shown to decrease the ductility of the NiCoCrAlY coatings at $\leq$ 750 °C because it increased the density of phase boundaries in the coatings. The phase boundaries were found to be the crack nucleation sites for the CoNiCrAlY coating and two NiCoCrAlY coatings during SPT testing.

Small punch creep (SPC) tests were also conducted at 750 and 850 °C to determine the creep properties of the CoNiCrAlY coating and two of the NiCoCrAlY coatings. These tests revealed the NiCoCrAlY coatings exhibited higher creep resistance at 750 and 850 °C compared to the CoNiCrAlY coating. At 750 °C, the stress exponents of the CoNiCrAlY and two NiCoCrAlY coatings were calculated as 7.5, 7.8 and 9.1 respectively. Higher phase fractions of β-NiAl and the addition of γ'-Ni_3(Al,Ta) were shown to improve the SPC lifetime of the coatings. The presence of σ-Cr_2Co decreased the SPC strain to fracture of the NiCoCrAlY coatings.

At 850 °C large displacements were observed for the CoNiCrAlY coating and one NiCoCrAlY coating over a rage of the experimentally applied stresses, leading to significantly increased strain to fracture and lifetime of the samples. A possible explanation for this phenomena is the onset of superplasticity.

The results provide important insights into the structure-property relationships of thin, HVOF sprayed bond coat alloys and the quantitative mechanical property data will be useful in the design of new TBC systems for superalloy turbine blades.

Acknowledgements

I would like to sincerely thank my supervisors, Professor Graham McCartney and Professor Wei Sun, for their guidance and support over the past four years. I would also like to express my gratitude to Mr. Shane Maskill for his technical guidance on small punch testing.

Thank you also to Mr. Tom Buss, Mr. Jason Greaves, Dr. Nigel Neate, Mr. Martin Roe, Mr. Graham Malkinson and all others that have helped me throughout my PhD project.

I would also like to take this opportunity to thank my friends, colleagues and family who have brought laughter and joy to the past four years of my life in Nottingham. I am sure they will be happy to hear that all those months of me 'getting there' finally paid off in the end.

Contents

List of Figures

Nomenclature

χ	Creep rupture power law exponent
δ	Specimen displacement (m)
δ^*	Specimen displacement at fracture (m)
$\dot{\varepsilon}_{min}$	Minimum Steady-State Strain Rate (s^{-1})
$\dot{\varepsilon}_{ss}$	Steady state creep rate (s^{-1})
λ	Wavelength of incident X-ray (m)
ν	Poisson's ratio
ϕ	Angle made by a SPC sample surface normal to the vertical axis (°)
σ	Stress (MPa)
σ_{YS}	Yield Stress (MPa)
σ_e	Equivalent uni-axial stress (MPa)
σ_{max}	Maximum bi-axial bending stress (MPa)
θ	ϕ at r=a_p / XRD diffraction angle (°)
θ_0	ϕ at the moving punch contact boundary (°)
ε	Equivalent strain at the specimen centre
ε_c	Equivalent strain at the punch contact boundary
ε_e	Elastic bi-axial strain
ε_q	Von Mises equivalent strain
${\varepsilon_p}^*$	Plastic bi-axial fracture strain
a_p	Radius of lower die receiving hole (m)
B	Norton power law constant (s^{-1} MPa^{-n})
C	Steady state creep parameter (s^{-1} MPa^{-n})
d	Grain size (m) / atom spacing in XRD (m)

E	Elastic Modulus (GPa)
F_e	Elastic-plastic transition load (N)
K_1	Monkman-Grant relationship constant (h s^m)
K_{sp}	SPC correlation factor
M	Creep rupture power law constant (h^{-1} $MPa^{-\chi}$)
m	Monkman-Grant relationship strain exponent
n	Stress exponent / Norton power law parameter
Q_{c}	Activation energy (J / mol)
R	Universal gas constant (J / K mol)
r'	Effective radius (m)
r_c	Contact radius (m)
R_s	Hemispherical punch head radius (m)
T	Temperature (°C)
T_{m}	Melting temperature (°C)
t_0	Specimen thickness (m)
t_f	Time to failure (h)
APS	Air plasma spraying
BCC	Body centred cubic
CTE	Coefficient of thermal expansion
DBTT	Ductile to brittle transition temperature
EB-PVD	Electron beam physical vapour deposition
EBSD	Electron back-scatter diffraction
EDX	Energy dispersive X-ray analysis
FCC	Face centred cubic
HVOF	High velocity oxy-fuel
LPPS	Low pressure plasma spraying
MDBT	Minature Disc Bend Test
MMC	Metal Matrix Composite
SEM	Scanning electron microscopy

SP	Small punch
SPC	Small punch creep
SPT	Small punch tensile
TBC	Thermal barrier coating
TCP	Tetragonal close packed
TGO	Thermally grown oxide
VPS	Vacuum plasma spraying
XRD	X-ray diffraction

Chapter 1

Introduction

The efficiency of gas turbines is largely dependent upon the maximum operating temperature of the turbine section. In modern day turbine sections, the operating temperature of the gas in the first stage turbine can exceed the melting temperature of the component alloys. This is largely made possible by the use of thermal barrier coatings (TBCs). TBCs are multilayer coatings that provide the component alloys with thermal protection through a ceramic top coat (eg yttria stabilised zirconia), and an oxidation and corrosion resistant bond coat, typically an MCrAlY alloy where M = Ni, Co or NiCo or an aluminide layer. During service an aluminium oxide typically forms at the interface between the top coat and the bond coat and is known as a thermally grown oxide layer or TGO. If the bond coat is an aluminide it is manufactured by a chemical pack diffusion process. More recently bond coats of the MCrAlY type (known as an overlay type) have become preferred and are commonly deposited as thin layers approximately 200 μm thick by thermal spraying. This can involve low pressure plasma spraying (LPPS) or high velocity oxy-fuel (HVOF) thermal spraying; the latter of growing interest due to its cost effectiveness.

HVOF coatings typically exhibit a combination of FCC γ-Ni phase, BCC β-NiAl phase, ordered FCC ($L1_2$) γ'-Ni3(Al,Ti) phase and TCPσ-Cr_2Co phase. The alloy composition and precise manufacturing process strongly influences the coating microstructure, which in turn governs the oxidation and corrosion resistance, as

well as the time-dependent and time-independent mechanical properties of the MCrAlY bond coat. Furthermore, the bond coat performance characteristics directly influence the failure of TBCs by mechanisms such as spallation, which is a critical feature in determining the lifetime of a component such as a turbine blade. Therefore, in order to improve the efficiency of gas turbines through the development of improved TBCs, it is necessary to understand the factors that affect the relevant mechanical properties of the MCrAlY bond coat. In this context it is important to distinguish between the properties of bond coat in the as-manufactured condition from that of a bulk alloy of the same composition. Unfortunately, the available data on the mechanical properties of thin MCrAlY bond coats is limited; in particular, how the properties are influenced by the coating microstructure. In order to evaluate the time-dependent and time-independent properties of thin MCrAlY bond coats it is necessary to use relevant test techniques capable of testing thin specimens. One such technique is the small punch test method, which is employed in this work to determine both the time dependent and time independent mechanical properties of thin, MCrAlY free standing coatings sprayed by the HVOF process. The research is novel in that three experimental alloys are studied and the small punch method is applied to both creep and tensile testing of the same alloys.

1.1 Aims and Objectives

The overall aim of this study was to investigate how the mechanical properties of thin ($\sim$ 400 μm) MCrAlY bond coats produced by HVOF thermal spraying are influenced by the coating microstructure. The specific objectives were:

i) Characterise the microstructures of HVOF-sprayed free-standing coatings; one commercially available CoNiCrAlY alloy and three novel experimental NiCoCrAlY alloys. Furthermore, to investigate microstructural evolution from feedstock powder to thermally sprayed coating and finally fully heat treated coating.

ii) Evaluate the suitability of the TTNI7 thermodynamic database for predicting phase equilibria in the novel NiCoCrAlY alloys using CALPHAD methods.

iii) Investigate the formation of oxide scales on the three experimental alloy coatings under accelerated oxidation conditions relevant to in-service behaviour in air at 1100 °C and compare their behaviour with the CoNiCrAlY commercial alloy coating.

iv) Determine the time-independent mechanical properties i.e. yield strength, elongation to failure and ductile to brittle transition temperature (DBTT) of the thin CoNiCrAlY coating and NiCoCrAlY coatings using the small punch tensile (SPT) test between room temperature and 750 °C, and characterise the fracture behaviour and failure mechanisms by microstructural analysis.

v) Determine the time-dependent i.e creep, properties of the CoNiCrAlY coating and NiCoCrAlY coatings at 750 and 850 °C using the small punch creep (SPC) test, and quantify the creep deformation behaviour of the thin coatings using the Norton power law, Monkman-Grant relationship and creep rupture power law, as well as characterise the fracture behaviour and failure mechanisms by microstructural analysis.

1.2 Thesis Structure

This thesis is divided into 8 chapters as described below:

1. The general introduction given above.

2. A literature review concerning the microstructure, processing and mechanical properties of current MCrAlY coatings. The SPC test and SPT test are also described, as well as areas where there is a lack of knowledge in the current literature and where future work is required to improve the understanding of the microstructure and properties of MCrAlY alloys used as bond coats in TBC systems.

3. A description of the experimental methods and techniques used in this work. The experimental procedures for the SPC and SPT tests are described, as well as the heat treatment procedure and material characterisation techniques, such as XRD, SEM, EDX and EBSD. A description of the CALPHAD methods used to calculate the phase equilibria in the MCrAlY alloys is also given. The work undertaken to design and develop the equipment and procedures for extending the SPC test to operate at 850 °C is given in Apendix A.

4. A study of the principal microstructural features of the MCrAlY alloy powders and HVOF coatings in the as-sprayed and heat-treated conditions. The oxidation behaviour of the NiCoCrAlY alloys is also described as well as the results of the CALPHAD calculations used to predict the phase equilibria of each alloy.

5. An investigation of the time-independent properties of the MCrAlY coatings as determined from SPT tests between room temperature (RT) and 750 °C. The macroscopic fracture patterns at each test temperature are presented and the microscopic fracture behaviour of each coating is evaluated using SEM and EBSD analysis. The time-independent properties are evaluated with respect to the coating microstructures.

6. A study of the creep properties of the MCrAlY coatings at 750 and 850 °C as determined from SPC tests with reference to the microstructure of the coatings. The accumulation of creep damage in the coatings is also studied using SEM and EDX analysis and creep results are quantified using the standard creep equations.

7. and 8. A summary of the main conclusions determined throughout the thesis and an outline of any possible future work respectively.

Chapter 2

Literature Review

2.1 Gas Powered Turbines

Gas based turbines are widely used for power generation, the two largest sectors of which are aeronautical and surface (land and sea) applications. The term 'gas powered turbine' refers to a mechanical system wherein power is generated from the combustion of a fuel and expansion of hot gases, typically through a compressor, combustor, and turbine [1]. The maximum power output of the gas turbine is directly influenced by the maximum operating temperature of the turbine section. The desire to increase the efficiency of gas turbines has led to the development of component alloys over the past 60 years, as shown in Fig.2.1 [2]. In modern day gas turbines, the operating temperature of the turbine section exceeds the melting temperature of the component alloys [3]. This is achieved through cooling channels, such as that shown in Fig.2.2, and high performance coating systems, such as thermal barrier coatings (TBCs).

2.2 Thermal Barrier Coatings

Thermal barrier coatings are multi-layer deposits applied to the surface of engineering components in order to protect them in high temperature operating

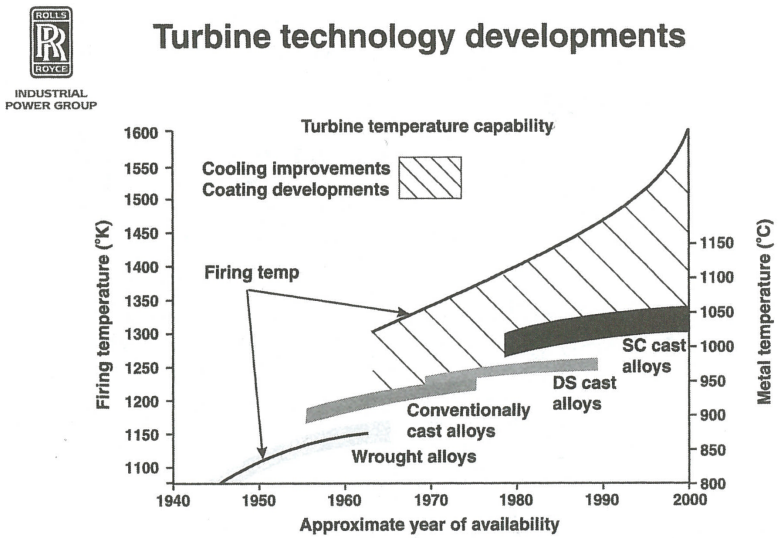

FIGURE 2.1: Development of turbine blade manufacturing process showing the increase in operating temperature of aero-engine gas turbines with improvements in materials and manufacturing technology over the past 60 years. Figure reproduced from [2].

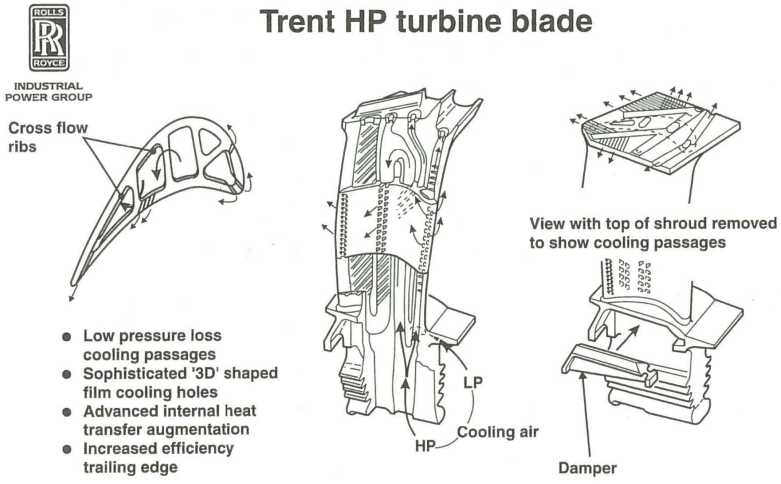

FIGURE 2.2: Cross section of modern day turbine blade with integrated gas cooling channels. Figure reproduced from [2].

environments. A TBC is best regarded as a multilayer composite system comprising: a ceramic top coat, typically a Y_2O_3 stabilised ZrO_2; an MCrAlY alloy bond coat, where M = Ni or Co; the substrate alloy, typically a Ni-based superalloy; and a thin oxide layer, known as the thermally grown oxide (TGO), which forms between the ceramic top coat and the bond coat during service [1–6].

The ceramic top coat provides thermal protection from the high temperature environment and is typically deposited by plasma spraying or electron beam

physical vapour deposition (EB-PVD) [4, 7]. The coating process employed influences the high temperature properties of the ceramic top coat, but a common feature amongst both deposition methods is that the top coat provides thermal protection but also allows for the easy diffusion of O and corrosive elements such as Na and S. The bond coat provides the substrate with oxidation and corrosion resistance through the formation of the TGO, typically an Al_2O_3 alumina scale, and also adheres the ceramic top coat to the substrate [2, 4–6, 8, 9].

Failure of the TBC system is typically characterised by spallation of the ceramic top coat, which leads to degradation of the substrate and component failure. Spallation occurs due to the development of stresses at the bond coat / TGO / top coat interfaces, caused by chemical and thermo-mechanical processes. Chemical processes include the formation of brittle spinel oxides at the bond coat / TGO and (or) TGO / top coat interfaces which fracture and cause delamination of the top coat [8, 10]. Chemical degradation can also occur via hot-corrosion where impurities such as Na, S and V destabilise the Y_2O_3 stabilised ZrO_2 ceramic top coat and cause a phase transformation from monoclinic phase to tetragonal phase at high temperature. The associated volume expansion can lead to cracking in the top coat and at the TGO / top coat interface [11].

Evans et al. [8] outlined three overarching principles to describe the thermo-mechanical failure of TBC's during thermal cycling. A brief description of each is as follows:

i) The thermal expansion mismatch between the bond coat, TGO and ceramic top coat can cause plastic deformation of the bond coat and buckling of the TGO, which contributes to delamination of the TGO and failure of the TBC.

ii) Delamination of the TGO due to the sequence of crack nucleation, propagation and coalescence within the vicinity of imperfections in, or around, the TGO. This type of failure is associated with a process called ratcheting caused by cyclic plasticity of the bond coat [12].

iii) Large scale buckling of the TGO due to separations at the bond coat / TGO interface. Separations form through the nucleation, propagation and coalescence of cracks and are influenced by creep and grain boundary sliding of the bond coat [4].

It is clear that the TGO and bond coat are instrumental in maintaining the integrity of TBCs. In particular, the ductility, plastic deformation and creep behaviour of the bond coat directly influences the failure mechanisms of TBCs [4, 8, 12]. As such, in order to develop new generations of TBCs capable of increasing the efficiency of gas turbines, it is essential to understand the relevant time-independent properties such as the elastic modulus, yield strength, ductile to brittle transition temperature (DBTT) and ductility, as well as the time dependent property known as creep. Understanding these properties is a main objective of this work.

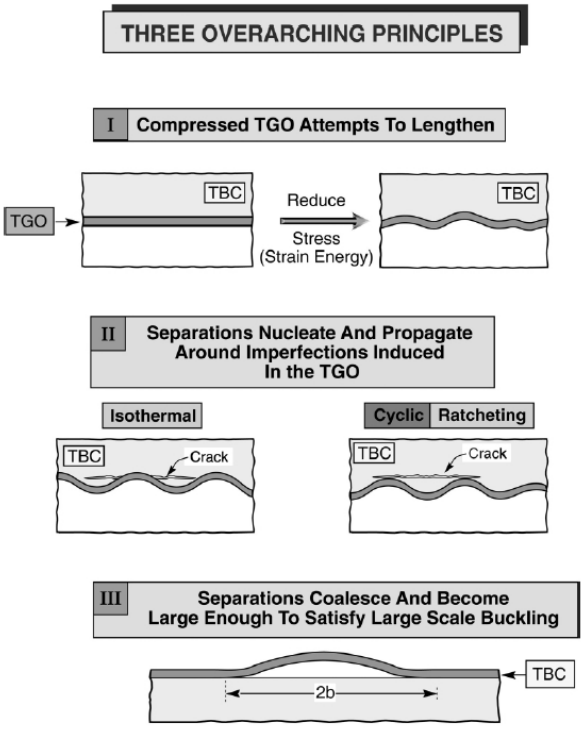

FIGURE 2.3: Schematic of the overarching mechanisms controlling thermal barrier coating failure. Figure reproduced from [8].

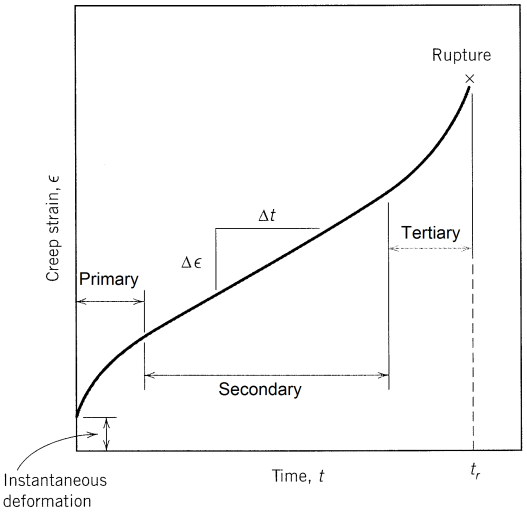

FIGURE 2.4: Typical uni-axial creep curve showing the primary, secondary and tertiary creep regions. Figure reproduced from [13].

2.3 Creep

Creep is defined as the time-dependent and permanent deformation of materials when subjected to a constant load or stress [13]. Creep is observed in all materials but for metals only becomes a concern above 0.4 T_m, where T_m is the absolute melting temperature of the material. This is because creep is a diffusion based mechanism and therefore heavily dependent upon temperature [14].

The creep behaviour of materials is conventionally investigated using uni-axial creep tests, where a specimen is subjected to a constant load and the strain of the specimen is measured with respect to time. Uni-axial creep curves typically exhibit three regions, as shown in Fig.2.4 [13]. The primary region exhibits a large initial strain rate associated with elastic loading, which reduces throughout the primary region until a constant strain rate is reached. The region of constant strain rate is defined as the secondary region, which is associated with steady-state creep. Once the tertiary region is reached, the strain rate accelerates, leading to failure.

The steady-state creep strain rate ($\dot{\varepsilon}_{ss}$) observed in the secondary region is often used to quantify the creep properties of materials and can be described by the following equation:

$$\dot{\varepsilon}_{ss} = C\sigma^{n} exp(\frac{-Q_c}{RT}) \tag{2.1}$$

where C is a constant, n is a constant known as the stress exponent, σ is the applied stress (Pa), Q_c is the activation energy for creep (J mol^{-1}), R is the universal gas constant (8.31 J mol^{-1}) and T is the absolute temperature (K) [14].

When failure occurs, the time to failure (t_f) is often found to be dependent upon the steady-state creep strain rate, as described by the Monkman-Grant relationship:

$$t_f = K_1 \, \dot{\varepsilon}_{ss}{}^{-m} \tag{2.2}$$

where K_1 and m are material constants.

The time to failure can also be described with reference to the uni-axial stress using the creep rupture power law:

$$\frac{1}{t_f} = M \, \sigma^{\chi} exp(\frac{-Q_c}{RT}) \tag{2.3}$$

where M is a material constant and χ is the rupture power law stress exponent.

Equations 2.1 and 2.3 show the steady-state creep strain rate is highly sensitive to temperature. Diffusional creep theories state that at high temperatures, where $T \geq 0.8T_{\mathrm{m}}$, atoms are able to diffuse though the lattice towards an area of high stress by jumping to the site of an adjacent vacancy. This process is known as bulk diffusion and generally referred to as Noble-Herring creep[14]. The flux of atoms under an applied stress in one direction is equalled by a flux of vacancies in the opposite direction, resulting in time-dependent creep deformation.

The diffusion of vacancies may also occur along the grain boundaries. This process is known as Coble creep and becomes the dominant creep mechanism as the temperature is decreased towards 0.4 $\mathrm{T_m}$.

Diffusional creep theories do not always account for the steady-state creep rate observed in uni-axial creep tests. Alternative theories suggest that creep also occurs through the movement of dislocations, in a process known as dislocation creep. Dislocations are often unevenly distributed within a material, which under loading, causes an uneven distribution of internal stress. The difference between the applied stress and the internal stress drives dislocation movement through the lattice [15].

Dislocations move through the lattice in a process known as dislocation glide [14]. When dislocations meet an obstacle they become trapped and dislocation pile up occurs. Dislocations are able to circumvent obstacles by moving out of the current slip plane in a process known as dislocation climb [16].

Diffusion and dislocation creep mechanisms occur simultaneously. The overall creep rate is the sum of the individual processes but a dominant mechanism is usually identified when the contribution of the other processes is negligible. The dominant creep mechanism is dependent upon the applied stress and temperature, as illustrated in the creep deformation map shown as Fig.2.5 [14]. The y axis is normalised shear stress, where σ_y is the yield stress (Pa) and G is the shear modulus (Pa), the x axis is normalised temperature, where T is the absolute temperature and T_m is the melting temperature.

The different stress / temperature regimes indicate which creep mechanisms may be expected to be dominant. The boundaries represent conditions where two or more mechanisms make a significant contribution to the creep rate. The different regimes are commonly associated with values for the stress exponent (n). Dislocation creep is typically associated with values of n greater than 4, whereas low values of n are associated with diffusional creep [15].

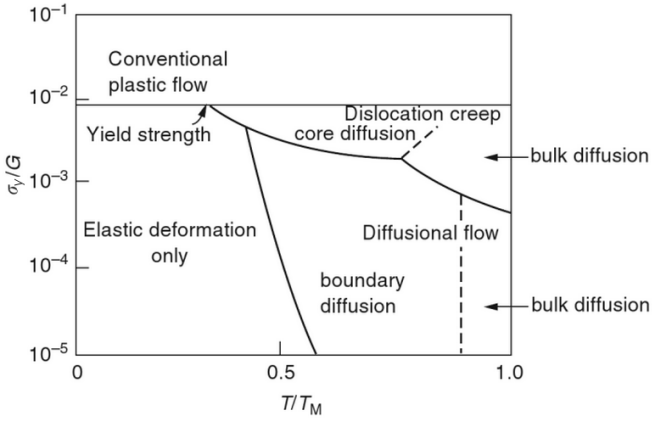

FIGURE 2.5: Typical creep deformation diagram for a metallic alloy. Figure reproduced from [14].

2.4 Metallurgy, Microstructure and Processing of Overlay Bond Coats

2.4.1 Metallurgy and Composition of Bond Coat Alloys

Bond coats typically fall into two categories; one is based on the NiCoCrAlY system and is termed an overlay system because it is normally deposited onto the substrate by a thermal spraying process; the second category is diffusion aluminide coatings manufactured by chemical processes such as chemical vapour deposition or pack aluminising. Overlay coatings are the topic of this thesis and are reviewed below. Details of diffusion coatings can be found elsewhere [4].

Bond coats based on the NiCoCrAlY system are commonly referred to as a MCrAlY, where M stands for Co, Ni or CoNi. Overlay coatings of this type allow the composition of the coating to be adjusted without needing to alter the composition of the substrate, offering greater flexibility over traditional diffusion coatings which require a coating composition similar to the substrate composition [2, 4, 5, 17].

The composition of an MCrAlY alloy can be tailored to achieve varying levels of oxidation and corrosion resistance. Fig.2.6 shows the relative oxidation and and corrosion resistance of different MCrAlY alloys [17]. High oxidation resistant

coatings typically have high levels of Al where as corrosion resistant coatings typically have high levels of Cr.

Al increases the oxidation resistance of MCrAlY alloys as it forms a stable Al_2O_3 alumina scale, referred to as the TGO. The oxidation resistance increases with Al content, but too much Al can also lower the ductility and melting temperature of the alloy [10, 18]. As such, the level of Al is typically controlled between an upper and lower limit, approximately 8-12 wt.%.

Cr improves corrosion resistance and also promotes the formation of a continuous alumina scale by increasing the activity and diffusivity of Al [17, 18]. This reduces the level of Al needed to form an Al_2O_3 scale, which is beneficial to the ductility and melting temperature of the alloy. Cr also lowers the activity of O at the oxide scale / alloy interface, which reduces the diffusion of O into the alloy and improves oxidation resistance. However, high levels of Cr promote the formation of Cr_2O_3 which may decompose into undesirable CrO_3 above 900 °C [4].

The major alloying constituents of MCrAlY alloys are Ni and Co. Ni is beneficial to the ductility and strength of MCrAlY alloys as it promotes the formation of the ductile γ-Ni phase and the high temperature strengthening phase γ'-Ni_3(Al,Ti) [4, 5]. Co provides microstructural stability by preventing detrimental phase and volume changes, but can also lower the oxidation resistance of the coating [4]. High Ni alloys typically provide high oxidation resistance whereas high Co alloys provide high corrosion resistance.

Minor alloying elements such as Y and Hf have been shown to improve the adherence of oxide scales [19–23]. Ta has also been shown to increase the creep resistance and tensile yield strength of MCrAlY coatings but often at the cost of reduced ductility [24, 25].

MCrAlY coatings typically exhibit FCC γ-Ni and BCC β-NiAl phases, but ordered FCC γ'-Ni_3(Al,Ti) and TCP σ-CrCo phases have also been reported [6, 26–28]. γ'-Ni_3(Al,Ti) phase occurs in alloys with high Ni content whereas σ-CrCo formation is caused by an excess of Cr.

Recent studies have used MCrAlY powders with compositions close to Co-32Ni-21Cr-8Al-0.5Y (wt.%) [9, 29–35] which produces coatings with an FCC γ-Ni matrix and approximately 30 vol.% BCC β-NiAl phase. Other studies have used MCrAlY powders with higher levels of Al ($\geq$ 10 wt.%) [36–43] which produce coatings with higher phase fractions of the β-NiAl phase.

The β-NiAl phase acts as an Al reservoir for the formation of the Al_2O_3 alumina scale, commonly known as the TGO. At high temperatures, the β-phase depletes due to a flux of Al towards the alumina scale and the size of the β-depletion zone, as well as the TGO thickness, increases over time. Large β-depletion zones have been shown to adversely affect the mechanical and chemical properties of MCrAlY coatings and accelerate the failure of a TBC system [8, 44, 45]. Higher levels of Al increase the phase fraction of β-phase and reduce the size of the β-depletion zone [8, 44–48], but also increase the growth of the TGO [49] and decrease the ductility of the alloy, which can also accelerate failure of the TBC.

It is clear that the phase fraction of β-NiAl influences the mechanical and chemical properties of MCrAlY alloys. The influence of β-NiAl needs to be understood if new TBC systems are to be developed. The phase fraction of β-NiAl phase in a MCrAlY bond coat is controlled by the level of Al and Ni in the alloy, but is also influenced by the method used to manufacture the bond coat, which is discussed in the next section.

2.4.2 Processing of Overlay Bond Coats

The first deposition method used to deposit MCrAlY coating was EB-PVD [7, 50]. Recently, MCrAlY overlay bond coats deposited by low-pressure plasma spraying (LPPS) or by high velocity oxy-fuel (HVOF) thermal spraying have become more widely used because of the advantages over EB-PVD such as low cost, better control of composition and the possibility to employ complex MCrAlY alloys with tailored microstructures [43, 47, 51]. HVOF thermal spraying offers the advantage of producing low-porosity coatings at relatively low cost compared to LPPS and

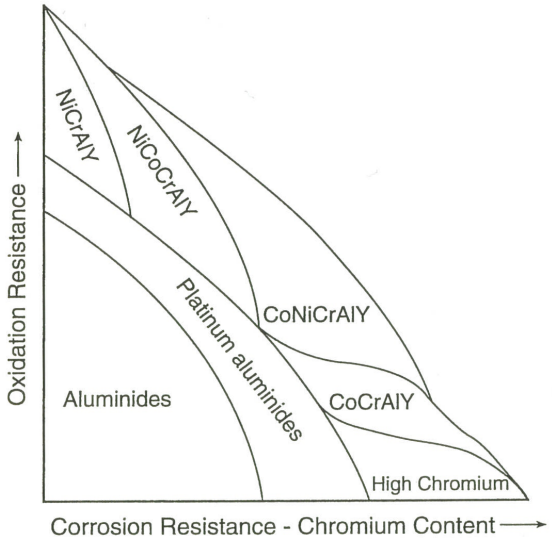

FIGURE 2.6: Optimum MCrAlY alloy compositions in relation to oxidation and hot-corrosion resistance. Figure reproduced from [17].

has been employed for the manufacture of MCrAlY coatings in previous works [29, 31, 36].

HVOF thermal spraying involves injecting a bond coat material, in the form of a feedstock powder, into a high temperature, high speed gas jet. The powder is fed into a combustion chamber, accelerated along a nozzle and fired towards the substrate. Depending upon the type of fuel used, the gas temperature and velocity may range between 1650-2700 °C and 1300-2000 ms^{-1} respectively, and the powder particles may obtain velocities between 480-1020 ms^{-1} [4].

In HVOF thermal spraying, the size of the powder particles influences their thermal history and velocity, which in turn can directly affect the level of porosity and oxide retained within the coating. One study by Thorpe and Richter [52] found the velocity of particles 10 μm and 50 μm in diameter to be 1050 ms^{-1} and 500 ms^{-1}. The precise velocities obtained are dependent upon the type of gun and fuel used, but the findings by Thorpe and Richter [52] provide a useful insight to the effect of powder particle size. Lugscheider et al. [43] and Seachua [53] have also reported significant velocity differences for differently sized powder particles.

Rajasekaran et al. [54] investigated the effect of powder size on the microstructure of HVOF sprayed MCrAlY bond coats and found that a powder size range of 5-37

μm produced coatings with lower porosity and higher oxide content compared to medium (11-62 μm) and coarse (45-75 μm) size ranges, whereas the coarse sized powder (45-75 μm) produced coatings with comparatively higher porosity and lower oxide content. Seachua [53] also reported similar observations.

Development of HVOF spraying as an industrial process for the manufacture of MCrAlY coatings has led to the use of spherical powders with a typical size range of 15-45 μm [55, 56]. MCrAlY powder size distributions are typically given as a range, specified by the sieving process used to separate the original gas atomised powder. For example, Saeidi [56] reported the median particle size for Praxair CO-210-24 powder (size range -45 +20 μm) to be approximately 34 μm with approximately 80 % of particles between 25-45 μm.

The gas temperature and gas velocity directly influence the degree to which a powder particle melts during flight. Melting of the powder particles can introduce oxides into the coating [51, 57], which have been shown to affect the mechanical properties of HVOF coatings [24]. Conversely, under-heating of the powder may introduce porosity into the coating. Several other spray parameters also need to be controlled during HVOF thermal spraying; the effect of spray distance, powder feed rate, fuel/oxygen ratio, fuel type and shroud gas have all been investigated and shown to affect the microstructures of thermally sprayed coatings [29, 43, 54, 57, 58]. As such, the type of HVOF gun employed, as well as the spray parameters, need to be carefully considered when manufacturing bond coats through HVOF thermal spraying.

First generation HVOF systems typically used a parallel sided nozzle and a gas fuel, such as hydrogen or propylene, and were able to obtain gas velocities of approximately 1300 ms^{-1} from gas temperatures around 2700 °C [59, 60]. Newer generation systems use liquid fuels such as kerosene and a converging-diverging throat between the combustion chamber and nozzle, which is able to significantly increase the gas velocity. The newer generation systems are able to produce gas velocities of 1700 ms^{-1} from gas temperatures around 2200 °C [61].

Bond coats are typically deposited onto the surface of a Ni or Co based superalloy [4]. The superalloy often undergoes a series of heat treatments and ageing treatments after the bond coat has been deposited. The heat treatment reduces the level of porosity within the bond coat, improves the adhesion between the bond coat and superalloy, and allows for strengthening and ageing of the superalloy. The exact heat treatments carried out are not generally published by the industry but a typical treatment may be 1-2 hours at 980-1150 °C for Inconel superalloys or up to 8 hours at 1080 °C for Nimonic alloys [62].

2.4.3 Microstructure of Overlay Bond Coats

Although the final microstructure of an overlay bond coat typically results from a vacuum heat treatment at $\sim$ 1100 °C (as described in the previous section), the as-deposited structure still has a significant influence on the final microstructural characteristics. It is well known that the as-deposited microstructure is highly dependent upon the deposition method and so this section reviews the main deposition methods used for overlay coatings and the typical as-deposited microstructures obtained by each method.

2.4.3.1 Air Plasma Spraying (APS)

Air plasma spraying (APS) involves injecting powder particles into a high pressure plasma gas stream, which can reach temperatures up to 15000 K [4]. A typical feature of APS is that powder particles are exposed to high temperature but a relatively low velocity gas stream; between 700-1000 ms^{-1}. The high temperature typically causes the powder particles to become fully molten during flight. This can cause extensive oxidation of the powder particles and results in APS coatings typically exhibiting lamellar splats with inter-splat oxides. An example of an APS deposited CoNiCrAlY coating is shown in Fig.2.7 [33]. APS coatings have been extensively used in the past but typically for non-rotating parts.

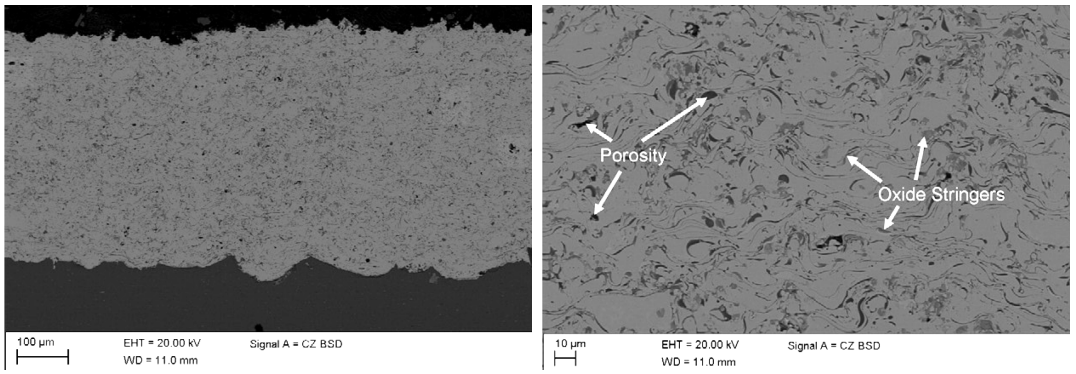

(a) (b)

FIGURE 2.7: Microstructure of an as-sprayed APS CoNiCrAlY coating. Figure reproduced from [33].

2.4.3.2 Low Pressure Plasma Spraying (LPPS)

Low pressure plasma spraying (LPPS), also referred to as vacuum plasma spraying (VPS), is a development of the APS process designed to reduce the level of oxidation in the as-sprayed coating. This is achieved by conducting the spraying process in a chamber held under partial vacuum and back-filled with inert gas [4]. The low pressure environment allows higher plasma gas velocities to be achieved, which means the stand-off distance between the gun and substrate is also increased. This results in the powder particles residing in the gas for longer time periods and staying at high temperature for longer. This allows the powder particles to become molten without being exposed to air, reducing the amount of oxide retained in the as-sprayed coating. As-deposited LPPS coatings can exhibit high porosity, which is eliminated during subsequent heat treatment. However, the absence of oxide in the coating means that during heat treatment, porosity can be eliminated and a defect free microstructure can develop. Fig.2.8 shows an example of an as-sprayed VPS coating, which exhibits significant porosity, alongside the defect-free microstructure of a heat treated VPS coating [56].

2.4.3.3 High Velocity Oxy-Fuel (HVOF) Thermal Spraying

MCrAlY bond coats deposited by HVOF thermal spraying, in the as-sprayed condition, typically consist of unmelted and partially melted powder particles

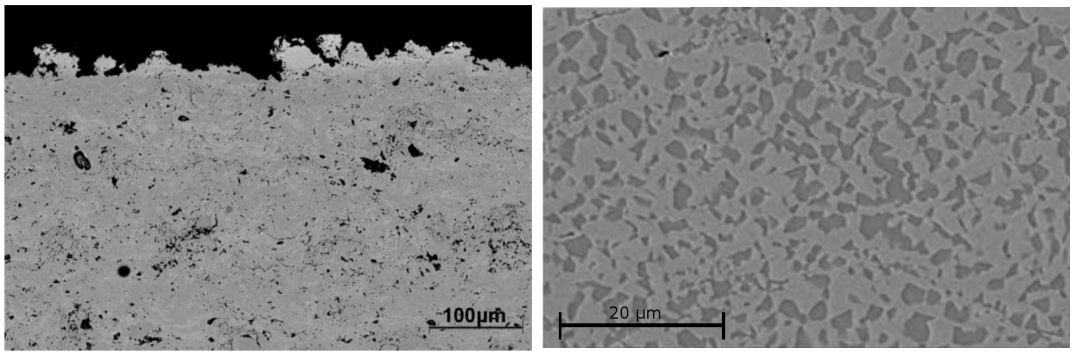

(a) (b)

FIGURE 2.8: Microstructure of an (a) as-sprayed and (b) heat treated VPS CoNiCrAlY coating. The as-sprayed microstructure exhibits significant porosity which is eliminated after heat treatment. Figure reproduced from [56].

interconnected by regions of material which fully melted during spraying and rapidly solidified upon cooling [56, 59, 63]. Depending upon the spray parameters used, there may also be varying levels of porosity and oxide retained in the as sprayed coating. A vacuum heat treatment of 2 hours at 1100 °C, which approximates to the heat treatment given to bond coats deposited onto Inconel superalloys, has been shown to homogenise the microstructure of the coating and reduce the level of porosity [56, 63]. The microstructure of a HVOF MCrAlY bond coat, deposited by a MetJet liquid fuel gun, in the as sprayed and heat treated condition is shown in Fig.2.9a and 2.9b respectively..

Chen [63] and Saeidi [56] investigated coatings manufactured from Praxair CO-210-24 using HVOF thermal spraying (MetJet liquid fuel gun) and VPS. Both authors found the HVOF liquid fuel and VPS coatings exhibited broadly similar microstructures after heat treatment, but with less oxide and porosity found in the VPS coatings. This is not surprising considering VPS is conducted under vacuum whereas HVOF is conducted under in air environment.

2.4.3.4 Electron Beam Physical Vapour Deposition (EB-PVD)

EB-PVD is the process by which ingots of the coating material are vaporised using focused electron beams. This creates a vapour cloud of the coating material which then deposits onto the superalloy substrate. The process is carried out in a highly

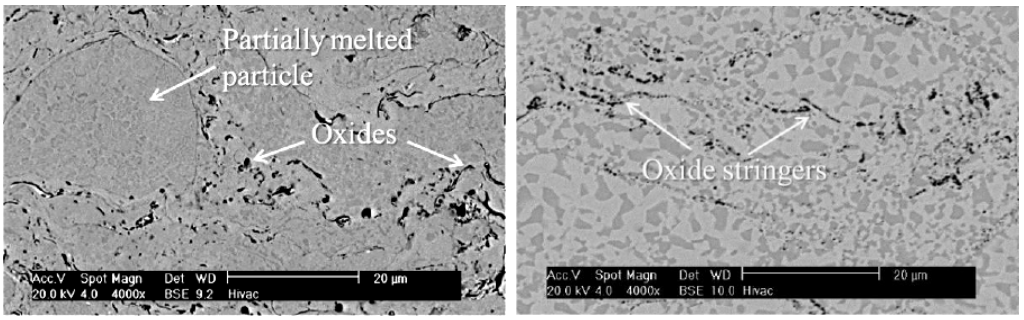

(a) As Sprayed (b) Heat Treated

FIGURE 2.9: Microstructure of a HVOF CoNiCrAlY bond coat in the (a) as sprayed and (b) heat treated condition. In the as sprayed coating partially melted and unmelted powder particles can be identified whereas the heat treated coating exhibits a homogeneous microstructure. Figure reproduced from [63].

evacuated chamber which reduces oxidation of the coating material [4]. EB-PVD coatings typically feature low porosity and low oxide content, but can also be highly textured as shown in Fig.2.10.

FIGURE 2.10: Microstructure of an EB-PVD CoCrAlY bond coat showing the aligned grain structure. The light and dark regions are γ-Ni phase and β-NiAl phase respectively. Figure reproduced from [4].

2.4.3.5 Microstructure Evolution due to Inter-Diffusion With Substrate

For bond coats deposited onto substrates, the microstructure of bond coats may evolve over time at high temperature due to the interdiffusion of elements between the superalloy substrate and the bond coat. Elements such as Ni, Co, Cr, Ti, W and Hf may diffuse into the bond coat and cause the precipitation of carbides and

Cr rich phases [4], which have a detrimental effect on the bond coat mechanical properties. Interdiffusion can also cause a loss of Al in the bond coat, which can increase β-depletion and have a detrimental effect on the oxidation resistance and mechanical properties of the bond coat.

In order to understand how the microstructure of MCrAlY alloys influences the mechanical properties, so to allow the development of enhanced MCrAlY bond coats, it is necessary to obtain consistent data from free-standing MCrAlY coatings (so as to remove the effect of interdiffusion) whilst maintaining the same deposition method and spray parameters. It is also necessary to understand the microstructure of the powder particle and its influence on the microstructure of the thermally sprayed coating.

2.5 Tensile Properties of MCrAlY Bond Coats

As discussed in section 2.2, the tensile and creep properties of the bond coat have a significant impact on the durability of TBCs. Both the tensile and creep properties are influenced by the coating composition, microstructure and manufacturing process. As such, understanding the tensile and creep properties with respect to these parameters is crucial if accurate life prediction models or new generations of TBCs are to be designed. The tensile properties, i.e. the yield strength, elastic modulus, ductility and DBTT, as well as the creep properties are discussed below.

2.5.1 Ductile to Brittle Transition Temperature (DBTT)

The ductility of a bond coat alloy is measured as the strain to initiate first cracking [64]. When the ductility is plotted as a function of temperature, as shown in Fig.2.11 [4], a transition from high temperature ductile behaviour to low temperature brittle behaviour can be observed, which allows the DBTT to be determined. Approximate values for the DBTT of various MCrAlY coatings are given in table 2.1. The DBTT can vary from below 100 °C to above

800 °C and is influenced by a variety of factors such as composition, phase distribution, microstructure and manufacturing process [4, 64]. It is therefore difficult to theoretically calculate the DBTT of a MCrAlY coating as a function of composition. However, a simple approximation is that increasing the Al content results in a higher DBTT [4, 64, 65] due to an increased phase fraction of the BCC β-NiAl phase, which can be considered the compound undergoing the brittle to ductile transition [4, 64, 66–70]. The brittle to ductile transition of β-NiAl occurs when the slip planes in the ordered BCC β-NiAl phase become thermally activated at high temperature [69]. Diffusion aluminides, which are predominately β-phase, exhibit higher DBTT's compared to MCrAlY coatings which contain both β-phase and γ-phase [66]. The DBTT is an important property of MCrAlY coatings as the tensile properties such as the yield strength, elastic modulus and ductility all change significantly across the DBTT. It is therefore essential that for any MCrAlY bond coat, an accurate DBTT is determined.

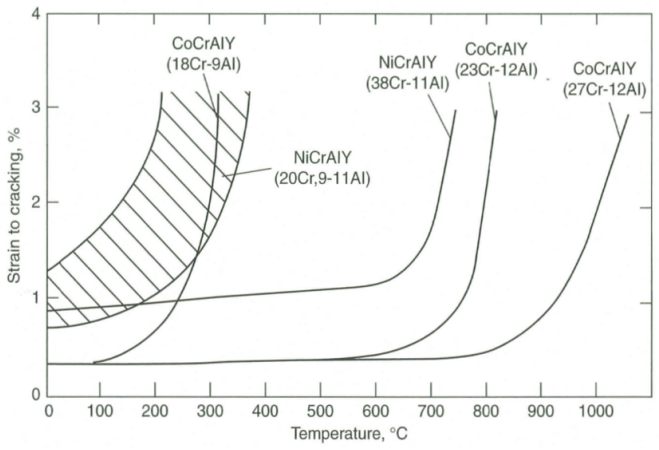

FIGURE 2.11: Strain to cracking as a function of temperature for MCrAlY coatings of various compositions. Figure reproduced from [4].

2.5.2 Yield / Fracture Strength and Elastic Modulus

A significant problem in determining the yield and fracture strength of MCrAlY bond coats is that bulk alloy samples, which are required for conventional test methods, are not equivalent to thin bond coats (approximately 200 μm) used in TBCs. The difficulties and cost involved in testing thin specimens means the

Coating Composition (wt.%)	Estimated DBTT (°C)
CoAl [4]	878-1070
Co-18Cr-9Al-Y [4]	150-200
Co-20Cr-12.5Al-Y [4]	600-650
Co-27Cr-12Al-Y [4]	800-900
Co-32Ni-21Cr-9Al-Y [71, 72]	600-700
NiAl [4]	868-1060
NiAl [70]	400-600
Ni Aluminide Coating [73]	693
52Al-36Ni-7Cr-4Ti-1Co [67] (Ni Aluminide Coating)	760
Ni-20Cr-9-11AlY [4]	25-200
Ni-20Co-18Cr-12.5Al-0.6Y [74]	650-750
Ni-38Cr-11-Al-Y [4]	600-650

TABLE 2.1: Estimated DBTT values for various MCrAlY alloys based on the literature, highlighting the significant variation in the DBTT with alloy composition.

available data on the yield/fracture strength of thin MCrAlY bond coats is limited. Nevertheless, the available data does show that the yield strength of free-standing MCrAlY coatings can vary from between 500-1200 MPa below the DBTT to less than 300 MPa above the DBTT [24, 39, 41, 71]. Figs.2.12 and 2.13 show how the yield strength of MCrAlY coatings can decrease rapidly above the DBTT, indicated by the marked increase in ductility.

It has also been shown that the yield strength is sensitive to coating composition and minor element additions [24], as well as the deposition method [75]. The elastic modulus of MCrAlY coatings has been reported to be more consistent at around 170 GPa [4, 76], however a review of the literature shows that the elastic modulus can vary from between 163 - 226 GPa depending upon the composition and deposition method [24, 35, 39, 58, 75, 77]. In an attempt to relate coating microstructure to the elastic modulus Saeidi et al. [58] measured the elastic modulus of the γ-phase and β-phase by nano-indentation. The elastic modulus of the γ-phase was measured as 231 GPa and the elastic modulus of the β-phase as 215 GPa. Webler et al. [78] however, reported the elastic modulus of the γ-phase and β-phase to be 216 GPa and 262 GPa respectively when measured by nano-indentation.

It is clear that the available data concerning the mechanical properties of thin MCrAlY bond coats is not comprehensive or conclusive. In order to quantitatively compare the tensile properties of different MCrAlY bond coats with respect to composition and microstructure, it is necessary to obtain consistent tensile property data from bond coats deposited by a single deposition method, which is one of the main objectives of this work.

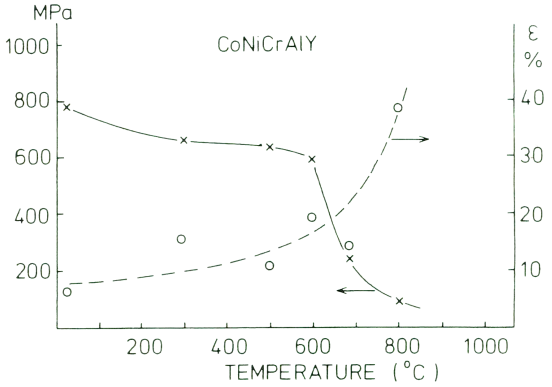

FIGURE 2.12: Yield strength (crosses) and ductility (circles) of a free standing CoNiCrAlY coating. Figure reproduced from [76].

2.6 Creep Properties of MCrAlY Bond Coats

The creep properties of MCrAlY bond coats are sensitive to composition, which means the creep properties of a bond coat deposited onto a superalloy substrate may evolve over time due to interdiffusion with the substrate. Therefore, in order to develop new MCrAlY alloys with improved creep resistance, it is necessary to understand the creep properties of free standing MCrAlY bond coats.

The available creep data is limited and is often obtained from bulk alloy samples, which may not be representative of thin bond coats. As such, consideration must be given to the manufacturing method used to produce the MCrAlY specimen when comparing the creep properties of different MCrAlY alloys. The available data on the creep properties of MCrAlY alloys is reviewed below.

As described in section 2.3, the creep properties of materials are often described with reference to the stress exponent n. Brindley and Whittenberger [79] reported

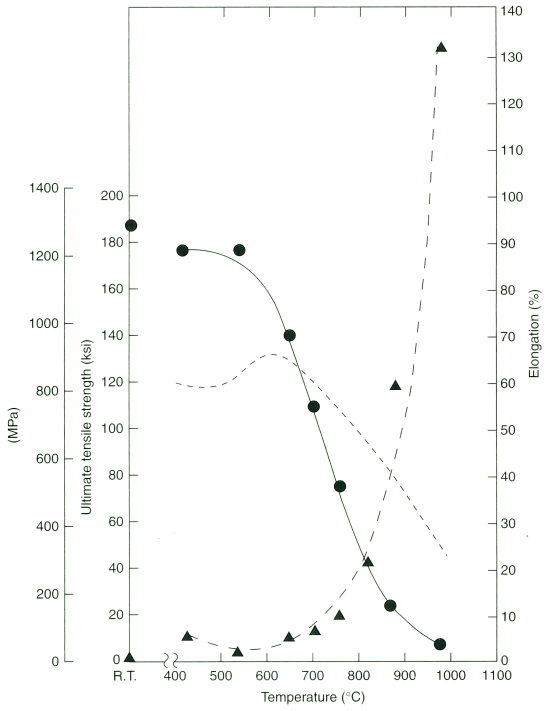

FIGURE 2.13: Yield strength (circles) and ductility (triangles) of a free standing LPPS deposited Co29Cr6AlY coating and yield strength of IN 738 alloy (dotted line). Figure reproduced from [4].

that n varies between 2.4-7.1 for different MCrAlY alloys. The value of n has been reported as 2.4-4.4 for a Co-32Ni-21Cr-8Al-0.5Y alloy [72, 80], 3.8-4.5 for various NiCrAlY alloys [80, 81] and 4.7-6.0 for a NiCoCrAlY alloy [82]. Zhang et al. [83] also reported n to be 6.5 for NiCr and NiCrAl coated Nickel 690 alloy specimens.

Hesbur and Miner [81] reported a NiCoCrAlY coating exhibited superplasticity between 850 - 1050 °C. Superplasticity is not well documented for MCrAlY alloys but has also been reported for a Ni-22Cr-10Al-Y alloy between 950-1150 °C [84]. The onset of superplasticity appears to decrease the value of the stress exponent to less than 2 [84]. It is also well established that the creep resistance of MCrAlY alloys decreases with temperature [72, 79, 80, 82].

It was shown by Taylor and Bettridge [24] that the creep behaviour of MCrAlY alloys is sensitive to oxide dispersions. This is highly significant as it means the method used to manufacture the MCrAlY creep specimens will affect the creep behaviour.

Multiple studies have used monolithic specimens i.e. specimens machined from bulk samples [24, 72, 79, 81, 82]. The production of the bulk samples is varied; some studies deposited thick coating samples onto substrates through thermal spray techniques [24, 79, 81] whilst other studies manufactured bulk samples through the isostatic hot pressing of powders [72] and casting techniques [82]. Taylor et al. [85] developed a composite specimen where a NiCrAlY alloy was deposited onto a core of austenitic steel, where the creep properties of the NiCrAlY alloy were investigated by comparing the creep behaviour of the composite specimen with the well established creep behaviour of the austenitic steel.

Other studies have investigated the creep properties of Ni-based superalloys coated with thin MCrAlY bond coats, but these studies focused on how the bond coat influenced the creep behaviour of the superalloy substrate, rather than attempting to evaluate the creep properties of the bond coat [83, 86].

It is unclear from the literature how the creep properties of MCrAlY coatings are influenced by the microstructure. Comparing the literature indicates that MCrAlY coatings with high Ni and Al content exhibit higher stress exponents, but there is little data evaluating the effect of the constituent phases and microstructure. Thompson et al. [80] demonstrated that a NiCrAlY coating exhibited a higher creep resistance than a CoNiCrAlY coating, but did not discuss the creep properties with reference to the microstructure of the coatings.

It is clear that in order to understand the creep behaviour of MCrAlY bond coats, with reference to composition and microstructure, it is necessary to obtain consistent creep data from specimens manufactured from a relevant thermal spray technique. It is also important that the creep properties of thin MCrAlY bond coats are distinguished from bulk alloy samples. As such, test techniques suitable for thin coating specimens must be employed.

2.7 Test Techniques For MCrAlY Bond Coats

A summary of the available data concerning the tensile properties of MCrAlY coatings, as well as the test techniques employed, is shown in table 2.2. The test techniques employed include; three or four-point bending [35, 47, 58], nano or spherical indentation [77, 78], micro tensile testing [24, 41, 74], and the small punch (SP) test, which is sometimes also referred to as the miniature disc bend test (MDBT) [39, 40, 63].

A summary of the available data concerning the creep behaviour of MCrAlY alloys, as well as the test techniques employed, is summarised in table 2.3. The majority of studies have employed uni-axial tensile testing [24, 72, 79–85], which require bulk alloy samples. Recently, Chen [63] tested 0.43 mm thick, free-standing MCrAlY coating specimens using the small punch creep (SPC) test method. Chen demonstrated the SPC test method offers the possibility to test MCrAlY specimens which more accurately resemble thin MCrAlY bond coats. However, the study was limited to a single alloy tested at 750 °C. The SPC method has not been widely applied to MCrAlY alloys but has been used to determine the creep properties of other steels [87–92].

The small punch test requires 8 mm diameter discs of approximately 0.5 mm thickness. The small specimen size and versatility of the small punch test makes it an attractive test method for testing MCrAlY bond coats and a limited number of previous studies have already employed it to evaluate the mechanical properties and creep performance of MCrAlY coatings [39, 40, 63, 67].

There exist two main types of small punch test: the SPC test, where a constant load is applied to the sample and the sample deformation is measured, and the small punch tensile (SPT) test, where a constant displacement rate is applied to the sample and the load is measured. Both the SPC test and SPT test may be run on a single small punch rig, but the analysis for each test is different. As such, the methodology for the SPT test and SPC test are considered separately.

Composition (wt.%)	Manufacturing Method	Microstructure (*Estimated)	Test Method	Yield Strength (MPa)	Elastic Modulus (GPa)
Co-32Ni-22Cr-8Al-0.5Y [58]	HVOF	71 vol.% γ 29 vol.% β	Three point bending	-	180 (200 °C) 160 (500 °C)
Co-32Ni-21Cr-8Al-0.5Y [75]	HVOF	70 vol.% γ * 30 vol.% β *	Lateral compression of a tube	-	70 (400 °C) 30 (700 °C)
	LPPPS				50 (400 °C) 35 (900 °C)
Co-32Ni-21Cr-8Al-0.5Y [24]	APS	70 vol.% γ * 30 vol.% β *	Micro tensile testing	770 (RT) 41 (800 °C)	169 (RT)
Co-18Cr-8Al-0.7Y [24]		-		34 (800 °C)	158 (RT)
Ni-15Co-20Cr-11Al-0.5Y [24]		-		95 (800 °C)	158 (RT)
Ni-23Co-17Cr-12Al-0.5Y [40]	APS	76 vol.% γ 24 vol.% β γ' precipitates	Small punch tensile test	860 (RT) (crack (initiation stress)	-
40Ni-19Co-16Cr-23Al-0.3Y [41] (at.%)	LPPS	53 vol.% γ 47 vol.% β	Micro tensile test	1200 (RT) 220 (500 °C)	-
Ni-22Co-17Cr-13Al-0.65Y [35]	HVOF	42 vol.% γ 58 vol.% β	Four point bending	-	138 (RT)
	LPPS				163 (RT)
Ni-23Co-17Cr-12-Al-0.5Y [39]	APS	76 vol.% γ 24 vol.% β γ' precipitates	Small punch tensile test	500 ($\leq$ 500 °C) 300 (800 °C)	226 (RT) 192 (800 °C)

TABLE 2.2: A summary of the available tensile data on MCrAlY alloys. An asterisk denotes the phase fractions which were not provided by the original authors and have been estimated based on the composition of the alloy.

Composition (wt.%)	Manufacturing Method	Test Method	Test Specimen	Stress Exponent n
Ni-16Cr-6Al-0.3Y [79]	APS	Tensile test (700-1000 °C) high strain $\approx 10^{-4}$ low strain $\leq 10^{-5}$	Cylindrical specimen 3 – 6.5 mm diameter	3 (high strain)
Ni-18Cr-12Al-0.5Y [79]				2.7 (high strain) 7.1 (low strain)
Ni-35Cr-6Al-0.95Y [79]				2.4 (high strain) 5.0 (low strain)
Ni-20Co-17Cr-14Al-0.5Y [81]	LPPS	Tensile Test	Tensile specimen 12.7 mm gauge length 3 mm diameter	3.8 (661-850 °C)
68Ni-25Cr-6Al-0.5Y [85]	APS	Tensile test	Composite *	Not given
Ni–23Co–19Cr–13Al-0.5Y [82] (Estimated)	Cast specimen	Tensile test	Not given	4.73 - 5.99 (700-950 °C)
Ni-22Cr-10Al-1Y [80] Co-32Ni-21Cr-8Al-0.5Y	VPS	Tensile test	Flat specimen 1.4 mm thick	2.9 - 4.5 (600-850 °C)
76Ni-18Cr-6Al [83] Ni 690 alloy substrate	APS	Tensile test	Flat tensile specimen 52 × 6 mm gauge length 3 mm substrate & 0.3 mm coating	6.48 (690 °C)
Ni-22Cr-10Al-Y [84]	Spark plasma sintering	Compression test	5 x 3 x 3 mm square bar	2 - 8 (950-1150 °C)
Co-32Ni-21Cr-9Al-0.5Y [72]	Hot isostatic pressing	Tensile test	Button-head tensile specimen 6.35 mm diameter 35 mm gauge length	2.8 - 4.41 (677-899 °C)
Co-32Ni-21Cr-8.6Al-0.5Y [24]	VPS	Tensile test	Flat tensile specimen 12.7 mm gauge length 6.4 mm wide and 1.5 mm thick	Ta and Pt improved creep resistance
Co-32Ni-21Cr-8.6Al-Y [63]	HVOF	Small punch creep	8 mm diameter disc 0.43 mm thick	7.5 (750 °C)

TABLE 2.3: A summary of the available creep data on MCrAlY alloys. * flat 25.4 × 6.4 mm tensile specimen with a 0.38 mm core of austenitic steel and 0.15 mm thick coatings on each surface [85].

2.8 Small Punch Tensile (SPT) Testing

The small punch tensile test was developed in the 1980's as part of efforts to develop small scale testing methods and since then has been employed to study materials for which test material is limited [93–100]. The standard geometry of the SPT test is shown in Fig.2.22. A specimen is clamped between an upper and lower die and the load is applied to the specimen through a hemispherical punch head.

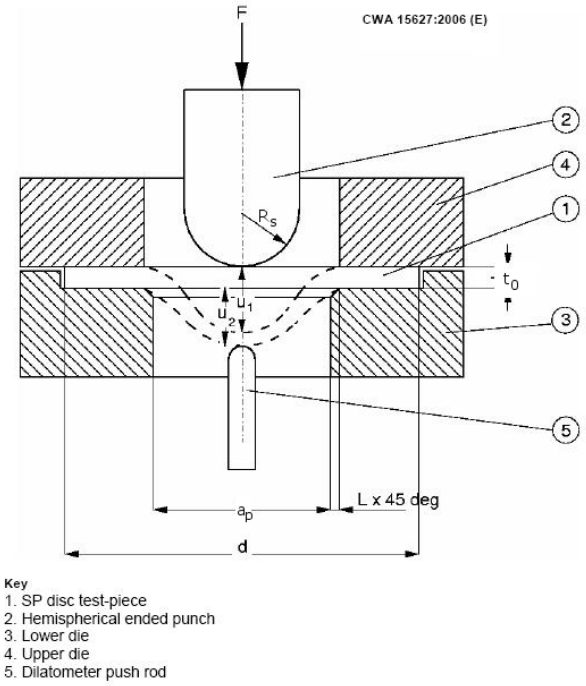

FIGURE 2.14: Standard geometry of the small punch (SP) test where a SP specimen is clamped between an upper and lower die and the load is applied through a hemispherical punch head. Figure reproduced from [101].

The small punch tensile (SPT) test was originally referred to as the miniature disc bend test (MDBT), and was developed to obtain load-displacement data from 3 mm diameter transmission electron microscopy (TEM) coupons. The first reported uses of the MDBT were by Huang et al. [93] and Manahan et al. [96]. The SP geometry was investigated by Baik et al. [94] who reported the optimum punch diameter to be 2.4 mm. Lucas et al [102] investigated the effect of punch radius, receiving-hole radius and specimen thickness but found no optimum geometry, stating that the geometry was subjective depending upon the objective of the

work. Li et al. [100] investigated the effect of clamping the SP specimens and noted that unclamped specimens produced greater unpredictability compared to clamped specimens due to the difficulty in ensuring a uniform contact area over the supporting die. Baik et al. [94] demonstrated that 10 mm x 10 mm square specimens could be used for SP testing provided they were clamped using the same upper and lower dies, as the test geometry is dependent upon the unclamped central region. In an effort to standardise testing procedures and results, the European Committee for Standardisation (CEN) created a workshop agreement in 2006 [101], which outlined that small punch tests should use clamped disc specimens of 8 mm diameter and 0.5 mm thickness, receiving holes of 2 mm radius and punch diameters between 2-2.5 mm. However, the sensitivity of the small punch test to rig geometry means efforts are still being made to standardise the SP geometry, testing procedure and data analysis [103–105].

2.8.1 Experimental Load-Displacement Behaviour

The main application of the small punch tensile test over the past 30 years has been to investigate neutron irradiation damage in nuclear reactor materials and lifetime assessment of structural materials in power plants. As such, there is comprehensive data on the load-displacement behaviour of numerous steels [94, 96, 99, 106, 107]. Recently, the small punch test has also been applied to thermally sprayed NiAl coatings [67], thermally sprayed MCrAlY coatings [39, 40, 63], Ni-based superalloys [108], Ti-6Al-4V alloys manufactured by electron-beam melting [109] and metal matrix composites (MMCs) [110].

The load-displacement curve obtained from the SPT test for a ductile material typically exhibits 4 distinct regions as shown in Fig.2.15 [100, 111, 112]: (i) an initial elastic regime associated with micro-yield under the punch head; (ii) a transition from elastic to plastic bending associated with the spread of the yield zone from the tensile surface and subsequent plastic bending; (iii) a transition from plastic bending to membrane stretching indicated by an inflection point in

the load-displacement curve; and (iv) failure region associated with a maximum load, localised thinning and crack initiation.

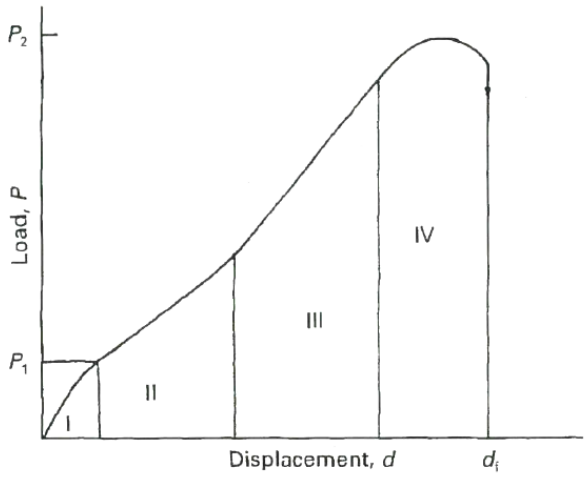

FIGURE 2.15: Schematic diagram of a typical SPT test load-displacement curve obtained for a ductile material. Figure illustrates the four distinct regions described in the text. Figure reproduced from [112].

The four distinct regions shown in Fig.2.15 are observed for materials with sufficiently high ductility. Materials with low ductility may fail shortly beyond the elastic region [93]. Fig.2.16 shows the load-displacement curves obtained at various temperatures for a Ni-Cr steel [94] which demonstrates the change in the material load-displacement behaviour with temperature. At -52 °C the steel exhibits all four regions shown in Fig.2.15 and ductile failure is indicated by a plateau in the load-displacement curve and gradual drop in the load. At -195 °C low-ductility failure occurs shortly after the transition to plastic bending as indicated by a sharp load drop. The load-displacement behaviour at -91 and -80 °C demonstrates the change in behaviour across the DBTT.

The change in material behaviour across the DBTT has also been observed for a NiAl diffusion aluminde coating as shown in Fig.2.17 [67]. The general features in SPT load-displacement curves can indicate whether a material has high or low ductility. Low ductility behaviour is characterised by predominately linear load-displacement curves and a sharp load-drop at failure, whereas high ductility behaviour is characterised by the four bending regions depicted in Fig.2.15.

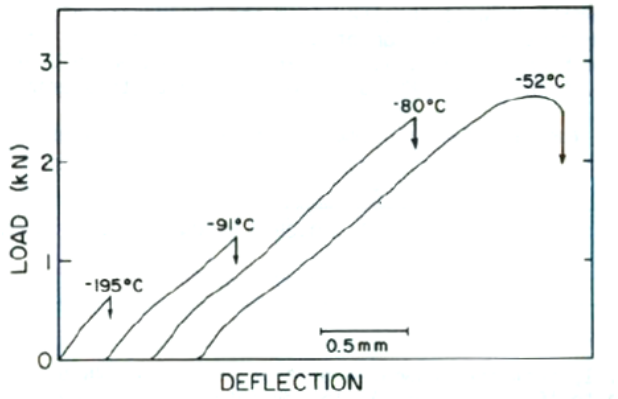

FIGURE 2.16: Load-displacement curves for a Ni-Cr steel tested at various temperatures showing the change in behaviour as the steel transitions from brittle to ductile behaviour. Figure reproduced from [94].

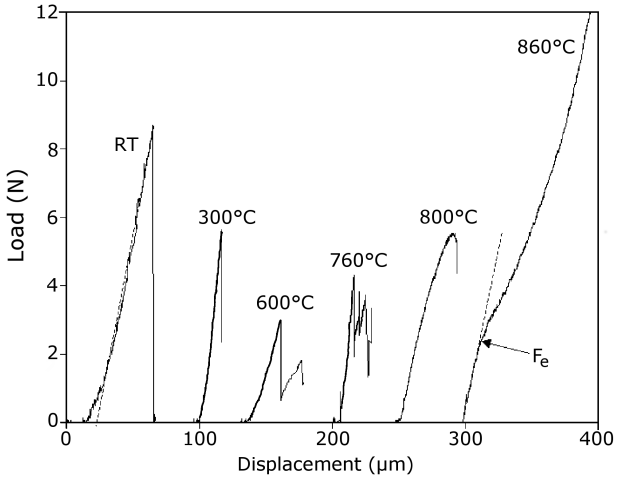

FIGURE 2.17: Load-displacement curves obtained for a NiAl coating by Eskner et al. [67] between RT and 860 °C showing the change in load-displacement behaviour as the NiAl coating experiences a transition from brittle to ductile behaviour. Figure reproduced from [67].

2.8.2 Development of Cracking Patterns in SPT Specimens

The stress distribution within a SPT test specimen evolves with respect to specimen deformation [96, 109, 113]. Thus, brittle and ductile materials exhibit different fracture patterns. Fig.2.18 [114] shows different cracking patterns and the corresponding load-displacement curves observed for brittle and ductile materials. The Al_2O_3 sample failed within the elastic region of the load-displacement curve and split into three evenly sized fragments in a star-like crack pattern. The

ferritic steel specimen at 20 °C exhibited a highly deformed central region and circumferential cracking, which is characteristic of ductile failure. The star like crack pattern and circumferential cracking have been widely reported for various brittle and ductile materials [63, 67, 94, 95, 99, 108, 115, 116].

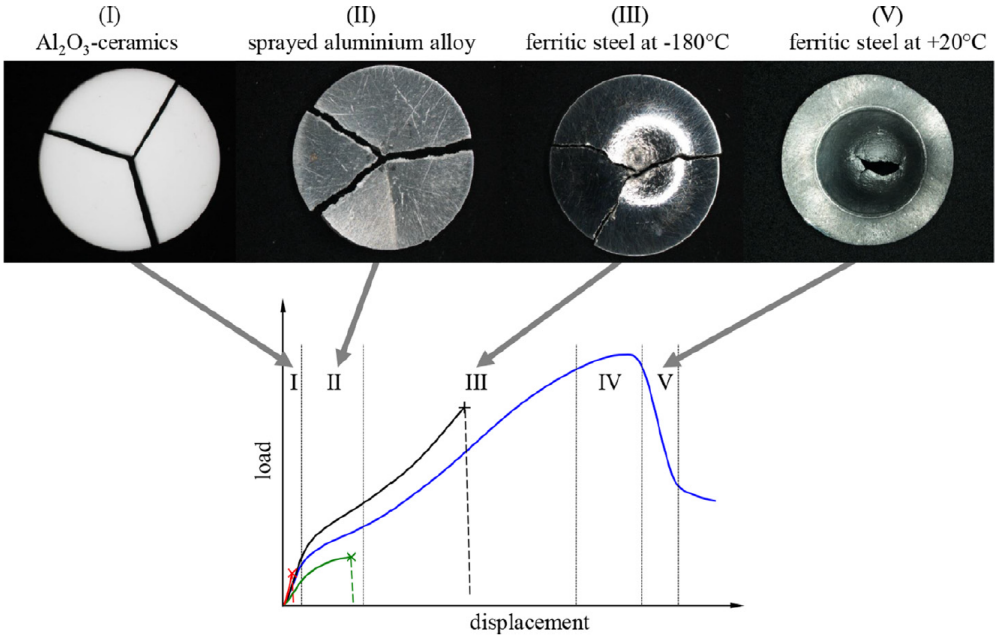

FIGURE 2.18: Different types of fracture for ductile and brittle materials and the corresponding schematic load-displacement curves indicating the different failure modes of SP specimens. Figure reproduced from [114].

2.8.3 Determination of Material Properties from SPT Test Data

Over the past 30 years, the SPT test has been validated as an effective method for determining the ductile to brittle transition temperature, yield strength and fracture strength of both brittle and ductile materials [39, 40, 67, 93, 97, 100, 105, 112, 117–119].

2.8.3.1 Ductile to Brittle Transition Temperature

The ductile to brittle transition temperature can be measured by two methods. The first method is to calculate the total absorbed energy during a SPT test and

plot it against temperature. This has been commonly employed for steels and provides data comparable to the Charpy-V notch (CVN) impact test [94, 95, 106, 112, 119]. The second method, which is more applicable for materials to be used as coatings, is to plot the strain at first cracking as a function of temperature. This provides DBTT data comparable to the literature described in section 2.5.1.

Depending upon whether the SPT specimen has undergone plastic deformation, the strain at first cracking may need to be calculated as an elastic bi-axial strain or a plastic bi-axial strain,. The elastic bi-axial strain (ε_e) can be calculated using the solution provided by Huang et al. [93]:

$$\varepsilon_e = \frac{t_0 \delta}{{a_p}^2 + \delta^2} \tag{2.4}$$

where δ = specimen displacement (m), t_0 = original specimen thickness (m) and a_p is the radius of the lower die receiving hole (m). The solution is based upon the assumption that the bent disc obtains the shape of a spherical cap under elastic bending and is only applicable to calculate the elastic bi-axial strain (ε_e).

The plastic bi-axial fracture strain (${\varepsilon_p}^*$) can be calculated using the semi-empirical relationship derived by Mao et al. [98], shown as Eq.2.5. where δ^* is the displacement at fracture (m) and t_0 is the original specimen thickness (m).

$${\varepsilon_p}^* = 0.15 \left(\frac{\delta^*}{t_0} \right)^{1.5} \tag{2.5}$$

2.8.3.2 Yield/Fracture Strength and Elastic Modulus

Elastic-Plastic Yield Load

The yield strength of a SPT test specimen is directly related to the load corresponding to the transition from elastic to plastic bending, referred to as the elastic-plastic yield load (F_{e}). The yield load can be measured by three methods, as shown in Fig.2.19. The first method is the offset method where F_{e} is defined as the intersect between the load-displacement curve and a line drawn parallel to the

elastic region. This method was introduced by Okada et al. [97] who suggested the line be offset by a distance of $t_0/10$ where t_0 is the original specimen thickness. Cheon and Kim [120] suggested offsetting the line by $t_0/100$ as yielding occurred early on in the SPT test.

The second method is the two tangents method suggested by Mao and Takahashi [99] where F_e is defined as the intersect of two tangents drawn parallel to the elastic and plastic regions. A modified version of this method is outlined in the CEN workshop agreement [101].

The third method defines the elastic-plastic load as the load corresponding to the point where the load-displacement curves stops being linear [110]. Garcia et al. [104] recently evaluated the different methods and found the offset method using $t_0/10$ to be the most appropriate for a variety of steels. Mak [110] argued that the offset and two tangent methods were not suitable for materials with low ductility and materials with undefined yield points, and that the point of non-linearity method should be used for those materials.

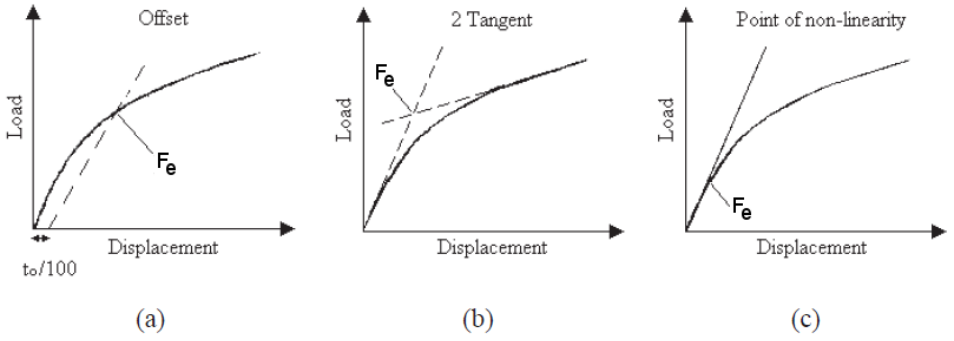

FIGURE 2.19: Plots showing different methods for determing the elastic-plastic load F_e: a) the offset method, b) two tangent method and c) point of non-linearity method for determining the elastic-plastic load F_e. Figure reproduced from [110].

Analytical Solution to Calculate the Yield/Fracture Strength and Elastic Modulus

The yield strength can be calculated from F_e by two methods. The first method is to use the analytical solution provided by Roark [121], shown as Eq.2.6. The

analytical solution is appropriate to the elastic regime of the load-displacement curve and is based upon the bi-axial bending of a thin disc which is clamped at its circumference. The maximum bi-axial bending stress on the tensile surface at the centre of the sample (σ_{max}) is given by:

$$\sigma_{max} = \frac{3F(1+\nu)}{2\pi {t_0}^2}\left(ln\frac{a_p}{r'}\right) \tag{2.6}$$

where F is the load in N, ν is the poisson's ratio, t_0 is the specimen thickness in m, a_p is the radius of the supporting jig in m, β is 0.435 for a disc and r' is the effective radius in m. The effective radius can be calculated using the equations below where r_c is the contact radius between the punch head and the specimen.

$$r' = \sqrt{1.6{r_c}^2 + t_0^2} - 0.675t_0 \qquad \text{for } r_c \leq 0.5t_0 \tag{2.7}$$

or

$$r' = r_c \qquad \text{for } r_c \geq 0.5t_0 \tag{2.8}$$

Li et al. [100] experimentally measured the punch contact radius by applying a static load equal to the yield load and then measuring the impression left on the surface of the sample. For a 264 μm thick Zr_3Al sample the indent was found to be 112 μm. Eskner et al. [67] measured the contact radius on NiAl specimens at various loads and found that the contact radius could be estimated as $t_0/3$.

Substituting F_e into Eq.2.6 provides an approximate value for the yield strength. For brittle materials that exhibit no plastic bending prior to failure, the fracture strength can also be calculated by substituting the fracture load into Eq.2.6.

The analytical solution assumes that the punch contact radius remains constant throughout the test and that friction between the punch and the sample is negligible. Mao et al. [98] demonstrated that the punch contact radius increases

throughout the test as plastic yielding occurs in the sample. As such, the Roark solutions are only valid for elastic bending where the punch contact radius can be assumed to be remain constant.

The slope of the linear region in the load-displacement curve is proportional to the elastic modulus (E) of the specimen [96, 100]. The elastic modulus can be calculated using the following solution provided by Roark [121]:

$$E = \left(\frac{F}{\delta}\right) \frac{3\,{a_p}^2(1-\nu^2)}{4\,\pi\,{t_0}^3} \tag{2.9}$$

where δ is the specimen displacement and the other symbols are the same as in Eq.2.6.

2.8.3.3 Empirical Approach to Calculate Equivalent Uni-axial Yield Strength

Where uni-axial test data exists, empirical relationships correlating the uni-axial yield strength of a SPT specimen and the parameter F_e/t_0^2 can be derived [99, 100, 102–105]. Empirical relationships allow SPT test data of small scale specimens to be directly compared to uni-axial test data of bulk specimens. Unfortunately, there is insufficient uni-axial test data available on MCrAlY alloys to allow empirical relationships to be derived. As such, for SPT testing of MCrAlY coatings, the analytical solutions have been used [39, 40].

2.8.4 Finite Element Modelling of the SPT Test

In order to calculate the bi-axial bending stress or strain during a SPT test after plastic deformation has occurred, it is necessary to use finite element (FE) modelling. Manahan et al. [111] studied the strain induced in a SPT test through finite element modelling and were able to identify the different regimes in the load-displacement curves described in Fig.2.15. Recent FE modelling has helped

to better understand the evolution of the principal stresses within a SPT test specimen [109, 113, 122–124].

Fig.2.20 shows an FE model developed by Lancaster et al. [109] which illustrates the maximum principal stresses in a SPT test specimen with respect to specimen deformation. The axisymmetric model was developed using DEFORM standard code where the SPT specimen was firmly clamped along it's entire contour. The specimen thickness and punch diameter were set as 0.5 mm and 2.5 mm respectively and the receiving hole radius set as 4 mm. The upper and lower dies and the punch head were treated as rigid bodies insensitive to deformation in all degrees of freedom. Isotropic material behaviour was assumed and a friction coefficient between the punch head and specimen was set as $\mu = 0.25$. A normalised Cockroft-Latham damage criterion value of 0.354 was input for the RT simulations but no criterion was input for the 400 °C simulations [109].

The model highlights that when the deformation is low there exists an area of high tensile stress in the centre of the lower surface of the specimen. For brittle materials, where failure occurs at low displacement, the area of high tensile stress causes crack initiation in the centre of the sample, the cracks then propagate radially resulting in the star crack patterns observed in Fig.2.18 [114]. As the displacement is increased the area of high tensile stress on the lower surface moves outwards from the centre of the specimen, and becomes concentrated in one area once the stress distribution reaches a steady state. This area of high tensile stress causes circumferential cracking, such as that shown in Fig.2.18 [114].

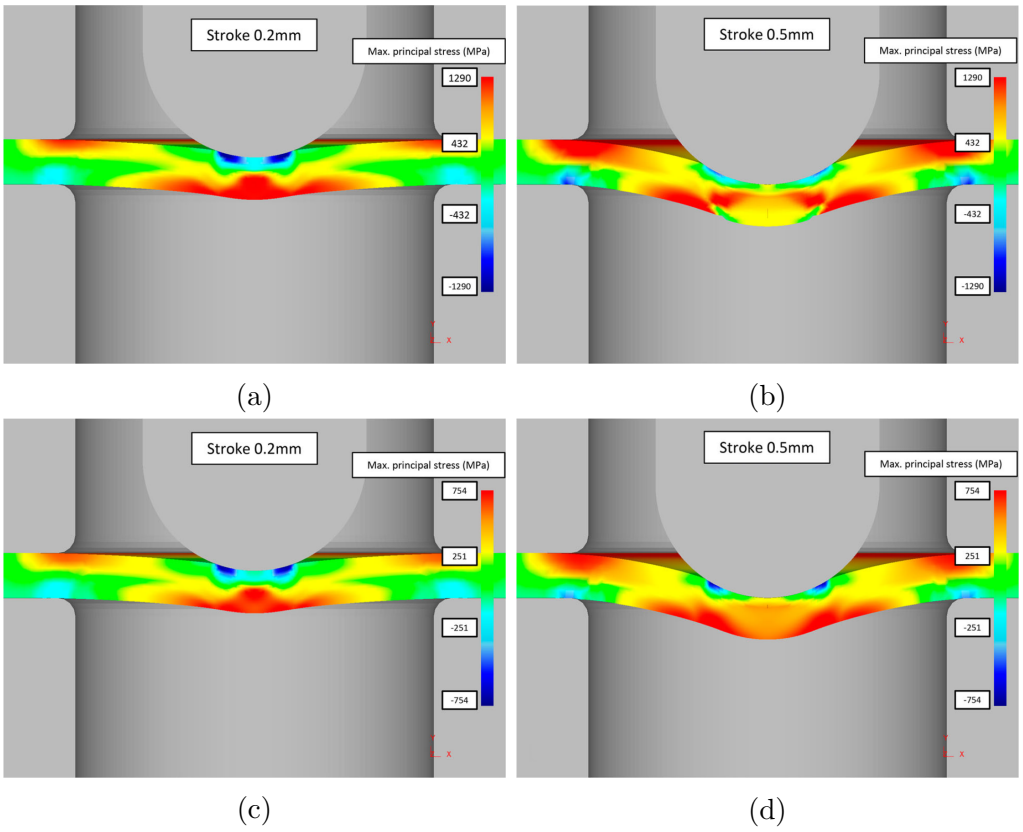

FIGURE 2.20: FEA simulation of a forged Ti-6Al-4V small punch specimen at (a-b) 20 °C and (c-d) 400 °C where stroke is specimen deformation. Figure reproduced from [109].

2.9 Small Punch Creep (SPC) Testing

2.9.1 Experimental Displacement-Time Behaviour

The small punch creep (SPC) test was first introduced by Parker and James [125], who suggested that the small punch test could be used to determine the creep properties of a material by applying a constant load to a SP specimen and recording the specimen displacement. Since then, the SPC test has been widely used to study the creep behaviour of numerous materials, in particular steels used in power plant and nuclear applications [87–90, 122].

A schematic of a typical SPC test displacement-time curve, based on the displacement-time curves reported in the literature [63, 87–90], is shown in Fig.2.21. The shape of the SPC test curve is similar to conventional uni-axial

creep curves; there is a primary region, a secondary steady-state region, and a tertiary region region. However, it has been shown that in SPC tests a constant displacement rate is not obtained until 10-15% strain, which would normally be associated with the tertiary region in a uni-axial creep test [90].

In a uni-axial creep test, significant creep damage is normally associated with the tertiary region. Kobayashi et al. [126] showed that for super duralumin, circumferential cracking may form in a SPC specimen as early as the primary deformation stage, which suggests the displacement rate in the secondary region is not primarily due to creep mechanisms. It has been suggested that the steady-state region in a SPC curve corresponds to a balance between geometric stiffening, due to a drastic change in shape of the SPC specimen, and a reduction in stiffness due to thinning of the specimen and the accumulation of damage such as voids or microcracks [90, 126, 127]. Therefore, the secondary steady-state region in a SPC test corresponds to tertiary creep, which dominates the life of a SPC specimen. This, as well as the complex bi-axial stress state in a SPC specimen, makes it difficult to accurately interpret the data from SPC tests. Nevertheless, simplified analytical models exist and significant progress has been made on modelling the SPC test through finite element modelling.

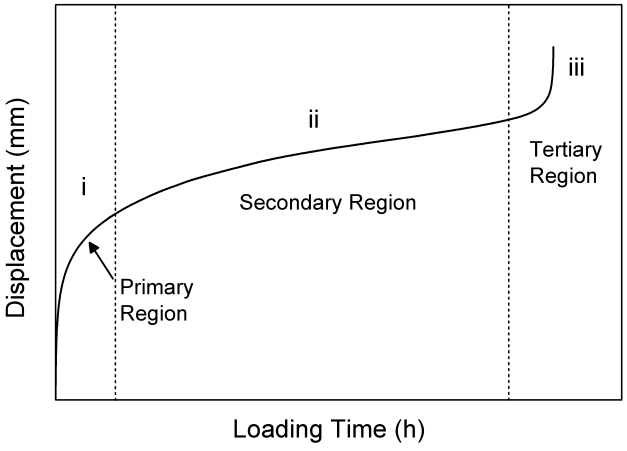

FIGURE 2.21: Schematic of a typical displacement-time curve obtained from SPC tests.

2.9.2 Modelling of the SPC Test

The reference model used for the analysis of the SPC test is the membrane stress model derived by Chakrabarty [128]. Chakrabarty derived an expression to calculate the von Mises equivalent strain for a membrane stretched over a hemispherical punch head. This was developed by Yang and Wang [129] who determined a semi-empirical polynomial expression to calculate the maximum equivalent strain at the centre of a disc specimen.

Li and Zhang [130] developed the work of Yang and Wang to determine a polynomial expression to calculate the maximum equivalent strain at the contact boundary between the punch head and the specimen (ε_c) for a punch head of 1 mm radius:

$$\varepsilon_c = 0.20465\delta + 0.12026\delta^2 + 0.00950\delta^3 \tag{2.10}$$

where δ is the displacement at the centre of the specimen.

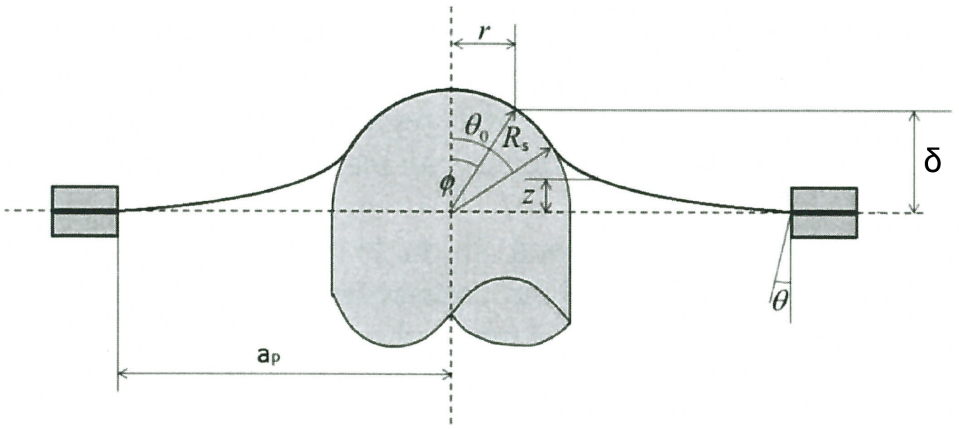

FIGURE 2.22: Chakrabarty's membrane stretch model. Figure reproduced from [128].

Chakrabarty's membrane stretch model was also used to derive an empirical solution to convert the SPC load to equivalent uni-axial stress. The solution, presented in the European Committee for Standardisation workshop agreement [101], is shown as equation 2.11:

$$\frac{F}{\sigma} = 3.33 K_{sp}\, a_p^{-0.2}\, R_s^{1.2}\, t_0 \tag{2.11}$$

where a_{p}, R_{s} and t_0 are the radius of the receiving hole, punch head radius and specimen thickness as shown in Fig.2.22. F is the load (N) and K_{sp} is a non-dimensional correction factor used to correlate SPC work with traditional uni-axial testing. K_{sp} is typically between 1.2∼1.3 but where uni-axial test data does not exist it is taken as 1.

In order to understand the complex stress distribution within a SPC specimen it is necessary to consider finite element models. Numerous finite element models exist employing a variety of techniques and approaches [127]. Details of the FE method are not pertinent to this work so only a brief description of the models shown in Figs.2.23 and 2.24 is presented. Further details of each model can be found at the specific references.

Fig.2.23 is an FE model illustrating the equivalent creep strain in a SPC specimen based on the elastic-plastic steady-state creep of a Gr91 steel SPC specimen [131]. The axisymmetric model was developed using Abaqus and the element type CAX4R. The upper and lower dies (4 mm diameter) and punch head (2.4 mm diameter) were defined as rigid bodies. The specimen thickness was 0.5 mm. The Gr91 steel was considered as an isotropic homogeneous material exhibiting elastic-plastic secondary creep. The model in Fig.2.23 illustrates the equivalent creep strain in a specimen during a SPC test, where red is high creep strain and blue is low creep strain. The region of highest creep strain exists at a radial offset (0.7 mm) from the centre of the specimen, which has also been reported for other FE models [92, 132–134]. The region of high creep strain in Fig.2.23 agrees with location of failure observed experimentally for SPC specimens [63, 87–89, 135]. The FE model shown in Fig.2.24, provides a good illustration of how FE models of the SPC test correspond to the experimentally observed cracking in a P91 steel. The model was based on a continuous creep damage model developed using Abaqus, with a punch diameter of 2.5 mm, upper and lower die diameter of 4 mm and specimen thickness 0.5 mm.

The stress distribution shown in Fig.2.23 is applicable to ductile SPC specimens which undergo a large deformation during the initial loading. However, it has been shown that for brittle SPC specimens, which do not exhibit a large initial deformation, failure may occur in the centre of the specimen [136, 137]. This is because the region of high tensile stress in a SPC specimen forms in the centre of the specimen and shifts radially as the displacement increases. Therefore, failure still occurs in the region of high tensile stress but for a brittle specimen this may be in the centre of the specimen.

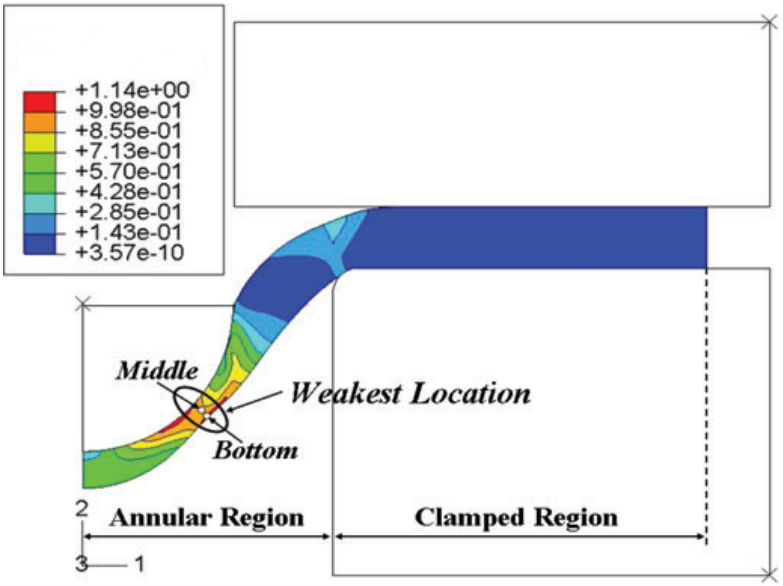

FIGURE 2.23: Finite element model showing the equivalent creep strain distribution within a SPC specimen. Figure reproduced from [131].

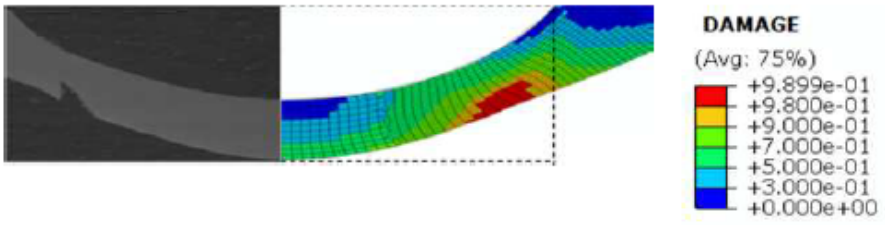

FIGURE 2.24: Experimentally observed cracking in a P91 steel at 600 °C compared to a finite element model. Figure reproduced from [132].

2.10 Evaluation of the Literature

From the reviewed literature, it is clear that understanding the time-dependent and time-independent properties of thin, free-standing MCrAlY bond coats is crucial to the development of new MCrAlY alloys which can improve the lifetime of TBC systems.

The time-dependent (creep) and time-independent (yield/fracture strength, elastic modulus and ductility) properties of free-standing MCrAlY bond coats have not been widely studied. In particular, it is not clear how the composition and multiphase microstructure influence the mechanical properties of the bond coat. In order to gain a clear understanding of this, it is necessary to obtain consistent data from thin, free-standing MCrAlY bond coat samples manufactured using a single thermal spray technique and consistent spray parameters. It is also important that the properties of thin ($\leq$ 0.5 mm) bond coats are distinguished from the properties of the bulk MCrAlY alloy of the same composition. This requires the use of relevant test techniques so that the properties of thin bond coat samples may be determined.

The small punch (SP) test method is one such cost-effective technique. It offers the opportunity to determine the properties of thin, free-standing MCrAlY bond coats in the form of 8 mm disc specimens approximately 0.5 mm thick. It has been demonstrated that the two variants of the SP test: the small punch creep (SPC) test and the small punch tensile (SPT) test, can successfully be employed to determine the creep and tensile properties respectively, of thin materials.

This study aims to use the SPC test and SPT test to investigate the creep and tensile properties of thin, free-standing MCrAlY bond coats manufactured by HVOF thermal spraying over a range of temperatures. The influence of composition and microstructure will be investigated by comparing the properties of three different MCrAlY bond coats with varying composition and microstructures. Attention will also be paid to how the microstructure influences the accumulation of creep damage under constant load conditions and the development of cracking

under constant displacement rate conditions. The work will be novel in that it will use higher creep temperatures than previously studied. In addition, tensile properties will be measured using an instrument capable of constant displacement rates rather than the dead-load systems previously used.

Chapter 3

Methodology

3.1 Introduction

In this chapter, the various experimental techniques used to investigate the microstructure and mechanical properties of different MCrAlY alloys are presented. Free-standing coatings were produced from each of the alloys by high velocity oxy-fuel (HVOF) thermal spraying and subsequently vacuum heat treated for 2 hours at 1100 °C. The microstructure of the as received alloy powders of each MCrAlY alloy, as well as the free-standing coatings in the as sprayed and heat treated conditions, were investigated by X-ray diffraction (XRD), scanning electron microscopy (SEM), energy dispersive X-ray analysis (EDX) and electron back-scatter diffraction (EBSD). Short oxidation trials were also conducted on the heat treated coatings. The oxidation behaviour of the coatings subjected to short oxidation trials was also investigated by SEM and EDX.

CALPHAD calculations were conducted to aid understanding of the phase equilibria of each MCrAlY alloy. Calculations were made using the Thermo-Calc software package and the TTNi7 database.

The high temperature mechanical properties of three of the four MCrAlY alloys were investigated by small punch creep (SPC) tests and small punch tensile (SPT) tests. Tests were conducted on the free-standing heat treated coatings on two small

punch rigs, referred to as rig 1 and rig 2. Fracture analysis of the failed specimens was conducted using SEM, EDX and EBSD analysis.

3.2 Raw Materials

One commercially available, gas atomised CoNiCrAlY powder, trade name Praxair CO-210-24, and three experimental gas atomised NiCoCrAlY powders, manufactured by H.C. Starck GmbH, were used for HVOF thermal spraying. The commercially available Praxair CO-210-24 powder is denoted C1 and the three experimental powders are denoted EP1, EP2 and EP3. The chemically analysed powder compositions are presented in table 3.1. The nominal powder size range was specified as -45 + 20μm for all powders.

	Element (wt.%)										
Powder	Ni	Co	Cr	Al	Y	Ta	Si	Hf	O	C	Fe
EP1	Balance	20.0	22.3	12.2	0.3	<0.01	0.5	0.4	0.03	0.012	0.04
EP2	Balance	20.0	11.1	12.6	0.4	6.0	0.2	0.4	0.01	0.01	0.04
EP3	Balance	20.0	22.3	12.2	0.3	4.2	0.5	0.4	0.03	0.012	0.04
C1	32.6	Balance	21.1	8.7	0.43	-	0.1	-	0.03	-	0.06

TABLE 3.1: Compositions of the commercial alloy powder C1 and novel MCrAlY alloy powders EP1, EP2 and EP3 as measured by chemical analysis.

3.2.1 Powder Density Measurements

The densities of the MCrAlY powders were measured using helium pycnometry. The method involves flowing a gas through known mass of material and measuring the infiltration volume by assessing the variation in pressure between the sample and reference cell [138].

Helium pycnometry was carried out using an AccuPyc II 1340 from Micromeritics in 99.99 % helium at a maximum pressure of 19.5 psi, utilising an equilibrium rate

of 0.005 psi g / min at 20 °C. Approximately 10 mg of alloy powder was analysed in a 12 cm^3 sample cell. Samples were purged 10 times followed by 10 cycles and an average density taken from the measurements. A maximum standard deviation of 0.008 g / cm^3 was found for each alloy powder.

3.3 High Velocity Oxy-Fuel (HVOF) Thermal Spraying

HVOF thermal spraying was used to create free-standing MCrAlY coatings. The C1, EP1, EP2 and EP3 powders detailed above were deposited onto mild steel substrates of dimensions 60 × 25 × 1.8 mm. The virgin powder (previously unused) was dried for 24 hours at 100 °C to remove any moisture before spraying. The mild steel substrates were ground with 1200 grade grit paper before spraying in order to aid debonding after spraying.

HVOF thermal spraying was carried out using a Met Jet III liquid-fuel thermal spray gun with the spray parameters shown in table 3.2. The spray parameters were selected from previous work carried out at the University of Nottingham [31, 53]. The mild steel substrates were mounted onto a rotating carousel whilst the spray gun was moved vertically. Each vertical traverse of the spray gun, referred to as one pass, deposited a layer of coating onto the substrate. The coatings were sprayed to a thickness of approximately 700 μm and subsequently debonded from the mild steel substrates by bending around a mandrel to produce free-standing coatings.

HVOF Spray Parameters	**C1**	**EP1**	**EP2**	**EP3**
Spray Distance (mm)	356	356	356	356
N_2 gas flow rate (L/min)	5.5	5.5	5.5	5.5
O_2 gas flow rate (L/min)	920	900	900	900
Kerosene flow rate (mL/min)	475	450	450	450
Nozzle length (mm)	100	100	100	100
Number of passes	30	16	12	14

TABLE 3.2: HVOF spray parameters used to manufacture thermally sprayed coatings from the alloy powders shown in table 3.1.

3.4 Vacuum Heat Treatment

Vacuum heat treatment was carried out on free-standing coatings in an Elite Thermal Systems TVH12 vacuum tube furnace held at approximately 10^{-9} bar. The coatings were heated from RT to 1100 °C at a rate of 3 $Kmin^{-1}$, held at 1100 °C for 2 hours and then furnace cooled to RT over a period of 6 hours, at approximately 3 $Kmin^{-1}$.

Vacuum heat treatment was applied in order to approximately replicate the initial heat treatment given to bond coats during the manufacture of thermal barrier coatings. This type of heat treatment has been shown to reduce the porosity within samples and allow the precipitation of secondary phases [56, 63].

3.5 Small Punch Testing

Small punch tests were carried out using two custom built small punch rigs, referred to as rig 1 and rig 2. Rig 1 was used for SPC testing of free-standing coatings. Rig 2 was used for SPC testing and SPT testing of free-standing coatings. For both rigs, a three tier, 3 kW furnace was used to heat the specimens. Three K-type thermocouples, accurate to $\sim \pm 5$ °C, were used to measure the furnace

temperature in the top, middle and bottom tiers. The three thermocouples were connected to a Severn Thermal Solutions temperature controller which controlled the temperature to ± 2 °C, giving an overall temperature tolerance of ∼ ± 7 °C for all tests on both rigs. All tests were carried out in a temperature controlled room held at 21 °C.

Specimens for SPC and SPT testing, in the form of 8 mm diameter discs, were cut from the heat treated free-standing coatings by electro-discharge machining and ground down from the as-deposited thickness to a final thickness of 400 μm on 1200 grade silicon carbide paper. The final thickness was controlled to within ± 5 μm as measured by a digital micrometer and both surfaces had the same finely ground surface finish.

Rig 1

Rig 1 is a dead-load system which has been used previously at the University of Nottingham for SPC testing [29, 63]. A detailed schematic is shown in Fig.3.1.

The rig is held within a steel frame (A). The specimen is held by the sample holder (B) which connects to the bottom of the steel frame and also supports the clamping head (C). The hemispherical punch head (D), of radius 1 mm, applies a constant load to the specimen. The load, in the form of weights, is placed on the pan head (E) which is connected to the punch head via the vertical rod (F). The sample is heated and held at a constant temperature by the furnace (G). The punch head displacement is measured by a LVDT (linear variable differential transformer) transducer (H) which is accurate to ± 1 μm. The specimens were placed in the rig and clamped prior to heating. Specimens were heated to test temperature and stabilised at that temperature for 5 h before the load was applied. All the tests were carried out in air at the selected temperatures.

Rig 2

Rig 2 is a custom built rig installed on a Tinius Olsen H5KS single column materials testing machine which was designed as part of this study. The design process is outlined in appendix A.

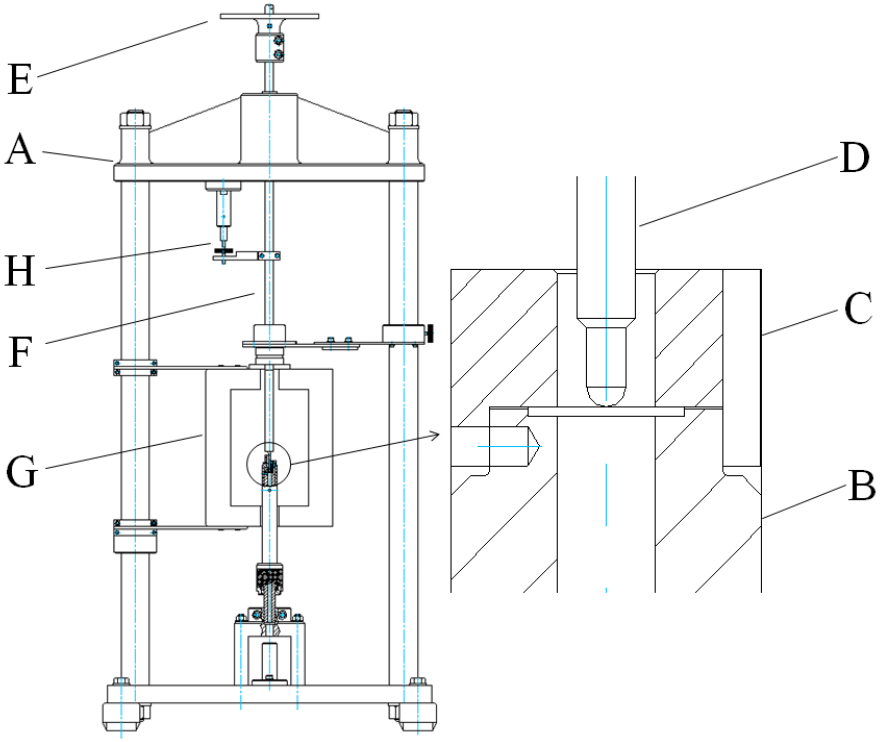

FIGURE 3.1: Schematic of custom built small punch creep rig, referred to as rig 1, with a punch head radius of 1.0 mm and a receiving hole diameter of 4.00 mm in accordance with the CEN workshop agreement [101]. Figure reproduced from [63]. A full description of the rig is provided in the text.

A schematic of the rig is shown in Fig.3.2. The load is applied via a 2.5 kN load cell and transmitted to the sample through a hemispherical punch head (a) of 1 mm radius. The punch head is aligned through an alignment bush (not shown) which is removed after alignment is complete. The specimen is clamped by screwing the top nut (b) onto the lower die (c), which presses a clamping disc (d) onto the specimen (e). Two pins (not shown) prevent the clamping disc from rotating and causing friction on the surface of the sample. The displacement was measured by two LDVT's which connect to the punch head at (f). The samples were heated to temperature prior to the application of the load and held at this temperature for 5 hours before the start of the test. The temperature was monitored by a thermocouple located at (g).

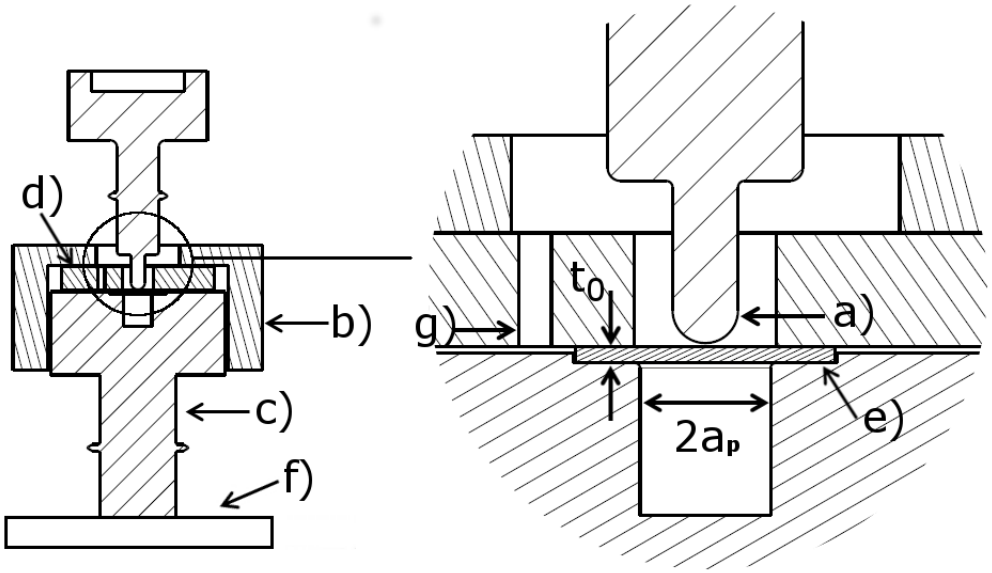

FIGURE 3.2: Schematic of custom built small punch creep rig, refereed to as rig 2, with a punch head radius of 1.0 mm and a receiving hole diameter of 4.00 mm in accordance with the CEN workshop agreement [101]. A full description of the rig is provided in the text.

3.5.1 Small Punch Tensile (SPT) Testing

Displacement controlled SPT tests were carried out on Rig 2 only. SPT tests were carried out at a displacement rate of 1 μms^{-1} at RT and between 500-750 °C using a 2.5 kN load cell. The displacement rate of 1 μms^{-1} was chosen in line with the CEN workshop agreement [101] and previous studies concerning SPT testing of coatings [40, 67]. The displacement of the specimen was recorded as the average of two LDVT's.

3.5.2 Small Punch Creep (SPC) Testing

Constant load SPC tests were carried out at 750 °C on rig 1 and at 750 and 850 °C on rig 2. 750 °C is the maximum operating temperature of rig 1.

Constant loads were applied to the specimens and displacement-time curves were recorded for each test. For rig 1, the load was applied as static weights whereas for rig 2, the load was applied through a 2.5 kN load cell.

3.6 Isothermal Oxidation

Isothermal oxidation was carried out on free-standing coating samples of the EP1, EP2 and EP3 alloys at 1100 °C in a Carbolite furnace at time intervals of 24, 48, 72 and 96 hours followed by air cooling. Isothermal oxidation was carried out in order to investigate the oxidation behaviour of the three MCrAlY coatings.

3.7 Metallurgical Sample Preparation

Cross sections of coating specimens were cut using a Struers Accutom cutting machine with a SiC cutting disc. Samples were hot mounted in a Polyfast conductive mounting resin using a Buehler Metaserv automatic mounting press before being ground and polished to a 1 μm finish. Cross sections of the alloy powders were achieved by distributing a small amount of powder into finely ground Polyfast conductive resin before mounting in the same fashion.

Samples for electron back-scatter diffraction (EBSD) required a further stage of chemical /mechanical polishing using colloidal silica to achieve a surface finish of 0.02 μm with minimal surface deformation.

Failed SP samples were mounted on carbon conductive tabs with the fracture surface face up and investigated through secondary electron (SE) imaging. Low and high magnification images were used for analysis of the fracture surface.

3.8 Microstructural Characterisation

3.8.1 Scanning Electron Microscopy and Energy Dispersive X-ray Analysis

Electron microscopy uses a high energy electron beam to examine objects on a very fine scale. When the primary electron beam interacts with matter in a

thick sample, various signals are created such as characteristic X-rays, secondary electrons (SE) and back scattered electrons (BSE), as shown in Fig.3.3 [138]. The scattered electrons are collected by detectors in the scanning electron microscope and the signals produced are used to form images. The contrast in SE images is due to sample topography and so are typically used to study surfaces. In BSE images, the contrast is proportional to the mean atomic number of the phase, which allows compositional differences in the sample to be detected [139]. A phase with low mean atomic number will appear darker than a phase with high mean atomic number.

The characteristic X-rays are emitted with an energy that is characteristic to an atom. They are used to identify atomic numbers and create EDX spectra based on how frequently an X-ray of specific energy is received.

When the primary electron beam interacts with the sample matter, it does so in an interaction volume, which determines the spatial resolution of the technique, as shown in Fig.3.4 [138]. The resolution of the SE image is similar to the diameter of the electron beam whereas the resolution of the BSE image is of the order of one half the interaction volume. The resolution of EDX analysis is equal to the interaction volume.

Scanning electron microscopy (SEM) was carried out using a tungsten filament FEI XL30 scanning electron microscope. Secondary electrons (SE) were used to image the fracture surfaces of specimens following SP testing and backscattered electrons (BSE) were used to form images of cross sections of mounted specimens.

Energy dispersive X-ray (EDX) analysis was carried out using the same tungsten filament FEI XL30 scanning electron microscope and an Oxford Instrument Link ISIS-3000 energy dispersive X-ray analysis (EDX) detector and INCA software. Semi-quantitative EDX was utilised to aid phase identification through chemical microanalysis. Chemical maps were also utilised to help image sample microstructures.

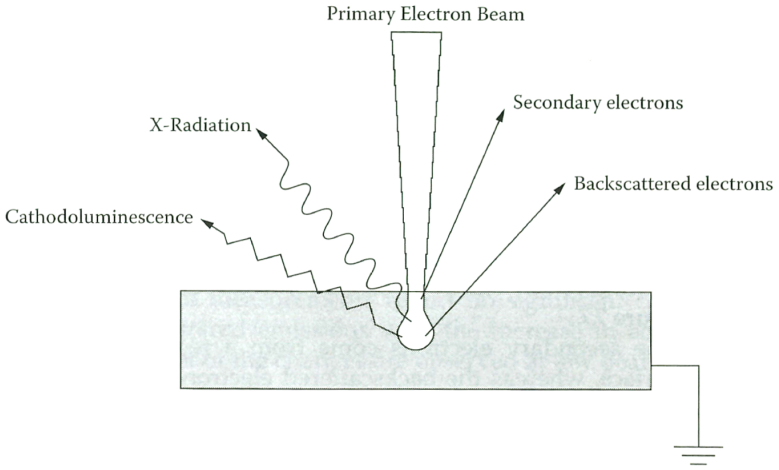

FIGURE 3.3: Schematic representation of the signals emitted during scanning electron microscopy. Figure reproduced from [138].

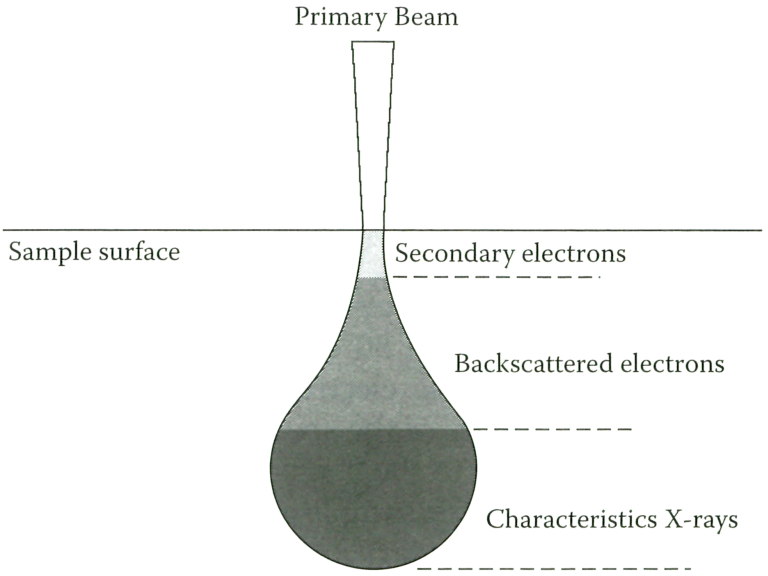

FIGURE 3.4: Schematic representation of the distribution of signals within the SEM interaction volume. Figure reproduced from [138].

3.8.2 Electron Back-Scatter Diffraction (EBSD)

Electron back-scatter diffraction involves directing an electron beam onto a sample tilted at 70 °. The high angle reduces the absorption of electrons and increases the scattering of back-scatter electrons, which are projected onto a phosphorous screen to produce Kikuchi diffraction patterns [140]. The Kikuchi patterns can be used to determine crystal orientation, crystal structure and grain size, which can be used to create phase maps and grain orientation maps.

SEM-based EBSD was carried out on a Zeiss 1530 VP field emission gun scanning electron microscope (Carl Zeiss, Inc., Maple Grove, MN) with an EDAX Pegasus combined electron back-scatter diffraction system (EDAX, Mahwah, NJ, USA). The EBSD patterns were recorded at a specimen tilt angle of 70 ° with an accelerating voltage of 20 kV and a beam current of 26 nA.

Electron back-scatter diffraction (EBSD) was carried out at Loughborough Material Characterisation Centre (LMCC) in Loughborough University and the Nanoscale and Microscale Research Centre (NMRC) in the University of Nottingham.

EBSD was utilised to reveal the grain structure of MCrAlY coating specimens through band contrast maps, inverse pole figures and phase maps. EBSD maps were collected for heat treated specimens over an area of 50 μm × 50 μm at a step size of 0.1 μm. Finer scale EBSD maps of varying dimensions and step size of 0.05-0.1 μm were used to investigate the microscopic crack propagation in the coatings following SPT testing.

3.8.3 Quantitative Image Analysis

Quantitative image analysis of BSE images and EBSD phase maps was used to measure the volume fraction of different phases in the MCrAlY coatings. Individual phases were recoloured white using the GIMP image manipulation programme and phase fraction measurements were made by adjusting the threshold in ImageJ to distinguish the white phase by contrast. The volume fraction of oxides/pores was measured by setting a low contrast threshold so that only black areas were measured.

For the BSE images 4 measurements were taken over areas approximately 40 μm × 30 μm. The average of the measurements was then compared to the measurements obtained from a single EBSD phase map of approximately 50 μm × 50 μm.

3.8.4 X-ray Diffraction Analysis

X-ray diffraction (XRD) involves directing a collimated beam of X-rays onto the surface of the sample. When the X-rays interact with the sample they diffract, as shown in Fig.3.5, according to Bragg's law [141]:

$$n\,\lambda = 2d\,sin\theta \tag{3.1}$$

where the integer n is the order of the diffracted beam, λ is the wavelength of the incident X-ray, d is the distance between adjacent planes of atoms and θ is the angle of incidence of the X-ray. The wavelength λ is known and θ is measured, which allows the spacing, d, to be calculated and lattice parameters determined.

XRD analysis was carried out using a Siemens D-500 X-Ray diffractometer combined with DIFFRAC PLUS software operated at 40kV and 25mA using a Cu-Kα with a wavelength of 0.15406nm. X-ray diffraction patterns were obtained for 2θ angles between 25 and 100°. A step size of 0.05° and step time of 2 s were used for the powders and heat treated coatings. A step size of 0.01° and step time of 4 s were used for the as sprayed coatings and for the heat treated coatings between 2θ angles of 25 to 55° in order to obtain clearer phase peaks.

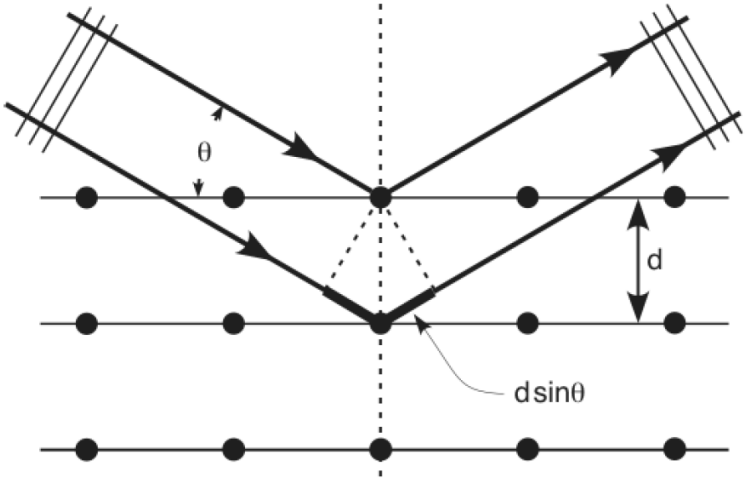

FIGURE 3.5: Example of X-Ray diffraction within a crystalline structure. Figure reproduced from [141].

3.9 CALPHAD Method Calculations

CALPHAD calculations were carried out using the Thermo-Calc software package and the thermodynamic database TTNi7. The phases included in the calculations were the β-NiAl, γ-Ni, γ'-Ni_3(Al,Ta), σ-Cr_2Co and α-Cr phases. Calculations were made using a starting temperature of 2000 °C and a step size of 1 °C. For each MCrAlY alloy, the phase fractions were plotted as a function of temperature between 600-1400 °C so that the phase equilibria of each alloy could be evaluated. The phase fractions were converted from wt.% to vol.% using the method outlined in appendix B.

Chapter 4

Investigation of Phase Evolution and Microstructure Formation in MCrAlY Alloys

4.1 Introduction

In this study, three experimental MCrAlY alloys were investigated with reference to one commercially available MCrAlY alloy, which has been the subject of much previous work [9, 30, 32, 33, 42, 56, 63]. The experimental MCrAlY alloys were designed as part of a project to create a new generation of MCrAlY bond coats for use in TBC systems. The alloys were designed to produce bond coats with improved resistance to oxidation as well as mechanical and chemical degradation compared to bond coats currently available. Full details of the design and selection process for the new experimental alloys can be found at [142].

Free standing MCrAlY coatings were manufactured from each of the MCrAlY alloy powders by high velocity oxy-fuel (HVOF) thermal spraying and then heat treated at 1100 °C for two hours under vacuum.

The microstructure of the as received alloy powders, as sprayed coatings and heat treated coatings were investigated by X-ray diffraction (XRD), scanning

electron microscopy (SEM), energy dispersive X-ray analysis (EDX) and electron back-scatter diffraction (EBSD).

Oxidation trials were conducted on the experimental alloys to assess their oxidation behaviour. Trials were conducted on the heat treated coatings at 1100 °C for 24-96 hours. The oxidation behaviour of each coating was investigated by SEM and EDX analysis.

CALPHAD methods were used to predict the phase formation, as a function of temperature, in each of the alloys under thermodynamic equilibrium. Calculations were made using the Thermo-Calc software package and the TTNi7 database.

The observed microstructures in the alloy powders, as sprayed coatings and heat treated coatings are presented separately for each alloy. The results of the oxidation trials on all three experimental alloys are then presented together. This is so that the oxidation behaviour of each experimental alloy may be assessed with reference to the others. The phase evolution modelling of each alloy is then presented with reference to the observed alloy microstructures.

4.2 Alloy Compositions

The chemical compositions of the as received alloy powders are shown in table 4.1. The novel MCrAlY powders are referred to as EP1, EP2 and EP3 and the commercially available MCrAlY powder, trade name Praxair CO-210-24, is referred to as C1. The nominal powder size range was specified as -45 + 20μm for all powders.

The EP1, EP2 and EP3 powders all contain 20 wt.% Co, between 40-49 wt.% Ni and between 12.2-12.6 wt.% Al whereas the C1 coating contains 37 wt.% Co, 32.6 wt.% Ni and 8.7 wt.% Al.

The C1, EP1 and EP3 powders contain between 21.1-22.3 wt.% Cr where as the EP2 powder contains 11.1 wt.% Cr.

The EP2 and EP3 powders contain 6.0 and 4.2 wt.% Ta respectively where as the EP1 and C1 powders contain $\leq$ 0.01 wt.% Ta. The amount of other minor elements is similar for all 4 powders.

	Element (wt.%)										
Powder	Ni	Co	Cr	Al	Y	Ta	Si	Hf	O	C	Fe
EP1	44.2	20.0	22.3	12.2	0.3	$\leq$ 0.01	0.5	0.4	0.03	0.012	0.04
EP2	49.2	20.0	11.1	12.6	0.4	6.0	0.2	0.4	0.01	0.01	0.04
EP3	40.0	20.0	22.3	12.2	0.3	4.2	0.5	0.4	0.03	0.012	0.04
C1	32.6	37.0	21.1	8.7	0.4	$\leq$ 0.01	0.1	$\leq$ 0.01	0.03	-	0.06

TABLE 4.1: Compositions of the commercial alloy powder C1 and powders EP1, EP2 and EP3 as measured by chemical analysis.

4.3 Microstructural Characterisation of Commercially Available Alloy C1

4.3.1 X-Ray Diffraction Analysis

X-ray diffraction (XRD) was carried out to determine the phases present in the C1 powder, as sprayed coating and heat treated coating. The observed X-ray diffraction patterns are shown in Fig.4.1. FCC peaks with a lattice parameter close to FCC Ni(Co) and BCC peaks with a lattice parameter close to BCC NiAl(CoAl) were identified in the powder and coatings. The FCC peaks correspond to a Ni-based solid solution with an FCC crystal structure normally termed γ-Ni phase. The BCC peaks correspond to an NiAl intermetallic phase with an ordered BCC crystal structure normally referred to as β-NiAl phase. Previous studies have reported γ-Ni and β-NiAl phase in coatings manufactured from the C1 powder and powders of similar composition [9, 30, 32, 33, 42, 56, 63]

The powder, as sprayed coating and heat treated coating all show main γ-phase peaks and minor β-phase peaks which suggests the γ-Ni phase is the matrix phase and the β-NiAl phase a secondary phase. There is evidence of peak broadening in the as sprayed coating diffraction pattern which is most likely due to microstrain or nanometre grain size in the coating after HVOF thermal spraying.

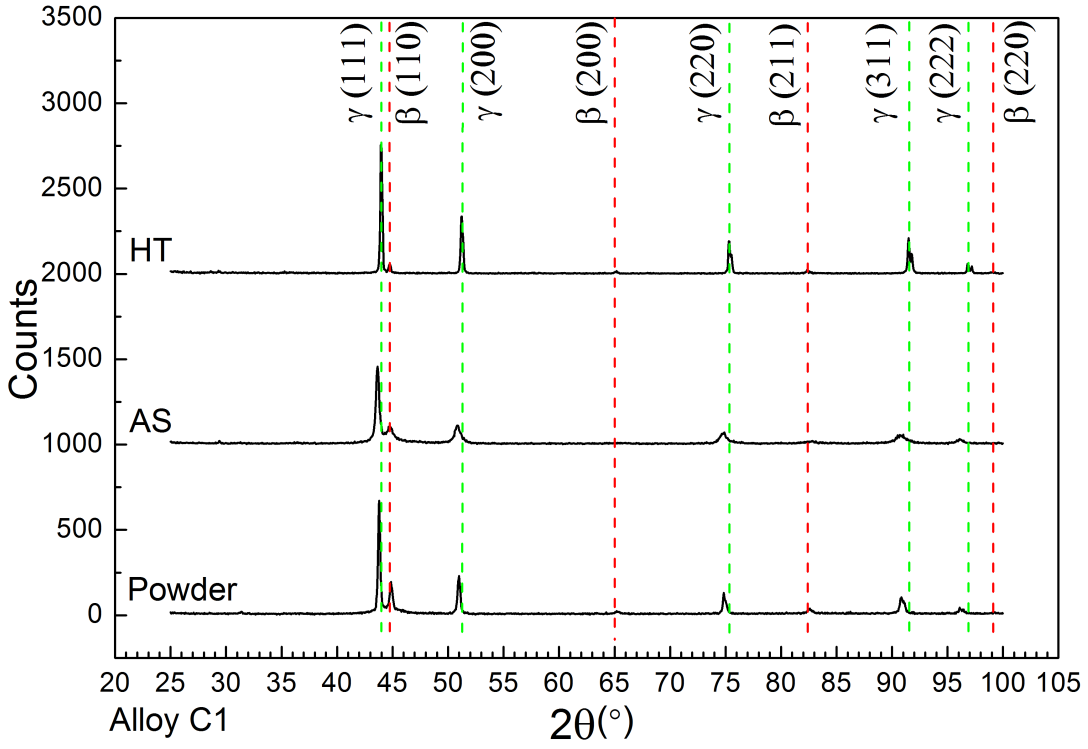

FIGURE 4.1: X-ray diffraction patterns of the C1 alloy, in the form of powder, as sprayed (AS) and heat treated (HT) coatings.

4.3.2 Scanning Electron Microscopy and Energy Dispersive X-ray Analysis

As Received Powder

The C1 powder, shown in Figs.4.2a and 4.2b, exhibits a two phase microstructure with a grey-contrast matrix phase in the form of dendrites and a dark-contrast interdendritic phase. It is well documented that the grey-contrast phase is the FCC γ-Ni phase and the dark-contrast phase is the BCC β-NiAl phase [9, 30, 32, 33, 42, 56, 63]. The C1 alloy powder has approximately 92 vol.% γ-phase and 8

vol.% β-phase as measured by image analysis. The phase fractions are summarised in table 4.2. No EDX measurements are provided for the C1 alloy powder as the spatial resolution was not high enough to differentiate between the two phases due to beam spreading.

As Sprayed Coating

A cross section of the as sprayed coating is shown in Figs.4.2c and 4.2d. Regions can be identified which appear to have retained their original powder microstructure during thermal spraying and undergone varying degrees of partial melting and deformation.

The higher magnification image shows that the as sprayed coating contains a complex microstructure. There are regions which have retained the powder particle microstructure (A), regions which have undergone microstructural coarsening (B), regions which have possibly melted and re-solidified as a single phase (C), and very dark regions which are presumably either Al_2O_3 oxides or pores (D), which are reported in the literature for coatings manufactured from the C1 alloy powder [9, 30, 32, 33, 42, 56, 63]. The black features indicate regions with a low mean atomic number as would arise from Al_2O_3.

The volume fractions of the separate phases were not measured as the BSE contrast between the resolidified regions and the γ-phase is too small to yield accurate results via image analysis.

Heat Treated Coating

The heat treated C1 coating is shown Figs.4.2e and 4.2f. The coating exhibits a three phase microstructure consisting of the grey contrast γ-Ni phase, dark-contrast β-NiAl phase and thin, black elongated regions identified by EDX as oxide stringers, probably Al_2O_3. The volume fractions of each phase are measured as approximately 68 vol.% γ-phase, 31 vol.% β-phase and 1 vol.% oxide, as summarised in table 4.2, which agrees with previous characterisation of coatings manufactured from Praxair CO-210-24 [9, 30, 32, 33, 42, 56, 63]. A small phase fraction of black phase may also be pores.

Phase compositions for the heat treated coating, as measured by EDX, are given in table 4.2 for the heat treated coating. The β-phase has a higher amount of Ni and Al compared to the γ-phase which has higher amounts of Co and Cr. The values presented are the average of four measurements and the error values represent the standard deviation. The EDX measurements are the average composition of an interaction volume which is approximately 2-3 μm deep and 2 μm diameter. Therefore, the measured compositions will be influenced by the beam spreading effect. The oxide phase in particular is likely to be Al_2O_3 even though Ni, Cr and Co are detected in the micron-sized regions analysed.

Phase	BSE Contrast	Phase Fraction (vol.%)		Phase Composition in HT Coating (wt.%)				
		Powder	HT	Ni	Co	Cr	Al	O
β-phase	Dark	8±2	31±2	40±4	29±4	14±3	15±2	-
γ-phase	Grey	92±2	68±2	26±2	42±2	26±1	4±1	-
Oxide	Black	-	1.4 ±1	13±1	23±2	16±1	25±2	21±2

TABLE 4.2: Phase fractions of the as received C1 alloy powder and heat treated coating as calculated by image analysis using ImageJ as well as the composition of phases in the heat treated C1 coating as measured by EDX. Average of 4 spectra. Errors shown are the standard deviations.

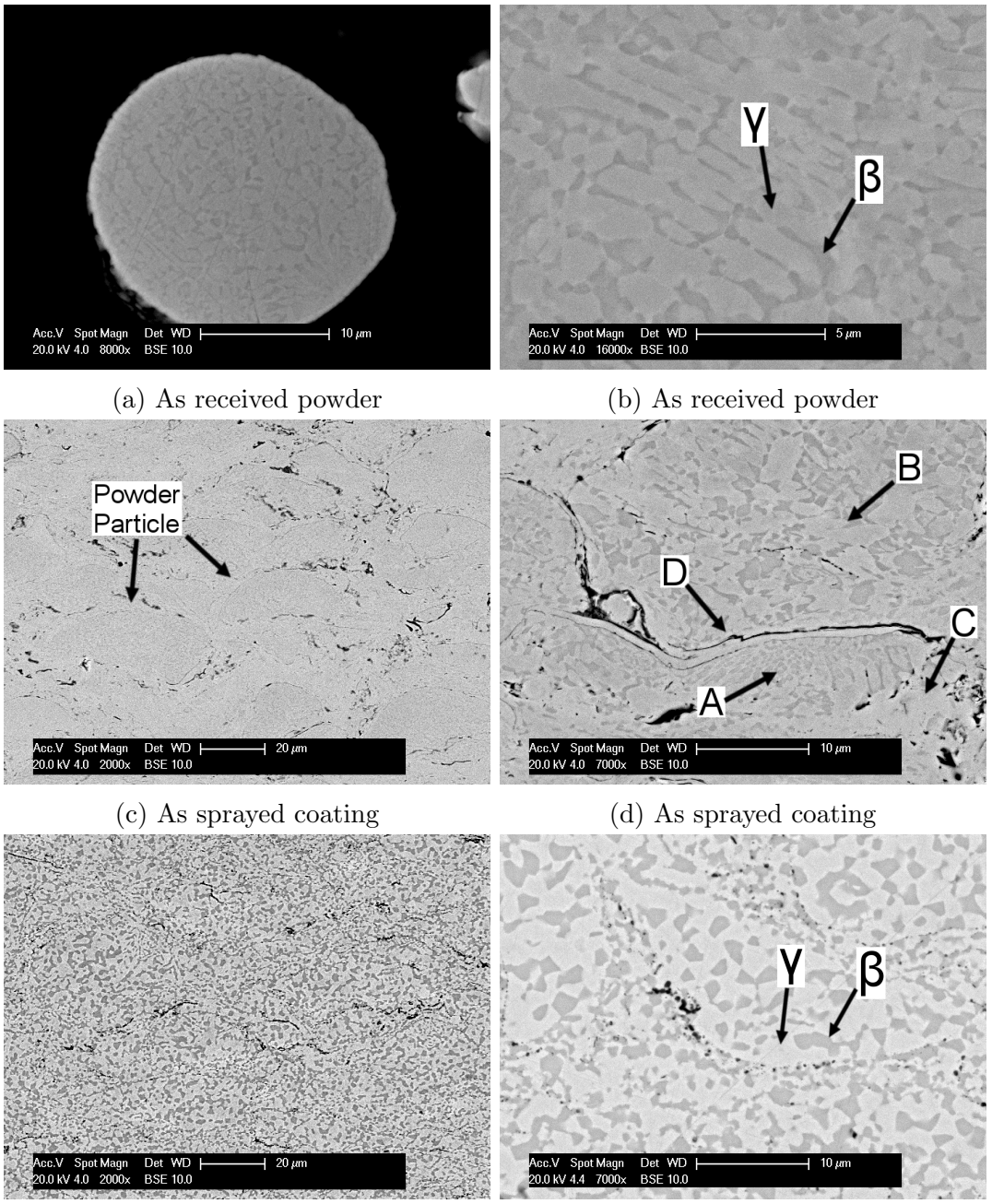

(a) As received powder (b) As received powder

(c) As sprayed coating (d) As sprayed coating

(e) Heat treated coating (f) Heat treated coating

FIGURE 4.2: BSE images of (a-b) C1 alloy powder, (c-d) as sprayed coating and (e-f) heat treated coating.

4.3.3 Electron Back Scatter Diffraction

Fig.4.3 shows a 50 µm × 50 µm region of the heat treated C1 coating imaged by EBSD. Fig.4.3a is a band contrast map showing grain boundaries, Fig.4.3b is a phase map in which the γ-phase is coloured green and the β-phase is coloured red, and Fig.4.3c is an inverse pole figure where individual grains are assigned a colour based on orientation.

The band contrast map shows that the coating does not have a uniform grain size and grains range from approximately 1-5 μm in size. It is also evident that the γ-phase regions seen in Fig.4.2f are in fact polycrystalline, which is not evident in the BSE image but can be observed by comparison of the band contrast and phase map. There is also evidence of twinning in the γ-phase, as indicated by C. The β-phase forms largely as single grains.

There is a region consisting of large grains, as indicated by A, which corresponds to a powder particle which retained its microstructure during spraying and underwent coarsening during heat treatment. There are also regions consisting of smaller grains, such as the one indicated by B. These regions possibly correspond to where the C1 alloy powder melted during thermal spraying and upon cooling, formed a single phase region. During heat treatment these regions probably transformed into dual phase regions but did not have sufficient time for coarsening. Regions of this type are identified in Fig.4.2d by the letter C.

The inverse pole figure shows that there is no preferred grain orientation for either phase.

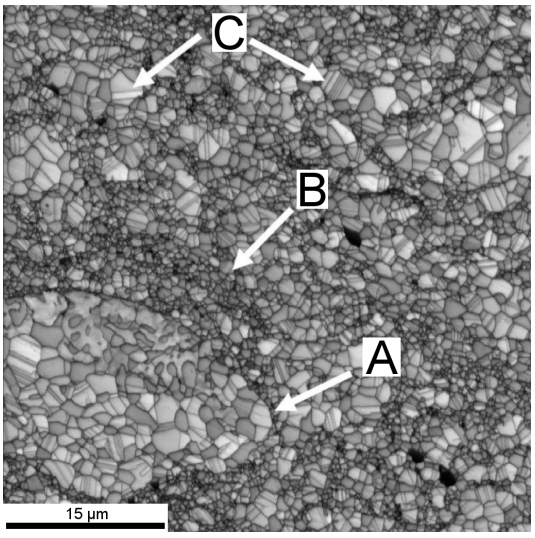

(a)

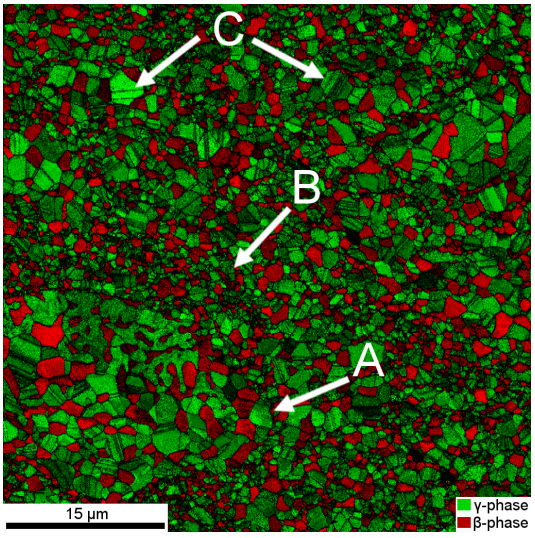

(b)

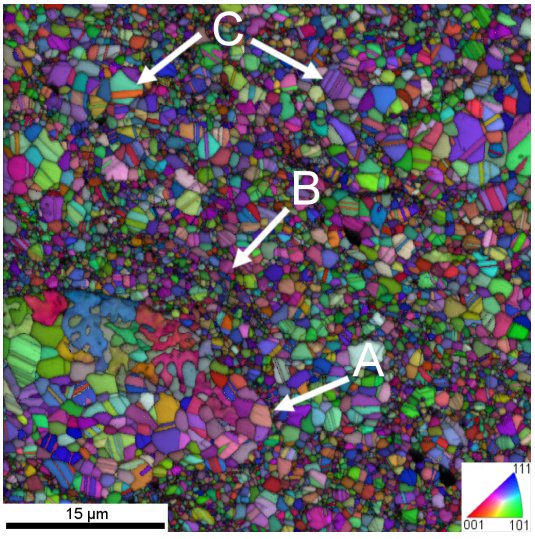

(c)

FIGURE 4.3: EBSD images of heat treated C1 coating where (a) is a band contrast map showing grain boundaries, (b) is a phase map in which the γ-phase is coloured green and the β-phase is coloured red, and (c) is an inverse pole figure map showing grain orientation.

4.4 Microstructural Characterisation of Alloy EP1

4.4.1 X-Ray Diffraction Analysis

The X-ray diffraction patterns obtained for the EP1 alloy powder, as sprayed coating and heat treated coating are shown in Fig.4.4. The powder, as sprayed coating and heat treated coating show strong BCC peaks which correspond to the β-NiAl phase observed in the C1 coatings. There is significant evidence of peak broadening in the as sprayed coating, as well as a small shoulder to the right of the main β-phase (110) peak. This is possibly due to microstrain or nanometre grain size in the coating after HVOF thermal spraying or because the lattice parameters of the β-phase vary slightly throughout the as sprayed coating, possibly due to variations in the composition of the β-phase.

The heat treated coating also shows FCC γ-Ni phase peaks and tetragonal close packed (TCP) peaks with a lattice parameter close to $Cr_{15}Co_9Si_9$, which corresponds to a complex crystal structure based around the atomic formula A_2B normally referred to as σ-phase [6]. Precipitation of the σ-phase is promoted by excessive amounts of Cr, Mo, and W and can vary in composition depending upon the material. Given the composition of the EP1 alloy, the σ-phase present is probably σ-Cr_2Co.

There is a small shift in the main β-phase peak between the powder, AS and HT patterns. This is probably caused by the composition of the β-phase changing during spraying and subsequent heat treatment. A slight change in the composition will alter the lattice parameter of the phase and cause small peak shift as seen in the diffraction patterns.

The alloy powder, as sprayed coating and heat treated coating all exhibit a phase peak with a lattice parameter close to Al_2O_3, which was observed in the C1 heat treated coating.

The detection limit for XRD analysis is approximately 2 wt.%. As such, it is possible that the γ and σ-phases exist in the powder and as sprayed coating at $\leq$ 2 wt.%.

4.4.2 Scanning Electron Microscopy and Energy Dispersive X-ray Analysis

As Received Powder

A cross section of the EP1 powder is shown in Figs.4.5a and 4.5b. There appears to be three phases; dark-contrast, grey-contrast and light-contrast but this does not agree with the XRD analysis of the EP1 alloy powder in which only the β-NiAl phase was identified. As such, it appears the EP1 powder consists of heavily segregated β-phase where the composition varies. Solutes such as Co, Cr, Y and in particular Hf, increase the mean atomic number of a phase and make it appear brighter in the BSE image. High levels of Al decrease the mean atomic number of a phase and make it appear darker.

The light-contrast phase, of which there is approximately 2 vol.%, could be regions particularly rich in solutes such as Y and Hf, or it could be a second phase which was not identified during XRD analysis due to the detection limit of 2 wt.%.

The structure observed in the EP1 powder can be explained by non-equilibrium cooling during solidification. During atomisation the powder was probably subjected to cooling rates of approximately 10^5 K s^{-1} [56, 143]. In this instance the β-phase solidified first to form β-NiAl phase cores, such as the one indicated by A, which rejected the solutes, such as Co, Cr, Y and Hf, into the surrounding liquid. As the surrounding liquid cooled a secondary interdendritic phase formed from the residual liquid. Once the final liquid cooled it formed solute rich regions which appear bright in the BSE image, such as the one indicated by B. Further explanation of non-equilibrium cooling can be found at [144].

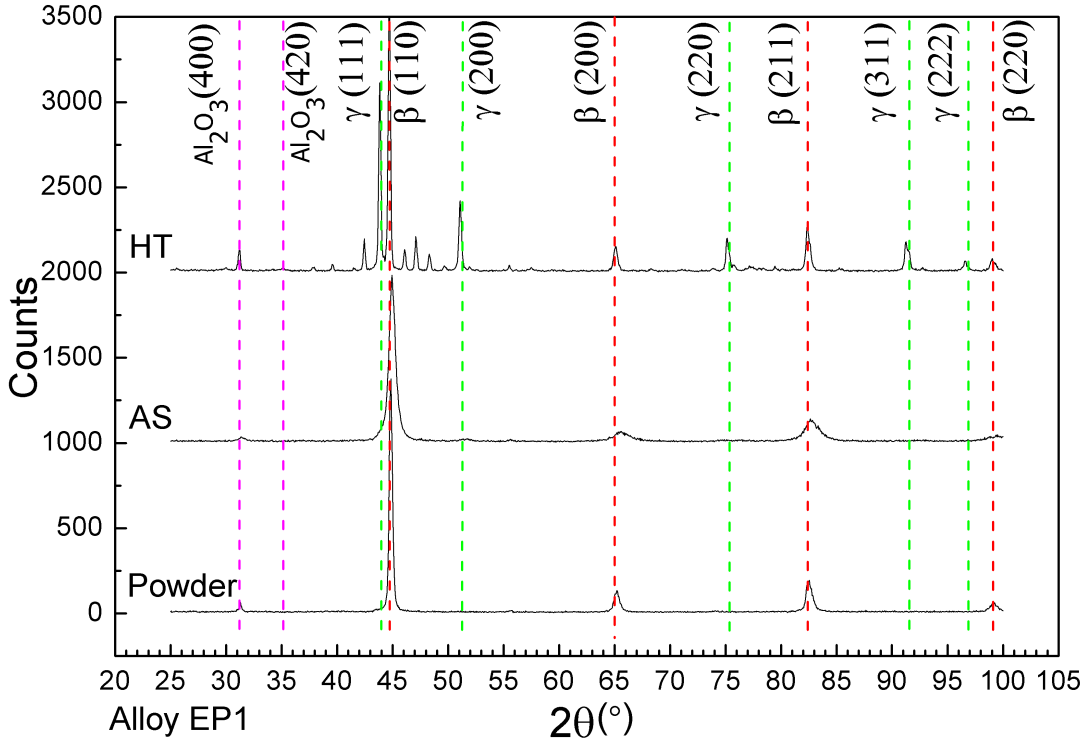

(a)

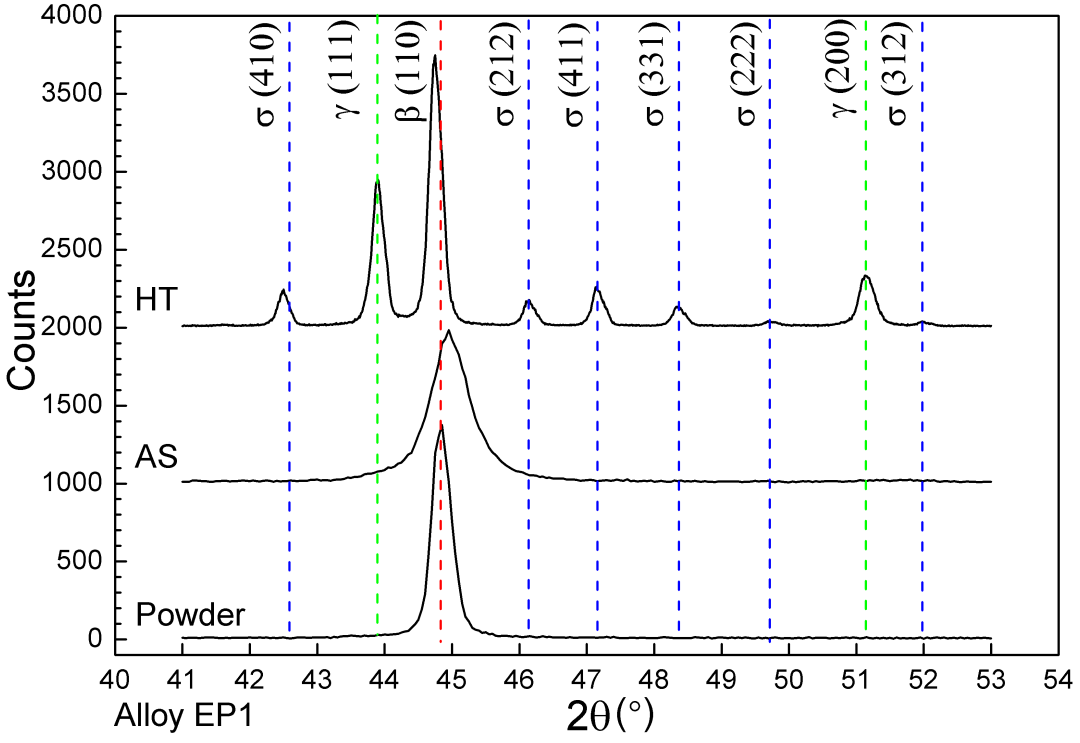

(b)

FIGURE 4.4: X-ray diffraction patterns of the EP1 alloy, in the form of powder, as sprayed (AS) and heat treated (HT) coatings. (a) shows the range 2θ = 25-100 ° and (b) shows the range 2θ = 41-53 °.

As Sprayed Coating

A cross section of the as sprayed coating is shown in Figs.4.5c and 4.5d. The EP1 as sprayed coating is similar to the C1 as sprayed coating; regions can be identified which appear to have retained their original powder microstructure, there regions which have retained the powder particle microstructure (A), regions which have undergone coarsening (B), regions which have fully melted and reformed as a single phase (C), and black regions (D) which are presumably either pores or Al_2O_3 oxide which was identified in the XRD patterns.

In the BSE image of the as sprayed coating there are dark-contrast, grey-contrast and light-contrast regions but only β-NiAl phase was identified in the XRD pattern. Therefore, it appears the as sprayed coating consists of heavily segregated β-phase as seen in the EP1 powder alloy.

The small shoulders observed on the main β-phase (110) peak in the as sprayed XRD pattern are probably caused by regions of β-phase which have slightly different lattice parameters due to small changes in the composition.

Heat Treated Coatings

The heat treated EP1 coating is shown Figs.4.5e and 4.5f. A dark-contrast, grey-contrast and black phase can be identified, which does not correspond to the four phases identified in the heat treated XRD pattern.

Point EDX measurements, shown in table 4.3, were made to aid identification of the phases. The EDX measurements are the average composition of the electron beam interaction volume and so are only an approximation to actual phase compositions. The dark-contrast phase is rich in Ni and Al and therefore is identified as the β-NiAl phase. Some regions of the grey-contrast phase have compositions that are rich in Ni, Co and Cr whereas other regions have compositions that are very rich in Cr and rich in Co but not rich in Ni or Al. This suggests that the grey-contrast region is in fact made up of two phases which would be consistent with the XRD pattern.

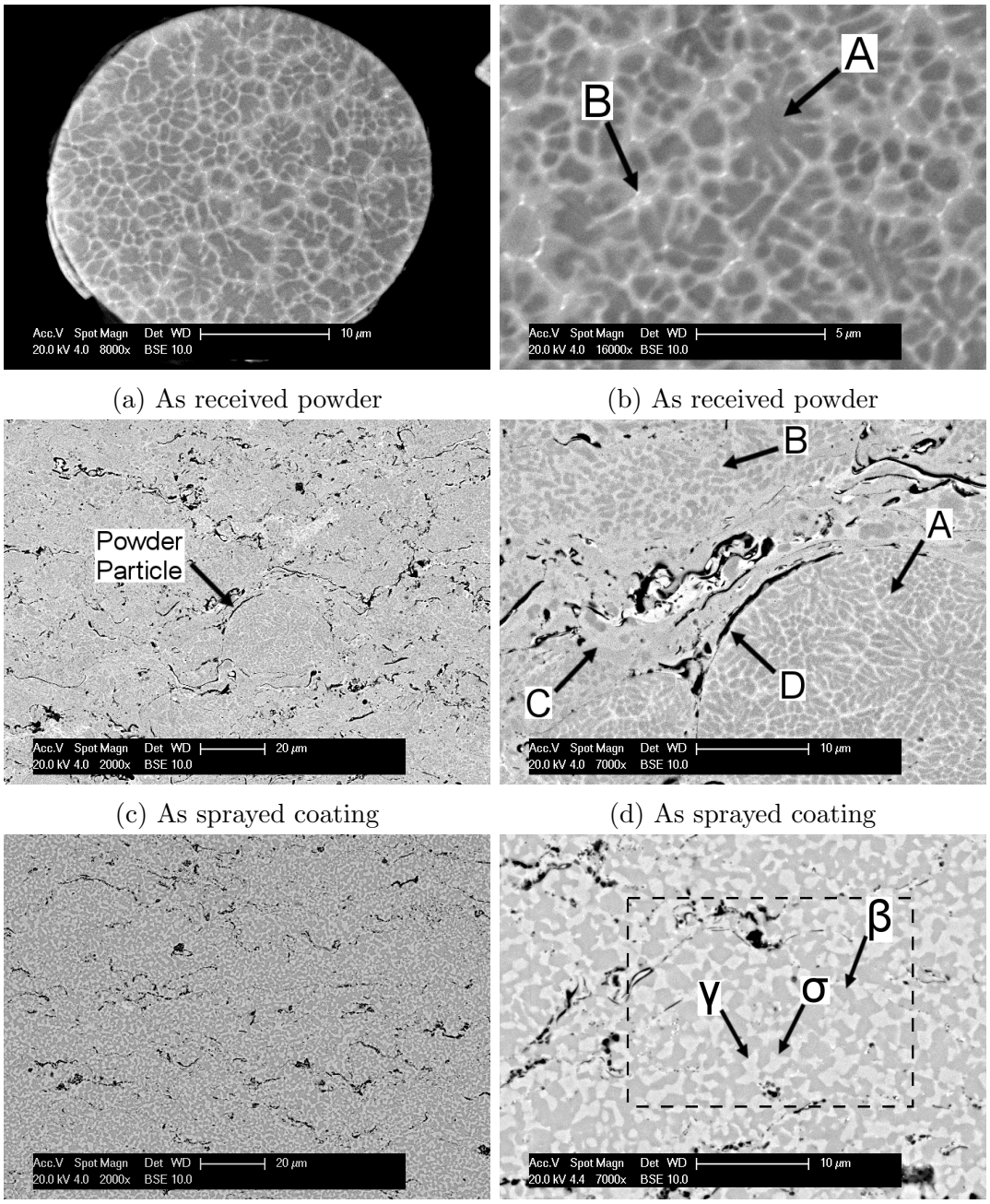

(a) As received powder (b) As received powder

(c) As sprayed coating (d) As sprayed coating

(e) Heat treated coating (f) Heat treated coating

FIGURE 4.5: BSE images of cross sections of the EP1 alloy powder (a-b), as sprayed coating (c-d) and heat treated coating (e-f). The black dotted box indicates the region shown in Fig.4.6.

The grey-contrast phase rich in Ni, Co and Cr is identified as the γ-Ni phase. The grey-contrast phase which is very rich in Cr and low in Ni is probably the σ-Cr_2Co phase. The thin, dark elongated regions are identified primarily as oxide stringers of Al_2O_3. A small phase fraction of black phase may be pores.

EDX maps of the EP1 coating are shown in Fig.4.6. The area shown corresponds to dotted black box in Fig.4.5f. The β-NiAl can be identified as the areas rich in Ni and Al, the γ-Ni phase as the areas rich in Ni and Co with moderate amounts of Cr, and the σ-Cr_2Co phase as the areas very rich in Cr but low in Ni. The EDX maps show the distribution of the γ and σ-phase but the spatial resolution is not high enough to allow phase fractions to be measured.

Phase	BSE Contrast	Phase Composition in HT Coating (wt.%)				
		Ni	Co	Cr	Al	O
β-phase	Dark	57±3	14±3	8±1	20±2	-
γ-phase	Grey	38±2	29±3	27±2	8±1	-
σ-phase	Grey	19±2	27±2	49±2	3±1	-
Oxide	Black	13±2	15±1	20±4	27±1	24±1

TABLE 4.3: Composition of the heat treated EP1 coating as measured by EDX for elements $\geq$ 1 wt.%. Average of 4 spectra. Errors shown are the standard deviations.

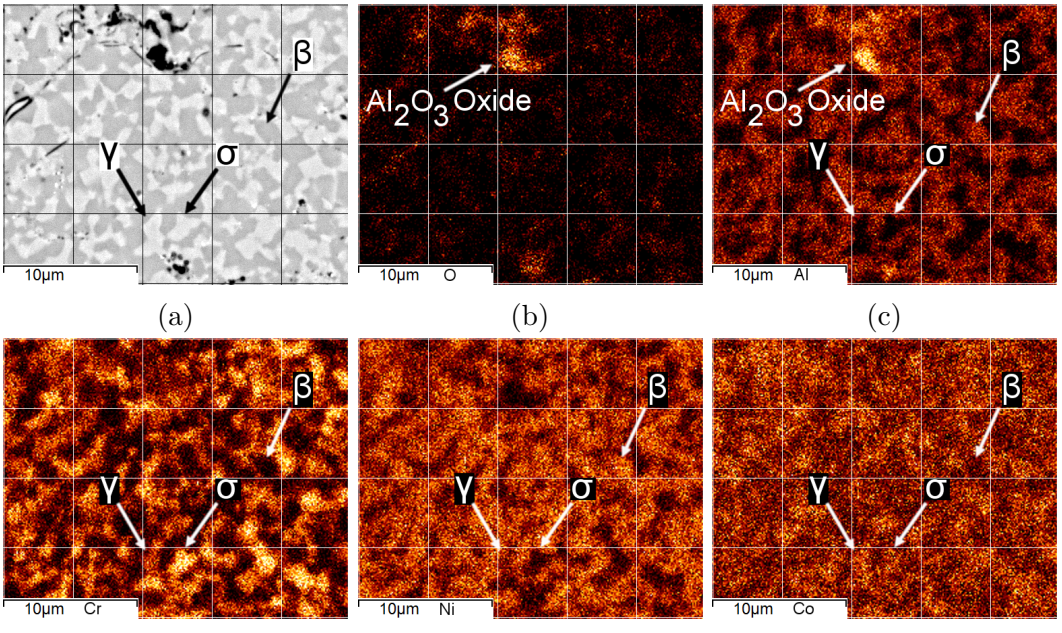

FIGURE 4.6: BSE image (a) and EDX maps (b-f) of the region highlighted by the black dotted box in Fig.4.5f. The β-phase is identified by areas rich in Al and Ni and low in Cr, the γ-phase is identified by areas rich in Co with medium levels of Cr and low Al and Ni, and the σ-phase is identified by areas very rich in Cr and low in Al and Ni.

4.4.3 Electron Back Scatter Diffraction

Fig.4.7 shows a 50 µm × 50 µm region of the heat treated EP1 coating imaged by EBSD. Fig.4.7a is a band contrast map showing grain boundaries and Fig.4.7b is a phase map in which three phases are clearly identified. The γ-Ni phase is coloured green, the β-NiAl phase is coloured red and the σ-Cr_2Co phase is coloured yellow. Fig.4.7c is an inverse pole figure where individual grains are assigned a colour based on orientation.

The band contrast map shows that the grain size in the EP1 coating is not uniform. There are regions consisting of large grains, indicated by A, and regions consisting of much finer grains, indicated by B, as was seen in the C1 coating. Comparison of the phase map and band contrast map also shows that all three phases are polycrystalline, which is not revealed in the BSE images. There is also evidence of twinning in the γ-phase, as indicated by C.

The phase map allows the volume fraction of each phase to be measured. The EP1 coating contains approximately 58 vol.% β-phase, 26 vol.% γ-phase and 13 vol.% σ-phase, as summarised in table 4.4.

The inverse pole figure shows there is no preferred orientation for any phase. There are a number of dark regions where the software could not accurately characterise the phase. These dark regions generally correspond to the σ-phase which has a more complex crystal structure than the β or γ-phase.

Phase	Structure	BSE Contrast	EBSD Colour	Phase Fraction (vol.%)
β-phase	BCC	Dark	Red	58 ±2
γ-phase	FCC	Grey	Green	25 ±2
σ-phase	TCP	Grey	Yellow	13 ±2
Oxide	-	Black	Black	4 ±1

TABLE 4.4: Phase fractions of the heat treated EP1 coating as calculated by image analysis of the EBSD phase map shown in Fig.4.7b.

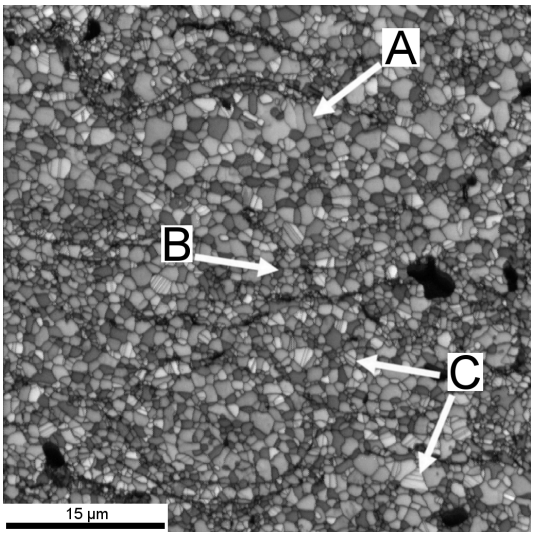

(a)

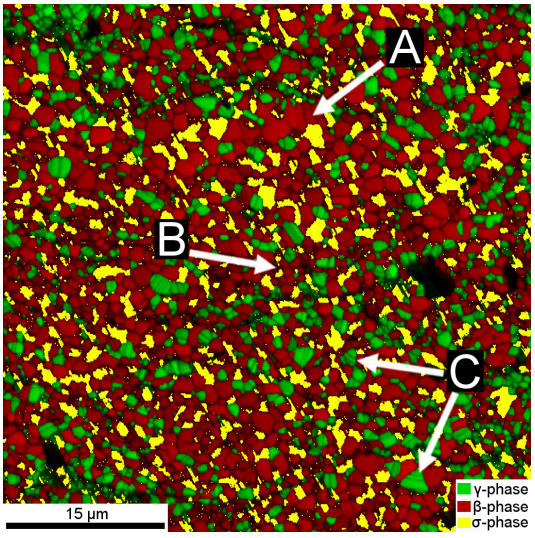

(b)

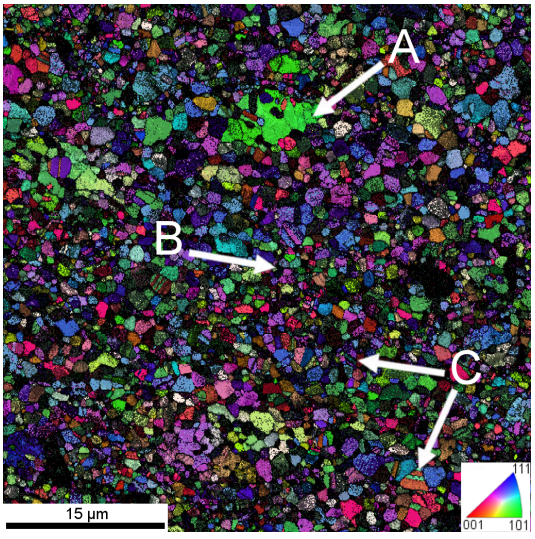

(c)

FIGURE 4.7: EBSD images of heat treated EP1 coating. (a) is a band contrast map showing grain boundaries and (b) is a phase map in which the γ-phase is coloured green, the β-phase is coloured red and the σ-phase is coloured yellow. (c) is an inverse pole figure map showing grain orientation. The letters A and B indicate areas of large and fine grains respectively. The letter C indicates twinning in the γ-Ni phase.

4.5 Microstructural Characterisation of Novel Alloy EP2

4.5.1 X-Ray Diffraction Analysis

The X-ray diffraction patterns obtained for the EP2 alloy powder, as sprayed coating and heat treated coating are shown in Fig.4.8. All three patterns exhibit strong BCC β-NiAl phase peaks and secondary FCC γ-Ni phase peaks, as well as minor Al_2O_3 peaks. There is a small shift in the main β-phase peak as was seen for the EP1 alloy.

There is clear evidence of peak broadening in the as sprayed coating, possibly due to microstrain or nanometre grain size in the coating after thermal spraying. The peak broadening has caused the main β-phase (110) peak and the main γ-phase (111) peak to overlap.

The heat treated coating exhibits FCC γ-Ni peaks which have clearly split. The split peaks are evidence of two FCC phases with lattice parameters which differ slightly. In this instance the two phases are FCC γ-Ni phase and FCC γ'-Ni_3(Al,Ta) phase. The EP2 heat treated coating also shows some minor TCP phase peaks which is evidence of a small amount of σ-Cr_2Co phase.

The detection limit for XRD analysis is approximately 2 wt.%, as such it is possible that the γ' and σ-phase exist in the powder and as sprayed coating at $\leq$ 2 wt.%.

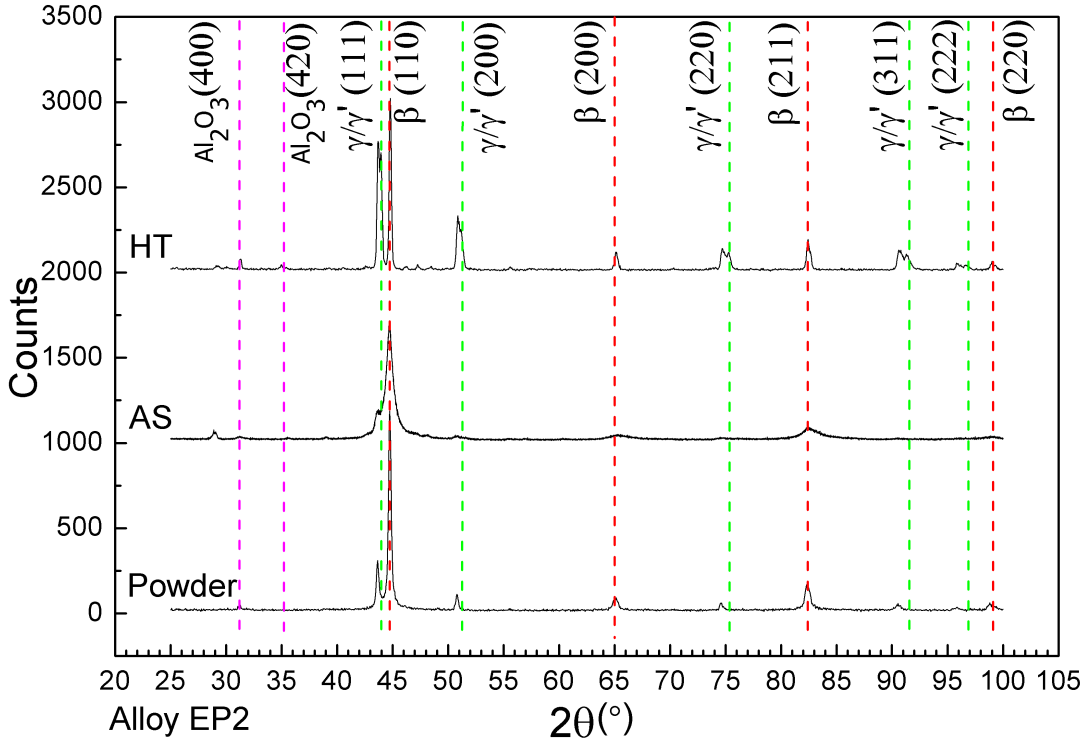

(a)

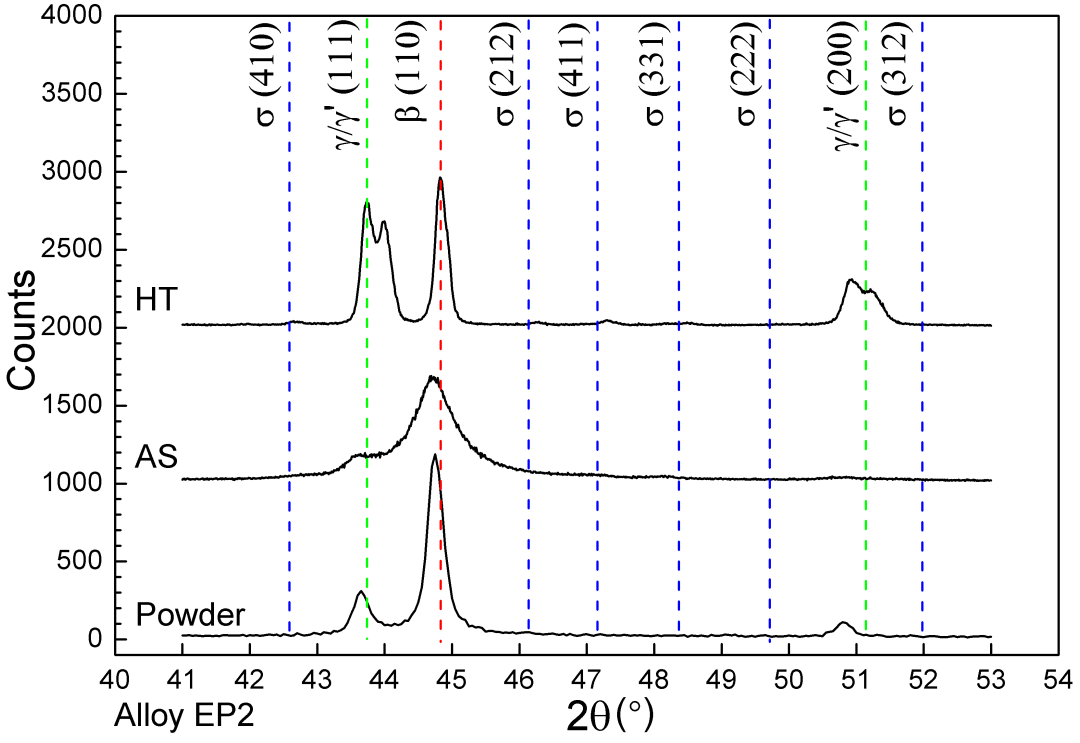

(b)

FIGURE 4.8: X-ray diffraction patterns of the EP2 alloy, in the form of powder, as sprayed (AS) and heat treated (HT) coatings. (a) shows the 2θ range 25-100 ° and (b) shows the 2θ range 41-53 °.

4.5.2 Scanning Electron Microscopy and Energy Dispersive X-ray Analysis

As Received Powder

A cross section of the EP2 powder is shown in Figs.4.9a and 4.9b. There is a two phase microstructure consisting of 64 vol.% dark-contrast dendrite phase and 36 vol.% grey-contrast interdendritic secondary phase. The dark-contrast and grey-contrast phase are probably the β-NiAl phase and γ-Ni phase identified in the XRD patterns.

Some areas of the grey-contrast phase appear brighter in the BSE image. These regions are probably rich in solutes such as Ta, Y and Hf which increase the mean atomic number of the phase.

The structure observed in the EP2 powder is the result of non-equilibrium cooling during solidification, which is described in section 4.4.2.

As Sprayed Coating

A cross section of the as sprayed coating is shown in Figs.4.9c and 4.9d. The EP2 as sprayed coating is similar to the C1 and EP1 as sprayed coatings. Retained powder particles can be identified at low magnification and at high magnification there are regions which have retained the original powder microstructure (A), regions which have undergone coarsening (B), regions which have fully melted and reformed as a single phase (C), and very dark regions (D) which are probably either pores or Al_2O_3 oxide which was identified in the XRD pattern.

Heat Treated Coatings

The heat treated EP2 coating is shown Figs.4.9e and 4.9f. Point EDX measurements obtained for the different phases are summarised in table 4.5 and EDX chemical maps are shown in the Fig.4.10 for the region indicated by the dotted black box in Fig.4.9f.

In the BSE images of the heat treated EP2 coating four phases can be identified; a dark-contrast phase identified as β-NiAl phase, a grey-contrast phase identified as γ-Ni phase, a light-contrast phase identified as Ni_3(Al,Ta)-γ' phase, and a black phase identified as primarily Al_2O_3 oxide. A small phase fraction of black phase may be pores.

The γ'-phase precipitates within regions of γ-phase to form regions of γ/γ'. A small number of single γ-phase regions can be identified but are uncommon.

A small amount of σ-Cr_2Co phase was identified by XRD analysis. The σ-phase probably has similar BSE contrast to the γ-phase, as in the the EP1 coating, but only exists at very low phase fractions in the EP2 coating which makes it difficult to identify by EDX analysis. No point EDX measurements showed compositions similar to the σ-phase and so the σ-phase could not be identified in the EDX maps.

Phase	BSE Contrast	Phase Composition in HT Coating (wt.%)					
		Ni	Co	Cr	Al	Ta	O
β-phase	Dark	53±2	19±1	7±2	19±1	2±1	-
γ-phase	Grey	38±2	30±1	21±2	6±1	4±1	-
γ'-phase	Light	47±2	19±2	7±1	7±1	20±2	-
Oxide	Black	25±2	14±2	10±2	28±3	≤ 1	22±3

TABLE 4.5: Composition of the heat treated EP2 coating as measured by EDX. Average of 4 spectra. Errors shown are the standard deviations.

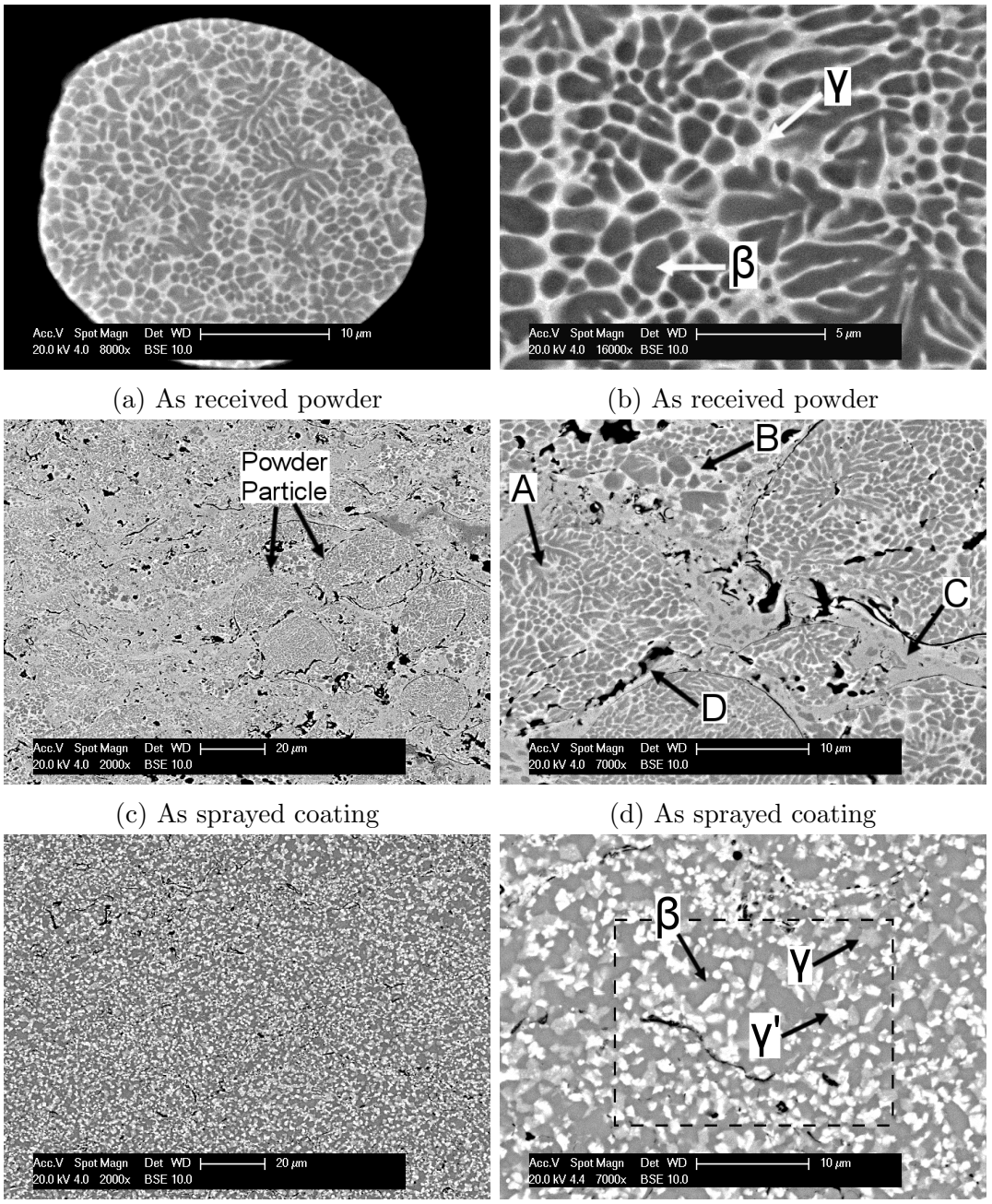

(a) As received powder (b) As received powder

(c) As sprayed coating (d) As sprayed coating

(e) Heat treated coating (f) Heat treated

FIGURE 4.9: BSE images of (a-b) EP2 alloy powder, (c-d) as sprayed coating and (e-f) heat treated coating. The black dotted box indicates the region shown in Fig.4.10.

4.5.3 Electron Back Scatter Diffraction

Fig.4.11 shows a 50 µm × 50 µm region of the heat treated EP2 coating imaged by EBSD. Fig.4.11a is a band contrast map showing grain boundaries and Fig.4.11b is a phase map in which three phases are clearly identified. The γ and γ'-phases both have an FCC crystal structure so are not readily distinguished by EBSD. As such, the γ and γ'-phases are both coloured green. The β-phase is coloured red and the σ-phase is coloured yellow. Fig.4.11c is an inverse pole figure.

The band contrast map shows that the grain size in the EP2 coating is not uniform. There are regions consisting of large grains, indicated by A, and regions consisting of much finer grains, indicated by B. Comparison of the phase map and band contrast map shows that the β phase and γ/γ' regions are polycrystalline, which is not revealed in the BSE images. There is also evidence of twinning in the γ/γ' regions, as indicated by C. The inverse pole figure shows that there is no preferred grain orientation for any phase.

As the γ and γ'-phases cannot be distinguished by EBSD analysis, the BSE images and EBSD maps must be used in conjunction in order to make phase fractions measurements. The phase fraction of γ/γ' regions in the EBSD phase map is approximately 47 vol.%. The phase fraction of the γ'-phase, as measured from the BSE images, is approximately 20 vol.%. Therefore the phase fraction of the γ-phase can be calculated at approximately 27 vol.%.

The phase fractions of the β-phase and σ-phase are approximately 49 and 1 vol.% respectively. The phase fraction measurements are summarised in table 4.6.

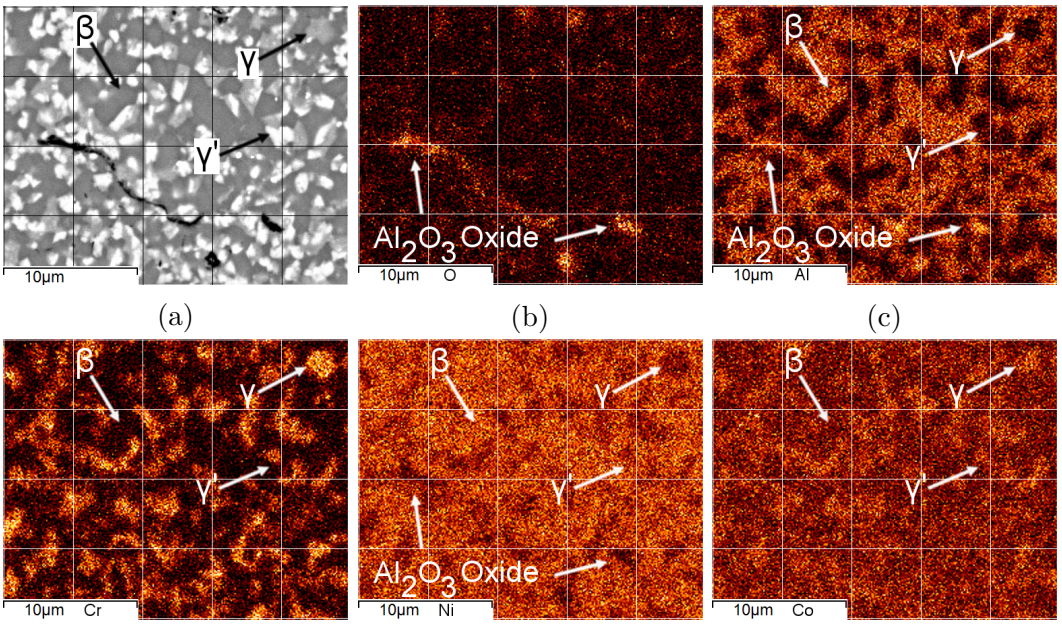

FIGURE 4.10: BSE image (a) and EDX maps (b-f) of the region highlighted by the dotted black box in Fig.4.9f. The β-phase is identified by areas rich in Al and Ni, the γ-phase is identified by areas rich in Cr and Co with low Al and Ni and the γ'-phase is identified by areas rich in Ni and low in Al, Cr and Co.

Phase	Structure	BSE Contrast	EBSD Colour	Phase Fraction (vol.%)	
				Powder	HT
β-phase	BCC	Dark	Red	64 ±2	49 ±2
γ-phase	FCC	Grey	Green	36 ±3	27 ±2
γ'-phase	FCC	Light	Green	-	20 ±2
σ-phase	TCP	Grey	Yellow	-	1 ±2
Oxide	-	Black	Black	-	2.7 ±1

TABLE 4.6: Phase fractions of the as recieved EP2 alloy powder and heat treated EP2 coating as calculated by image analysis. Measurements are are combination of analysis of SEM and EBSD images.

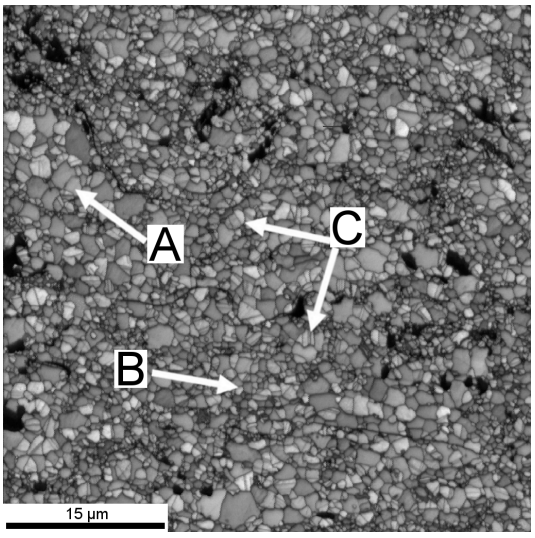

(a)

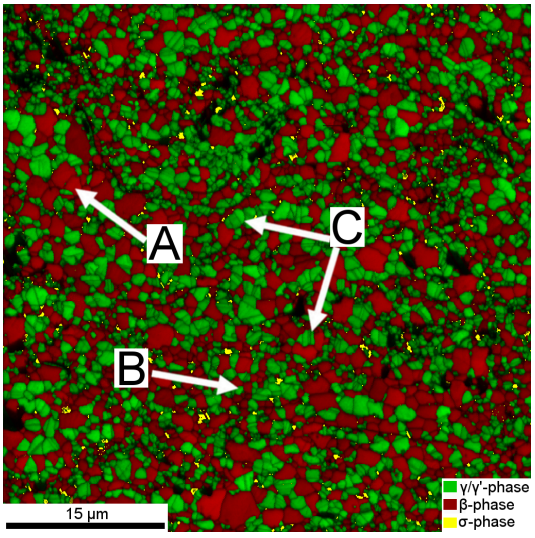

(b)

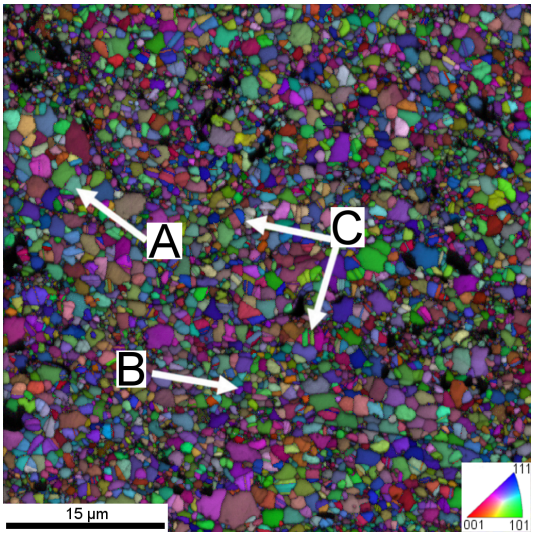

(c)

FIGURE 4.11: EBSD images of heat treated EP2 coating. (a) is a band contrast map showing grain boundaries and (b) is a phase map in which the γ and γ'-phases are coloured green, and the β-phase is coloured red and the σ-phase is coloured yellow. (c) is an inverse pole figure map showing grain orientation. The letters A and B indicate areas of large and fine grains respectively. The letter C indicates twinning in the γ/γ'-phase.

4.6 Microstructural Characterisation of Novel Alloy EP3

4.6.1 X-Ray Diffraction Analysis

The X-ray diffraction patterns obtained for the EP3 alloy powder, as sprayed coating and heat treated coating are shown in Fig.4.12. All three patterns show strong BCC β-NiAl phase. There is evidence of considerable peak broadening in the as sprayed pattern and a shift in the main β-phase peak as was seen in the EP1 and EP2 as sprayed coatings.

The heat treated coating also shows TCP σ-Cr_2Co phase peaks as well as overlapping FCC γ-Ni phase and FCC Ni_3(Al,Ta)-γ' peaks. At 2θ = 44 ° the γ and γ'-phase peaks (111) appear as a single wide peak with a rounded top but at higher 2θ values the peaks become wider and eventually split into two separate peaks.

The detection limit for XRD analysis is approximately 2 wt.%, as such it is possible that the γ, γ' and σ-phase exist in the powder and as sprayed coating at $\leq$ 2 wt.%.

4.6.2 Scanning Electron Microscopy and Energy Dispersive X-ray Analysis

As Received Powder

A cross section of the EP3 powder is shown in Figs.4.13a and 4.13b. The EP3 powder has a similar microstructure to the EP1 powder. There appears to be heavily segregated β-NiAl phase with some regions rich in solutes. The very light regions constitute 8 vol.% of the EP3 powder so are unlikely to be a separate phase which was not detected during XRD analyis (detection limit of $\approx$ 2 wt.%). The very light regions are probably areas rich in Ta.

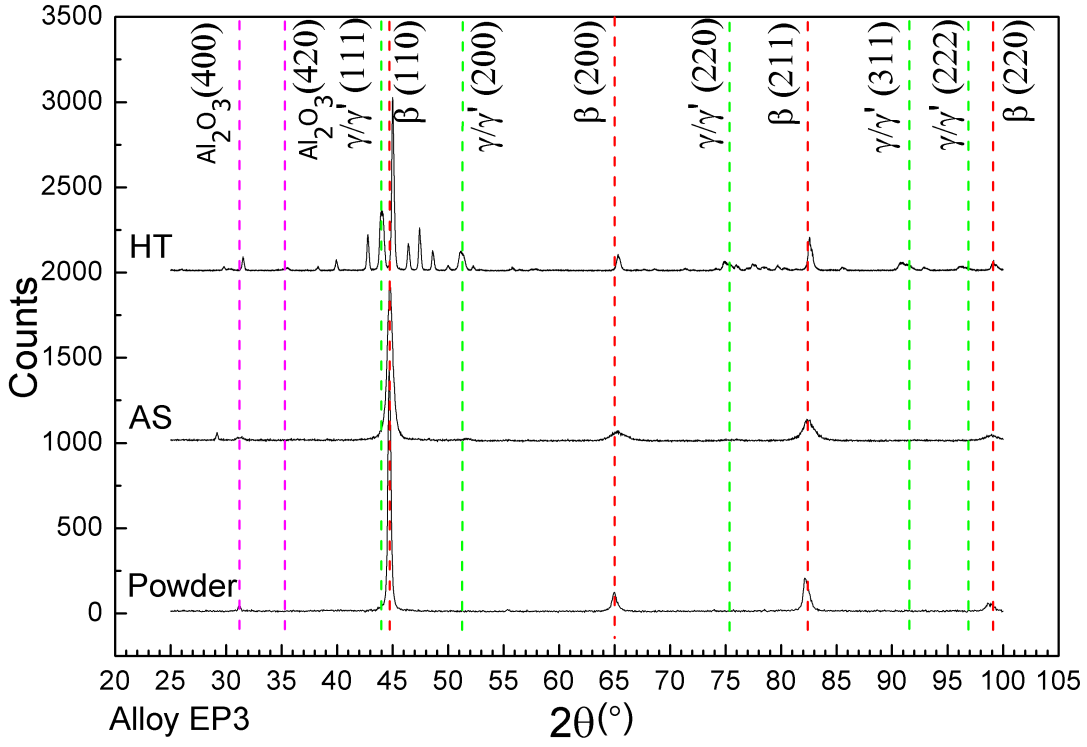

(a)

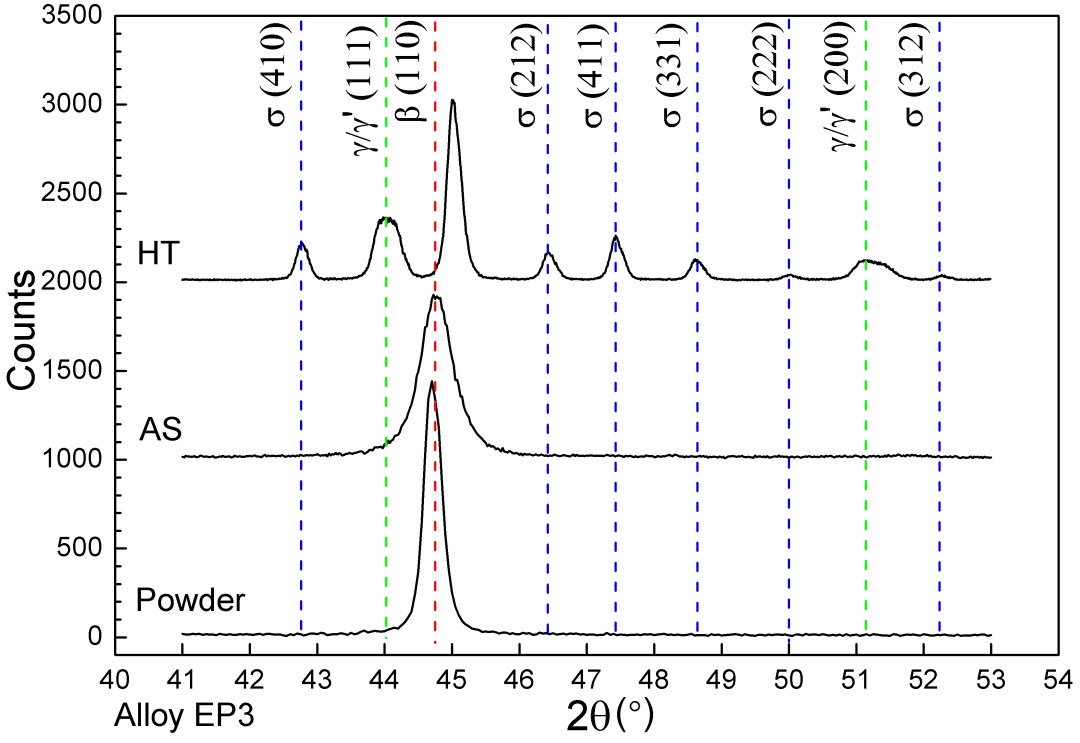

(b)

FIGURE 4.12: X-ray diffraction patterns of the EP3 alloy, in the form of powder, as sprayed (AS) and heat treated (HT) coatings. (a) shows the 2θ range 25-100 ° and (b) shows the 2θ range 41-53 °.

As Sprayed Coating

A cross section of the as sprayed coating is shown in Figs.4.13c and 4.13d. The EP3 as sprayed coating is similar to the EP1 and EP2 as sprayed coatings. Powder particles can be identified and the different regions are identified by A-D.

The EP3 as sprayed coating appears to consist of heavily segregated β-phase, as observed in the EP1 as sprayed coating and EP3 alloy powder. The varying composition of the β-phase explains some of the peak broadening observed in the XRD pattern.

Heat Treated Coatings

The heat treated EP3 coating is shown in Figs.4.13e and 4.13f. Point EDX measurements are summarised in table 4.7 and EDX maps of the region highlighted by the black dotted box in Fig.4.13f are shown in Fig.4.14.

The EP3 heat treated coating exhibits the dark-contrast β-NiAl phase, the grey-contrast phase which is either γ-Ni or σ-Cr_2Co phase, the light-contrast Ni_3(Al,Ta)-γ' phase and the black phase which is primarily Al_2O_3 oxide. A small phase fraction of black areas may be pores.

There is sufficient σ-phase in the EP3 coating to allow it to be distinguished from the γ-phase in the EDX maps but the accuracy of the EDX measurements is not high enough to allow for phase fraction measurements.

Phase	BSE Contrast	Composition of Phases in HT Coating (wt.%)					
		Ni	Co	Cr	Al	Ta	O
β-phase	Dark	52±2	17±1	9±1	20±2	2±1	-
γ-phase	Grey	36±4	23±1	27±4	10±2	3±1	-
γ'-phase	Light	48±2	15±1	8±1	10±1	18±1	-
σ-phase	Grey	18±2	27±1	47±2	3±1	4±1	-
Oxide	Black	23±4	16±1	22±3	22±2	≤ 1	16±2

TABLE 4.7: Composition of the heat treated EP3 coatings as measured by EDX. Average of 4 spectra. Errors shown are the standard deviations.

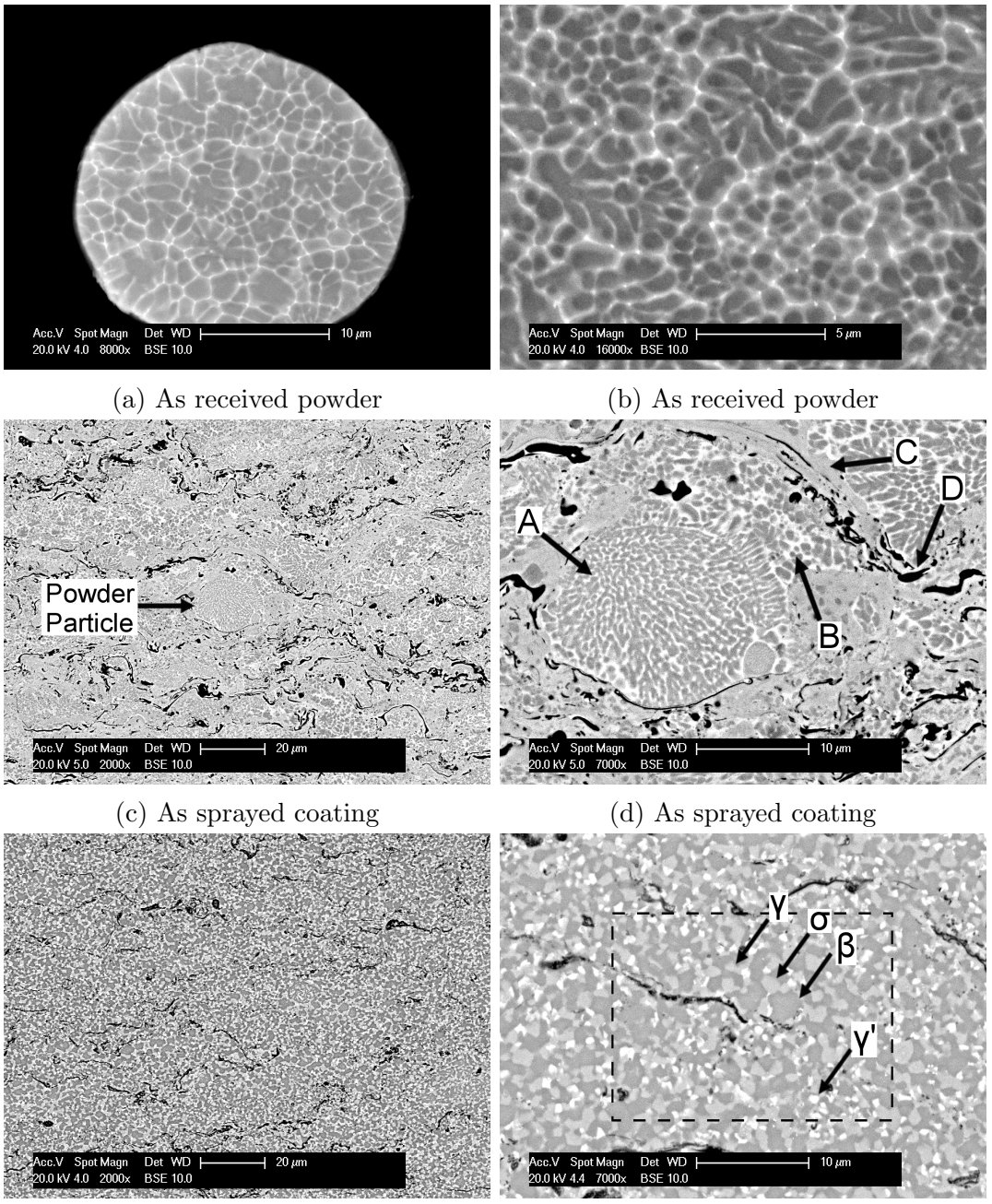

(a) As received powder (b) As received powder

(c) As sprayed coating (d) As sprayed coating

(e) Heat treated coating (f) Heat treated coating

FIGURE 4.13: BSE images of cross sections of the EP3 alloy powder (a-b), as sprayed coating (c-d) and heat treated coating (e-f). The black dotted box indicates the region shown in Fig.4.14.

4.6.3 Electron Back Scatter Diffraction

Fig.4.15 shows a 50 µm × 50 µm region of the heat treated EP3 coating imaged by EBSD. Fig.4.15a is a band contrast map showing grain boundaries and Fig.4.15b is a phase map in which three phases are clearly identified. The γ and γ'-phases are coloured green, β-phase is coloured red and the σ-phase is coloured yellow. Fig.4.15c is an inverse pole figure.

The grain size in the EP3 coating is not uniform. There are regions of large and small grains as indicated by A and B respectively. There is also evidence of twinning in the γ/γ'-phase as indicated by C. Comparison of the phase map and band contrast map shows that all the phases are polycrystalline, which is not revealed in the BSE images.

The inverse pole figure shows there is no preferred orientation for either phase. The dark regions in the inverse pole figure generally correspond to the σ-phase where the software struggled to accurately characterise the complex crystal structure.

The phase fractions are summarised in table 4.8. The heat treated EP3 coating contains approximately 59 vol.% β-phase and 18 vol.% σ-phase. The γ/γ' phase constitutes approximately 19 vol.% of the EBSD phase map and the phase fraction of the γ'-phase in the BSE image (Fig.4.13f) is approximately 7 vol.%. Therefore, the phase fraction of the γ-phase is calculated as approximately 12 vol.%.

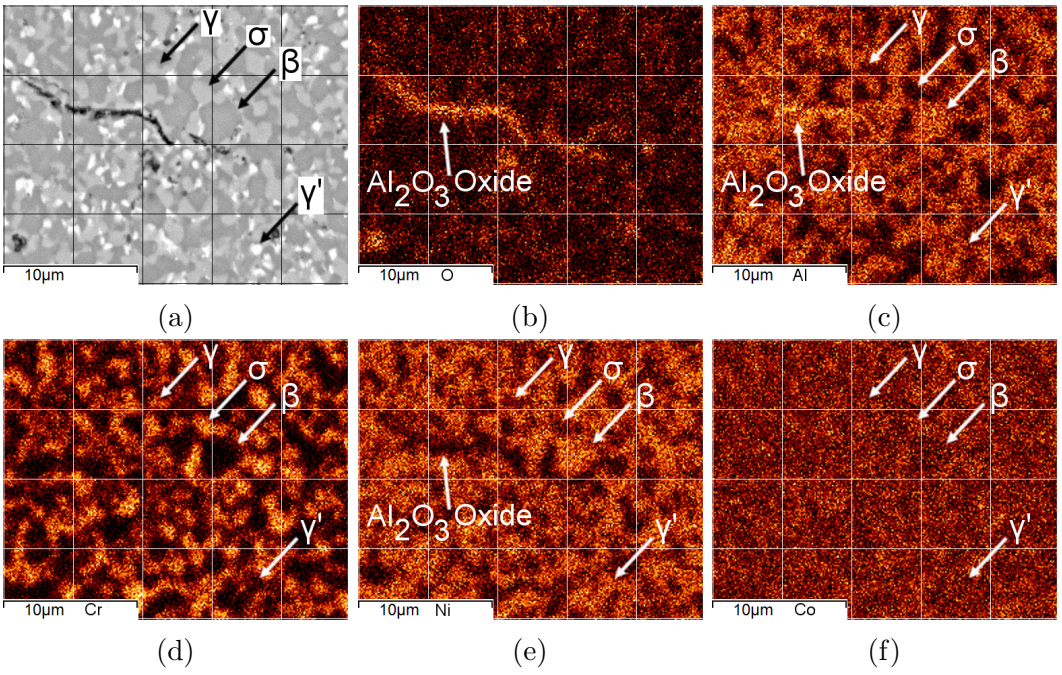

FIGURE 4.14: BSE image (a) and EDX maps (b-f) of the black dotted box highlighted in Fig.4.13f. The β-phase is identified by areas rich in Al and Ni, the γ-phase is identified by areas rich in Cr and Co with low Al and Ni, the γ'-phase is identified by areas rich in Ni and low in Al, Cr and Co, and the σ-phase is identified by regions ver rich in Cr and low in Al and Ni.

Phase	Structure	BSE Contrast	EBSD Colour	Phase Fraction (vol.%)
β-phase	BCC	Dark	Red	59 $\pm$2
γ-phase	FCC	Grey	Green	12 $\pm$2
γ'-phase	FCC	Light	Green	7 $\pm$2
σ-phase	TCP	Grey	Yellow	18 $\pm$2
Oxide	-	Black	Black	4 $\pm$1

TABLE 4.8: Phase fractions of the heat treated EP3 coating as calculated by image analysis. Measurements are are combination of analysis of SEM and EBSD images.

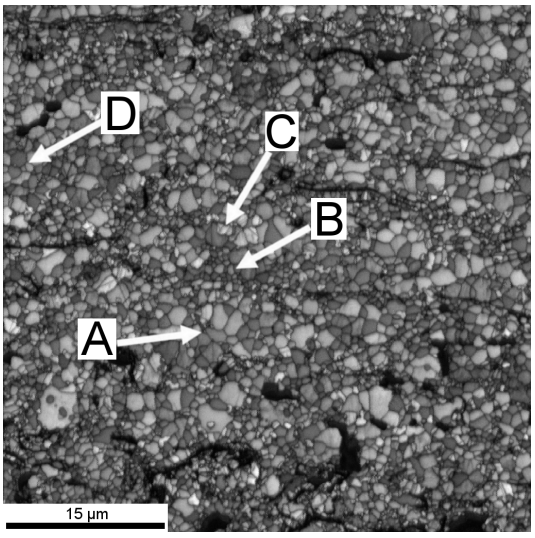

(a)

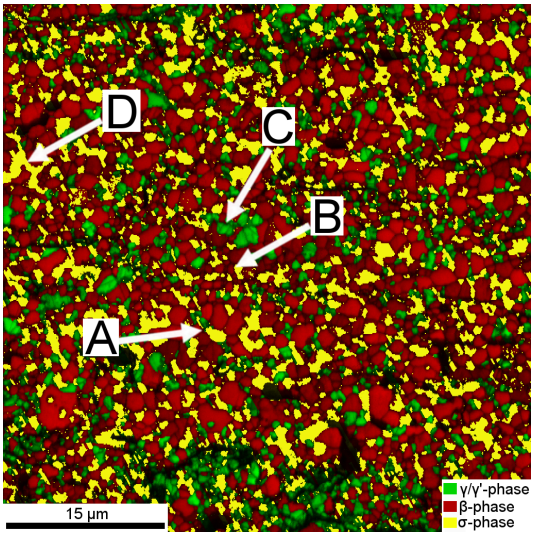

(b)

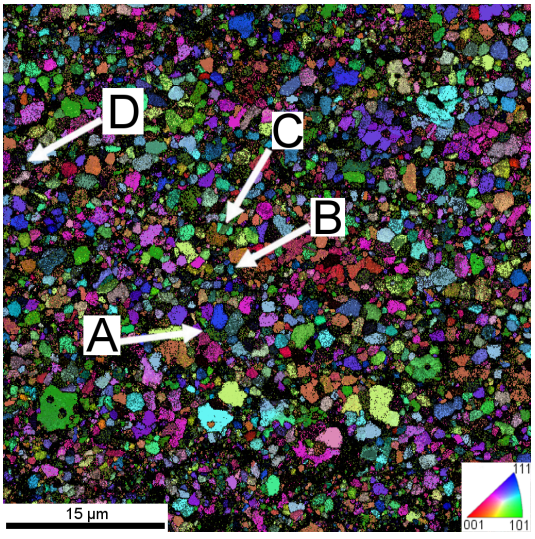

(c)

FIGURE 4.15: EBSD images of heat treated EP3 coating. (a) is a band contrast map showing grain boundaries and (b) is a phase map in which the γ and γ'-phases are coloured green, and the β-phase is coloured red and the σ-phase is coloured yellow. (c) is an inverse pole figure map showing grain orientation. The letters A and B indicate areas of large and fine grains respectively. The letter C indicates twinning in the γ/γ'-phase.

4.7 Oxidation Trials of Coatings EP1, EP2 and EP3

The novel EP1, EP2 and EP3 alloys were designed to be Al_2O_3 formers with oxidation resistance comparable to existing MCrAlY alloys. In order to assess the oxidation behaviour of the EP1, EP2 and EP3 alloys, short, accelerated oxidation trials were conducted at 1100 °C in air for 24, 48, 72 and 96 hours on the heat treated coatings. 1100 °C is above the normal operation temperature for an MCrAlY bond coat (approximately $\leq$ 950 °C) and allows the accelerated oxidation behaviour to be assessed over a short time period in air. Oxidation trials at 1100 °C have been widely used previously to assess the oxidation behaviour of MCrAlY alloys [32, 33, 42, 56, 63].

BSE images of cross sections of the EP1, EP2 and EP3 coatings following 24 and 96 hours at 1100 °C are shown in Fig.4.16. Chemical maps, obtained by EDX analysis, for all three coatings after 24 and 96 hours are shown in Figs.4.17 and 4.18 respectively.

After 24 hours the EP1, EP2 and EP3 coatings have formed alumina scales approximately 3.0, 4.2 and 3.9 μm thick. There is no evidence of any other oxides forming for any of the coatings.

In the alumina scale of the EP2 coating after 24 hours there are bright regions, probably caused by solutes such as Ta, Hf and possibly Y, which suggest the alumina scale is not single phase Al_2O_3. Similar bright regions can be seen in the alumina scale of the EP3 coating after 24 hours but to a lesser extent. There is also a crack in the alumina scale of the EP2 coating after 24 hours.

Near the surface of all three coatings there is a β-depletion zone. This is known to form in MCrAlY coatings during oxidation [63] and is caused by a flux of Al towards the growing oxide. The width of the β-depletion zone is approximately linked to the rate of oxidation [46]. The EP1 coating exhibits the smallest β-depletion zone and the EP2 coating exhibits the largest.

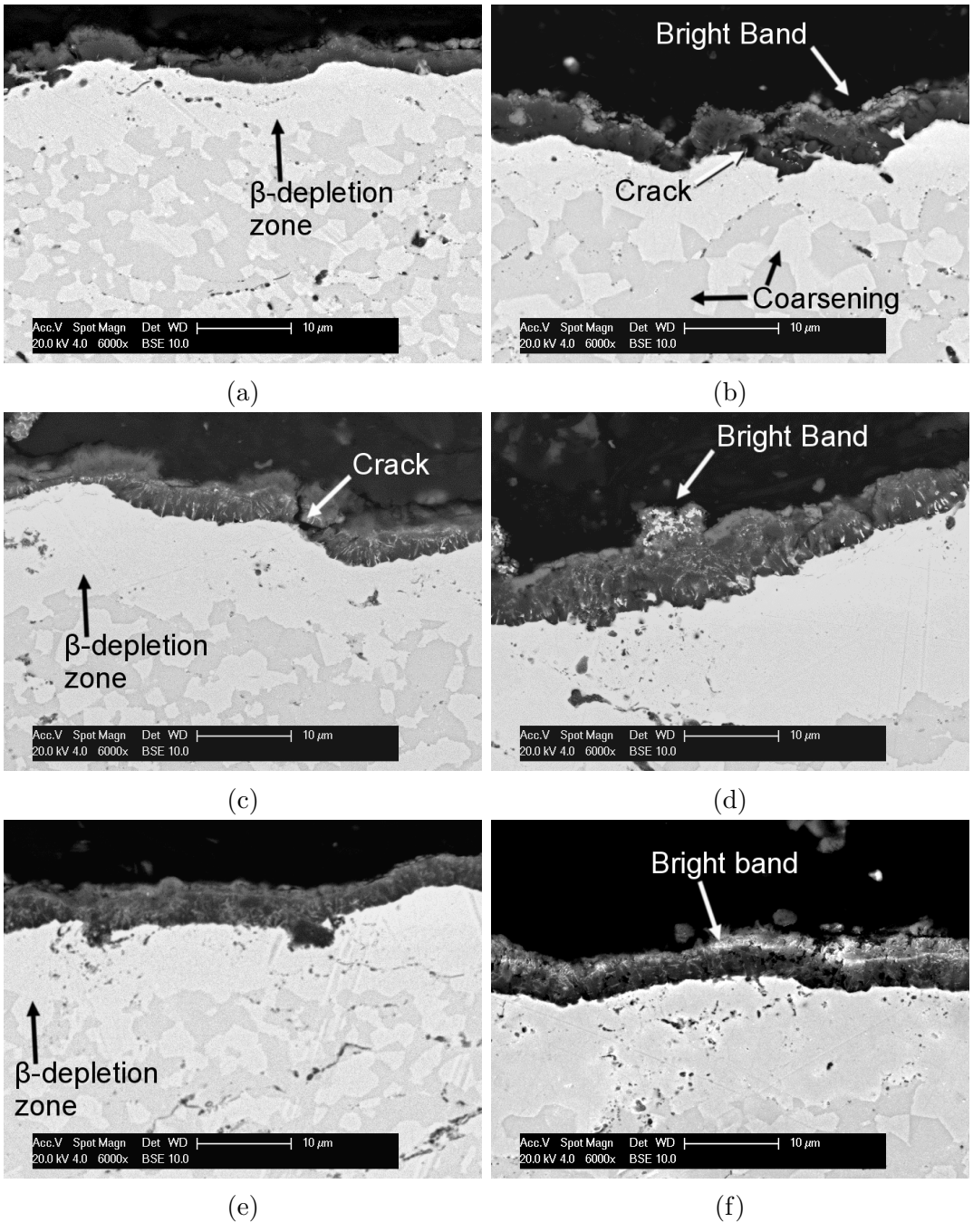

FIGURE 4.16: BSE images of heat treated EP1, EP2 and EP3 coating following oxidation at 24 hours (left) and 96 hours (right) at 1100°C.

After 96 hours the alumina scales on the EP1, EP2 and EP3 coatings have grown to approximately 5.0, 7.5 and and 6.8 μm respectively. The EP1 coating exhibits the lowest oxide growth and the EP2 coating exhibits the highest, which agrees with previous oxidation studies of these coatings [142].

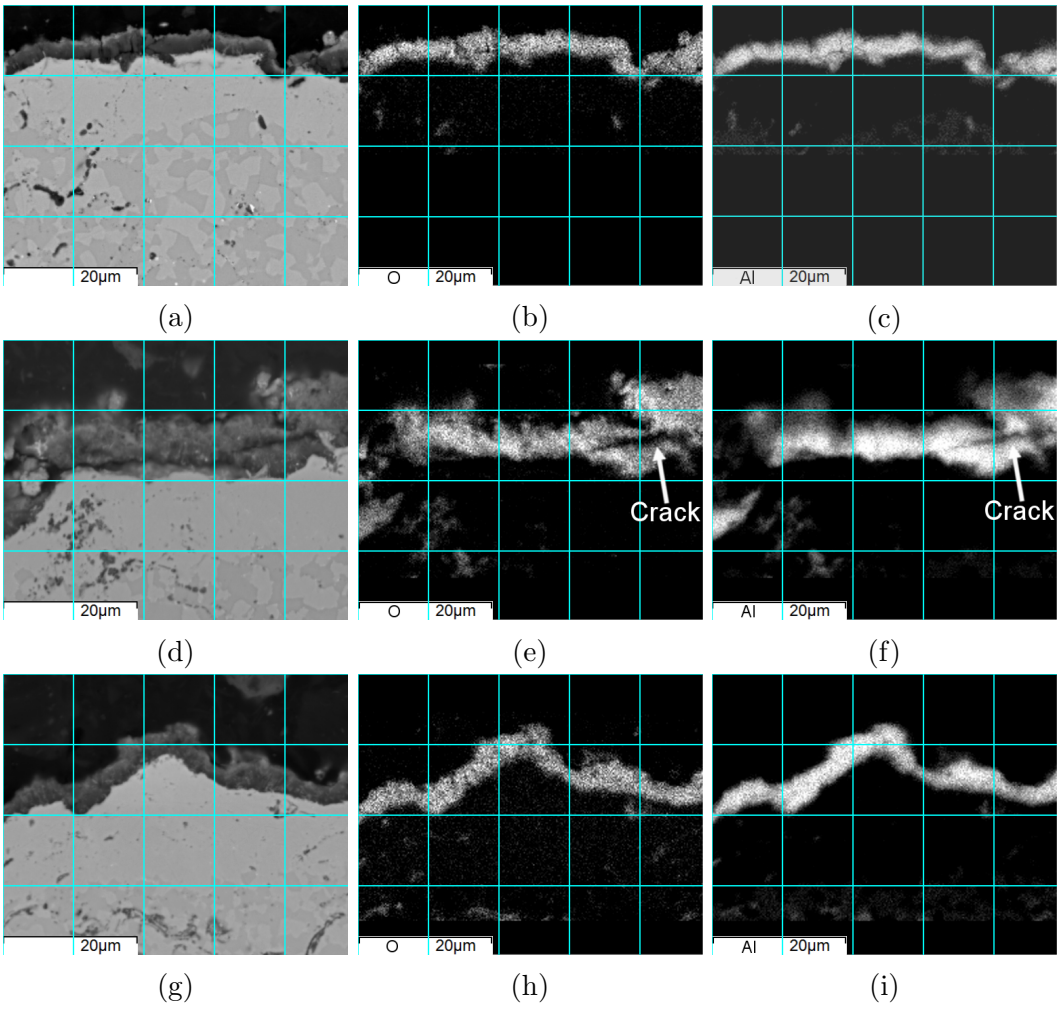

FIGURE 4.17: BSE images and EDX maps of the oxide scale formed on coatings EP1, EP2 and EP3 following 24 hours at 1100°C.

The β-depletion zone has grown in all three coatings. The EP2 coating exhibits the largest β-depletion zone and the EP1 coating exhibits the smallest. There is also significant evidence of coarsening of the β-phase in the EP1 coating after 96 hours.

There are bright bands in the alumina scales of all three coatings after 96 hours. These are possibly due to spinel oxides containing Co, Cr or Ni, or contamination of minor solutes such as Ta, Hf and Y.

There are also cracks observable in the alumina scale of all three coatings after 96 hours.

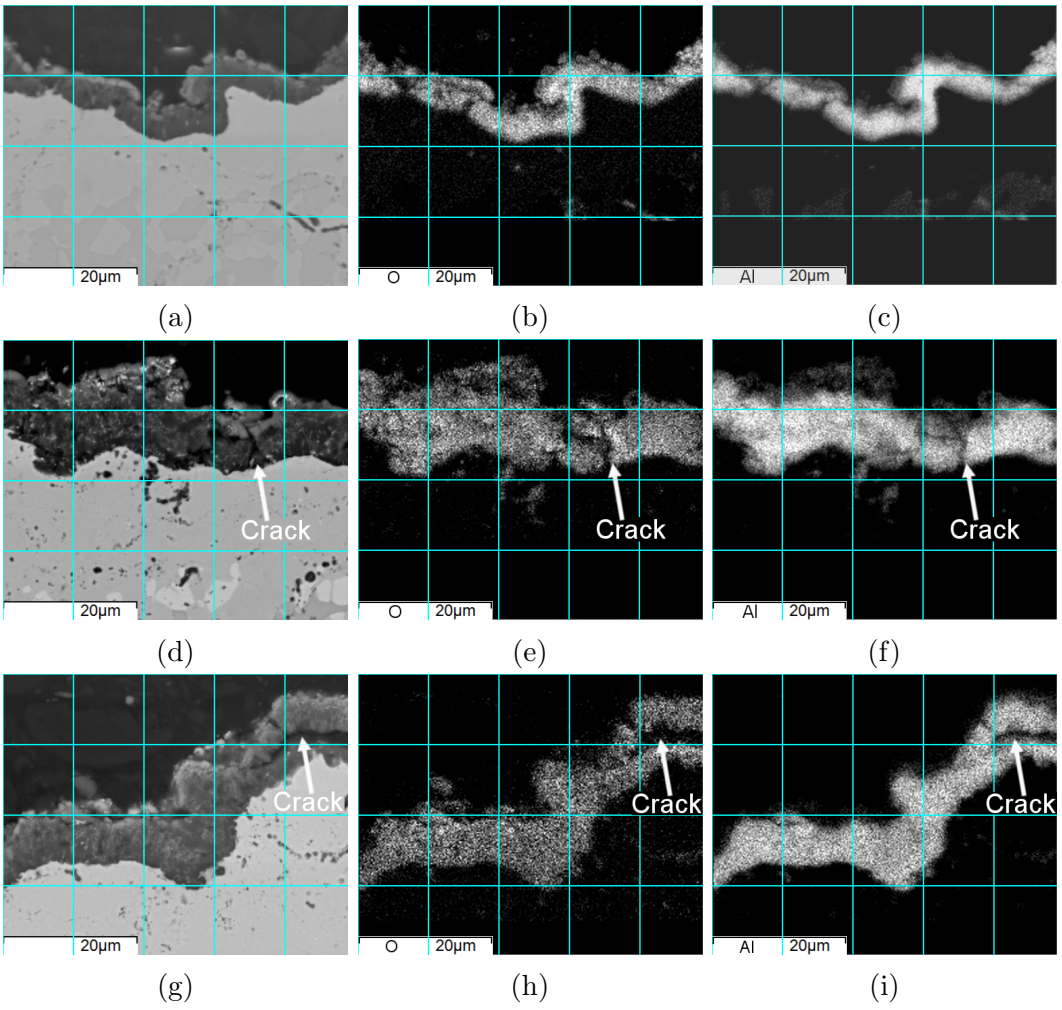

FIGURE 4.18: BSE images and EDX maps of the oxide scale formed on coatings EP1, EP2 and EP3 following 96 hours at 1100°C.

The average Al_2O_3 oxide thickness after 24, 48, 72 and 96 hours at 1100 °C for each of the coatings is shown in Fig.4.19. The error bars show the standard deviation of the measurements. An oxide thickness of 2 μm after 96 hours is plotted for the C1 coating. This is an average value based on the reported oxidation of coatings manufactured from Praxair CO-210-24 alloy powder [32, 33, 42, 56, 63]. All three coatings show a higher oxide growth rate than that reported for the C1 coating.

The short oxidation trial has shown that all three coatings are Al_2O_3 formers. There is also some evidence of spinel oxides and minor solutes in the alumina scales of all three coatings, in particular the EP2 coating. It is clear that the EP1, EP2 and EP3 alloys show a higher oxide growth than the C1 alloy.

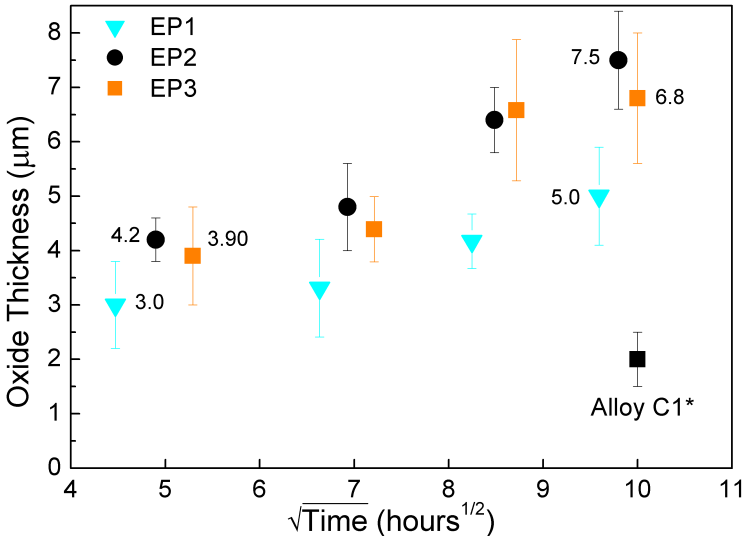

FIGURE 4.19: Plot of oxide thickness vs time$^{1/2}$ for the EP1, EP2 and EP3 coatings following 24, 48, 72 and 96 hours at 1100 °C. The value for alloy C1 is based on values reported in literature [32, 33, 42, 56, 63].

4.8 Modelling of Phase Evolution

Thermodynamic equilibrium calculations were carried out for each of the alloys in order to predict phase formation. Calculations were made using the Thermo-Calc software package and the TTNi7 database. The phases included in the calculations were the β-NiAl, γ-Ni, γ'-Ni_3(Al,Ta), σ-Cr_2Co and α-Cr phases, which have been previously reported to exist in MCrAlY coatings [5, 6, 26, 27, 32, 33, 42, 48, 56, 63, 145–147].

The calculations are represented in Fig.4.20 as plots of phase mass fraction vs temperature. The equilibrium phase fraction ratios (wt.%) of each alloy at 750, 850 and 1100 °C are summarised in table 4.9. The coatings were heat treated at 1100 °C and SPC tested at 750 and 850 °C, as described in chapter 6.

The composition of each equilibrium phase as a function of temperature is shown in Figs.4.21 and 4.22.

4.8.1 Alloy C1

The phase evolution of the C1 alloy under equilibrium cooling can be described as:

$$L \xrightarrow{1343^{\circ}C} L{+}\gamma \xrightarrow{1327^{\circ}C} L{+}\gamma{+}\beta \xrightarrow{1326^{\circ}C} \gamma{+}\beta \xrightarrow{851^{\circ}C} \gamma{+}\beta{+}\sigma \xrightarrow{650^{\circ}C} \gamma{+}\beta{+}\sigma{+}\gamma'$$

The γ-phase is predicted to form on cooling from the liquid at 1343 °C and the β-phase at 1327 °C. The phase fraction of the γ-phase steadily decreases with decreasing temperature whilst the phase fraction of the β-phase increases. At 851 °C and 650 °C respectively, the σ and γ'-phases are predicted to form.

The predicted compositions of the β-NiAl and γ-Ni phases in the C1 alloy under thermodynamic equilibrium are shown in Figs.4.21a and 4.21b respectively. The σ and γ'-phases are not shown as they were not observed in the heat treated coating.

The composition of the β-phase remains approximately constant between 1327 and 600 °C. The composition of the γ-phase changes over the temperature range but not significantly. The levels of Co and Al increase and decrease respectively, whilst the level of Cr and Ni fluctuate but remain approximately constant.

4.8.2 Alloy EP1

The phase equilibria of the EP1 alloy can be described as follows:

$$L \xrightarrow{1390^{\circ}C} L+\beta \xrightarrow{1299^{\circ}C} L+\beta+\gamma \xrightarrow{1279^{\circ}C} \beta+\gamma \xrightarrow{1145^{\circ}C} \beta+\gamma+\alpha\text{-Cr}$$
$$\xrightarrow{1028^{\circ}C} \beta+\gamma+\alpha\text{-Cr}+\sigma \xrightarrow{1008^{\circ}C} \beta+\gamma+\sigma \xrightarrow{732^{\circ}C} \beta+\gamma+\sigma+\gamma' \xrightarrow{700^{\circ}C} \beta+\sigma+\gamma'$$

The calculations predict that the β-phase and γ-phase form at 1390 and between 1299-700 °C respectively. The σ-phase is predicted to form at 1028 °C and the γ'-phase at 732 °C. The calculations also predict α-Cr forms between 1145-1008 °C.

The phase mass fractions of β, σ and γ'-phases increase slowly with decreasing temperature whilst the phase fraction of the γ-phase decreases.

The predicted compositions of the phases in the EP1 alloy under thermodynamic equilibrium are shown in Figs.4.21c and 4.21d respectively.

The compositions of the β, σ and γ'-phases remain approximately constant below 1390, 1028 and 732 °C respectively. The composition of the γ-phase fluctuates between 1299 and 700 °C but remains approximately constant.

4.8.3 Alloy EP2

The phase equilibria of the EP2 alloy can be described as follows:

$$L \xrightarrow{1425°C} L+\beta \xrightarrow{1298°C} L+\beta+\gamma \xrightarrow{1265°C} \beta+\gamma \xrightarrow{1007°C} \beta+\gamma+\gamma' \xrightarrow{861°C} \beta+\gamma+\gamma'+\sigma \xrightarrow{671°C} \beta+\gamma'+\sigma$$

The β, γ' and σ phases are predicted to form at 1425, 1007 and 861 °C respectively. The γ-phase is predicted to form between 1298 and 671 °C. The phase mass fractions of the β and γ-phases decrease with decreasing temperature whilst the phase fractions of the σ and γ'-phases increase.

The predicted compositions of the phases in the EP2 alloy under thermodynamic equilibrium are shown in Figs.4.22a and 4.22b respectively.

For the β-phase, the level of Ni decreases slowly between 1425 and 600 °C whilst the levels of Al and Cr remain approximately constant. Below 1007 °C the levels of Co and Ta increase and decrease respectively.

The composition of the γ-phase is approximately constant between 1298-1007 °C but changes significantly between 1007-671 °C, which coincides with formation of the γ'-phase. The composition of the γ'-phase is relatively constant between 1007-600 °C, as is the composition of the σ-phase between 861-600 °C.

4.8.4 Alloy EP3

The phase equilibria of the EP3 alloy can be described as follows:

$$L \xrightarrow{1408°C} L+\beta \xrightarrow{1307°C} L+\beta+\alpha\text{-Cr} \xrightarrow{1278°C} L+\beta+\alpha\text{-Cr}+\gamma \xrightarrow{1263°C} \beta+\alpha\text{-Cr}+\gamma \xrightarrow{1041°C} \beta+\alpha\text{-Cr}+\gamma+\sigma \xrightarrow{971°C} \beta+\gamma+\sigma \xrightarrow{780°C} \beta+\gamma+\sigma+\gamma' \xrightarrow{712°C} \beta+\sigma+\gamma' \xrightarrow{1041°C} \beta+\sigma+\gamma'+\alpha\text{-Cr}$$

The β, σ and γ'-phases are predicted to form at 1408, 1041 and 780 °C respectively. The γ-phase is predicted to form between 1278-712 °C and α-Cr is predicted to form between 1307-971 °C.

The phase mass fractions of the σ and γ'-phases increase with decreasing temperature whilst the phase fraction of γ-phase decreases. The phase fraction of β-phase increases with decreasing temperature above 790 °C but decreases below 790 °C.

The compositions of the phases in the EP3 alloy under thermodynamic equilibrium are shown in Figs.4.22c and 4.22d respectively.

The compositions of the β and σ-phases remain approximately constant. The composition of the γ-phase fluctuates between 1278-712 °C but remains approximately constant. The composition of the γ'-phase changes between 780-712 °C but remains approximately constant below 712 °C.

Alloy	Equilibrium Phases (wt.%)										
	750 °C				850 °C				1100 °C		
	γ	β	σ	γ'	γ	β	σ	γ'	γ	β	α-Cr
C1	48	43	9	-	61	39	-	-	70	30	-
EP1	17	63	20	-	21	63	16	-	43	55	2
EP2	6	50	9	35	19	56	2	23	38	62	-
EP3	11	60	25	4	17	62	21	-	33	58	9

TABLE 4.9: Equilibrium phase mass fractions of the C1, EP1, EP2 and EP3 alloys as calculated using Thermo-Calc and the TTNi7 database.

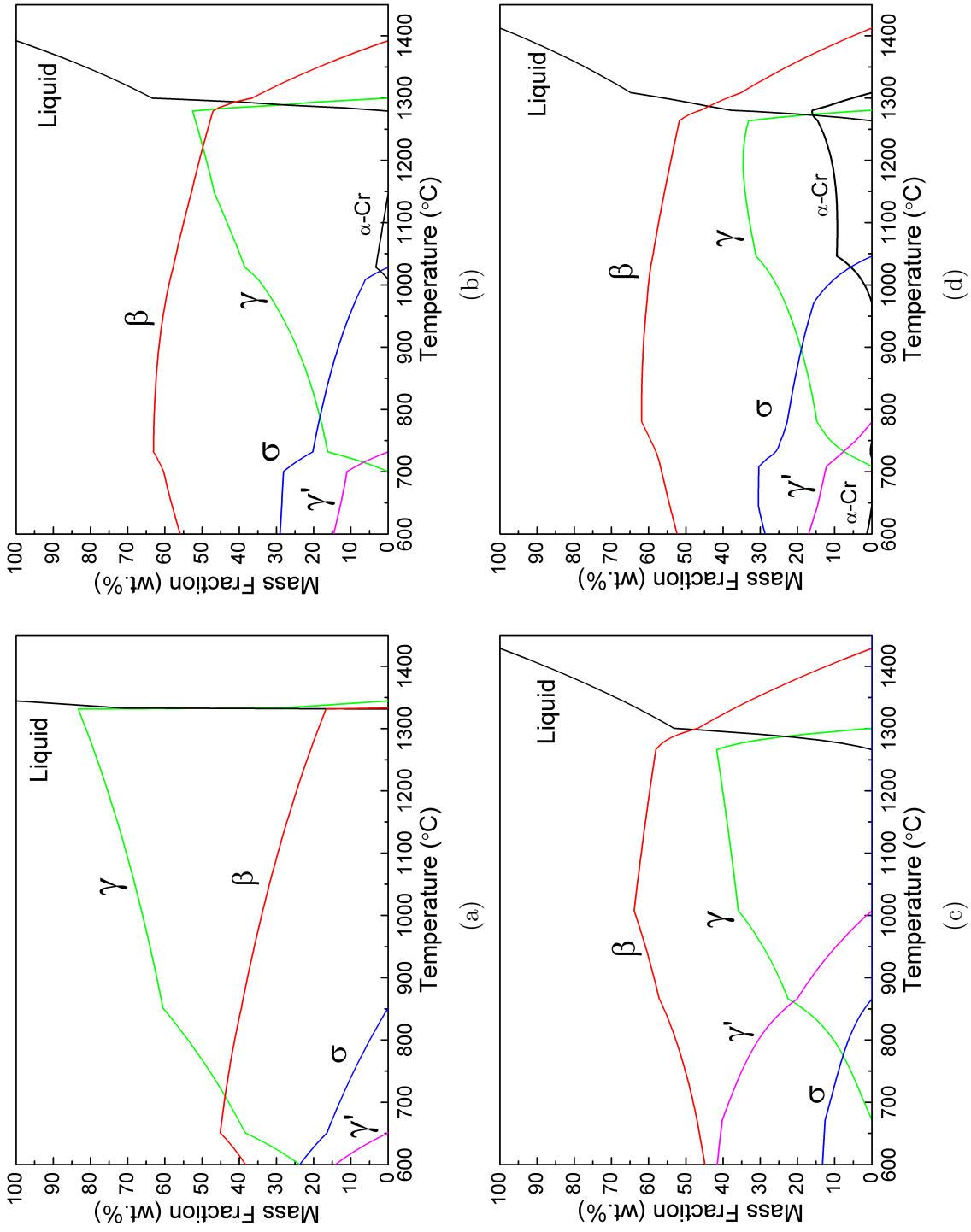

FIGURE 4.20: Phase mass fractions as a function of temperature under thermodynamic equilibrium in alloys (a) C1, (b) EP1, (c) EP2 and (d) EP3. Calculated using the Thermo-Calc software package and the TTNi7 database.

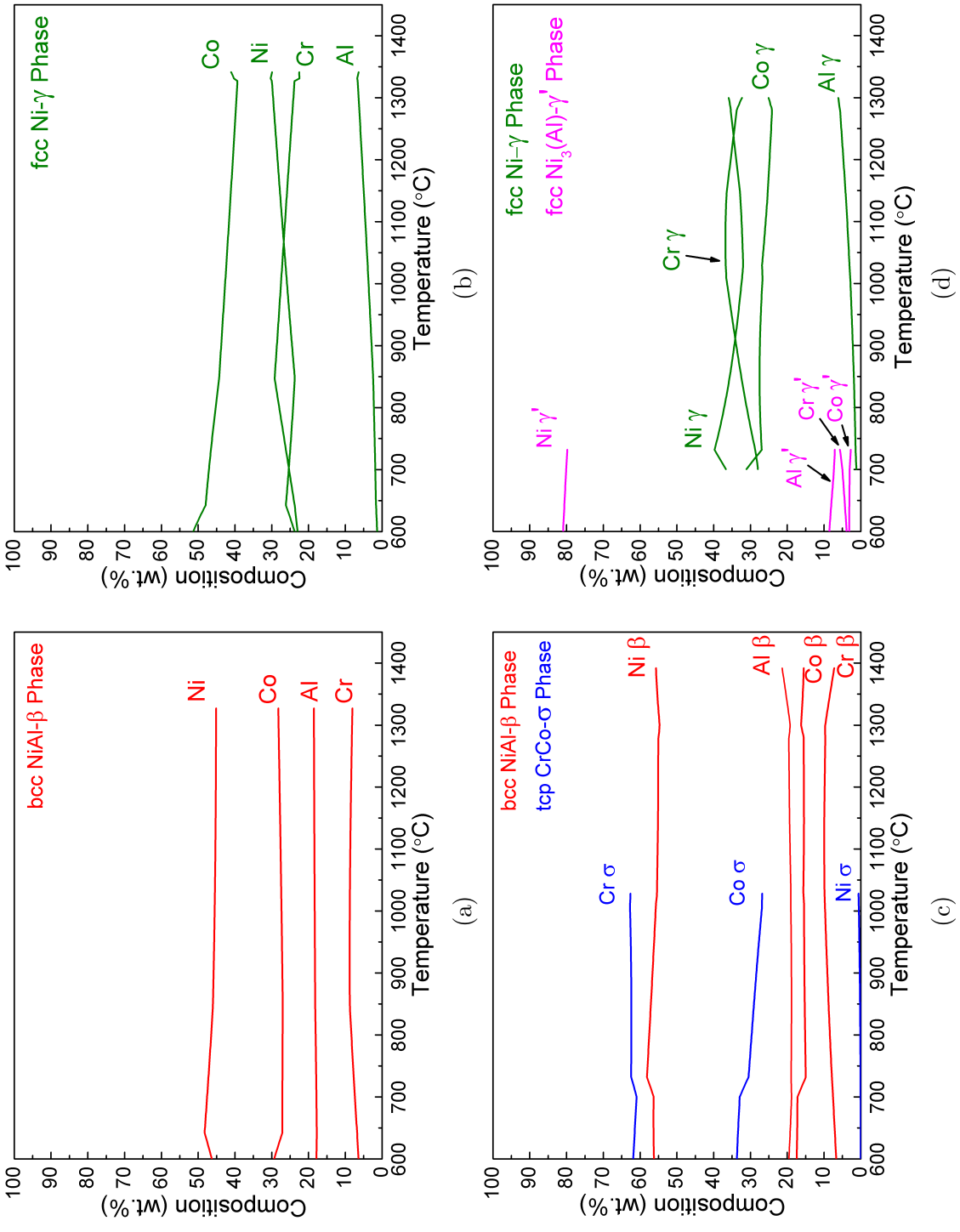

FIGURE 4.21: Composition of the phases present in the C1 (a-b) and EP1 (c-d) alloys under thermodynamic equilibrium. Calculated using the Thermo-Calc software package and the TTNi7 database.

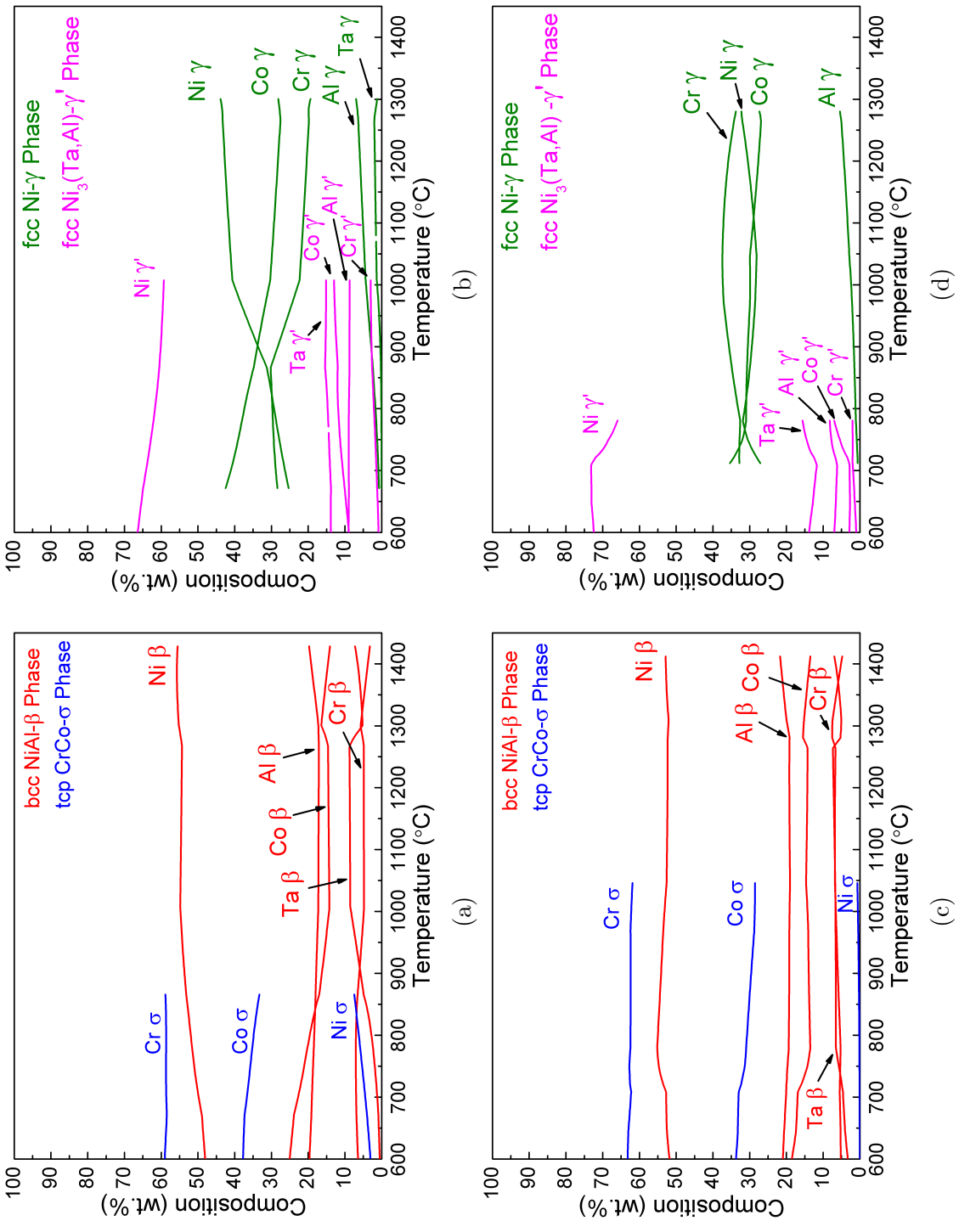

FIGURE 4.22: Composition of the phases present in the EP2 (a-b) and EP3 (c-d) alloys under thermodynamic equilibrium. Calculated using the Thermo-Calc software package and the TTNi7 database.

4.9 Discussion

The purpose of this section is to evaluate the key microstructural features of the C1, EP1, EP2 and EP3 alloys. Firstly, the observed microstructures in the alloy powders, as sprayed coatings and heat treated coatings for each alloy are discussed with reference to the CALPHAD calculations made using Thermocalc and the TTNi7 database. Then the microstructures of the heat treated coatings are compared to coatings of similar composition and finally, the oxidation behaviour of the coatings is discussed with reference to the microstructures of the coatings.

4.9.1 Powder Solidification

Gas atomised powders between approximately 20-50 μm diameter, which is similar to the C1, EP1, EP2 and EP3 alloy powders, experience cooling rates in the proximity of 10 $^{-4}$ K/s [143]. Smaller powder particles experience higher cooling rates than larger powder particles, which means the phase evolution under cooling differs between differently sized powders, making it difficult to accurately predict the phase mass fractions of alloy powders using CALPHAD methods. Nevertheless, the equilibrium phase fraction plots are useful in predicting which phases form first during the atomisation process.

For the C1 powder, the γ-Ni phase is predicted to form first followed by the β-NiAl phase, resulting in a γ-matrix. This agrees with the microstrucutre observed for the C1 alloy powder.

For the EP1, EP2 and EP3 powders, β-NiAl phase is predicted to form first, which results in a β-phase matrix under rapid cooling, as observed in the alloy powders. At the high cooling rates experienced by the powders, the β-phase forms as dendrites. The dendrites exhibit coring and the surrounding liquid becomes enriched in Co, Cr and Ta. This enriched liquid can subsequently form γ-Ni phase upon further cooling, as observed for the EP2 alloy. The formation of γ-Ni phase, as well as other solid state phase changes, can be suppressed by fast cooling which leaves the powders in a metastable state, as observed for the EP1 and EP3 alloys.

4.9.2 Development of As Sprayed Microstructures

The as sprayed coatings of the C1, EP1, EP2 and EP3 alloys all exhibited similar microstructures. There were regions which retained the original powder particle microstructure, regions which underwent microstructural coarsening and regions which appeared to have melted and re-solidified as a single phase. Similar microstructures have been reported previously for as sprayed HVOF coatings [43, 56, 57, 59, 63].

It has been reported that during HVOF thermal spraying, the powder particles may be comprised of fully melted regions, partially melted regions and unmelted cores [56, 59, 143]. Upon contact with the gas flame, the outside of the spherical powder particle melts first, causing a temperature gradient to form between the hot surface and the cooler core of the particle, with a semi-molten region forming across the gradient. The degree to which a particle melts is dependent upon its size. As feedstock powders contain a range of particle sizes, a range of molten, semi-molten and unmelted powder particles impact the substrate during spraying [59].

For large powder particles, the unmelted core retains the original powder microstructure, regions of which were identified in all of the as sprayed coatings. For some powder particles, the molten surface may oxidise during spraying and cause oxide stringers to be retained in the coating. The molten, as well as semi-molten regions, also undergo extensive deformation when impacting the substrate. The degree of deformation is dependent upon the size of the powder particle but can often be determined by the oxide stringers retained in the coatings, which adopt the shape of the deformed particle.

Smaller powder particles, which may become fully molten during spraying, undergo rapid cooling upon impact with the substrate and solidify into a single phase region. The formation of secondary phases is suppressed by the high cooling rate [59]. For the C1 alloy the single phase regions are presumably γ-Ni phase but for the experimental alloys it is likely the single phase regions are β-NiAl phase.

The regions which exhibited microstructural coarsening may be where semi-molten powder retained, in part, the original powder microstructure but also underwent coarsening during spraying.

As multiple layers of powder are deposited during HVOF thermal spraying, it can be assumed that regions of the already deposited coating exhibit thermal spikes as subsequent layers are deposited. These thermal spikes may have allowed secondary phases to precipitate in single phase regions and also contributed to the microstructural coarsening observed in other regions.

4.9.3 Development of Heat Treated Microstructures

The thermal cycle used for the heat treatment of the coatings was: heating from RT to 1100 °C at 3 K/min, annealing at 1100 °C for 2 hours, and furnace cooling from 1100 °C to RT at approximately 3 K/min.

Because of the fine scale microstructure of the coatings, it can be expected that an equilibrium state is approached during two hours at 1100 °C. It also possible that phase evolution took place under furnace cooling. The temperature range in which phase evolution took place can be estimated by comparing the observed heat treated microstructures with the predicted phase fractions at 900 and 1100 °C. The predicted phase fractions, converted from wt.% to vol.% using the method outlined in appendix B, are shown in table 4.10 alongside the phase volume fractions observed in the heat treated coatings.

The predicted phase fractions of the C1 alloy at 1100 °C show good agreement with the observed phase fractions of the heat treated C1 coating, which indicates little phase evolution took place below 1100 °C.

For the EP1 and EP2 alloys, the observed phase fractions show better agreement with the predicted phase fractions at 900 °C than at 1100 °C. This indicates phase evolution took place under furnace cooling above approximately 850-950 °C.

For the EP3 alloy, γ'-phase was observed in the heat treated coating but is not predicted to form above 780 °C in the CALPHAD calculations. It is unlikely that phase evolution took place in the EP3 coating at lower temperatures than in the C1, EP1 and EP2 coatings. This suggests the phase modelling for the EP3 alloy is slightly inaccurate. One reason for this could be the α-Cr phase, which is predicted to form between 1307-971 °C but is not observed in the heat treated coatings.

Fig.4.23 shows the phase fraction plots for the EP3 alloy when α-Cr is included in the calculations and when it is removed. When α-Cr is removed from the calculations the formation temperatures of the σ and γ'-phase, as well as the dissolution temperature of the γ-phase, are increased by approximately 150 °C. This appears to be a more accurate calculation of the solvus of γ', which has been previously reported to be approximately 800-900 °C in MCrALY alloys [26, 148]. However, the γ-Ni phase is predicted to become unstable when the γ'-Ni_3(Al,Ta) phase forms, which is not accurate since both phases were observed in the heat treated EP3 coating. The actual phase evolution in the EP3 alloy is probably a combination of Figs.4.23a and 4.23b.

The CALPHAD calculations predict the formation of α-Cr occurs at high temperature when the σ-phase becomes unstable, presumably because of the limited solubility of Cr in the γ-Ni phase. This agrees with previous work by Toscano et al. [27], who reported that the formation of α-Cr is promoted when the σ-phase becomes unstable above 880 °C.

In this study, the composition of α-Cr phase was predicted to be $\geq$ 65 wt.% Cr with approximately 20 wt.% Co, which is a similar composition to the σ-phase. Toscano et al. [27] however, reported the precipitates of α-Cr to be $\geq$ 90 at.% Cr.

The CALPHAD calculations, using the TTNi7 database, appears to be a reasonably accurate model of the phase evolution in the alloys, but is less accurate for the EP3 alloy when α-Cr is included. The TTNi7 database does not appear to be able to accurately predict the composition of α-Cr phase or it's influence on the formation of other phases.

Alloy	Equilibrium Phases (vol.%)							Observed Phase Fraction (vol.%)			
	900 °C				1100 °C						
	γ	β	σ	γ'	γ	β	α-Cr	γ	β	σ	γ'
C1	58	42	-	-	66	33	-	69	31	-	-
EP1	22	65	13	-	39	59	2	27	60	13	-
EP2	24	62	-	14	35	65	-	28	51	1	21
EP3	17	65	18	-	30	61	9	13	62	18	7

TABLE 4.10: Equilibrium phase mass fractions of the C1, EP1, EP2 and EP3 alloys at 900 and 1100 °C as calculated using Thermo-Calc and the TTNi7 database alongside the phase volume fractions observed in the heat treated coatings. The observed phase fractions have an error of ±2-3 vol.%.

4.9.4 Comparison With Related Alloys

Thermally sprayed coatings, manufactured from the C1 alloy and alloys of similar composition, commonly exhibit a γ-Ni matrix phase and precipitates of β-NiAl phase [9, 30, 32, 33, 36, 42, 56, 63], which agrees with the heat treated C1 coating. The grain size of coatings manufactured from the C1 alloy has also been reported as ≤ 3 μm [34, 63, 149]. It is clear the observed microstructure of the C1 alloy powder and C1 coatings is consistent with the literature.

The web-like microstructure observed in the EP1, EP2 and EP3 alloys has previously been observed for an MCrAlY alloy with high levels of Al [35]. A NiCoCrAlY alloy with a high Al content and composition similar to the EP1 alloy has been reported to exhibit only β-NiAl phase as a powder but both γ-Ni and β-NiAl phases when deposited as a thermally sprayed coating [43]. Other coatings manufactured from high Al MCrAlY alloys have also been reported to exhibit γ-Ni and β-NiAl phase [150]. Therefore, it can be concluded the lack of γ-phase in the EP1 and EP3 alloy powders is due to the high cooling rate during atomisation and not the composition of the alloys.

A number of MCrALY alloys exhibit the σ-Cr_2Co phase [26, 27, 145, 146], which is reported to form in Ni-based superalloys due to an excess of Cr [6]. The alloys which have been reported to precipitate σ-phase typically have 20 wt.% Cr, similar to the C1 alloy, but low levels of Co (approximately 20 wt.%.), similar to the EP1,

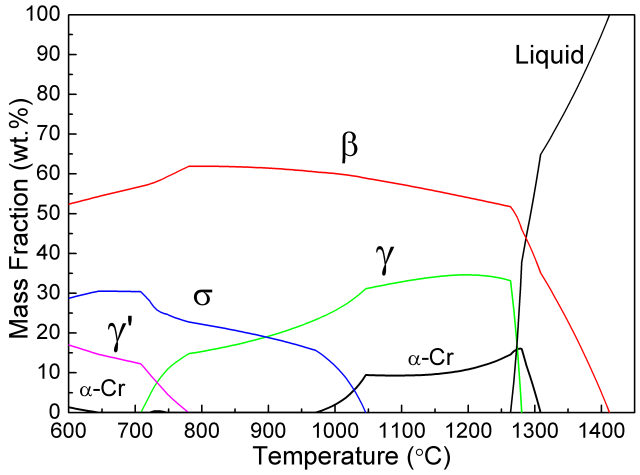

(a)

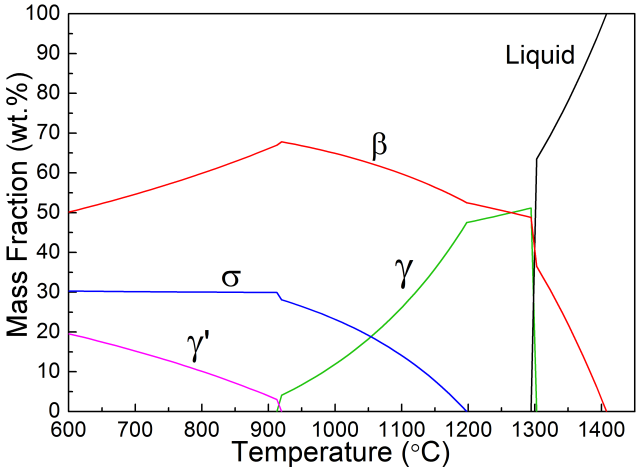

(b)

FIGURE 4.23: Phase fractions as a function of temperature under thermodynamic equilibrium for alloy EP3 including α-Cr (a) and excluding α-Cr (b). Calculated using the Thermo-Calc software package and the TTNi7 database.

EP2 and EP3 alloys. It is therefore the relative levels of Cr and Co which causes σ-phase to precipitate in the EP1, EP2 and EP3 alloys. The EP2 alloy has the highest ratio of Co to Cr and so exhibits the lowest amount of σ-phase. The σ-phase has also been reported to have the same BSE contrast as the γ-Ni phase [27].

The γ'-Ni_3(Al,Ta) is only present in the EP2 and EP3 alloys which suggests Ta promotes the formation of the γ'-phase. Ta is reported to promote γ'-phase [6] and has been reported in an NiCoCrAlY alloy with levels of Ta similar to the EP3 alloy [147]. However, the formation of γ'-phase is very complex and can form in

alloys without Ta. It has also been reported in a high Al, low Co NiCoCrAlY alloy [148] as well as in CoNiCrAlY and NiCoCrAlY alloys with 8 and 12 wt.% Al respectively [146]. Therefore, the presence of γ'-Ni_3(Al,Ta) in the EP2 and EP3 alloys can be attributed to the addition of Ta but a direct correlation between Ta and γ'-phase cannot be drawn.

4.9.5 Oxidation Behaviour

The EP1, EP2 and EP3 alloys were designed to be Al_2O_3 formers with oxidation resistance comparable to existing MCrAlY alloys. All three alloys developed Al_2O_3 oxides and also exhibited β-phase depletion zones which have been reported previously for MCrAlY coatings [9, 30, 46, 50, 151].

The oxide growth of the experimental alloys was much higher than that previously reported for the C1 alloy [32, 33, 42, 56, 63]. This can be attributed to the higher levels of Al in the EP1, EP2 and EP3 alloys, which has been shown to increase the oxidation rate of MCrAlY alloys [17, 49, 152].

The oxide growth of thermally sprayed MCrAlY coatings can also be affected by numerous factors including the thermal spray parameters [43, 54, 56], the composition of the alloy [146], the grain size of the coating [153], oxidation of the powder during spraying [30] and the initial heat treatment given to the coatings [31]. All of these factors have been optimised for the C1 alloy through numerous studies, but have not been optimised for the EP1, EP2 and EP3 alloys. Therefore, it is not surprising that the C1 alloy exhibits lower oxide growth than the EP1, EP2 and EP3 coatings.

The EP1, EP2 and EP3 coatings exhibit β-depletion zones approximately 12, 20 and 14 μm wide respectively. The β-depletion zone in a C1 alloy coating was recently reported as approximately 28 μm wide after 96 hours at 1100 °C [46]. The smaller β-depletion zones can be attributed to the higher levels of Al, which has been shown to reduce the size of the β-depletion zone [48] due to a higher volume fraction of β-phase.

The experimental alloys exhibit higher oxide growth than the C1 alloy but also smaller β-depletion zones. The lifetime of a TBC system can be reduced by both high oxide growth and large β-depletion zones [8, 44, 45, 50]. As such, it is not clear how the oxidation behaviour of EP1, EP2 and EP3 alloys would influence the lifetime of TBC systems without further oxidation trials.

4.10 Summary of Phase Evolution and Microstructure Chapter

The measured phase fractions (vol.%) of the heat treated coatings, normalised to exclude oxide content, are given in table 4.11. The appearance of each phase in the BSE images and EBSD phase maps is summarised in table 4.12.

All four MCrAlY alloys contain FCC γ-Ni and BCC β-NiAl phase. The TCP σ-Cr_2Co phase was found in the EP1, EP2 and EP3 alloys and FCC γ'-Ni_3(Al,Ta) phase was found in the EP2 and EP3 alloys.

In the BSE images, the β-phase appeared as a dark contrast phase, the γ'-phase appeared as a light phase and oxides/pores appeared as a black phase. The γ and σ-phases both appeared as a grey-contrast phase and could not be distinguished in the BSE images.

In the EBSD phase maps, the phases were designated a colour based on crystal structure. The BCC β-phase was coloured red and the TCP σ-phase was coloured yellow. The FCC γ-phase and FCC γ'-phase could not be distinguished and were both coloured green. Regions of oxide/pores were not characterised and appeared black.

In order to evaluate the suitability of the EP1, EP2 and EP3 alloys for industrial applications the mechanical properties of each alloy need to be evaluated. Unfortunately, it was not possible to test all three alloys within the time frame of this project. The alloys selected for further testing were the C1 alloy, which

has already been widely studied and provides a reference to existing data, and the EP1 alloy, which exhibits the simplest microstructure of the experimental alloys.

The EP3 alloy was selected as the third alloy to be studied as it has a similar composition to the EP1 alloy and contains a similar phase fraction of β-NiAl phase. Previous work concerning the experimental alloys [142] also recommended studying the EP1 and EP3 alloys over the EP2 alloy, as the EP2 alloy exhibited detrimental oxidation behaviour.

Alloy	Composition (wt.%)							Phase Fraction (vol.%)			
	Ni	Co	Cr	Al	Y	Ta	Others	γ	β	σ	γ'
C1	32.6	37.0	21.1	8.7	0.4	≤ 0.01	≤ 0.2	69	31	-	-
EP1	44.2	20.0	22.3	12.2	0.3	≤ 0.01	≤ 0.1	27	60	13	-
EP2	49.2	20.0	11.1	12.6	0.4	6.0	≤ 0.7	28	51	1	21
EP3	40.0	20.0	22.3	12.2	0.3	4.2	≤ 0.1	13	62	18	7

TABLE 4.11: Alloy composition and normalised phase fractions of the C1, EP1, EP2 and EP3 heat treated coatings. Phase fraction measurements are a combination of image analysis of SEM and EBSD images, are normalised to exclude oxide/pore content and are accurate to 2-3 vol.%.

Phase	Structure	BSE Contrast	EBSD Colour
β-NiAl	BCC	Dark	Red
γ-Ni	FCC	Grey	Green
γ'-$Ni_3(Al,Ta)$	FCC	Light	Green
σ-Cr_2Co	TCP	Grey	Yellow
Oxide	-	Black	Black

TABLE 4.12: BSE contrast, EBSD colour and crystal structure of the phases observed in the C1, EP1, EP2 and EP3 alloys.

Chapter 5

Small Punch Test for Tensile and Fracture Behaviour of MCrAlY Bond Coats

5.1 Introduction

The small punch tensile (SPT) test is an effective small-scale specimen technique for studying materials for which resources are limited, such as irradiated steels [93–100]. The test involves applying a constant displacement rate to a SP specimen in order to produce load-displacement curves. The load-displacement curves can be used to evaluate the mechanical properties and ductile to brittle transition temperature (DBTT) of the test material, as described in section 5.2. The geometry of the SPT test is described in detail in section 3.5.1.

The SPT results for the C1, EP1 and EP3 coatings between RT-750 °C are presented in this chapter. The load-displacement curves are described with reference to the macroscopic fracture patterns observed on the tensile surface of the specimens. The yield/fracture strength and DBTT of each coating is presented. The microscopic fracture surfaces and fracture paths for each

coating are investigated through scanning electron microscopy (SEM) and electron back-scatter diffraction (EBSD).

5.2 Data Analysis

5.2.1 Load-Displacement Behaviour

A typical load-displacement curve for an elastic-brittle material is shown in Fig.5.1. This illustrates a linear elastic region followed by a sharp load drop at the fracture load F_f. This type of behaviour had been reported in previous papers [67, 94] and the load-drop is reported to correspond to brittle cracking.

A typical load-displacement curve obtained for a ductile material is shown in more detail in Fig.5.2 [103]. F_m is the maximum load (N), u_m is the displacement (m) corresponding to F_m and F_e (N) is the load indicating the transition from elastic to plastic bending. A ductile material typically exhibits four bending regions as indicated in Fig.5.2 i.e. elastic bending (i), plastic bending (ii), membrane stretching (iii) and maximum load and progressive plastic instability (iv).

Failure is indicated by a progressive plateau of the load-displacement curve which occurs due to progressive plastic instability. For ductile materials failure is measured at the maximum load.

5.2.2 Elastic Bi-axial Strain in a Disc

The elastic bi-axial strain (ε_e) of a SPT specimen can be calculated using the solution provided by Huang et al. [93], based upon the assumption that the bent disc obtains the shape of a spherical cap, where δ = central specimen displacement (m), t_0 = original specimen thickness (m) and a_p is the radius of the receiving die (m) as shown in Fig.5.3. This solution is only applicable for calculating the strain within the elastic regime of the load-displacement curve.

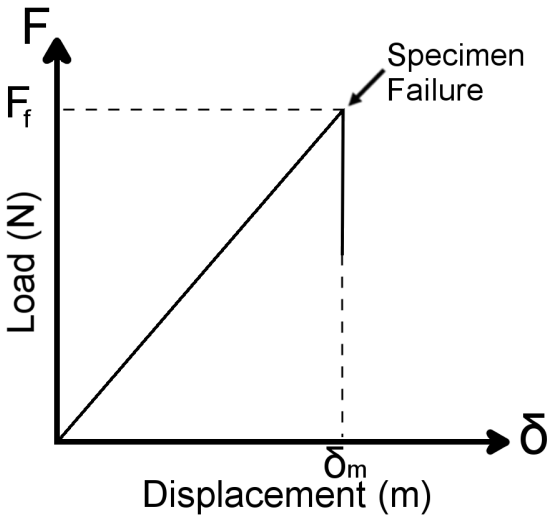

FIGURE 5.1: Load-displacement schematic of an elastic-brittle material.

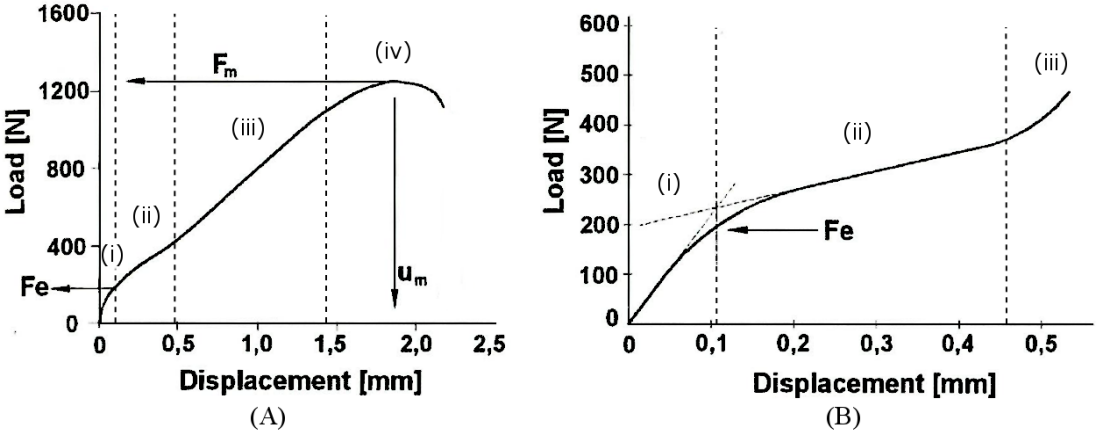

FIGURE 5.2: Load-displacement schematic of a ductile material [103] showing the different regions; elastic bending (i), plastic bending (ii), membrane stretching (iii) and maximum load and progressive plastic instability (iv).

$$\varepsilon_e = \frac{t_0\,\delta}{{a_p}^2 + \delta^2} \tag{5.1}$$

5.2.3 Elastic Bi-Axial Stress in the Disc and Young's Modulus

The elastic bi-axial stress can be calculated from the load F via analytical solutions appropriate to the elastic regime. In the case of bi-axial disc bending of a flat disc

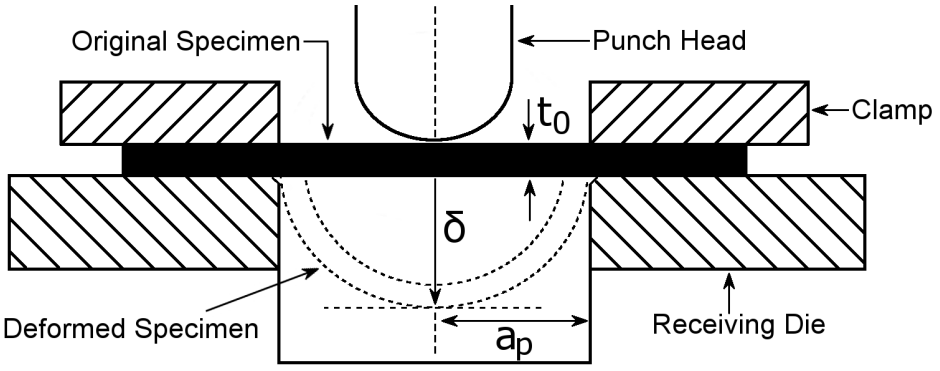

FIGURE 5.3: Schematic of SPT test where a_p is the radius of the receiving hole (2 mm), t_0 is the specimen thickness (0.4 mm) and δ is the displacement of the specimen.

fixed at its circumference, the elastic bi-axial stress on the tensile surface at the centre of the sample (σ_{max}) is given by Roark [121]:

$$\sigma_{max} = \frac{3\,F\,(1+\nu)}{2\,\pi\,{t_0}^2}\left\{ln\frac{a_p}{r'}\right\} \tag{5.2}$$

where

$$r' = \sqrt{1.6{r_c}^2 + t_0^2} - 0.675t_0 \qquad \text{for } r_c \leq 0.5t_0 \tag{5.3}$$

or

$$r' = r_c \qquad \text{for } r_c \geq 0.5t_0 \tag{5.4}$$

F is the load (N), ν is the poisson's ratio, t_0 is the original specimen thickness (m), a_p is the radius of the receiving hole (m), β is 0.435 for a disc, r_c is the punch contact radius and r' is the effective radius (m). The effective radius is approximated as $t_0/3$ which has been shown to be a valid approximation for a NiAl coating by Eskner et al. [67].

The yield load F_e can be measured using the bi-linear fit method outlined in the CEN workshop agreement [101] and depicted in Fig.5.2. Hence the yield stress (σ_{YS}) is calculated by setting F=F_e.

For a brittle material, where a F_e value cannot be measured, the load at which the material experiences failure (F_f in Fig.5.1) can be used to calculate the fracture stress.

Li et al. [100] demonstrated that the slope of the linear region in the load-displacement curve is proportional to the Young's modulus (e) which can be calculated using the following solution provided by Roark [121].

$$E = \left(\frac{F}{\delta}\right) \frac{3\,{a_p}^2(1-\nu^2)}{4\,\pi\,{t_0}^3} \tag{5.5}$$

where δ is the displacement and all other values are the same as above. This enables the Young's modulus to be calculated by either the yield load F=F_e or the elastic fracture load F_f.

For a typical yield load of 100 N, with a_p = 2 mm, t_0 = 0.4 mm and ν=0.3, the yield displacement would be approximately 0.01 mm (assuming E ≈ 180 GPa). Therefore, accurate and precise methods are needed to record the actual specimen displacement if accurate values of the Young's modulus are to be found.

Where uni-axial test data exist, empirical relationships correlating the uni-axial yield strength of a material and the parameter F_e/t_0^2 can be derived [99, 100, 102–105], where F_e is the bi-axial yield load and t_0 is the original specimen thickness (m). For the coatings of interest in the present study, no uni-axial test data exist due to the difficulty in manufacturing specimens for uni-axial testing.

5.2.4 Fracture Strain Following Plastic Deformation

For ductile materials which exhibit plastic deformation before fracture the solution provided by Huang et al. [93] ceases to be applicable. The semi-empirical relationship derived by Mao et al. [98] can be used to calculate the bi-axial fracture strain of a ductile material following plastic deformation ($\varepsilon_p{}^*$), where δ^* is the specimen displacement at fracture (m) and t_0 is the original specimen

thickness (m). This solution can be used to calculate the approximate plastic bi-axial strain at fracture for SP specimens exhibiting plastic deformation.

$$\varepsilon_p{}^* = 0.15\left(\frac{\delta^*}{t_0}\right)^{1.5} \tag{5.6}$$

5.2.5 Methodology to Identify Failure Onset in Bond Coat Samples

In order to interpret the load-displacement curves obtained from small punch tensile testing of bond coat samples it is necessary to identify the point of first cracking. For ductile materials the point of failure is often taken as the maximum load (F_m) or 0.8 F_m [101]. However, brittle materials may exhibit load drops prior to the maximum load, which are known to be associated with cracking in the sample [109]. Materials may also exhibit a characteristic change in slope of the load-displacement curve. Such changes may occur due to cracks forming on the tensile surface of the specimen. The deflection of the disc varies as the cube of the thickness, hence the load-displacement curve will be strongly altered when the outside fibres of the disc first crack [93]. As such the point of failure onset is defined as the first measurable load-drop or a characteristic change in the slope of the load-displacement curve which is not associated with one of the four bending regions shown in Fig.5.2.

As an example, the load-displacement curve obtained at 500 °C for the C1 coating is shown in Fig.5.4. The tensile surface of the same specimen is shown in Fig.5.5. Cracking has occurred in the centre of specimen which demonstrates that the load drops observed in the load-displacement curves correspond to crack formation on the tensile surface of the specimen.

This was also observed for the EP3 coating. The load-displacement curve obtained for the EP3 coating at 600 °C is shown in Fig.5.6. The tensile surface of the specimen is shown in Fig.5.7. Multiple cracks have propagated radially from the centre of the specimen. Comparison of the C1 and EP3 specimens demonstrates

that the magnitude of the load drop in the load-displacement curve is also possibly related to the magnitude of cracking in the SPT specimen.

In both the C1 and EP3 specimens first cracking has occurred in the centre of the specimen, which corresponds to the area of maximum tensile stress when sample deformation is low [109]. As such, cracking in this location is representative of material failure. Thus, a higher load beyond first cracking represents behaviour due to test geometry and not the material behaviour.

Therefore, for a SPT specimen, failure onset is defined as:

a) The first measurable load drop in the load-displacement curve as this is due to brittle crack formation.

   or

b) A discontinuous change in the slope of the load-displacement curve which does not correspond to one of the four bending regions. This represents a sudden change in a samples resistance to bending and can be interpreted as crack formation in the sample which did not grow sufficiently to cause a load drop.

5.2.5.1 Ductile to Brittle Transition Temperature

The ductile to brittle transition temperature (DBTT) can then be evaluated by measuring the strain required to cause first cracking (ε^*) [64] at different temperatures. For brittle materials, which exhibit negligible plastic deformation, the strain at failure onset is calculated using Eq.5.1 for elastic bi-axial strain. For ductile materials, which exhibit plastic deformation before fracture, the strain at failure onset is calculated using Eq.5.6 for the plastic fracture strain.

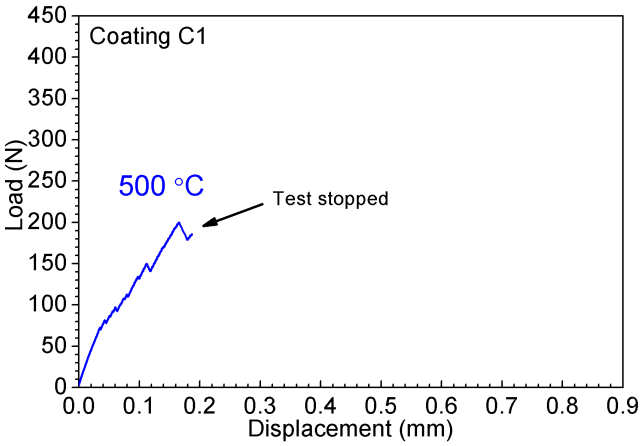

FIGURE 5.4: Load-displacement curve obtained for C1 coating at 500 °C and a constant displacement rate of 1 μms^{-1}

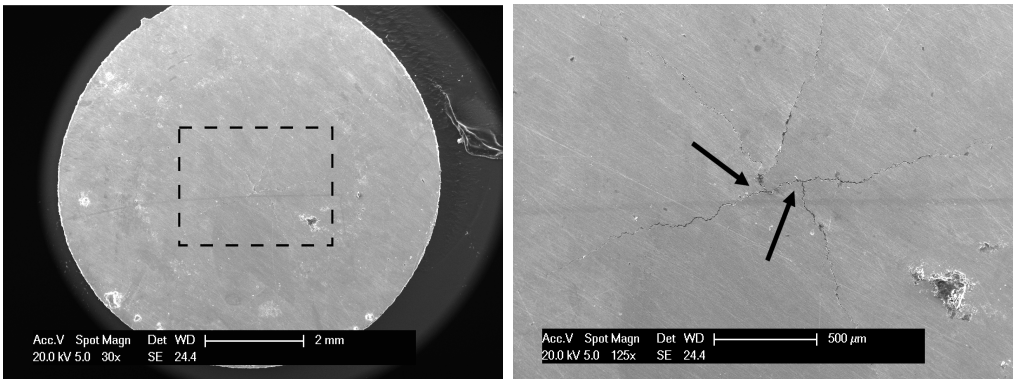

(a) Low magnification (b) High magnification

FIGURE 5.5: Tensile surface of heat treated C1 coating following SPT testing at 500 °C where the test was stopped prior to the maximum load as indicated in Fig.5.4. The black dotted box in (a) denotes the area shown in (b).

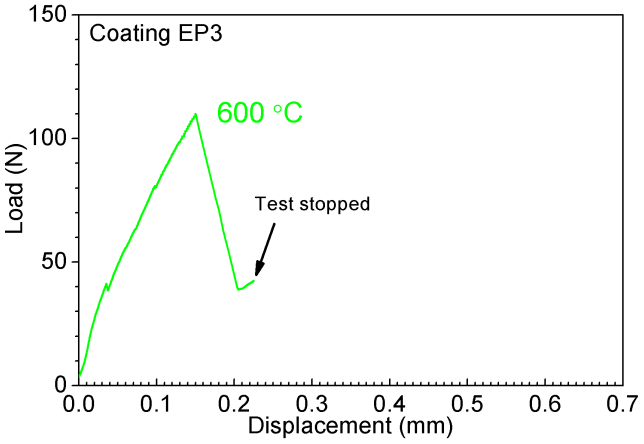

FIGURE 5.6: Load-displacement curve obtained for EP3 coating at 600 °C and a constant displacement rate of 1 μms^{-1}.

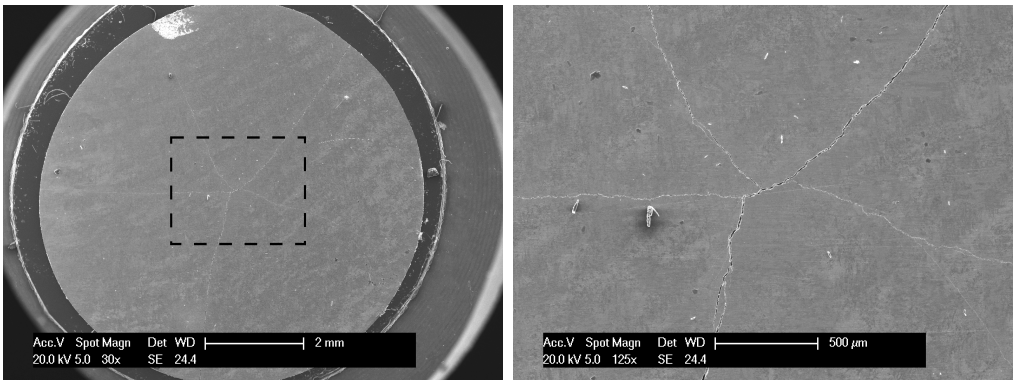

(a) Low magnification (b) High magnification

FIGURE 5.7: Tensile surface of the EP3 coating specimen following SPT testing at 600 °C. Test was stopped before prior to the maximum load as indicated in Fig.5.6. The black dotted box in (a) denotes the area shown in (b).

5.3 Small Punch Tensile Results of Coating C1

As reported in section 4.3, coating C1 is a dual phase material with approximately 68 vol.% γ-Ni (fcc) phase, 31 vol.% β-NiAl (BCC) phase and 1 vol.% oxides/pores.

5.3.1 Load Displacement Curves and Macroscopic Fracture Patterns

Representative load-displacement curves recorded for heat treated C1 samples tested at room temperature (RT) and between 500-750 °C are shown in Fig.5.8. Where possible, the different regimes normally observed in a SP load-displacement curve i.e. elastic bending (i), plastic bending (ii), membrane stretching (iii) and maximum load and progressive plastic instability (iv), have been identified and labelled. The load at failure onset for each test is indicated by an arrow.

The load-displacement curves are interpreted with respect to the macroscopic fracture patterns observed at each temperature. The microscopic fracture patterns observed for the C1 coating between RT and 750 °C are shown in Fig.5.9.

700-750 °C

The specimens tested at 700-750 °C are discussed first as they show typical ductile behaviour reported elsewhere for ductile materials [67, 107, 117, 118]. The load-displacement curves shown in Figs.5.8e and 5.8f exhibit all four bending regions and failure occurs via progressive plastic instability.

The macroscopic fracture patterns shown in Figs.5.9e and 5.9f show that specimen failure occurred through the growth of a circumferential crack, which developed at a radial offset to the centre of the specimen and propagated along a circumferential path. This type of circumferential cracking is caused by thinning of the sample due to membrane stretching and is known to be associated with ductile failure during SPT testing [115]. At 750 °C the SPT test was continued beyond the point of failure which allowed the punch head to travel through the specimen and cause the central region to detach.

The load-displacement curves indicate that at 700 and 750 °C the C1 coating specimens underwent a large amount of plastic deformation. This is evident in Figs.5.9e and 5.9f as the centre of the specimens have deformed into a conical shape. The boundary of the central deformation corresponds to the clamping boundary, which is equal to a_p in Fig.5.3.

The load at failure onset and corresponding displacement is 276 N and 1.08 mm at 700 °C and 168 N and 0.98 mm at 750 °C.

Room Temperature

The C1 specimen tested at RT does not show typical ductile behaviour. The load-displacement curve, shown in Fig.5.8a, is predominately linear and shows multiple load drops prior to reaching a maximum load. These load drops, which appear as serrations in the curve, are interpreted as the formation of cracks on the tensile surface of the specimen[109]. There appears to be multiple cracking events occurring before the maximum load is reached. The tensile surface of the RT specimen is shown in Fig.5.9a. There is a large 3-star crack which has propagated radially from the centre of the specimen which is evidence that the serrations observed in the load-displacement curve were the result of cracks forming on the

surface. The 3-star crack is much larger than the crack observed in Fig.5.5 which suggests the crack has grown through multiple cracking events, which appear as multiple load drops in the load-displacement curve.

Beyond the first load-drop, as indicated by the arrow in the load-displacement curve (Fig.5.8a), there is a reduction in the C1 coatings resistance to bending. This can be associated with a reduction in the specimen load bearing thickness as the crack propagates through the sample. The continuous increase in the measured load is a result of the cracked fragments deforming normal to the specimen surface and resisting the punch displacement after the initial cracking events, which can be seen in Fig.5.9a. It is clear that the first cracking event, signified by the arrow at the first load drop at 237 N and 0.181 mm, indicates material failure.

There is little evidence of plastic deformation in the load-displacement curve before the onset of failure is observed. There is also little plastic deformation in the areas of the RT specimen which have not cracked (the black circle indicates the clamping boundary).

It is clear that at RT the C1 coating exhibits low-ductile behaviour and failure is caused by cracks forming in the centre of the tensile surface and propagating radially.

500 °C

At 500 °C the load-displacement curve is predominately linear and features a discontinuous change in the slope of the load-displacement curve at 260 N and 0.20 mm, which is evidence of cracking on the tensile surface of the specimen.

The macroscopic fracture pattern of the 500 °C specimen is shown in Fig.5.9b. The centre of the specimen has fractured into 5 fragments which is probably the result of a crack forming in the centre of the specimen and propagating radially. This type of fracture has been observed for low-ductility materials such as NiAl [114]. The deformation of central fragments normal to the specimen is due to the punch head moving through the specimen.

The first cracking event, indicated by the arrow, was not large enough to cause a load-drop in the load-displacement curve which suggests that the first crack was small. The large extent of cracking seen in Fig.5.9b is the result of slow crack growth through the specimen. The gradual decrease in the resistance to bending after the initial cracking can be attributed to the reduction in specimen thickness as the cracks grew through the specimen.

There is also a small amount of plastic deformation in the 500 °C specimen, indicated by non-linearity in the load-displacement curve, as before the onset of fracture but it is not possible to identify any evidence of plastic deformation in the 500 °C specimen due to the large deformation of the central region. Cracking can be observed at the clamping boundary, indicated by the black circle, which demonstrates little or no plastic deformation occurred in that area of the specimen.

It can be concluded that at 500 °C the C1 coating exhibits low-ductile behaviour and failure is caused by cracks forming in the centre of the tensile surface and propagating radially. The magnitude of the initial cracking event at 500 °C was smaller than at RT which suggests a small increase in ductility.

600 °C

At 600 °C the load-displacement curve exhibits regions of elastic bending (i) and plastic bending (ii). The onset of failure is indicated by a load drop at 288 N and 0.4 mm. The load-drop indicates the formation of a crack on the tensile surface of the specimen and a large 4-star crack can be seen in Fig.5.9c.

There is a gradual decrease in the slope of the load-displacement curve prior to specimen failure. This can be associated with a reduction in the materials resistance to bending due to thinning of the specimen during plastic deformation. Thinning of the specimen during SPT testing is normally associated with membrane stretching, it is possible that membrane stretching occurred at 600 °C but it is not possible to identify the inflection point in the load-displacement curve normally associated with it. It is clear in Fig.5.9c that the centre of the

specimen started to deform into a conical shape but it is unclear if this was due to membrane stretching or plastic deformation.

It is clear from the load-displacement curve that the 600 °C specimen underwent a significant amount of plastic deformation prior to failure. The macroscopic fracture pattern indicates the centre of the specimen plastically deformed before cracks formed on the tensile surface. It also appears that there was less crack growth than at RT and 500 °C which indicates the crack growth was slower at 600 °C.

The C1 coating at 600 °C appears to exhibit a combination of the low-ductility behaviour observed at RT and 500 °C and the ductile behaviour observed at 700-750 °C. It can be concluded that the C1 coating is experiencing a transition from brittle to ductile behaviour at 600 °C.

650 °C

The C1 coating specimen tested at 650 °C exhibits similar ductile behaviour to the specimens tested at 700-750 °C. It exhibits elastic bending (i), plastic bending (ii), membrane stretching (iii) and progressive plastic instability (iv) but the mode of failure was not completely ductile. The onset of failure is indicated by a large and sudden change in the slope of the load-displacement curve at 281 N and 0.76 mm.

The tensile surface of the specimen is shown in Fig.5.9d. The specimen appears to have failed due to a circumferential crack and there is a number of small of cracks propagating radially into the specimen. The circumferential cracking is evidence of ductile behaviour but the micro-cracks indicate the C1 coating still retains some low-ductility characteristics at 650 °C. This type of fracture has been reported elsewhere for a material showing both ductile and low-ductility behaviour [109].

Representative load-displacement curves for each temperature are plotted on a common axes in Fig.5.10. The load-displacement curve obtained at 550 °C is shown in Fig.5.10 but was omitted from Fig.5.8 as the results at 500 °C are representative of the C1 coating behaviour at 500 and 550 °C.

There is a gradual increase in plasticity, illustrated by a decrease in the resistance to bending, as the temperature is increased. The load at failure onset, as indicated by the arrow, increases slowly between RT and 600 °C, it then gradually decreases up to 700 °C before falling sharply at 750 °C. The amount of plastic deformation before failure increases with temperature. Membrane stretching is only observed between 650-750 °C.

The macroscopic fracture patterns at RT and 500 °C show little or no plastic deformation and failure is characterised by a star shape crack on the tensile surface of the specimen. The macroscopic fracture patterns at 700-750 °C are characterised by a deformed central region and circumferential cracking. The macroscopic fracture patterns at 600 and 650 °C exhibit a combination of ductile and low-ductility failure.

The load-displacement curves and macroscopic fracture patterns indicate that the C1 coating undergoes a brittle to ductile transition between 500-700 °C.

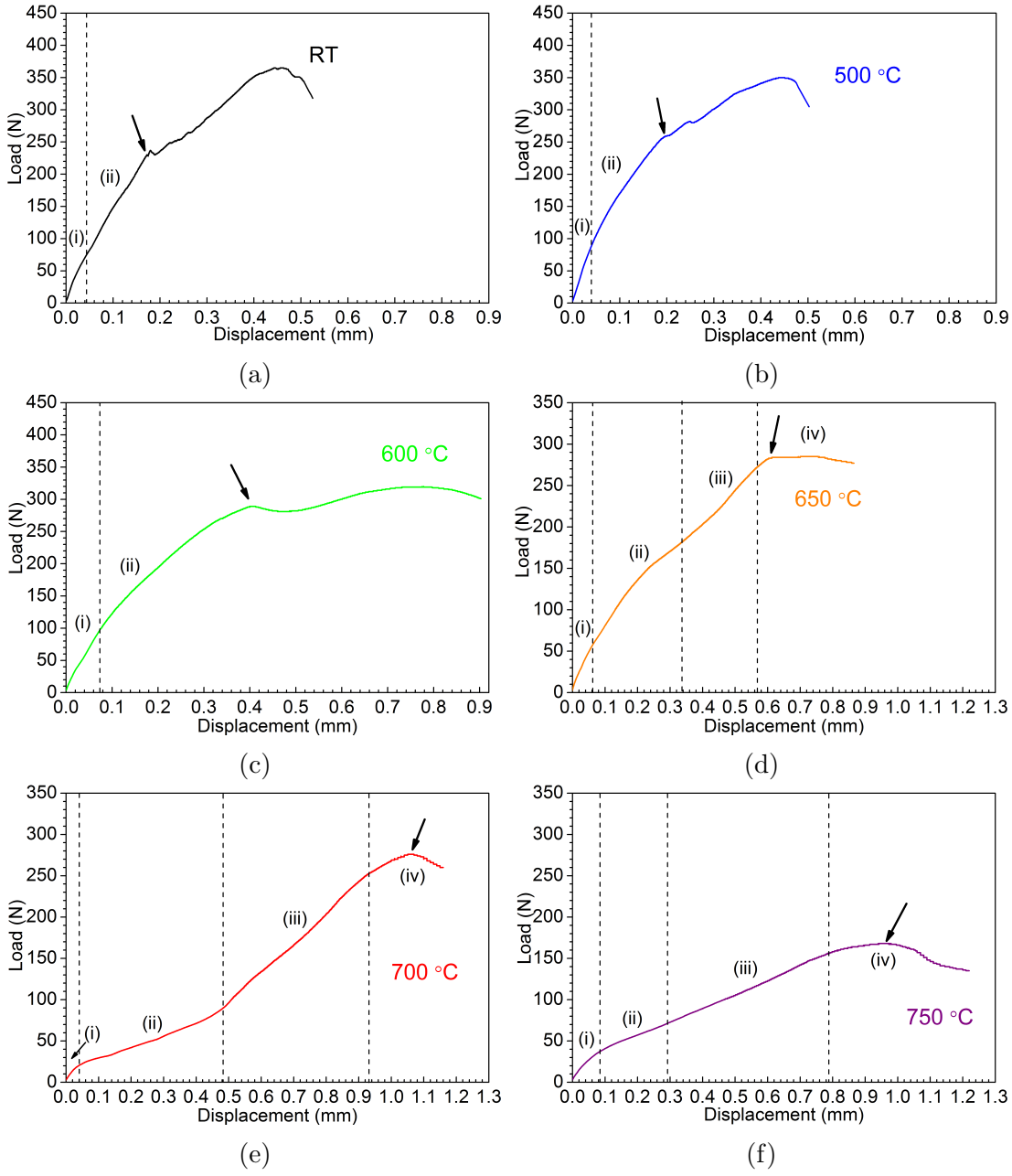

FIGURE 5.8: Load-displacement curves obtained for the C1 coating at a constant displacement rate of 1 μms^{-1} between RT and 750 °C. The arrows indicate the load at failure onset and the labels refer to elastic bending (i), plastic bending (ii), membrane stretching (iii) and maximum load and progressive plastic instability (iv).

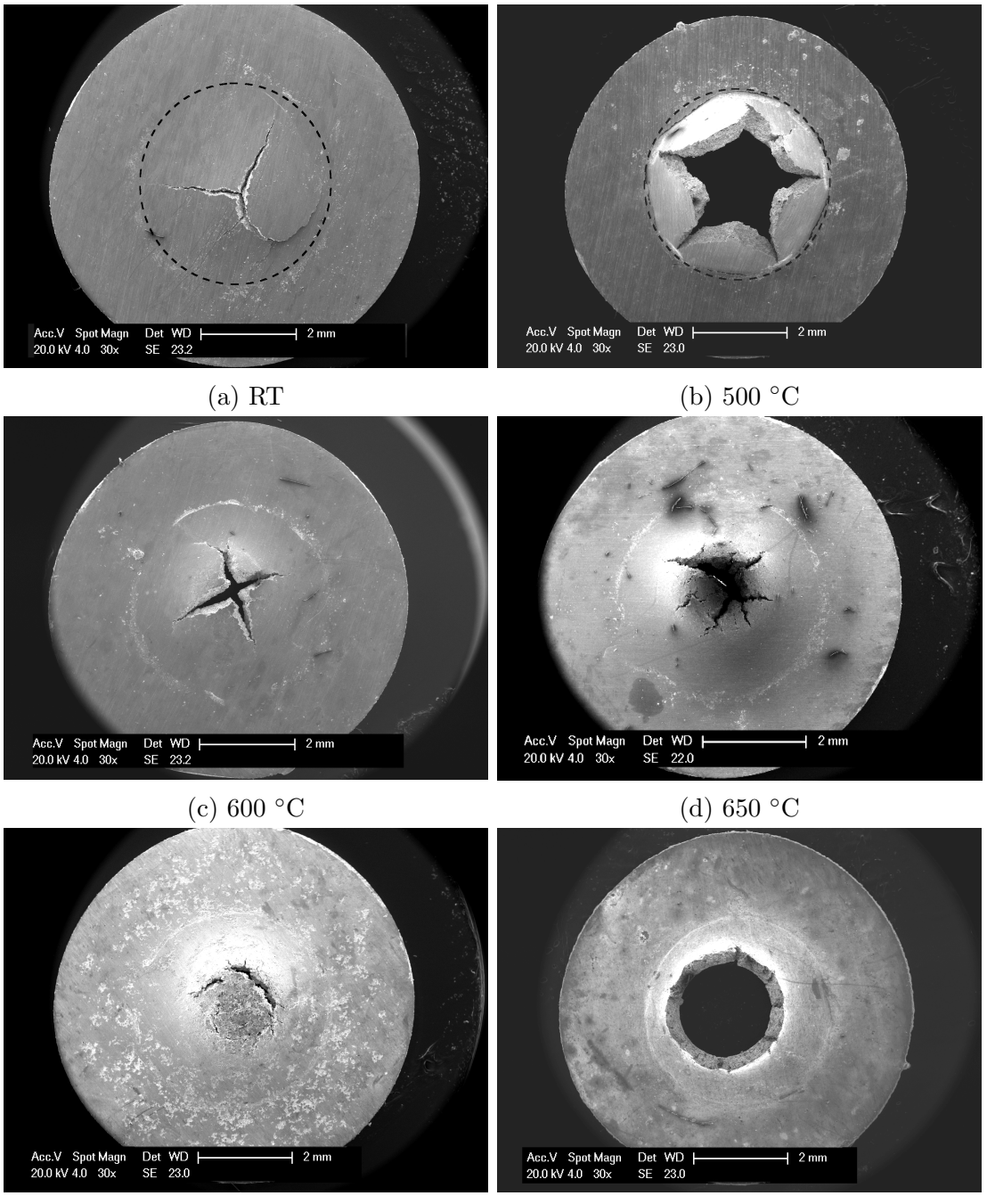

(a) RT (b) 500 °C

(c) 600 °C (d) 650 °C

(e) 700 °C (f) 750 °C

FIGURE 5.9: Macroscopic fracture patterns of C1 coating specimens following SPT tests at (a) RT, (b) 500 °C, (c) 600 °C, (d) 650 °C, (e) 700 °C and (f) 750 °C. The black dotted circle indicates the clamping boundary.

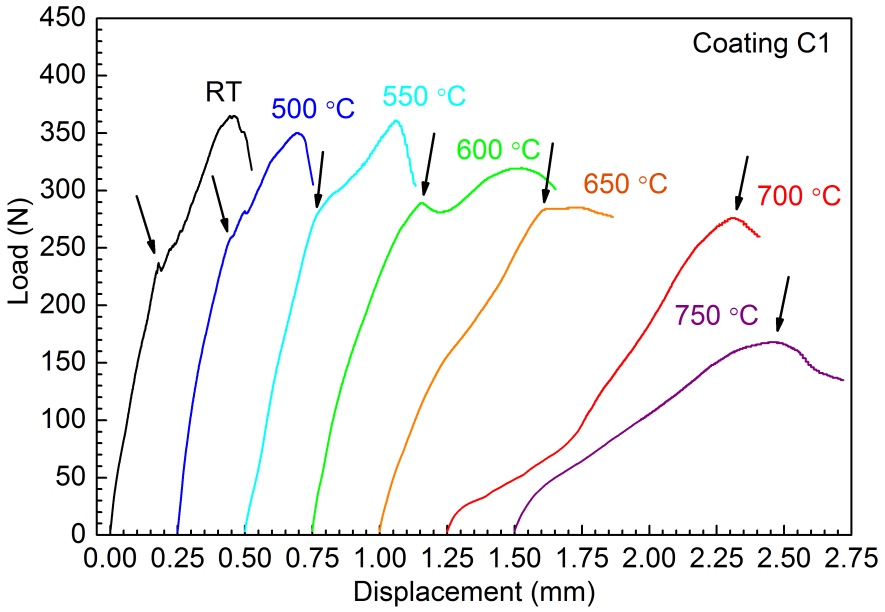

FIGURE 5.10: Load-displacement curves obtained for heat treated C1 coatings at a constant displacement rate of 1 μms^{-1} between RT and 750 °C. Failure onset is indicated by the arrow. Curves have been displaced at 0.25 mm intervals on the displacement axis.

5.3.2 Material Properties

Ductile to Brittle Transition Temperature

Fig.5.11 demonstrates how the strain at 1st cracking changes with temperature for a MCrAlY alloy [4]. The DBTT is defined as the region where there is a significant increase in the strain at first cracking. This is typically measured as a temperature range rather than a single temperature.

The load-displacement curves and macroscopic fracture patterns exhibit evidence that the C1 coating undergoes a ductile to brittle transition between 500-700 °C. In order to quantitatively assess the DBTT the strain at first cracking is plotted as a function of temperature in Fig.5.12a. Between RT and 550 °C the elastic strain at first cracking was calculated using Eq.5.1. Between 600-750 °C the plastic strain at first cracking was calculated using Eq.5.6. Two data points are presented at 500 and 550 °C as repeat tests were conducted at those temperatures.

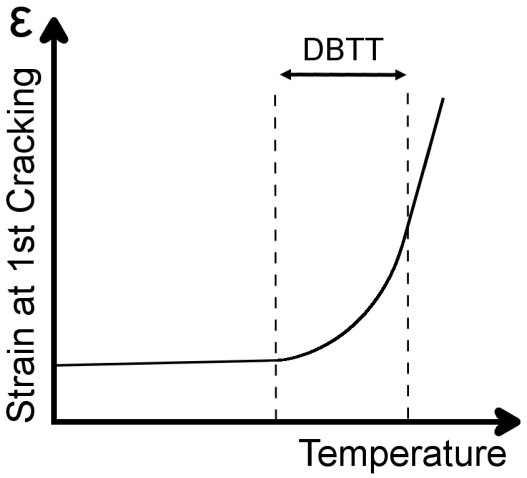

FIGURE 5.11: Schematic of strain to cracking vs temperature for an MCrAlY alloy exhibiting a DBTT. Figure created based on the information at [4].

Fig.5.12a shows that between 550 and 700 °C there is a large increase in the strain at first cracking which demonstrates a significant change in the ductility of the C1 coating. There is also a small increase in the strain at first cracking between 500-550 °C. As such, the DBTT of the C1 coating can be defined as 500-700 °C. Since a mixture of low-ductility and ductile behaviour is observed in Fig.5.9, it is believed the C1 coating exhibits a transition in behaviour between 600-650 °C.

At 750 °C the strain at first cracking is slightly lower than at 700 °C. The difference is considered to be due to the variability of the SPT test; small differences are possible if the specimen has similar ductility at 700-750 °C.

With reference to the macroscopic fracture patterns shown in Fig.5.9, it is possible to say that cracking on the tensile surface of the C1 coating specimen is associated with brittle fracture and circumferential cracking is associated with ductile failure. This agrees with the cracking patterns reported by Rasche et al. [114].

Bi-Axial Yield Strength

The bi-axial yield strength of the C1 coating was calculated using Eq.5.2. The yield strength as a function of temperature is shown in Fig.5.12b and summarised in table 5.1.

The bi-axial yield strength decreases significantly above 550 °C from approximately 1300 MPa at 550 °C to approximately 225 MPa at 700 °C. Below 550 °C there is a lack of clear elastic-plastic transition so values estimated at RT and 500 °C could be lower than the true values.

Values of Young's modulus could not be accurately determined because the LVDT's used to measure displacement in the SP rig are not sufficiently sensitive to record actual specimen displacements.

Temp. (°C)	Yield Load (N)	Displacement at Yield (mm)	Load at 1st Crack (N)	Displacement at 1st Crack (mm)	σ_{YS} (MPa)	Strain at Fracture
RT	60	0.03	237	0.18	912	0.018 †
500	114	0.05	268	0.18	1623	0.018 †
550	127	0.10	280	0.25	1682	0.025 †
600	107	0.07	288	0.41	2216	0.154 ⊙
650	50	0.04	282	0.61	1334	0.277 ⊙
700	22	0.04	275	1.08	816	0.651 ⊙
750	35	0.06	167	0.98	408	0.562 ⊙

TABLE 5.1: Material property data for the C1 coating where † indicates elastic strain calculated using Eq.5.1 and ⊙ indicates plastic strain calculated using Eq.5.6.

5.4 Characterisation of Fracture Behaviour in Coating C1

5.4.1 Microscopic Fracture Surfaces

Secondary electron images of the RT and 700 °C fracture surfaces are shown in Fig.5.13. On the RT fracture surface there are large flat features which appear as ledges. There is also a concave feature approximately 30 μm across which

corresponds to the shape of powder particle. This suggests the boundary of powder particles are weak areas that act as paths for crack propagation. The distinct powder particle shape and flat surfaces are evidence that fracture of the C1 coating occurred via brittle cleavage, indicating low-ductility behaviour at RT.

On the fracture surface of the 700 °C specimen most of the features appear to have a rounded appearance which at high magnification are seen to correspond to elongation of the fracture surface and evidence of ductile tearing.

It is clear that between 500 and 700 °C the C1 coating transitions from low-ductility fracture to ductile failure.

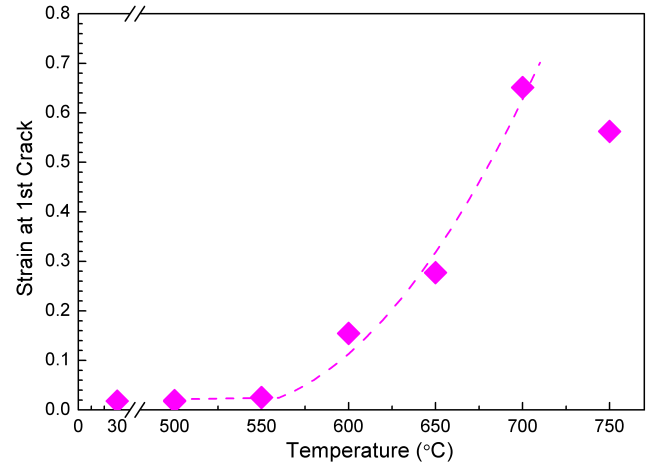

(a)

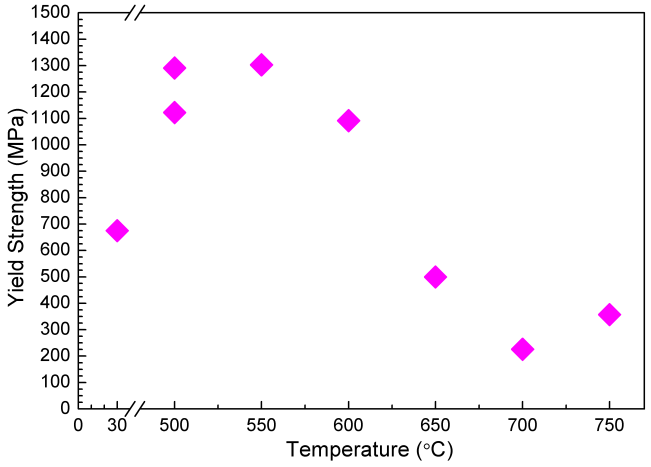

(b)

FIGURE 5.12: Strain at first cracking (a) and yield strength (b) calculated for the C1 coating between RT and 750 °C.

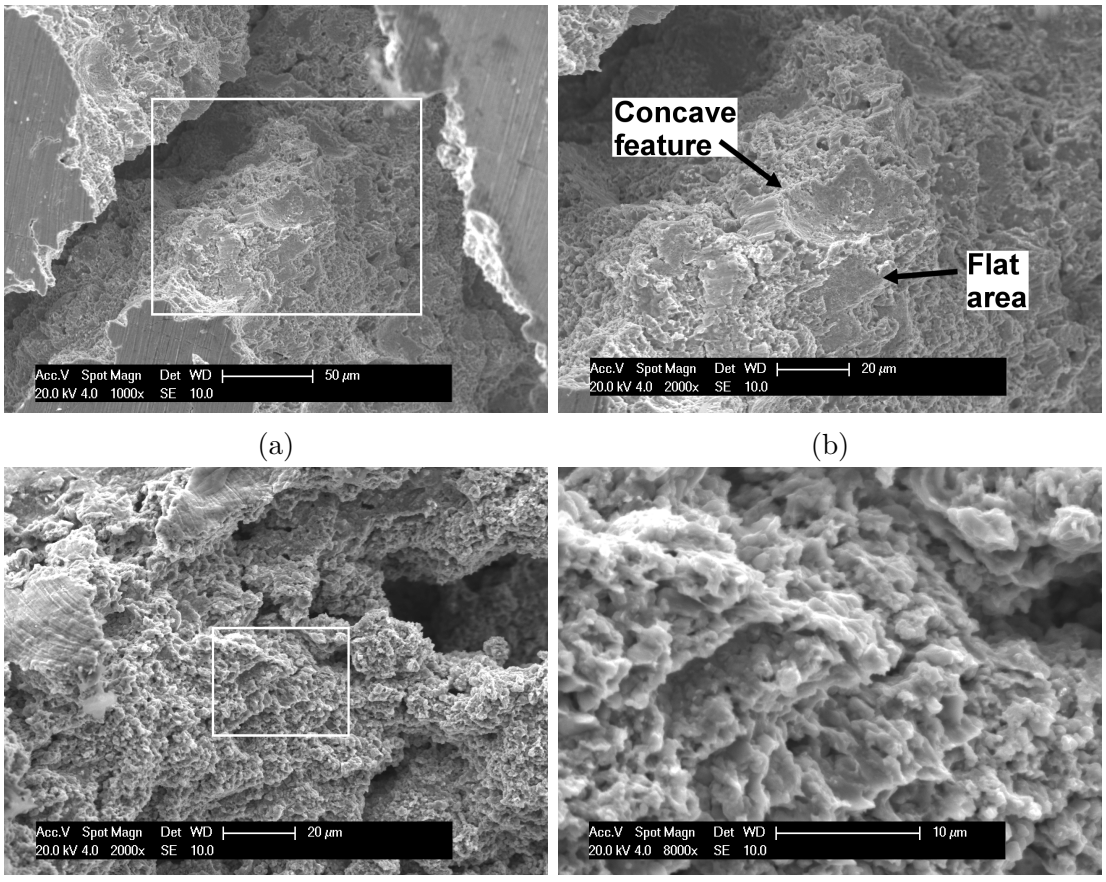

FIGURE 5.13: Fracture surfaces of the C1 coating specimens following SPT testing at RT (a-b) and 700 °C (c-d) where the white boxes outline the areas shown in the higher magnification images (right).

5.4.2 Fracture Path Analysis

Low Temperature Crack Development

Fig.5.14a is a plan view of the RT specimen showing the centre of the specimen. The large cracks either side of the central region are cracks which propagated radially from the centre of the specimen. The area outlined by the white box indicates the area shown at higher magnification in the proceeding image. In the BSE images the dark contrast phase is the β-phase and the light contrast phase is the γ-phase.

In Fig.5.14c an example of crack propagation through the C1 coating at RT is shown. EBSD maps of the same area are shown in Fig.5.15 where Figs.5.15a, 5.15b and 5.15c are a band contrast map showing grain boundaries, a phase map in which the γ-phase is green and the β-phase is red and an inverse pole figure map showing grain orientation.

The band contrast map shows that many γ-phase regions in the BSE images comprise multiple grains and that there is a much finer grain structure than is apparent in the BSE images.

In the BSE image and EBSD maps the crack appears to have propagated predominately through regions of β-phase, evidenced by the large amount of β-phase adjacent to the crack. The letter A indicates evidence of intergranular fracture along the γ/β grain boundaries. The letter B indicates possible evidence of transgranular fracture through the β-phase, evidenced by a similar orientation of the β-phase grains adjacent to the crack. This could also be evidence of intergranular fracture along the grain boundaries of β-phase grains with similar orientation. As such, intergranular fracture along the β-phase boundaries appears to be the preferential crack propagation path. The letter C indicates an example of intergranular fracture along the grain boundaries of the γ-phase.

As the γ-Ni phase is FCC and the β-NiAl phase is BCC it is likely that the γ/β interface is incoherent. This could cause the γ/β interface to have a lower

shear strength than the γ/γ and β/β interfaces, making it an easy path for crack propagation.

Further plan view BSE images of the C1 coating following testing at RT are shown in Fig.5.16. The side profile of the fracture surface exhibits an inconsistent shape with some sharp jagged features which correspond to the shape of the β-phase regions. The jagged profile of the fracture surface matches the topography of the fracture surface shown in Fig.5.13b.

The letter F indicates the boundary of a powder particle which is identified by the oxide stringer. Thin layers of oxide form on powder particles during thermal spraying and retain the shape of the powder particle after heat treatment. A similar shape can be identified in the profile of the fracture surface in Fig.5.16b. This is evidence that crack propagation has occurred along a powder particle boundary. This corresponds to the large concave features observed on the fracture surface in Fig.5.13b. It can be concluded that the oxide stringers are a weak area in the C1 coating at RT and act as an easy path for crack propagation.

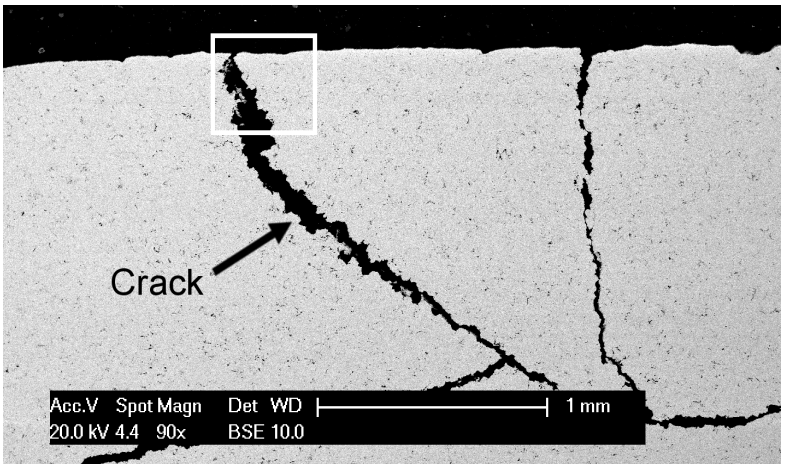

(a)

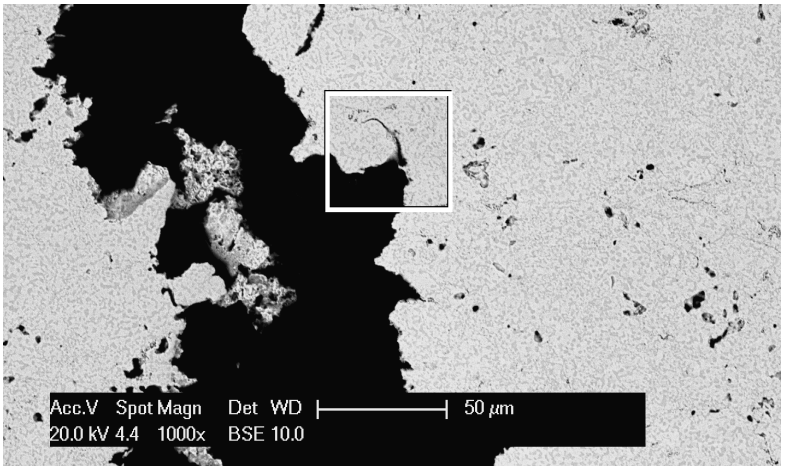

(b)

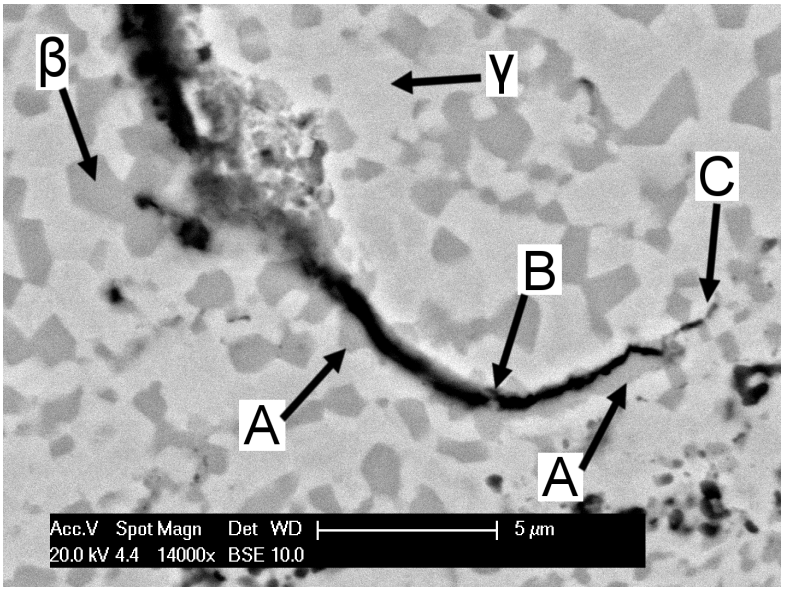

(c)

FIGURE 5.14: BSE images of a plan view of the C1 coating following SPT testing at RT where the white box indicates the area shown at higher magnification in the proceeding image. (c) has been rotated 180 °. The letter A indicates evidence of intergranular fracture along the γ/β-phase boundaries. The letter B indicates evidence of transgranular fracture through the β-phase. The letter C indicates intergranular fracture along the grain boundaries of the γ-phase.

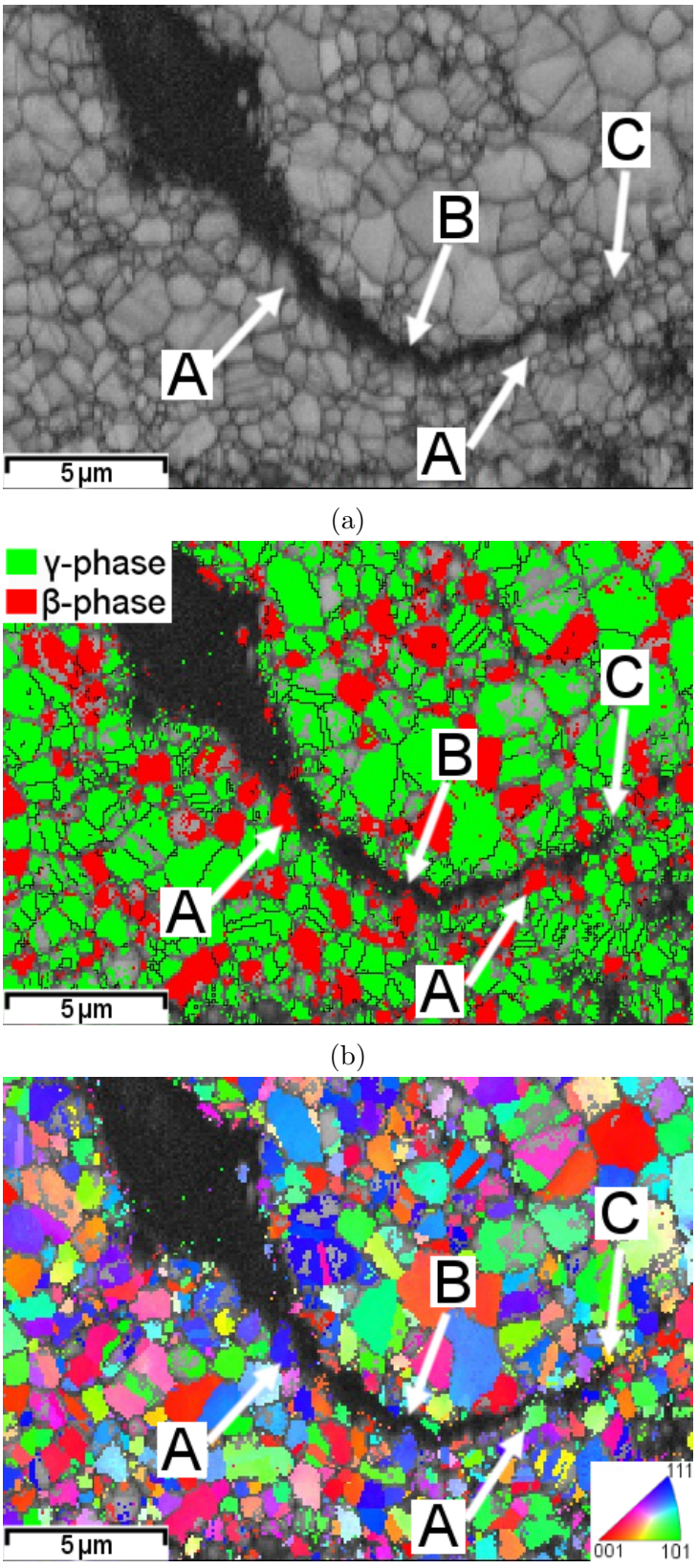

FIGURE 5.15: EBSD maps of the region in Fig.5.14c where (a) is a band contrast map showing grain boundaries, (b) is a phase map in which the γ-phase is coloured green and the β-phase is coloured red and (c) is an inverse pole figure map showing grain orientation. The letter A indicates evidence of intergranular fracture along the grain boundaries of the β-phase. The letter B indicates evidence of transgranular fracture through the β-phase. The letter C indicates intergranular fracture along the grain boundaries of the γ-phase.

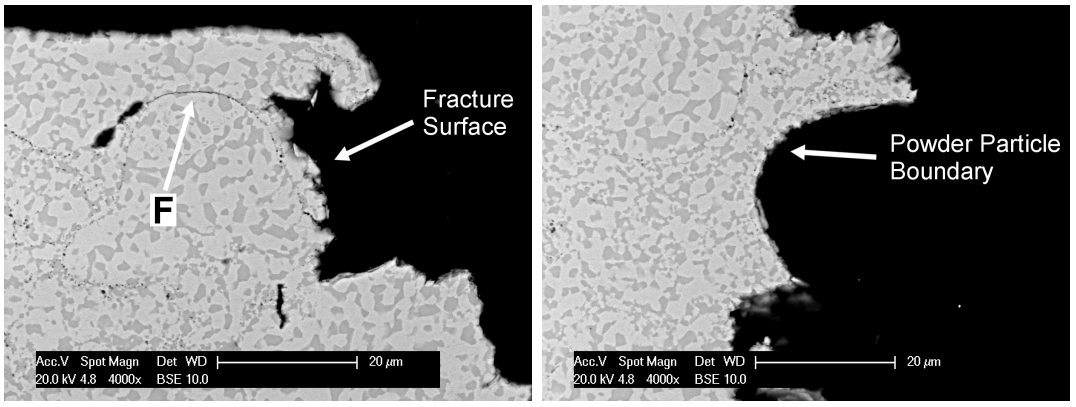

(a) (b)

FIGURE 5.16: BSE images of cross sections of the C1 coating specimen following SPT testing at RT where the edge of the specimen in each image is the fracture surface. The letter F indicates an oxide stringer.

High Temperature Crack Development

A BSE image of the cross section of the C1 coating following SPT testing at 700 °C is shown in Fig.5.17. A large through-thickness crack can be observed at a radial offset from the centre of the specimen. This offset location corresponds to the circumferential cracking shown in Fig.5.9e. In addition to the through-thickness crack multiple microcracks can be observed on the tensile surface of the coating. There is also noticeable thinning of the specimen in the region which was in contact with the punch head.

The solid and dotted white boxes indicate the areas shown at higher magnification in Figs.5.18 and 5.19 respectively.

Fig.5.18 shows a crack which has spread into the specimen in an area adjacent to the large through thickness crack. Fig.5.18c shows there are clear regions of γ-phase and β-phase adjacent to the crack path and the crack tip is growing at the interface of a γ and β-phase region which indicates intergranular fracture along the phase boundaries. There is also a void forming at a phase boundary just ahead of the crack tip which demonstrates where void formation occurs in the C1 coating at 700 °C.

Void formation can be more readily observed in Fig.5.19. EBSD maps of the region shown in Fig.5.19c are shown in Fig.5.20, where Figs.5.20a, 5.20b and 5.20c are a band contrast map showing grain boundaries, a phase map in which the γ-phase is coloured green and the β-phase is coloured red, and an inverse pole figure map showing grain orientation.

The letter A indicates evidence of void formation at phase boundaries between the β-phase and γ-phase which is where most voids appear to form. There are also examples of voids forming at the grain boundaries of γ-phase grains, as indicated by B, but there are fewer examples of this type of void formation. Void formation at the phase boundaries probably occurs due to strain incompatibility between the ductile γ-phase and harder undeformable β-phase. Similar void formation has been shown to occur in dual-phase metal matrix composites [110].

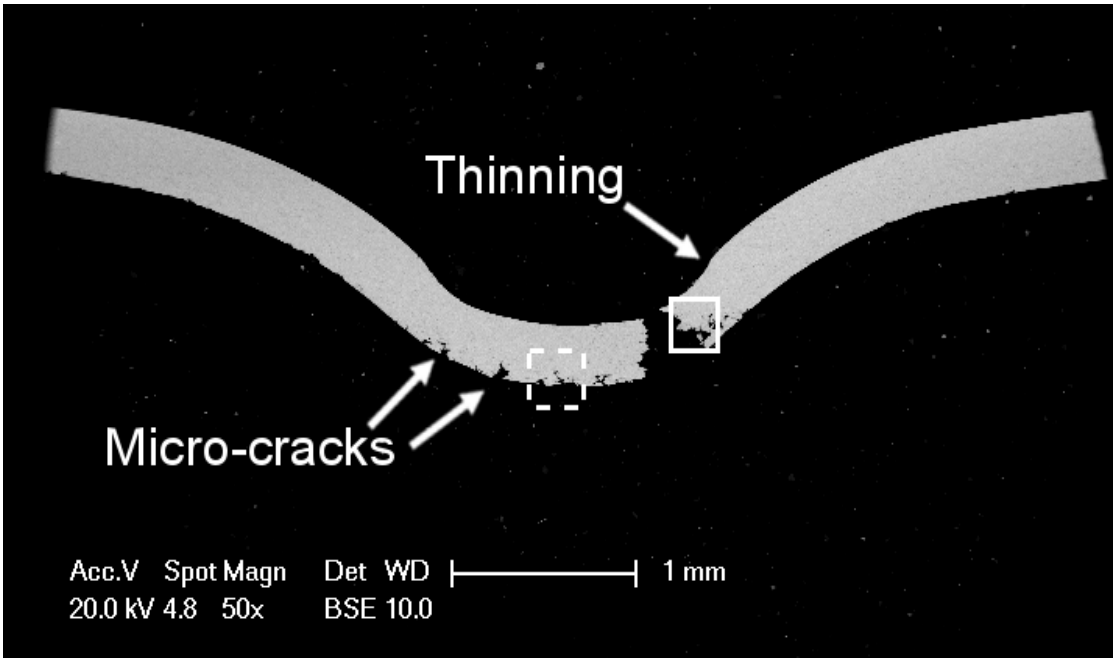

FIGURE 5.17: BSE image of a cross section of a C1 coating specimen following SPT testing at 700 °C. The solid white box outlines the area shown at higher magnification in Fig.5.18. The dotted white box outlines the area shown in Fig.5.19.

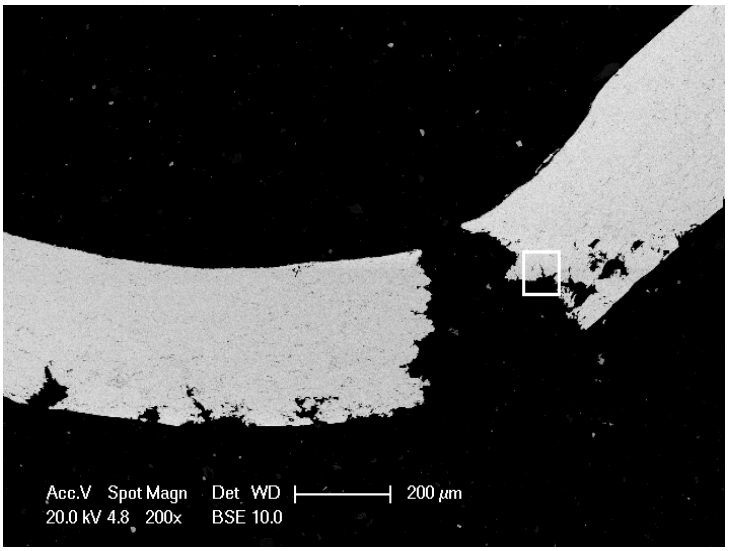

(a)

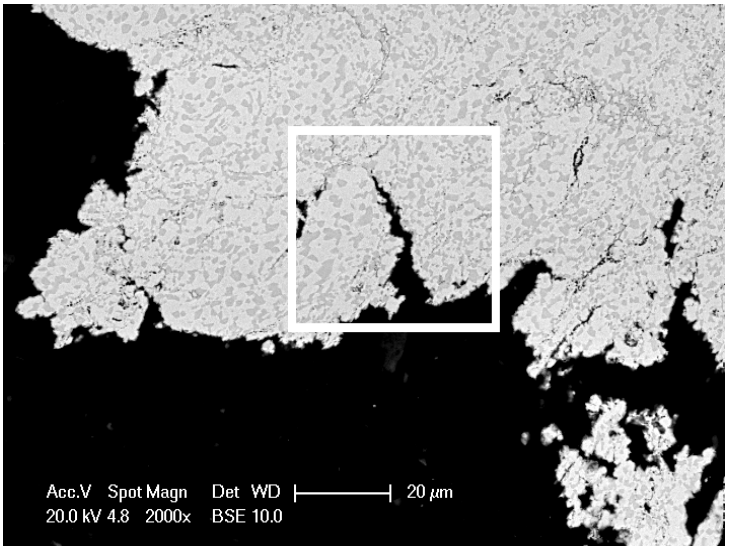

(b)

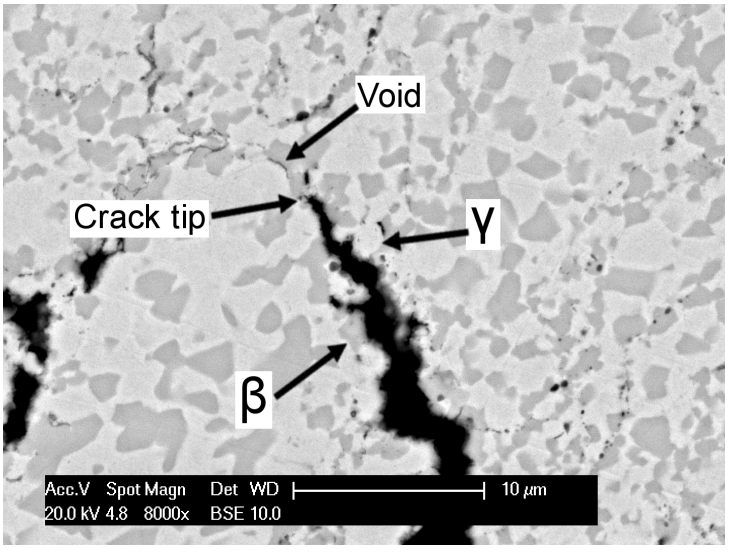

(c)

FIGURE 5.18: BSE images of a cross section of the C1 coating specimen following testing at 700 °C where the white boxes outline the area shown at higher magnification in the proceeding image. The crack tip is growing at the phase boundary between the β-phase and γ-phase.

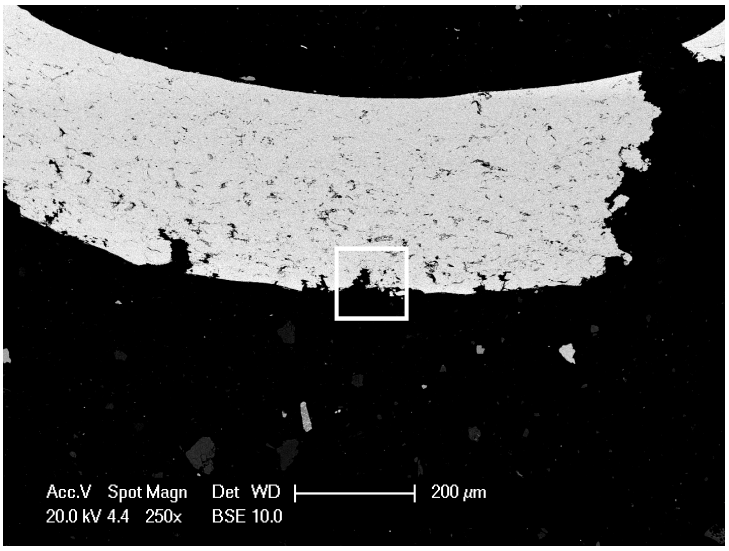

(a)

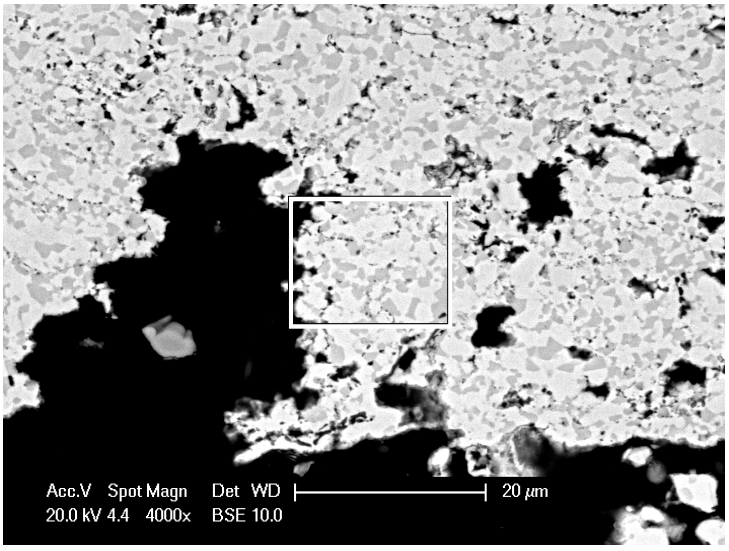

(b)

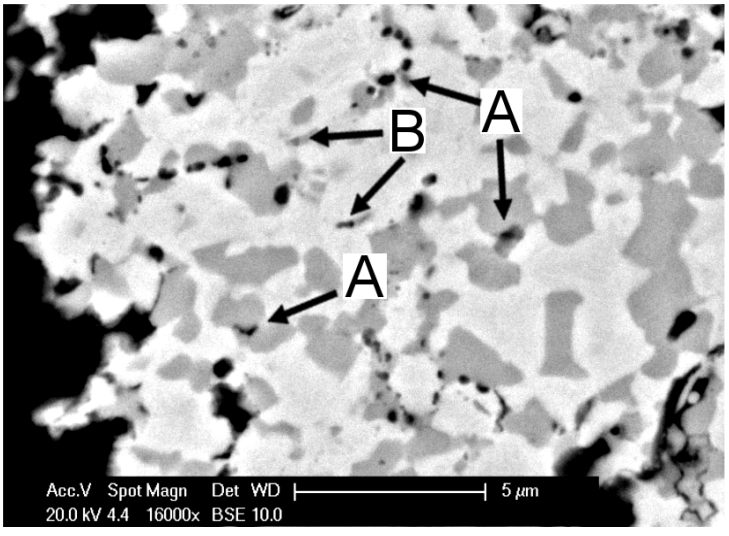

(c)

FIGURE 5.19: BSE images of a cross section of the C1 coating specimen following testing at 700 °C where the white boxes outline the area shown at higher magnification in the proceeding image.

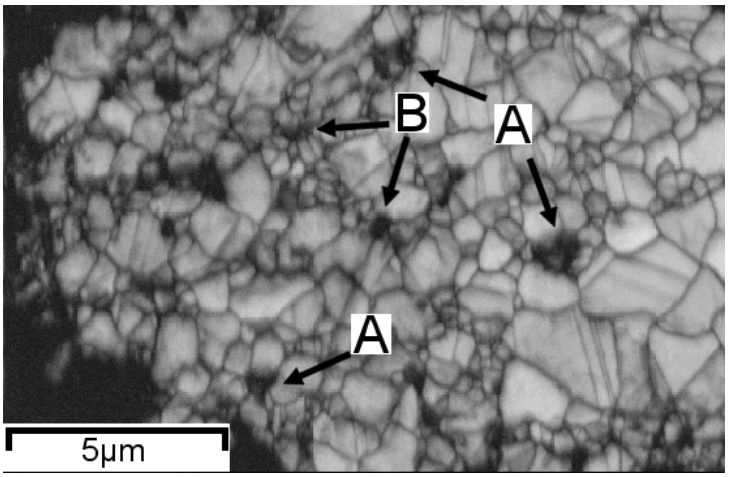

(a)

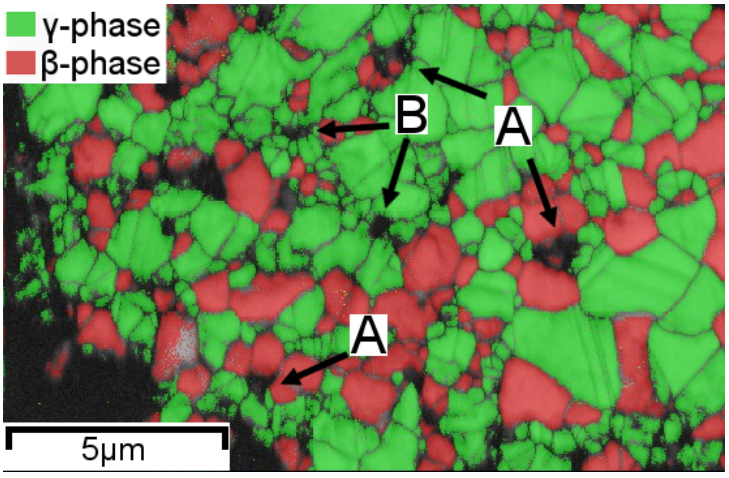

(b)

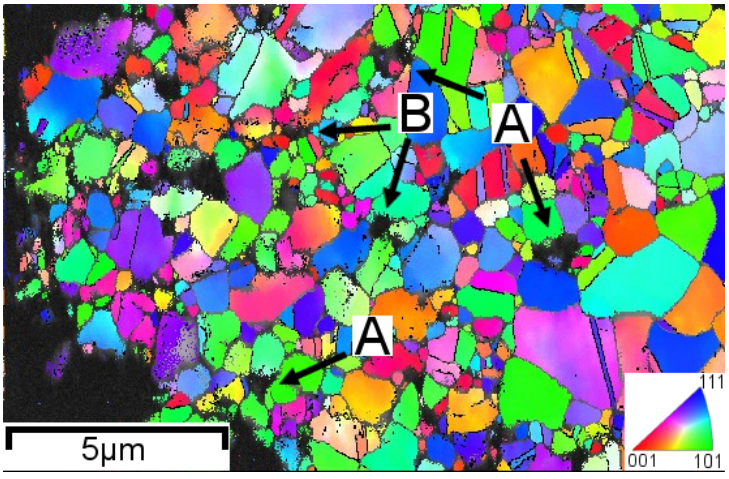

(c)

FIGURE 5.20: EBSD maps of the C1 coating specimen following SPT testing at 700 °C where (a) is band contrast map showing grain boundaries, (b) is a phase map in which the γ-phase is coloured green and the β-phase is coloured red. (c) is an inverse pole figure map showing grain orientation. The letter A indicates evidence of void formation at phase boundaries between the β-phase and γ-phase. The letter B indicates evidence of void formation at the grain boundaries of adjacent γ-phase grains.

5.5 Small Punch Tensile Results of Coating EP1

Coating EP1 is a three phase coating with approximately 25 vol.% fcc γ- Ni phase, 58 vol.% BCC β-NiAl phase, 13 vol.% TCP σ-Cr_2-phase and 4 vol.% oxides/pores. Full details of the EP1 microstructure are given in section 4.4.

5.5.1 Load Displacement Curves and Macroscopic Fracture Patterns

The load-displacement curves obtained for the EP1 coating between RT and 750 °C are shown in Fig.5.21. Where possible, the different regimes normally found in a SP load-displacement curve i.e. elastic bending (i), plastic bending (ii), membrane stretching (iii) and maximum load and progressive plastic instability (iv) [67, 107, 117, 118], have been identified and labelled. The load at failure onset for each test is indicated by an arrow.

The load-displacement curves are interpreted with respect to the macroscopic fracture patterns observed at each temperature. The microscopic fracture patterns observed for the EP1 coating between RT and 750 °C are shown in Fig.5.22.

700-750 °C

At 700 and 750 °C the load-displacement curves exhibit the elastic bending (i), plastic bending (ii) and membrane stretching (iii) regions. Failure is indicated by a maximum load followed by progressive plastic instability (iv). This is similar to the load-displacement curves observed for the C1 coating, shown in Figs.5.8e and 5.8f.

The macroscopic fracture patterns at 700 and 750 °C are shown in Figs.5.22g and 5.22h. In both specimens large circumferential cracks have initiated at a radial offset from the centre of the specimen and propagated along circumferential paths, as was seen for the C1 coating.

Room Temperature

At RT the load-displacement curve is predominately linear and there is very little evidence of plastic deformation before fracture occurs at 89 N, as indicated by the arrow in the load-displacement curve. The sharp load drop is representative of cracking on the tensile surface of the specimen, shown in Fig.5.22a and at higher magnification in Fig.5.22b. The five star crack, highlighted by the black dotted lines, has propagated radially from the centre of the specimen. The observed crack is the result of two cracking events which appear as load-drops in the load-displacement curves.

Beyond the first load-drop there is a reduction in the EP1 coatings resistance to bending which is associated with a reduction in the specimen thickness as the crack propagates through the sample.

500-600 °C

Between 500 and 600 °C the load-displacement curves are predominately linear but exhibit small regions of plastic bending (ii) before fracture occurs. Fracture is indicated by a sharp load drop at 160, 163 and 216 N at 500, 550 and 600 °C respectively.

The sharp load-drops indicate cracking on the tensile surface of the specimen but the centre of the 500, 550 and 600 °C specimens detached during testing and are not shown in Figs.5.22c-5.22e. It is therefore difficult to determine how fracture occurred. It is likely that the first cracking event, indicated by the arrows in the load-displacement curves, caused the centre of the specimen to develop multiple radial fractures and split into fragments. The fragments then eventually sheared away from the specimen due to the displacement of the punch head. The white areas surrounding the centre of the specimens are evidence of layers of material shearing away from the lower surface of the specimen.

The size of the central hole in the specimens indicates the distance to which the radial fractures propagated. At 600 °C the radial fractures propagated further into the specimen than at 500 and 550 °C. This can be attributed to the area of

maximum tensile stress having spread further into the specimen at 600 °C than at 500-550 °C [98, 109].

650 °C

At 650 °C the EP1 coating exhibits the elastic bending (i), plastic bending (ii) and membrane stretching (iii) regions. There is a significant amount of plastic deformation and membrane stretching before fracture occurs at 406 N indicating that the EP1 coating exhibits more ductile behaviour at 650 °C than between 500-600 °C. Failure of the specimen at 650 °C is indicated by a sharp load drop which indicates that the specimen failed due to cracking on the tensile surface of the specimen.

The detached centre of the 650 °C specimen is shown in Fig.5.23. The centre is a conical shape, showing clear evidence of significant plastic bending. There appears to be a small crack at the centre of the specimen which has propagated radially before splitting into separate radial cracks. These cracks have propagated towards the clamping boundary, which corresponds to the size of the hole in the specimen. The specimen appears to have sheared along the clamping boundary, resulting in the centre of the sample detaching as a whole piece. This is likely due to the area of contact between the specimen and the clamping boundary acting as an area of high stress concentration.

In Fig.5.24 the load-displacement curves between RT and 750 °C are plotted on a common axes for comparative purposes. The displacement at failure onset increases with temperature between RT and 750 °C indicating a gradual increase in ductile behaviour with temperature. The slope of the load-displacement curves also gradually decrease with temperature indicating a decrease in the EP1 coatings resistance to bending as the temperature increases.

The load at failure onset increases steadily with temperature between RT and 650 °C and increases significantly between 600-650 °C. The load at failure onset then remains approximately constant between 650-700 °C before decreasing at 750 °C. At 650 °C and below failure is indicated by a sharp load-drop indicating cracking in

the specimen and low-ductility behaviour. At 700 °C and above failure is indicated by plastic instability which is evidence of ductile behaviour at 700 °C.

The load-displacement curves demonstrate that the EP1 coating becomes ductile at 700 °C and that between 550-700 °C there is a transition from low-ductility behaviour to ductile behaviour.

5.5.2 Material Properties

Ductile to Brittle Transition Temperature

The load-displacement curves and macroscopic fracture patterns exhibit evidence that the EP1 coating undergoes a ductile to brittle transition between 550-700 °C. In order to quantitatively assess the DBTT of the EP1 coating the strain at first cracking is plotted as a function of temperature in Fig.5.25a.

Between RT and 600 °C the elastic strain at first cracking was calculated using Eq.5.1. Between 650-750 °C the plastic strain at first cracking was calculated using Eq.5.6.

There is a small increase in the strain at first cracking between RT and 600 °C indicating that the ductility of the EP1 coating does not change significantly over that temperature range. Between 600 and 750 °C there is a large increase in the strain at first cracking which demonstrates there is a significant change in the ductility of the coating. The macroscopic fracture patterns in Fig.5.22 show that the EP1 coating exhibits typical ductile behaviour at 700 °C. As such, the DBTT of the EP1 coating can be defined as 600-700 °C.

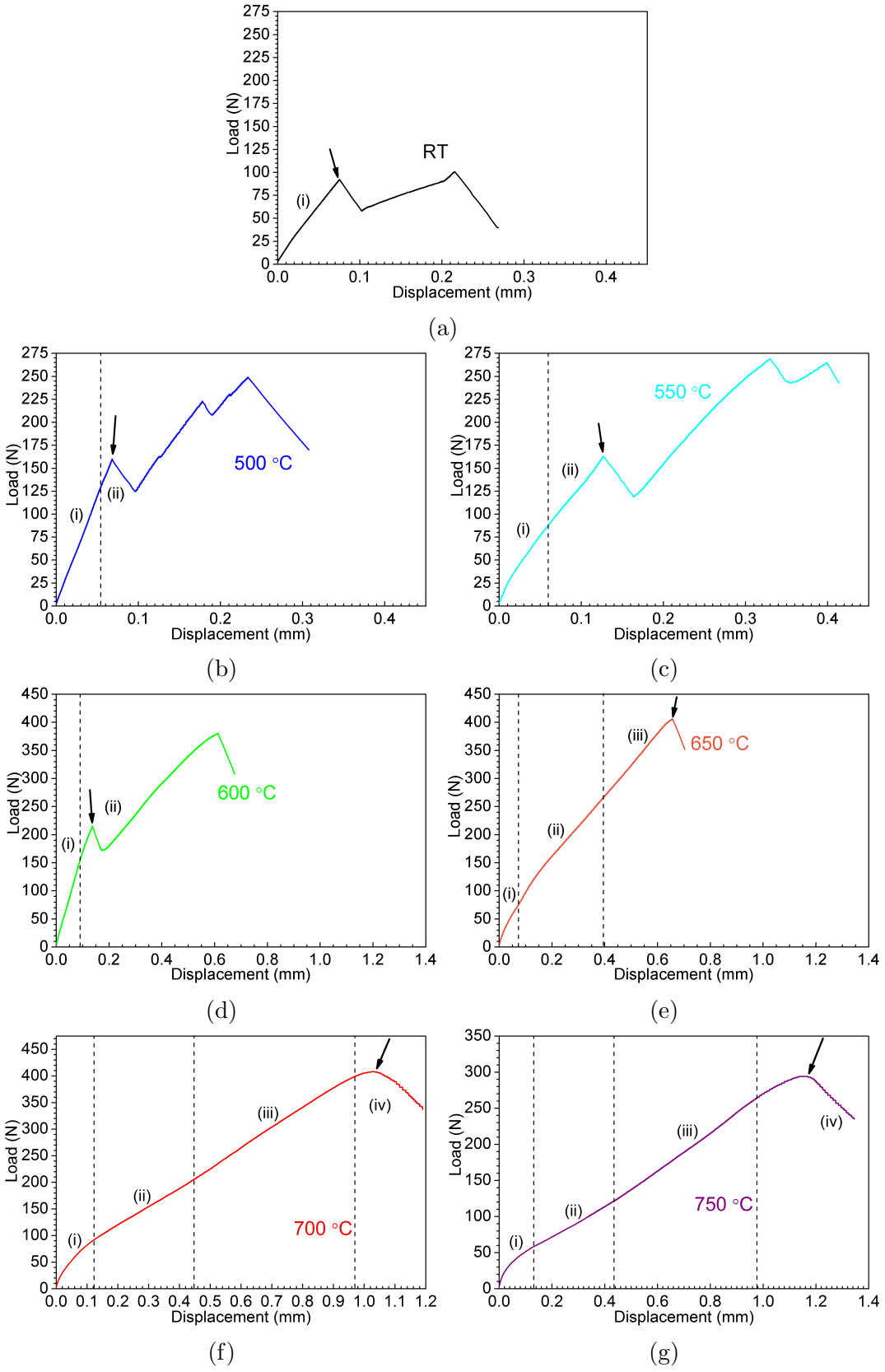

FIGURE 5.21: Load-displacement curves obtained for EP1 coatings at a constant displacement rate of 1 μms^{-1} between RT and 750 °C. The arrows indicate the load at failure onset and the labels refer to elastic bending (i), plastic bending (ii), membrane stretching (iii) and maximum load and progressive plastic instability (iv).

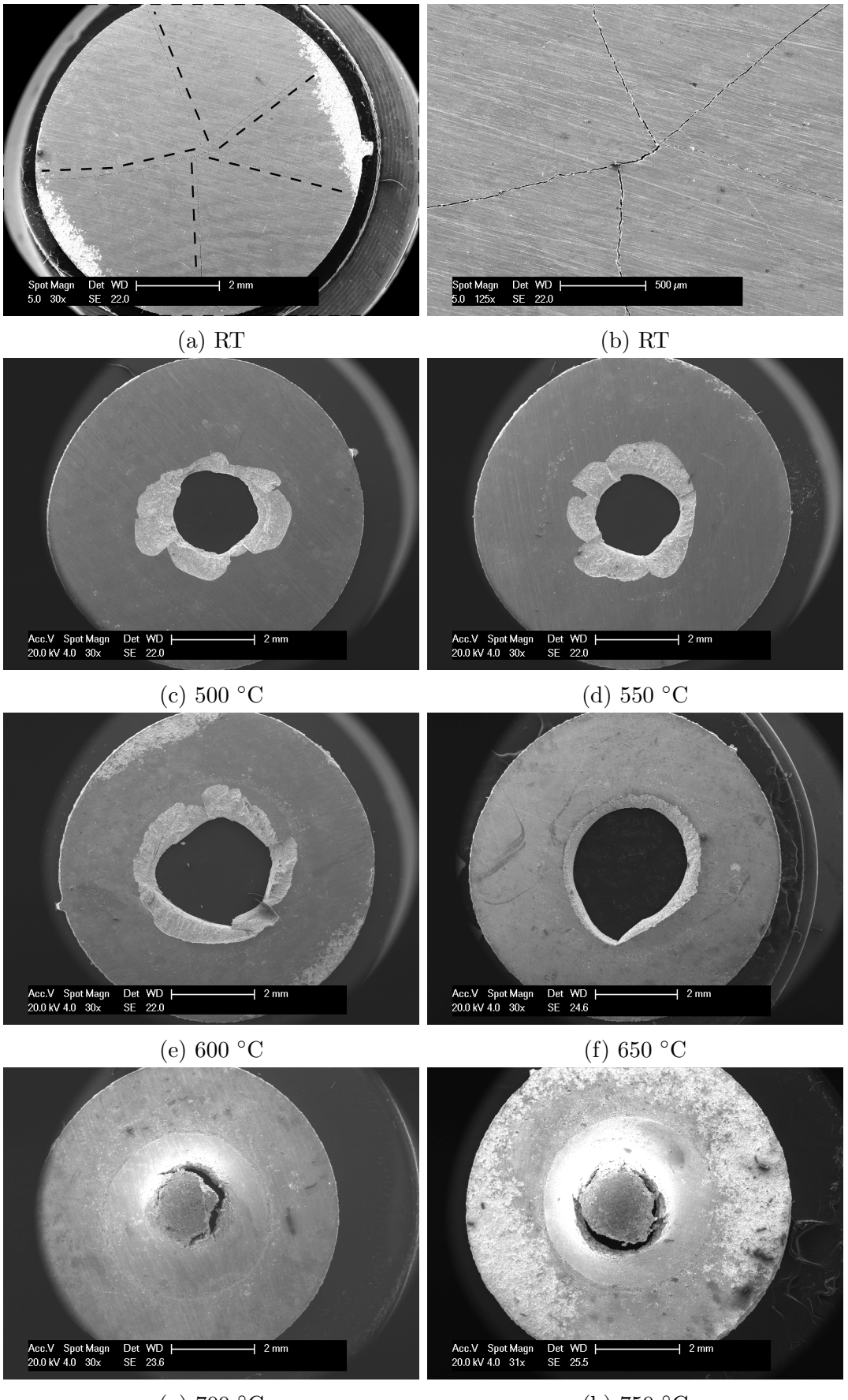

(a) RT (b) RT

(c) 500 °C (d) 550 °C

(e) 600 °C (f) 650 °C

(g) 700 °C (h) 750 °C

FIGURE 5.22: Tensile surfaces of the EP1 coating specimens following testing between (a-b) room temperature, (c) 500 °C, (d) 550 °C, (e) 600 °C, (f) 650 °C, (g) 700 °C and (h) 750°C. The black dotted lines in (a) highlight the cracks in the specimen which are also shown at higher magnification in (b).

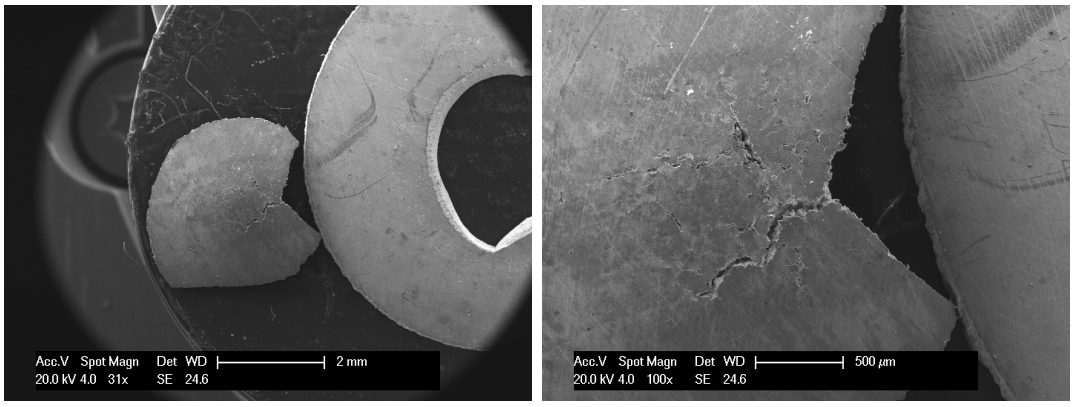

(a) (b)

FIGURE 5.23: SE image showing the central fragment of the EP1 coating specimen which detached during SPT testing at 650 °C.

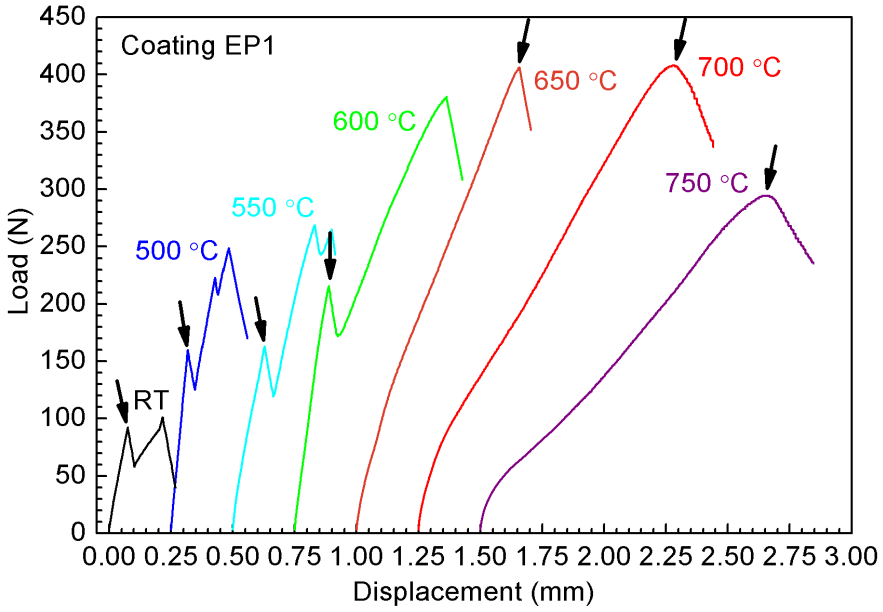

FIGURE 5.24: Load-displacement curves obtained for heat treated EP1 coatings at a constant displacement rate of 1 μms^{-1} between RT and 750 °C. The arrows indicate load at failure onset. Curves have been displaced at 0.25 mm intervals on the displacement axis.

Bi-Axial Yield/Fracture Strength

The bi-axial yield/fracture strength as a function of temperature for the EP1 coating is shown in Fig.5.25b. The fracture strength was calculated between RT and 600 °C where no clear transition from elastic to plastic bending could be identified before fracture occurred. The fracture strength (σ_{FS}) was calculated using the load at the point of fracture, indicated by the arrows in Fig.5.24.

Between 650-750 °C a clear elastic-plastic transition could be identified and the bi-axial yield strength (σ_{YS}) was calculated using the yield load F_e. The measured values and calculated material properties are summarised in table 5.2.

The bi-axial fracture strength increases between RT and 600 °C and the yield strength decreases significantly between 650-750 °C. The yield strength appears to decrease as the ductility increases.

Values of Young's modulus could not be accurately determined because the LVDT's used to measure displacement in the SP rig were not sufficiently sensitive to resolve the actual specimen displacement and contributions due to the flexural rigidity of the SP rig.

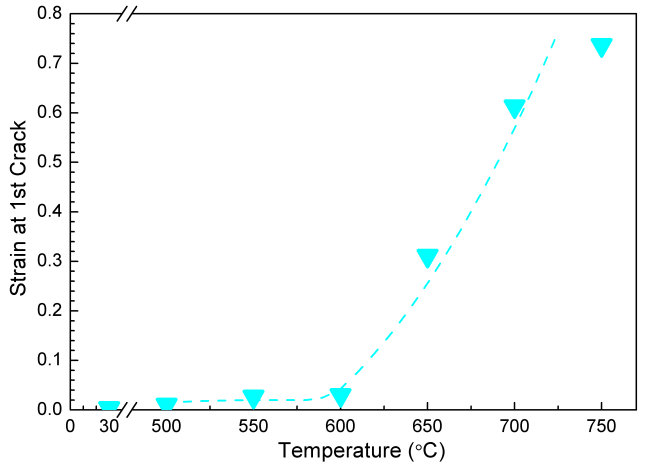

(a)

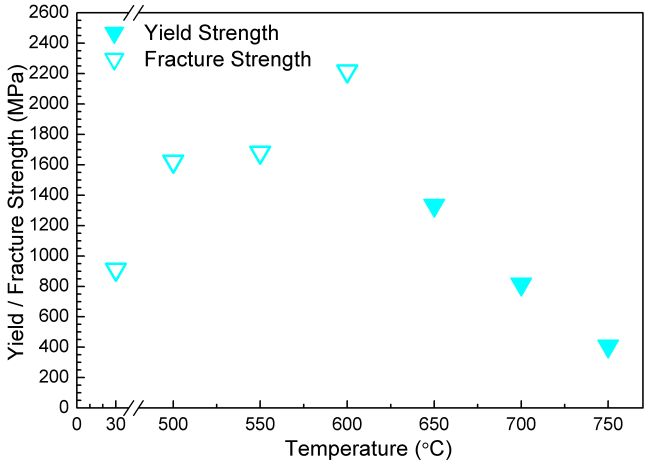

(b)

FIGURE 5.25: Strain at first cracking (a) and yield/fracture strength (b) calculated for the EP1 coating between RT and 750 °C.

Temp. (°C)	Yield Load (N)	Displacement at Yield (mm)	Load at 1st Crack (N)	Displacement at 1st Crack (mm)	σ_{YS} ◁ or σ_{FS} □ (MPa)	Strain at Fracture
RT	-	-	89	0.07	912 □	0.007 †
500	-	-	160	0.07	1623 □	0.007 †
550	-	-	163	0.13	1682 □	0.013 †
600	-	-	216	0.14	2216 □	0.014 †
650	130	0.14	406	0.66	1334 ◁	0.311 ⊙
700	80	0.10	408	1.04	816 ◁	0.613 ⊙
750	40	0.06	294	1.17	408 ◁	0.737 ⊙

TABLE 5.2: Material property data for the EP1 coating where ◁ and □ refer to yield stress (σ_{YS}) and fracture stress(σ_{FS}) respectively, † indicates elastic strain calculated using Eq.5.1 and ⊙ indicates plastic strain calculated using Eq.5.6.

5.6 Characterisation of Fracture Behaviour in Coating EP1

5.6.1 Microscopic Fracture Surfaces

Secondary electron images of the EP1 coating fracture surfaces following SPT testing at 500 and 700 °C are shown in Fig.5.26. The 500 °C fracture surface exhibits numerous small flat regions which often appear as ledges. This type of fracture surface is evidence of brittle cleavage. There are also flat areas which correspond to the shape of powder particles as was observed for the C1 coating.

The 700 °C fracture surface shows rounded features, which at high magnification can be seen to correspond to elongation of the coating and evidence of ductile tearing.

There is a clear change in fracture behaviour between 500-750 °C.

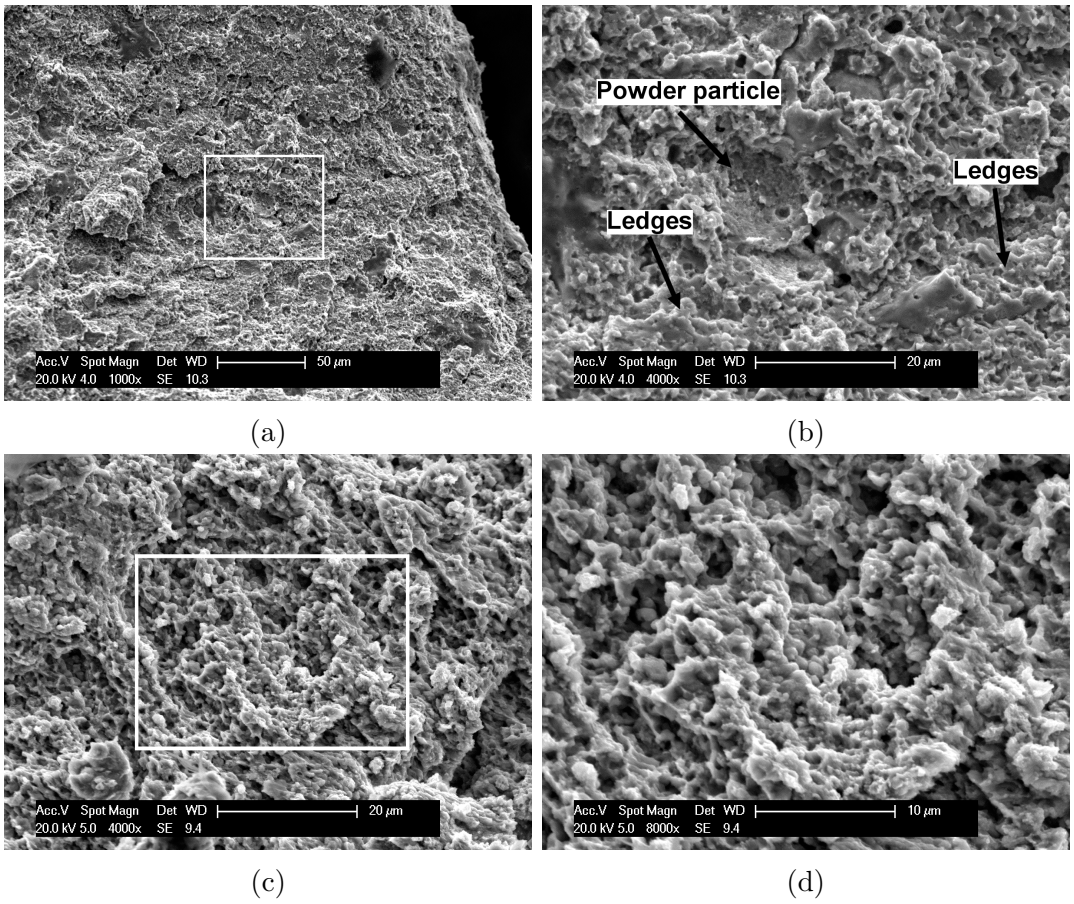

FIGURE 5.26: Fracture surfaces of the EP1 coating specimens following SPT testing at 500 °C (a-b) and 700 °C (c-d) where the white boxes outline the areas shown in the higher magnification images (right).

5.6.2 Fracture Path Analysis

Low Temperature Crack Development

A plan view of the EP1 coating following SPT testing at 500 °C is shown in Fig.5.27. The area indicated by the white box is shown at higher magnification in Fig.5.28a alongside EBSD maps of the same area where Fig.5.28b is a band contrast map showing grain boundaries, Fig.5.28c is a phase map in which the γ-phase is coloured green, the β-phase is coloured red and the σ-phase is coloured yellow, and Fig.5.28d is an inverse pole figure map showing grain orientation.

In Fig.5.28a the dark contrast phase is the β-phase and the light contrast phase is either the γ-phase or the σ-phase. This can be observed by comparing the BSE

image and the phase map; an example is shown where one light contrast region is detected as γ-phase another light contrast region is detected as σ-phase. The similar appearance of the two phases in BSE imaging means BSE imaging and EBSD analysis must be used together to describe the crack propagation in the EP1 coating.

The band contrast map shows that certain regions of the coating have a finer grain size than is apparent from the BSE image and that all three phases are polycrystalline which is not revealed in the BSE image.

The letter A indicates evidence of transgranular fracture through the β-phase, evidenced by a similar orientation of the β-phase grains either side of crack path. The letter B indicates evidence of intergranular fracture along the phase boundaries between the matrix β-phase and the secondary γ and σ-phases. This is the dominant mode of fracture in the EP1 coating at 500 °C. The letter C indicates evidence of transgranular fracture through a grain of σ-phase. Transgranular fracture through the β and σ-phases appears to occur when the phase boundary is at a large angle to the direction of crack growth. There is no evidence of transgranular fracture through a grain of γ-phase.

It can be concluded that intergranular fracture along phase boundaries is the dominant mode of fracture and transgranular fracture through the β and σ-phases is a secondary mode of fracture.

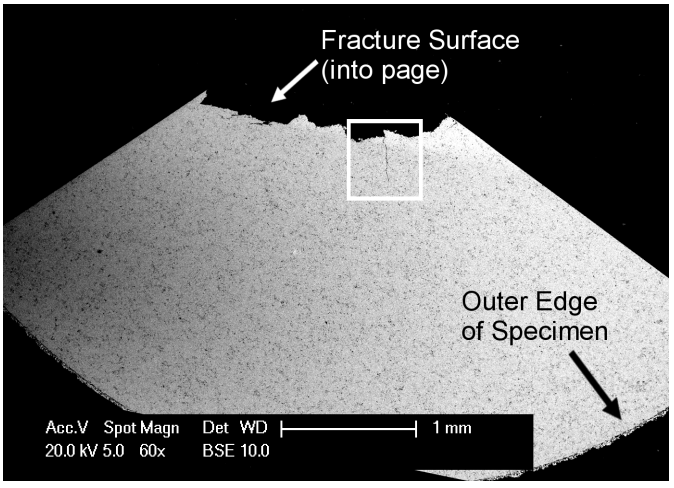

FIGURE 5.27: Plan view of the EP1 coating following testing at 500 °C. The white box indicates the area shown at higher magnification in Fig.5.28.

High Temperature Crack Development

A cross section of the EP1 coating following testing at 700 °C is shown in Fig.5.29a. The solid white box and dotted white box indicate the regions shown at higher magnification in Figs.5.29b-5.29c and Fig.5.30 respectively.

There is a large through thickness crack at a radial offset from the centre of the specimen which corresponds to circumferential cracking of the specimen as shown in Fig.5.22g. There is also noticeable thinning of the specimen as was observed for the C1 coating.

The area of the coating adjacent to the through-thickness crack is shown in Fig.5.29b. There are black bands forming along the direction of the tensile stress, which are either voids or micro-cracks. It is likely that the voids grow in bands and develop into cracks, eventually forming large cracks, such as the one indicated. It is probable that specimen failure was the result of successive linkage of such cracks through the thickness of the specimen.

An example of crack growth at 700 °C is shown in Fig.5.29c. There are well defined regions of the dark contrast β-phase adjacent to the crack path, as well as regions of the light contrast phase which could be either the γ-phase or σ-phase, it is not possible to differentiate the two phases in BSE images. The shape of the γ/σ-phase regions adjacent to the crack path are well defined which suggests intergranular crack growth along the boundaries of the γ/σ-phase regions. There is no evidence of transgranular fracture through the γ/σ-phase. The shape of the β-phase regions adjacent to the crack path are not clearly defined which suggests transgranular crack growth through the β-phase.

The area outlined by the white dotted box in Fig.5.29 is an area of high tensile stress during SPT testing. There is a through thickness crack in the specimen which was either an individual crack not large enough to cause specimen failure or an example of the circumferential cracking growing into a different area of the specimen. An area adjacent to the crack is shown at higher magnification in Fig.5.30. The dotted white box in Fig.5.30b indicates the region shown in Fig.5.31.

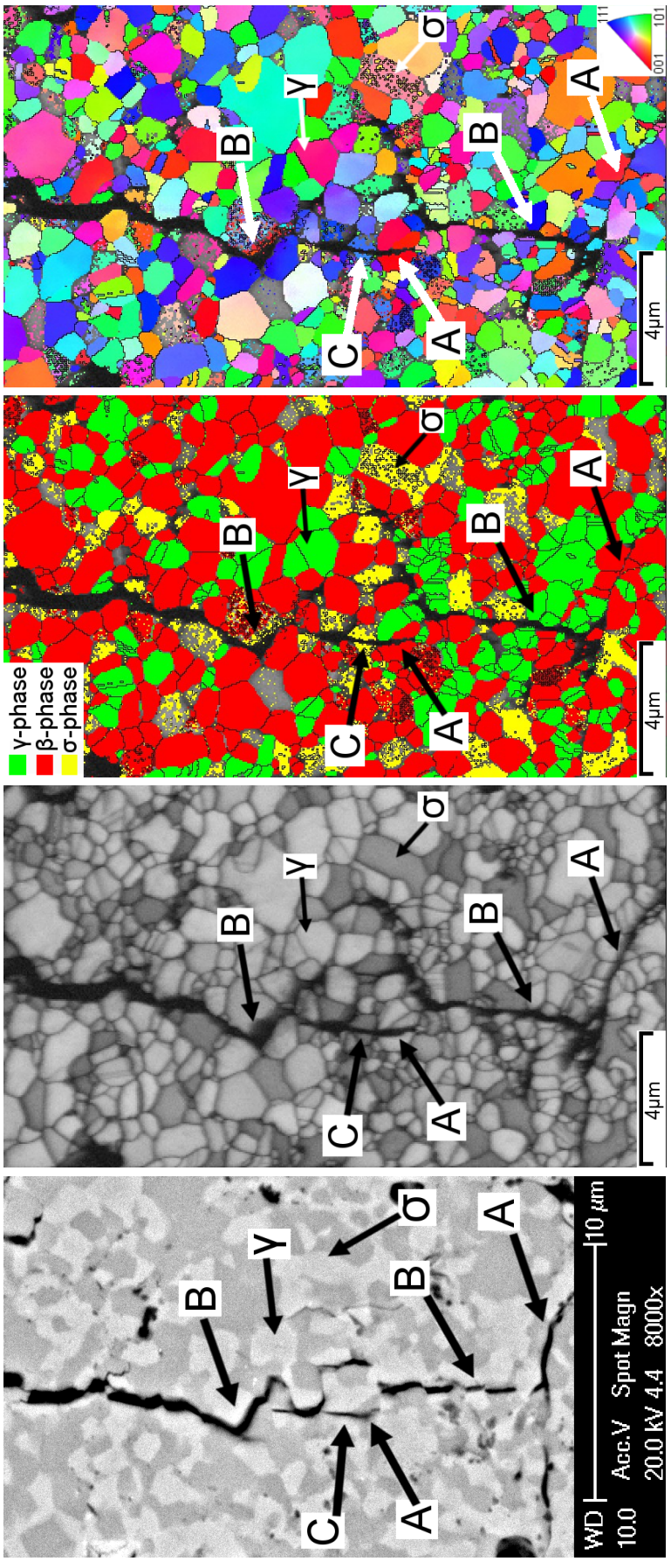

FIGURE 5.28: BSE image and EBSD maps of the EP1 coating specimen following testing at 500 °C where (a) is a higher magnification image of the region marked by the white box in Fig.Fig:TAF-BSE-Fracture-EP1-500, (b) is a band contrast map showing grain boundaries, (c) is a phase map in which the γ-phase is coloured green, the β-phase is coloured red and the σ-phase is coloured yellow and (d) is an inverse pole figure map showing grain orientation. The letter A indicates evidence of transgranular fracture through the β-phase. The letter B indicates evidence of intergranular fracture along the phase boundaries between the matrix β-phase and the secondary γ and σ-phases. The letter C indicates evidence of transgranular fracture through a grain of σ-phase.

Fig.5.31a is a BSE image showing an example of void formation in the area of high tensile stress. Figs.5.31b, 5.31c and 5.31d are a band contrast map, a phase map in which the γ-phase is coloured green,the β-phase is coloured red and the σ-phase is coloured yellow, and an inverse pole figure respectively.

The letter A indicates evidence of void formation at the phase boundaries between the β-phase, the γ-phase and/or the σ-phase. This is the only type of void formation identifiable in the EP1 coating at 700 °C. Linkage of the voids at the phase boundaries explains the intergranular crack growth along the γ/σ phase boundaries observed in Fig.5.29c.

Some of the void formation at the phase boundaries occurs at the grain boundaries of adjacent β-phase grains. The asterisks in Fig.5.31 indicate examples of this. Void formation at the β-phase grain boundaries may explain why the crack growth in Fig.5.29c appeared transgranular through the β-phase.

Void formation at the phase boundaries is a result of strain incompatibility, as described in section 5.4.2 for the C1 coating.

Overall, it can be concluded that failure of the EP1 coating at 700 °C is due to voids forming along the phase boundaries between the β-phase, the γ-phase and/or the σ-phase, which then link together to form void bands along the direction of tensile stress. These bands subsequently develop into small cracks and eventually into through-thickness cracks causing specimen failure.

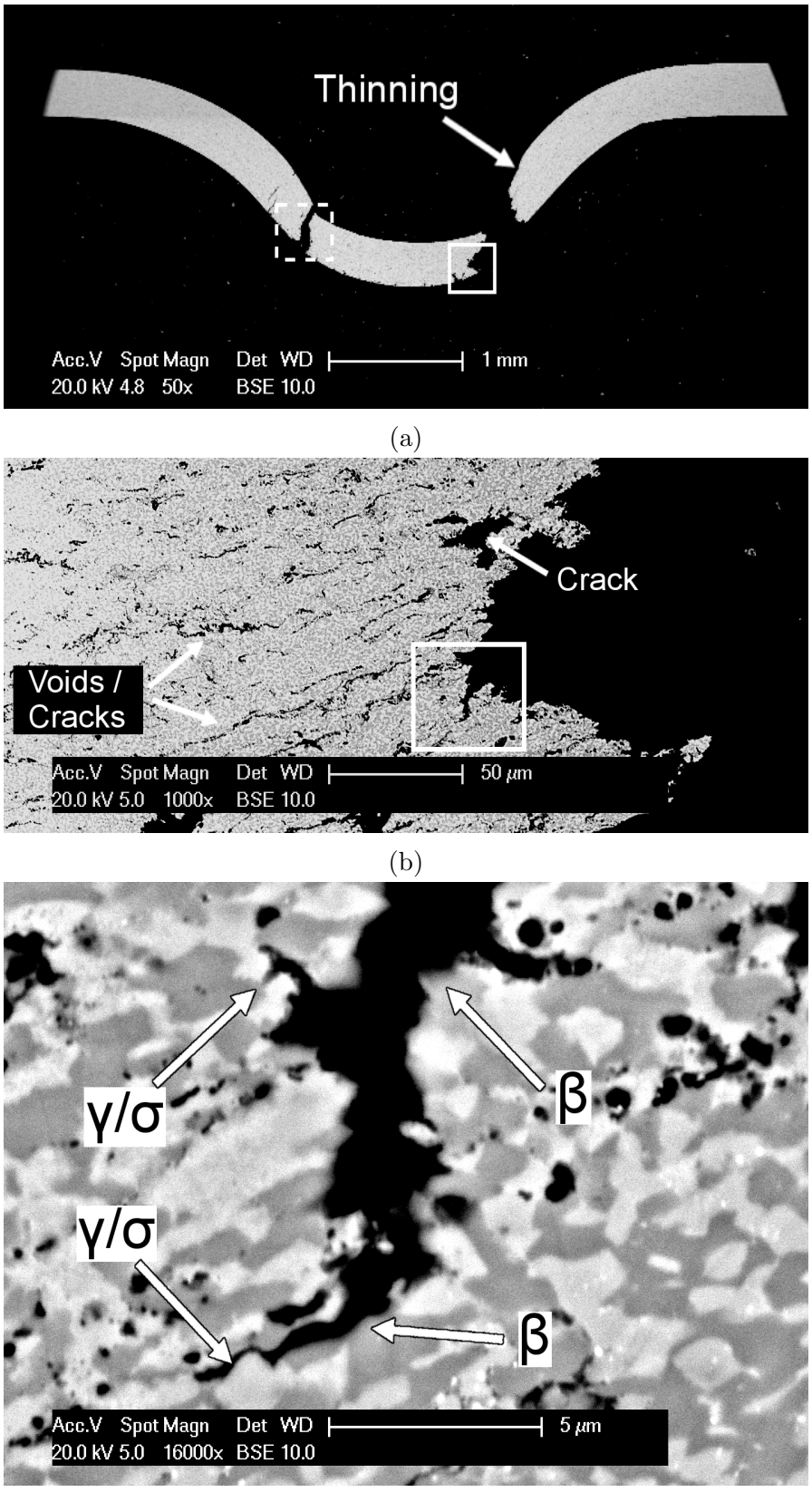

FIGURE 5.29: Cross sections of a EP1 coating specimen following SPT testing at 700 °C where the solid white boxes indicate the area shown in the proceeding image. In (c) the crack tip is growing through a region of β-phase.

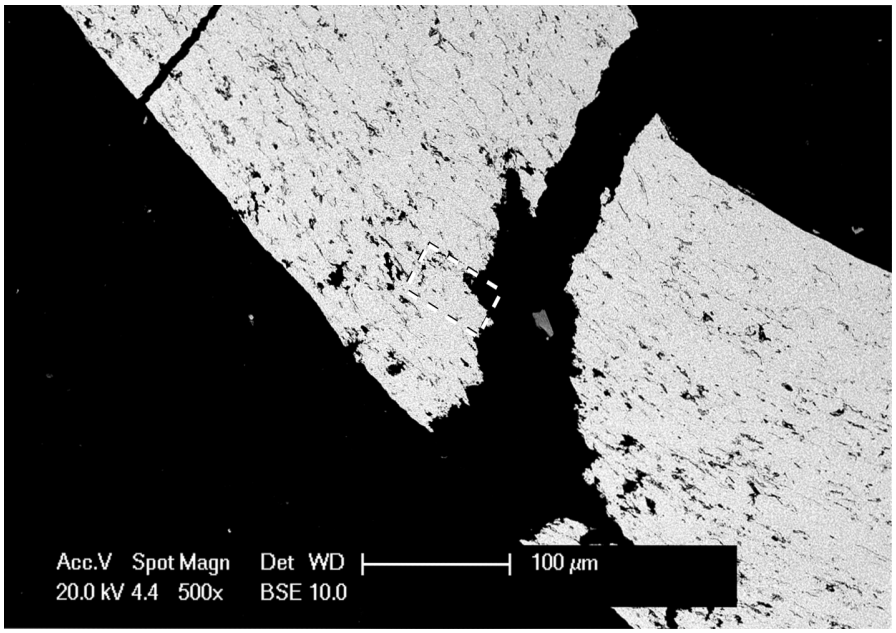

(a)

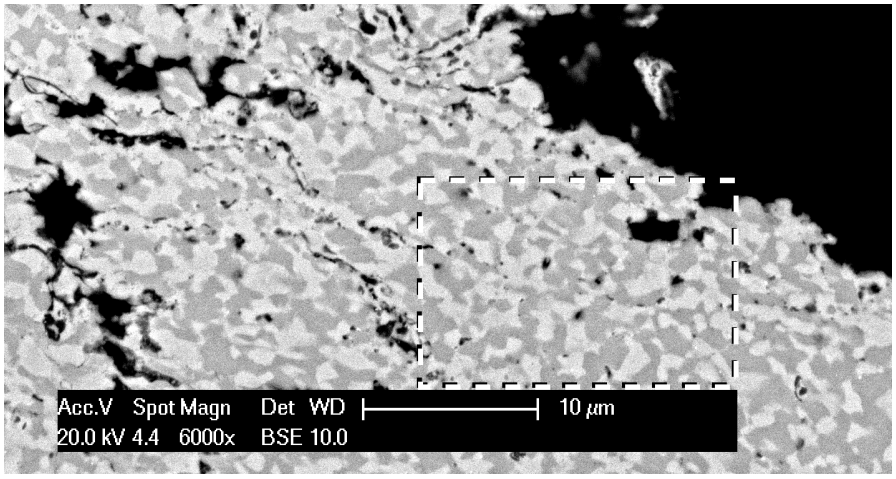

(b)

FIGURE 5.30: Cross sections of a EP1 coating specimen following SPT testing at 700 °C where (b) is a higher magnification image of the region marked by the dotted white box in (a). The white box in (b) indicates the region shown in Fig.5.31d.

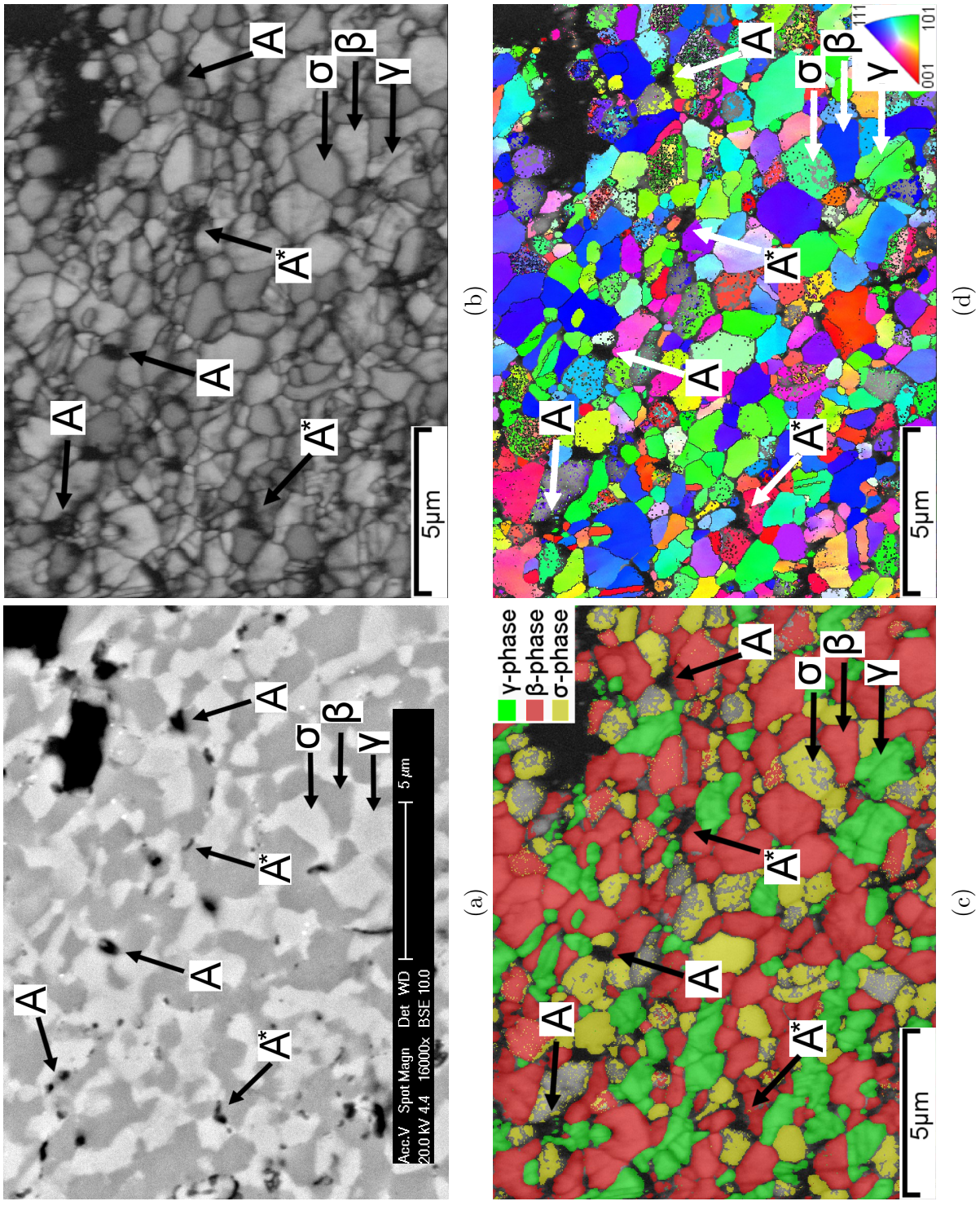

FIGURE 5.31: BSE image and EBSD maps of the EP1 coating specimen following SPT testing at 700 °C where (a) is the region outlined by the white dotted box in Fig.5.30b, (b) is band contrast map showing grain boundaries, (c) is a phase map in which the γ-phase is coloured green,the β-phase is coloured red and the σ-phase is coloured yellow and (d) is an inverse pole figure map showing grain orientation. The letter A indicates evidence of void formation at the phase boundaries between the β-phase, the γ-phase and/or the σ-phase. An asterisk indicates void formation between two grains of β-phase.

5.7 Small Punch Tensile Results of Coating EP3

Coating EP3 is a four phase coating with a β:σ:γ:γ' ratio of 59:18:12:7 vol.% with approximately 4 vol.% oxides/pores.

In the BSE images the β and γ'-phases are clearly visible but the γ and σ-phases bother appear as a grey contrast phase and cannot be distinguished. In the EBSD maps the β and σ-phases are clearly identified but the γ and γ'-phases cannot be distinguished. As such, BSE images and EBSD maps must be used in conjunction in order to evaluate the microstructure of the EP3 coating.

The microstructure is detailed in full in section 4.6.

5.7.1 Load Displacement Curves and Macroscopic Fracture Patterns

The load-displacement curves obtained for the heat treated EP3 coating are shown in Fig.5.32. Where possible, the different regimes normally observed in a SP load-displacement curve have been identified and labelled. The load at failure onset for each test is indicated by an arrow.

The load-displacement curves are interpreted with respect to the macroscopic fracture patterns observed at each temperature. The microscopic fracture patterns observed for the EP3 coating between RT and 750 °C are shown in Fig.5.33.

In Fig.5.34 the load-displacement curves are plotted on a common axes for comparative purposes.

750

At 750 °C the load-displacement curve exhibits all four bending regions typically associated with ductile behaviour. The tensile surface of the 750 °C specimen, shown in Fig.5.33f, shows a large circumferential crack, which is evidence of ductile failure at 750 °C.

There are some micro-cracks propagating radially into the 750 °C specimen. These cracks do not appear to have contributed to the specimen failure as they have propagated from the circumferential crack and not the centre of the specimen, indicating the micro-cracks formed after the circumferential crack.

700

At 700 °C the load-displacement curve exhibits the regions of elastic bending (i), plastic bending (ii) and membrane stretching (iii). Failure is indicated by a discontinuous change in the slope of the load-displacement curve which indicates cracking on the tensile surface of the specimen.

The tensile surface of the EP3 specimen tested at 700 °C is shown in Fig.5.33e. There is a hole in the centre of the specimen and two fragments which have deformed away from the specimen. This is the result of the centre of the specimen developing multiple radial fractures and splitting into fragments. Many of the fragments have subsequently broken away from the specimen.

The dotted black circle highlights where the 700 °C specimen has plastically deformed at the clamping boundary which is evidence of ductile behaviour. The load-displacement curve and macroscopic fracture pattern demonstrate that at 700 °C the EP3 coating is experiencing a transition from brittle to ductile behaviour.

Room Temperature

At RT the load-displacement curve is predominately linear and exhibits no evidence of plastic deformation before fracture occurs at 75 N, as indicated by the arrow. The point of fracture is indicated by a sharp load-drop in the load-displacement curve which indicates cracking on the tensile surface of the specimen.

The tensile surface of the RT specimen is shown in Figs.5.33a and 5.33b. The black dotted lines in Fig.5.33a highlight the cracks on the surface of the specimen which are shown at higher magnification in Fig.5.33b. It is clear that the load-drops in the load-displacement curve correspond to cracking on the tensile surface of the specimen.

500-650 °C

Between 500-650 °C the load-displacement curves are predominately linear and show the elastic bending (i) and plastic bending (ii) regions. The amount of plastic bending increases with temperature. The point of failure is indicated by a sharp load-drop in each of the load-displacement curves which indicates cracking on the tensile surface of the specimens. The point of fracture, indicated by the arrows, occurs at 72, 81 and 102 N at 500, 600 and 650 °C respectively.

The tensile surfaces of the 500 and 600 °C specimens are shown in Figs.5.33c and 5.33d respectively. At 500 °C the centre of the specimen has split into fragments due to multiple radial fractures. The fragments have started to shear away from the specimen and one fragment has completely detached to leave a hole in the specimen. The radial fractures have propagated to the edge of the specimen on the tensile surface but only propagated through the thickness of the specimen in the centre, otherwise the entire specimen would have split into fragments.

The specimen tested at 600 °C broke into multiple fragments. It is clear that failure was caused by multiple radial fractures but the continuation of the test at 600 °C caused the entire specimen to break into multiple fragments. Multiple cracking events can be seen in the load-displacement curve.

The specimen tested at 650 °C was not recovered after the test. Given the similarity of the 500, 600 and 650 °C load-displacement curves it can be concluded that specimen failure at 650 °C was similar to that seen at 500-600 °C.

The load-displacement curves at each temperature are shown in Fig.5.34. The load at failure onset, indicated by the arrows, remains approximately constant between RT and 600 °C but increases with temperature above 650 °C. The displacement at failure increases with temperature. The slope of the load-displacement curves, prior to failure, decreases with temperature showing a decrease in the EP3 coatings resistance to bending as the temperature is increased.

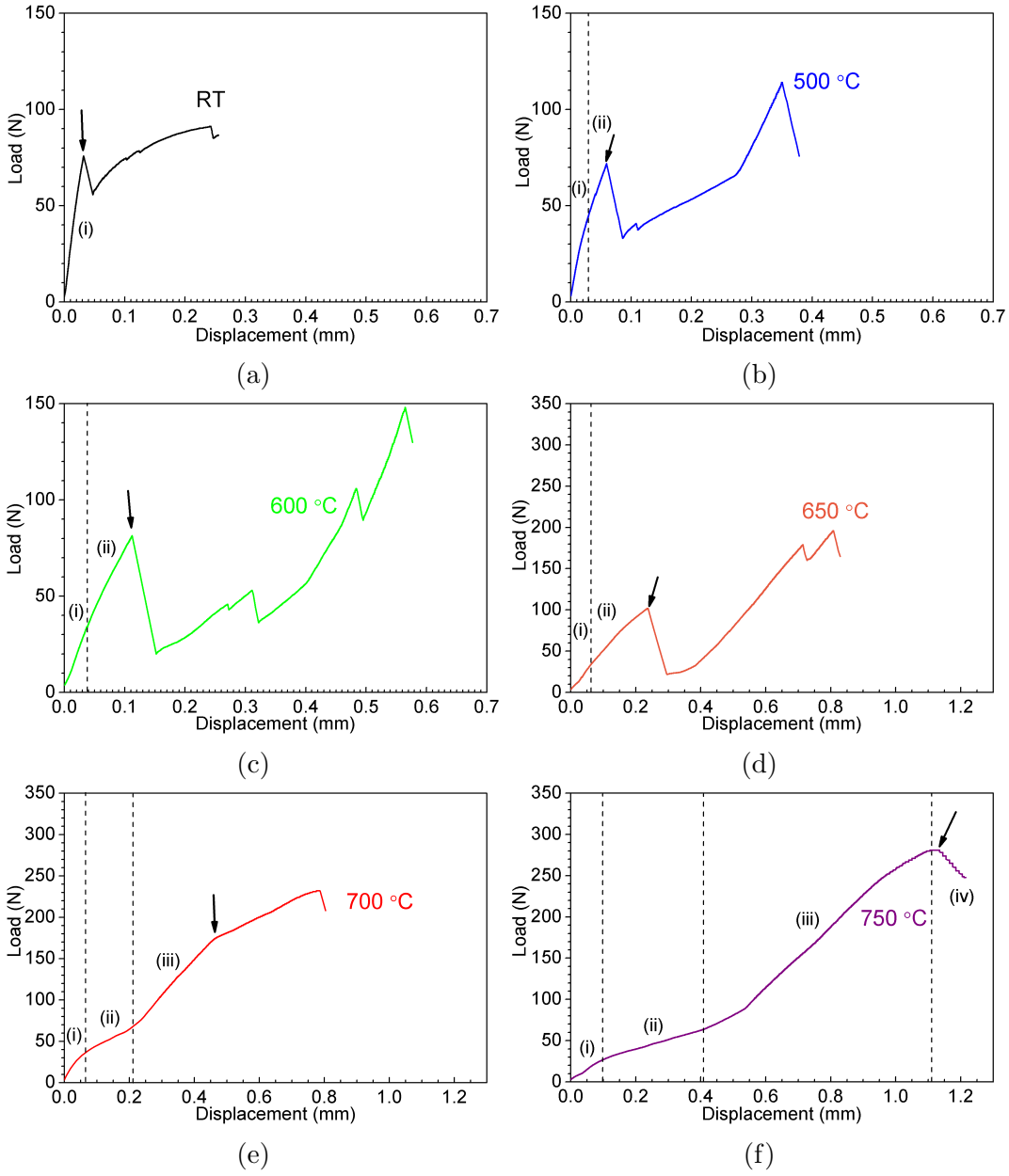

FIGURE 5.32: Load-displacement curves obtained for the EP3 coating at a constant displacement rate of 1 μms^{-1} between RT and 750 °C. The arrows indicate the load at failure onset and the labels refer to elastic bending (i), plastic bending (ii), membrane stretching (iii) and maximum load and progressive plastic instability (iv).

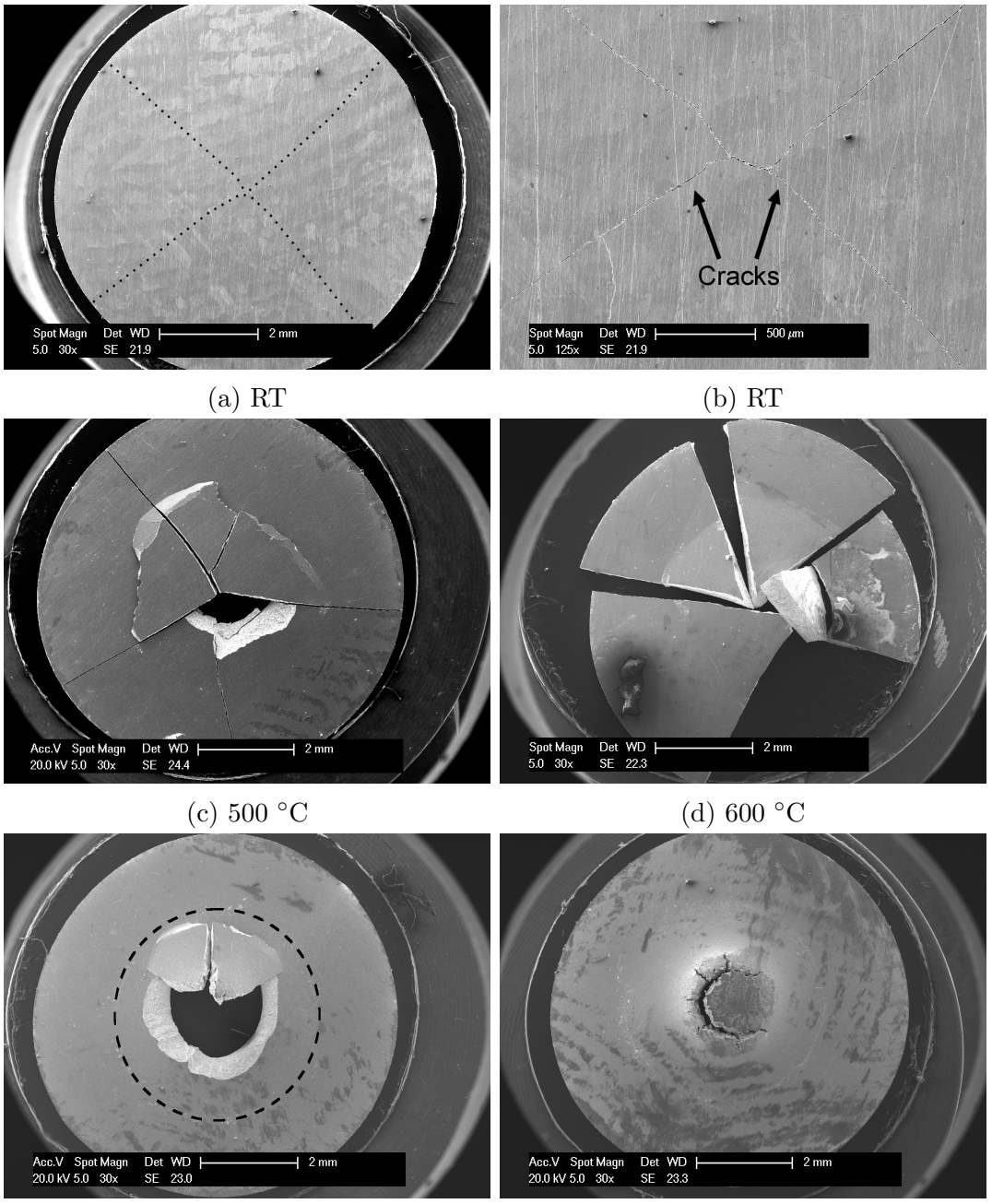

(a) RT (b) RT

(c) 500 °C (d) 600 °C

(e) 700 °C (f) 750 °C

FIGURE 5.33: Tensile surfaces of EP3 coating specimens following SPT testing at (a)-(b) RT, (c) 500 °C, (d) 600 °C, (e) 700 °C and (f) 750 °C. The dotted black lines in (b) highlight the cracks in the specimen and in (e) indicate the clamping boundary.

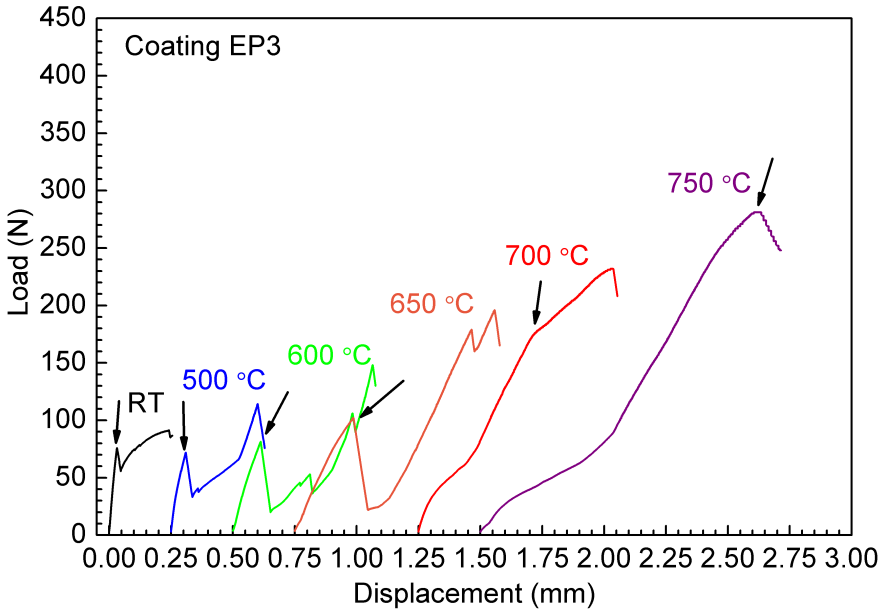

FIGURE 5.34: Load-displacement curves obtained for the EP3 coating at a constant displacement rate of 1 μms^{-1} between RT and 750 °C. The arrows indicate load at failure onset. Curves have been displaced at 0.25 mm intervals on the x axis.

5.7.2 Material Properties

Ductile to Brittle Transition Temperature

The strain at first cracking for the EP3 coating is plotted as a function of temperature in Fig.5.35a. Between RT and 650 °C the elastic strain at first cracking was calculated using Eq.5.1. Between 700-750 °C the plastic strain at first cracking was calculated using Eq.5.6.

The strain at first cracking does not change significantly between RT and 650 °C. Between 650 and 750 °C there is a large increase in the strain at first cracking which demonstrates there is a significant increase in the ductility of the coating. As such, the DBTT of the EP3 coating can be defined as 650-750 °C.

Bi-Axial Yield/Fracture Strength

The bi-axial yield/fracture strength as a function of temperature for the EP3 coating is shown in Fig.5.35b. The fracture strength was calculated between RT and 650 °C where the EP3 coating showed very little or no plastic deformation

before fracture occurred. The bi-axial yield strength (σ_{YS}) was calculated at 700 and 750 °C where a clear elastic-plastic transition could be identified.

The bi-axial fracture strength increases between RT and 650 °C. The bi-axial yield strength of the EP3 coating is much lower than the fracture strength and appears to decrease with temperature but no conclusions can be made from only two data points. The material property data for the EP3 coating is summarised in table 5.3.

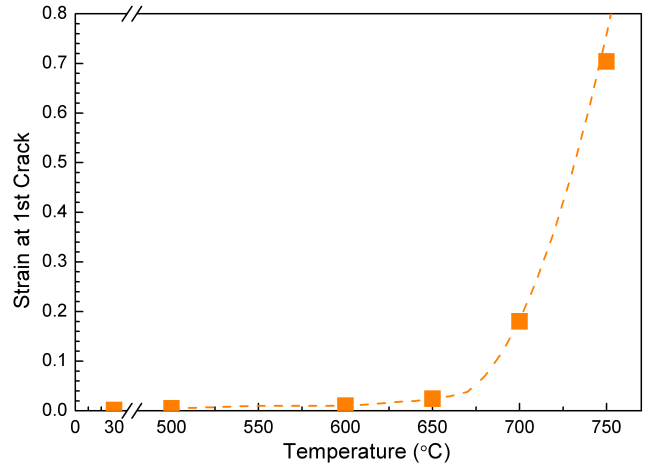

(a)

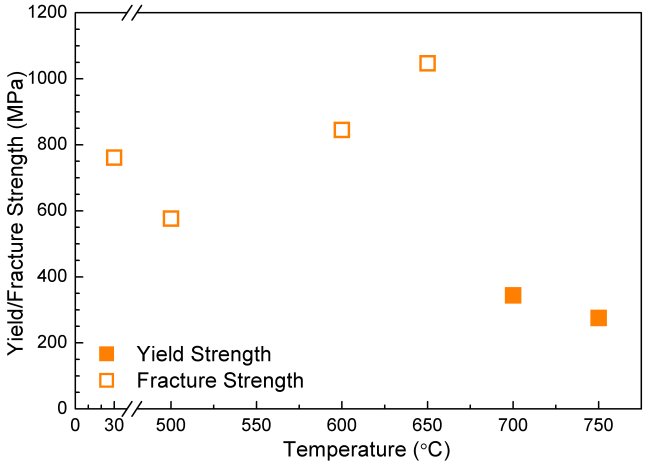

(b)

FIGURE 5.35: Strain at first cracking (a) and Yield/fracture strength (b) calculated for the EP3 coatings between RT and 750 °C.

Temp. (°C)	Yield Load (N)	Displacement at Yield (mm)	Load at 1st Crack (N)	Displacement at 1st Crack (mm)	σ_{YS} ◁ or σ_{FS} □ (MPa)	Strain at Fracture
RT	-	-	76	0.03	761 □	0.003 †
500	-	-	56	0.04	577 □	0.004 †
600	-	-	81	0.11	845 □	0.011 †
650	-	-	102	0.21	1047 □	0.024 †
700	34	0.04	174	0.46	344 ◁	0.184 ⊙
750	27	0.09	281	1.14	275 ◁	0.704 ⊙

TABLE 5.3: Material property data for the EP3 coating where ◁ and □ refer to yield stress (σ_{YS}) and fracture stress(σ_{FS}) respectively, † indicates elastic strain calculated using Eq.5.1 and ⊙ indicates plastic strain calculated using Eq.5.6.

5.8 Characterisation of Fracture Behaviour in Coating EP3

5.8.1 Microscopic Fracture Surfaces

Secondary electron images of the EP3 coating fracture surfaces following SPT testing at 500 and 750 °C are shown in Fig.5.36. The 500 °C fracture surface exhibits numerous small flat regions which are evidence of cleavage and low-ductility fracture.

The fracture surface of the 750 °C specimen has a more rounded appearance which at higher magnification can be seen to correspond to elongation of the material and evidence of ductile tearing.

The fracture surfaces show there is a clear change in fracture behaviour between 500 and 750 °C.

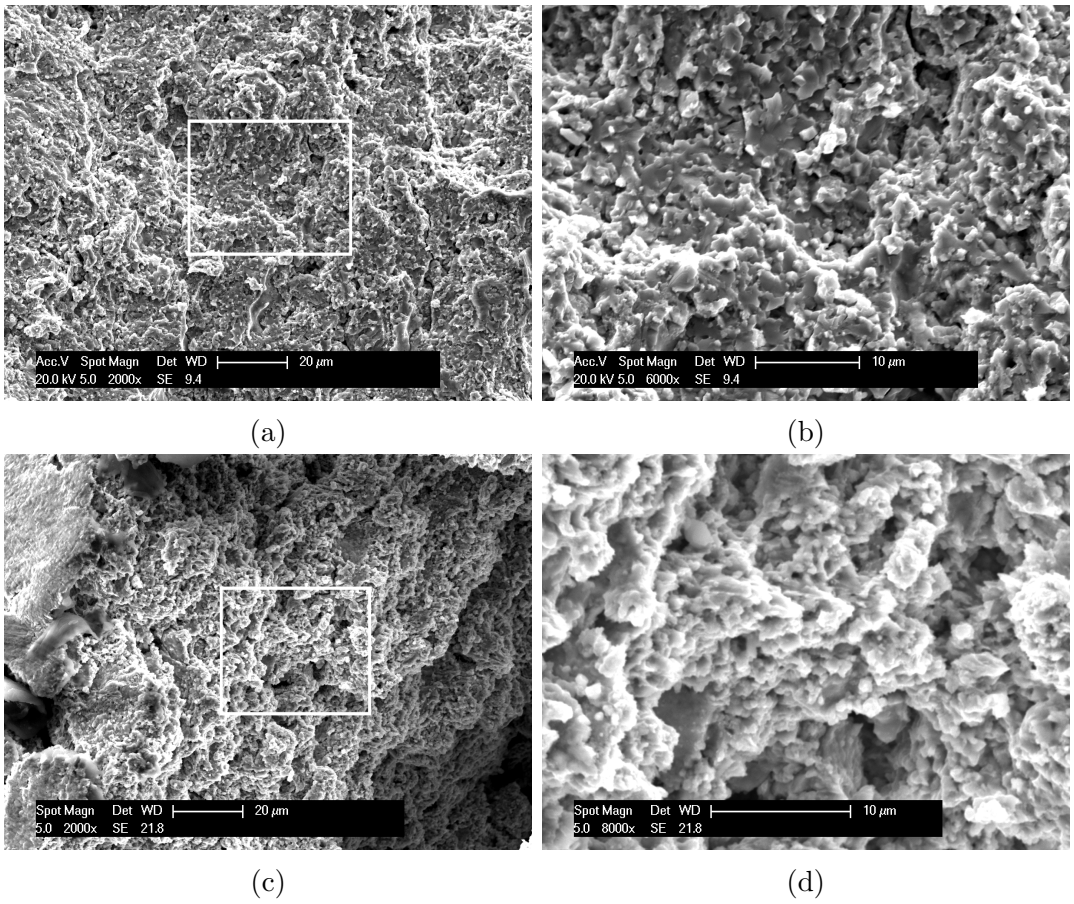

FIGURE 5.36: Fracture surfaces of the EP3 coating specimens following SPT testing at 500 °C (a-b) and 750 °C (c-d) where the white boxes outline the areas shown in the higher magnification images (right).

5.8.2 Fracture Path Analysis

Low Temperature Crack Development

A plan view of the EP3 coating following SPT testing at 500 °C is shown in Fig.5.37. The white boxes outline the areas shown at higher magnification in the proceeding images.

The areas denoted 1 and 2 in Fig.5.37c identify the areas shown at higher magnification in Figs.5.38 and 5.39 respectively.

Figs.5.38 and 5.39 show examples of crack propagation in the EP3 coating at 500 °C. They show a BSE image, a band contrast map showing grain boundaries, a phase map in which the γ-phase is coloured green, the β-phase is coloured red

and the σ-phase is coloured yellow, and an inverse pole figure map showing grain orientation.

In the BSE images the dark contrast phase is the β-phase and the bright white phase is the γ'-phase. The light contrast phase is either γ-phase or σ-phase. An example is shown in Fig.5.38 where one light contrast phase is detected as γ-phase and another is detected as σ-phase.

Fig.5.38 shows two well defined cracks in which different modes of fracture can be observed. The letter A indicates evidence of transgranular fracture through a grain of β-phase. The letters B and C indicate evidence of intergranular fracture along the grain boundaries of the β/σ-phase and β/γ'-phase respectively. The letter D indicates evidence of transgranular fracture through a grain of σ-phase. There is no evidence of intergranular fracture between two grains of β-phase.

The preferential path for crack propagation in the EP3 coating is variable. One mode of fracture is transgranular fracture through the β-phase; there is clear evidence of this in Figs.5.38 and 5.39 as well as evidence of a crack originating within a grain of β-phase in Fig.5.38. Another mode of fracture is intergranular fracture along phase boundaries which is the dominant mode of fracture where phase boundaries exist. The third mode of propagation is transgranular fracture through the σ-phase. This type of fracture appears to occur when the direction of the phase boundary is at a large angle to the direction of the crack growth. There is no evidence of transgranular through the γ or γ'-phase.

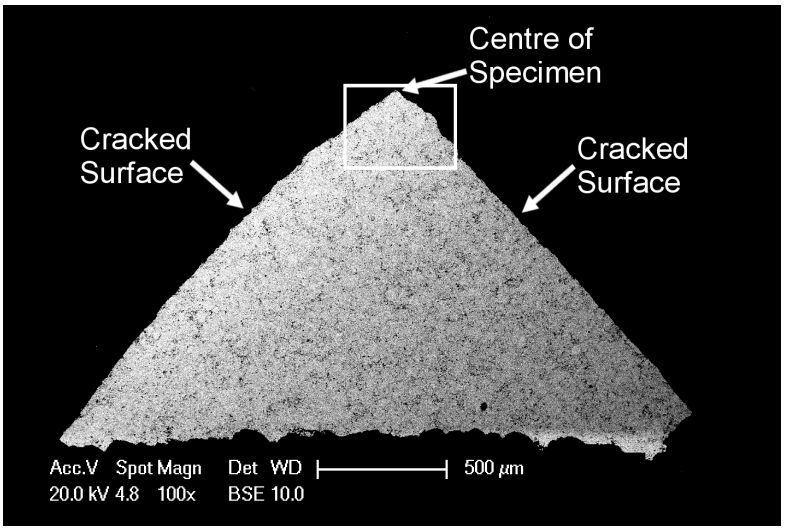

(a)

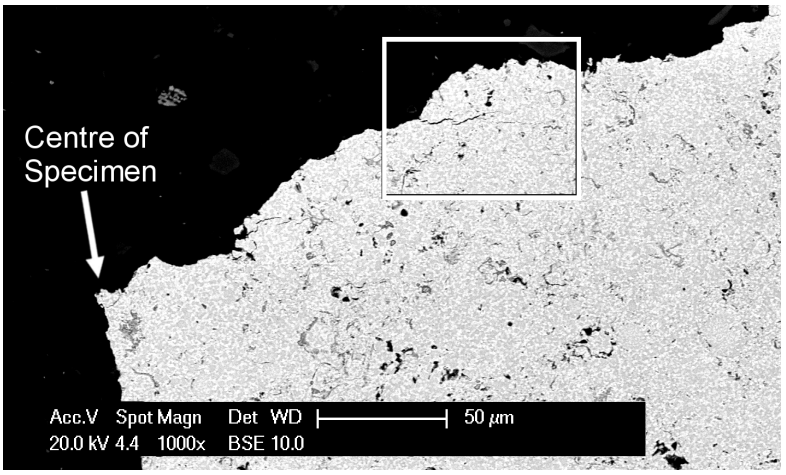

(b)

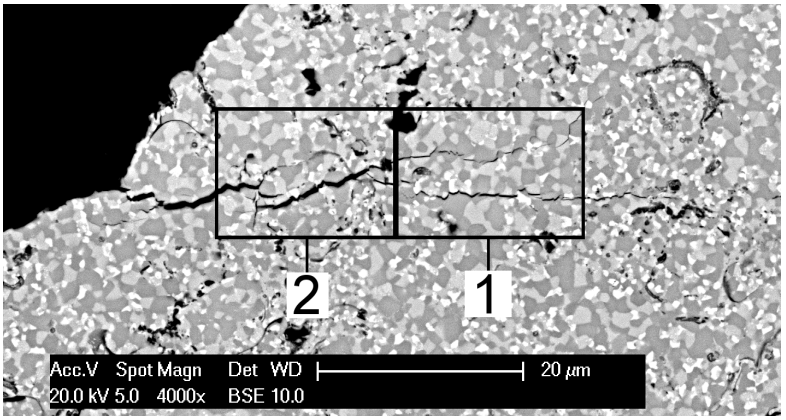

(c)

FIGURE 5.37: Cross sections of a EP3 coating specimen following SPT testing at 500 °C where (c) is a higher magnification image of the region marked by the white box in (b). Figs. (b) and (c) have been rotated to align the crack in the horizontal direction. The areas denoted 1 and 2 in Fig.5.37c identify the areas shown at higher magnification in Figs.5.38 and 5.39 respectively.

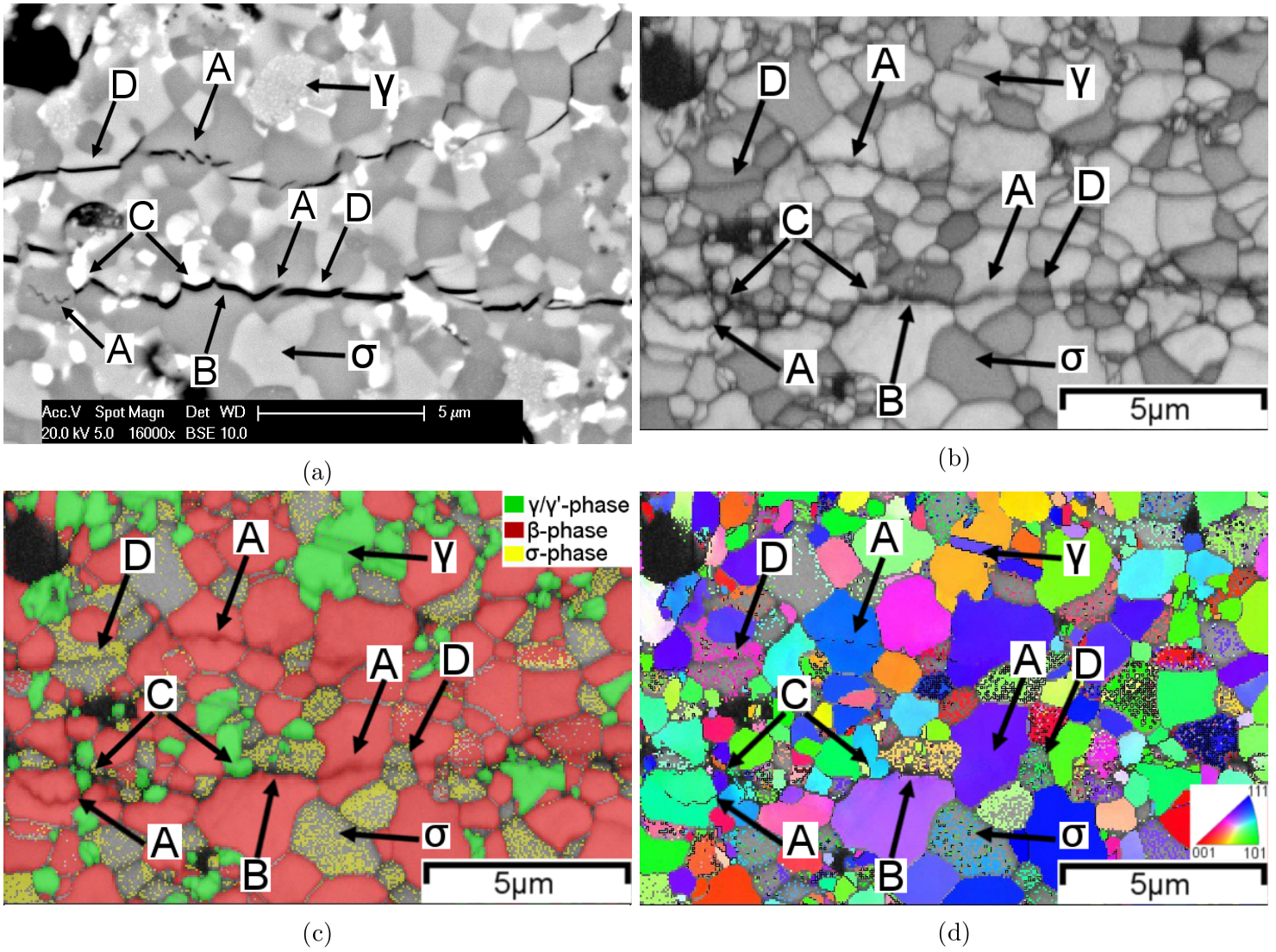

FIGURE 5.38: EBSD maps of the EP3 coating specimen following SPT testing at 500 where (a) is a band contrast map showing grain boundaries, (b) is a phase map in which the γ-phase is coloured green, the β-phase is coloured red and the σ-phase is coloured yellow. (c) is an inverse pole figure map showing grain orientation. The letter A indicates evidence of transgranular fracture through a grain of β-phase. The letters B and C indicate evidence of intergranular fracture along the grain boundaries of the σ-phase and γ'-phase respectively. The letter D indicates evidence of transgranular fracture through a grain of σ-phase.

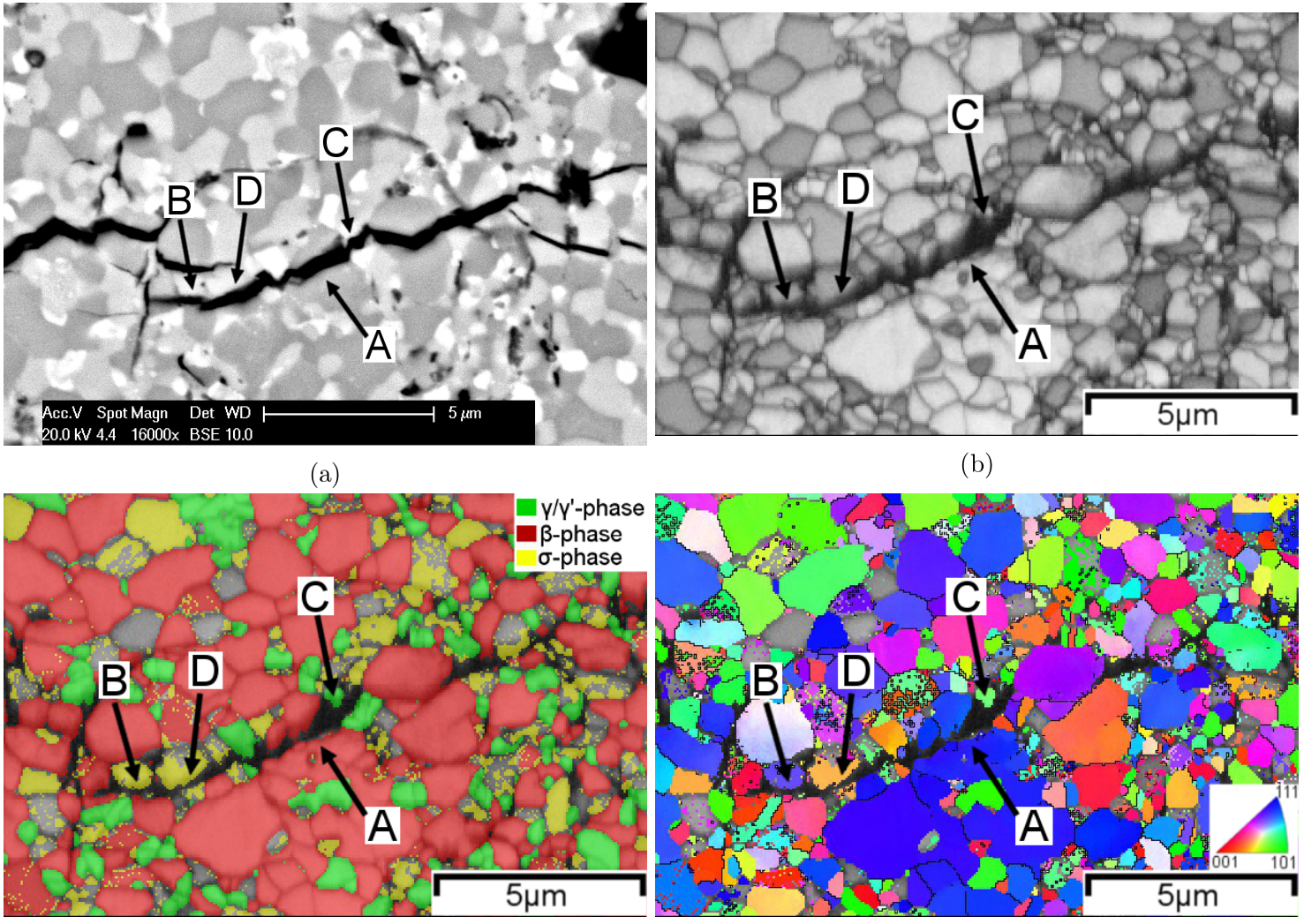

FIGURE 5.39: BSE image and EBSD maps of the EP3 coating specimen following SPT testing at 500 where (b) is a band contrast map showing grain boundaries, (c) is a phase map in which the γ-phase is coloured green, the β-phase is coloured red and the σ-phase is coloured yellow. D) is an inverse pole figure map showing grain orientation. The letter A indicates evidence of transgranular fracture through a grain of β-phase. The letters B and C indicate evidence of intergranular fracture along the grain boundaries of the σ-phase and γ'-phase respectively. The letter D indicates evidence of transgranular fracture through a grain of σ-phase.

High Temperature Crack Development

A cross section of the EP3 coating following small punch testing at 750 °C is shown in Fig.5.40 where the boxes indicate the area shown at higher magnification in the proceeding image. There is a large through thickness crack at a radial offset from the centre of the specimen and thinning in the specimen, as was observed for the C1 and EP1 coatings.

Fig.5.40 shows an example of void formation and crack growth in the EP3 coating at 750 °C. EBSD maps of the same area are shown in Fig.5.41 where Fig.5.41a is a band contrast map showing grain boundaries, Fig.5.41b is a phase map in which the γ-phase is coloured green, the β-phase is coloured red and the σ-phase is coloured yellow, and Fig.5.41c an inverse pole figure map showing grain orientation.

In Figs.5.40-5.41, the letter A indicates evidence of void formation at the phase boundaries between the β-phase, the γ-phase and/or the σ-phase which appears to be the only type of void formation in the EP3 coating.

The letter B indicates evidence of intergranular crack growth along the grain boundary of the β-phase and the letter C indicates evidence of intergranular crack growth along the phase boundaries between the β-phase and/or the γ/σ-phase. Both examples of intergranular crack growth are along the grain boundary of the β-phase as this is the matrix phase. Intergranular crack growth along the β and γ/σ phase boundaries appears to be the dominant mode of crack growth. Intergranular growth along the grain boundaries of the β-phase is a secondary mode of fracture which occurs when there are no β and γ/σ phase boundaries.

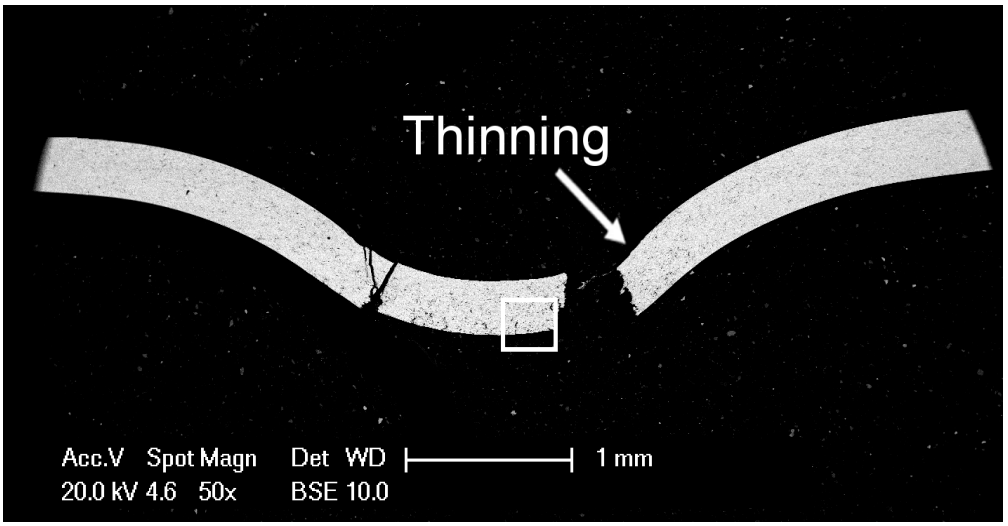

(a)

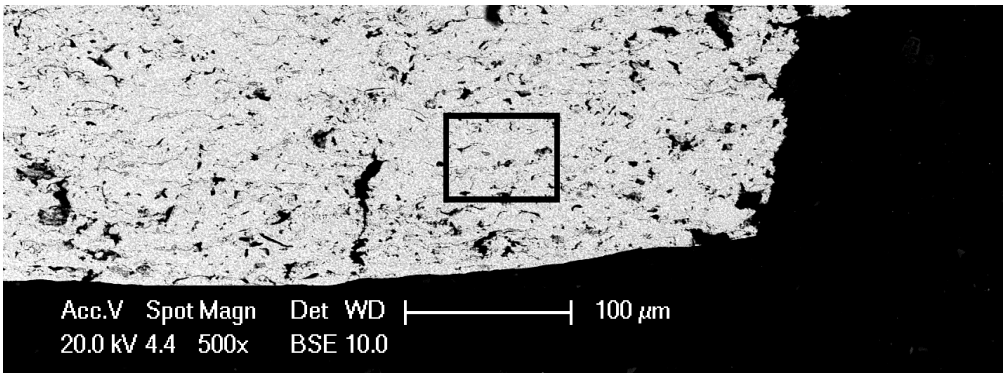

(b)

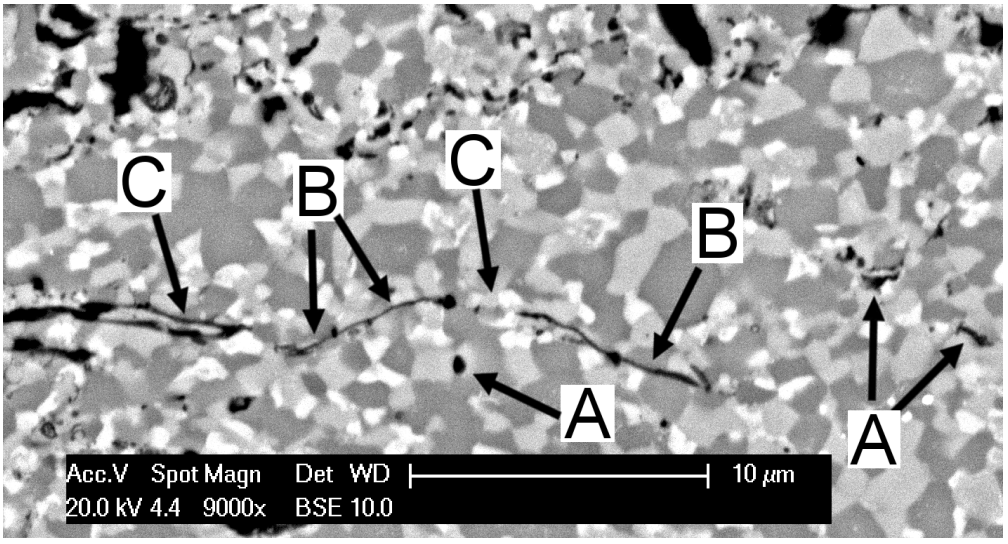

(c)

FIGURE 5.40: Cross sections of the EP3 coating specimen tested at 750 °C where the boxes indicate the region shown at higher magnification in the proceeding image. The letter A indicates evidence of void formation at the phase boundaries between the β-phase, the γ-phase and/or the σ-phase. The letter B indicates evidence of intergranular crack growth along the grain boundary of the β-phase and the letter C indicates evidence of intergranular crack growth along the phase boundaries between the β-phase and/or the γ/σ-phase.

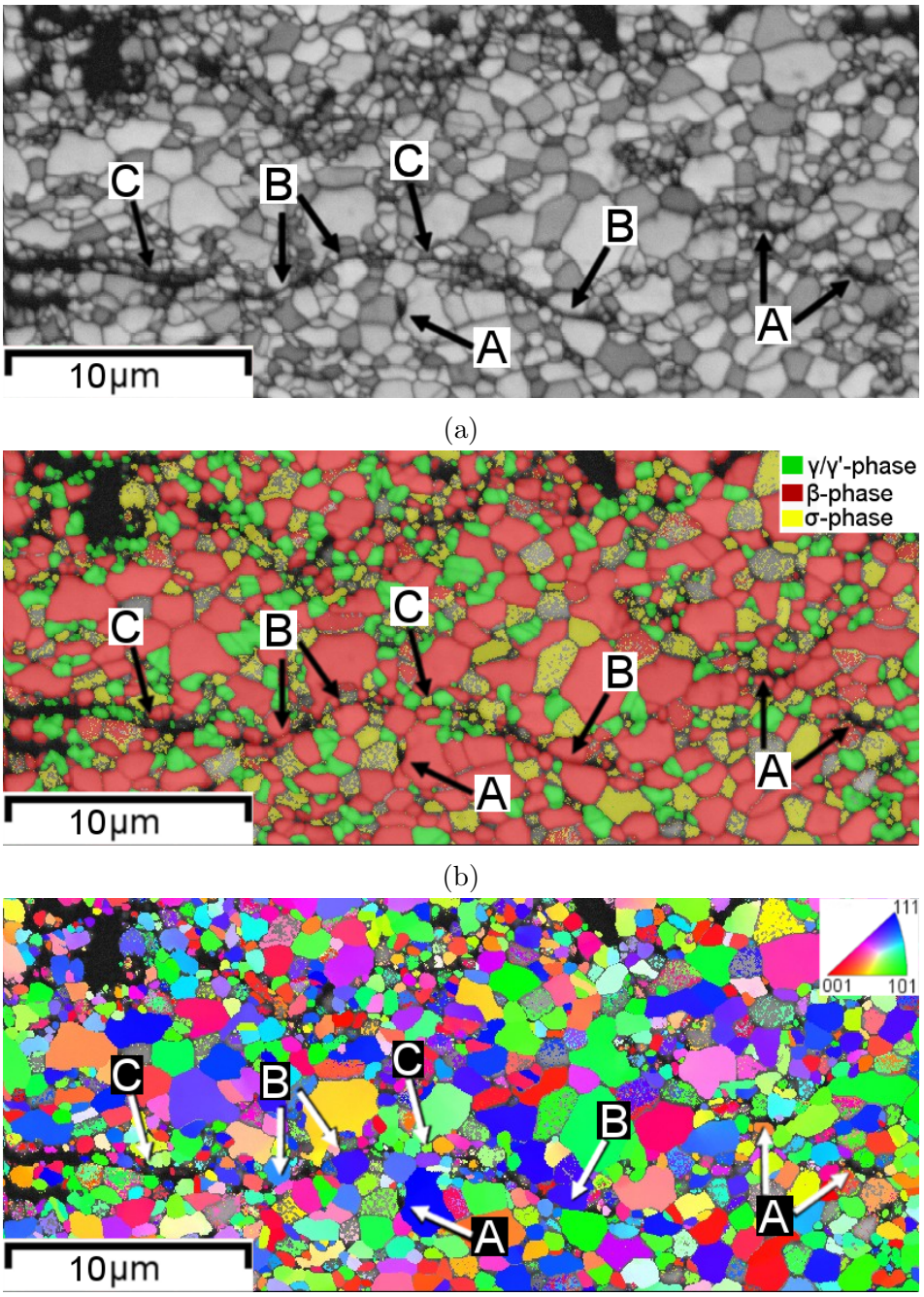

FIGURE 5.41: EBSD maps of the EP3 coating specimen following SPT testing at 700 °C where (a) is a band contrast map showing grain boundaries, (b) is a phase map in which the γ-phase is coloured green,the β-phase is coloured red and the σ-phase is coloured yellow. (c) is an inverse pole figure map showing grain orientation. The letter A indicates evidence of void formation at the phase boundaries between the β-phase, the γ-phase and/or the σ-phase. The letter B indicates evidence of intergranular crack growth along the grain boundary of the β-phase and the letter C indicates evidence of intergranular crack growth along the phase boundaries between the β-phase and/or the γ/σ-phase.

5.9 Discussion

The purpose of this section is to consider possible explanations for a number of the characteristic features of the SPT test behaviour. First, key microstructural features of the alloys used in this work will be summarised along with the mechanical properties of their constituent phases as obtained from the literature. Secondly, the temperature dependent properties found in the present study will be compared with the literature concerning MCrAlY alloys both in bulk form and, where available, as thin samples. Thirdly, the macroscopic fracture patterns observed will be considered in relation to loading in the SPT test and current finite element models of the stress distribution. Finally, possible mechanisms for microscopic crack initiation and propagation in different temperature regimes will be examined across all the alloys.

5.9.1 Alloy Constitution and Properties of the Constituent Phases

5.9.1.1 Alloy Constitution

A summary of the phase fractions for each alloy is provided here to aid understanding of the SPT test behaviour. A full description of the coating microstructures and phase evolution can be found in chapter 4.

The phase fractions observed in the heat treated coatings, normalised to exclude oxide content, are shown in table 5.4. As the SPT tests were conducted over a short time period (less than 6 hours), it can be reasonably assumed that little or no phase evolution took place in any of the coatings during the SPT tests. Therefore, the microstructures of the coatings during the SPT tests between RT-750 °C are similar to the values shown in table 5.4. All three coatings also exhibited a fine scale microstructure with individual grains ranging from less than 1 μm to 5 μm.

Phase	Phase Fraction (vol.%)		
	C1	EP1	EP3
β-phase	31 ±2	60 ±2	56 ±2
γ-phase	69 ±2	27 ±2	14 ±2
γ'-phase	-	-	9 ±1
σ-phase	-	13 ±2	21 ±2

TABLE 5.4: Normalised phase fractions of the C1, EP1 and EP3 coatings. Measurements are a combination of image analysis of SEM and EBSD images. Values are normalised to exclude oxide/pore content.

5.9.1.2 Temperature Dependent Properties of Constituent Phases From the Literature

In order to understand how the deformation and fracture behaviour of the coatings changed with temperature, particularly in reference to the DBTT, it is necessary to consider the tensile properties of the individual phases with respect to temperature.

The yield stress of a Ni-Cr-Al alloy with varying levels of γ-Ni phase and γ'-Ni_3Al phase is shown in Fig.5.42a with respect to temperature [6]. In general, the yield stress of the alloy containing only γ-Ni phase alloy decreases with temperature, but between 300-600 °C the yield strength increases slightly before decreasing again above 600 °C. The yield stress of a purely γ'-alloy is similar to the γ-alloy below 200 °C but then increases significantly with temperature up to 900 °C before decreasing again. The addition of γ' has a marked increase on the yield strength of a γ alloy.

The γ-Ni phase is known to be a ductile and does not exhibit a DBTT. Understanding how the ductility of the γ-phase changes with temperature can be gained from the tensile properties of predominately γ-Ni phase alloys. The tensile properties of IN625 are shown in Fig.5.42b [154]. The yield strength is approximately constant below 800 °C but above 650 °C there is a marked increase in the elongation of the alloy.

An example of the temperature dependence of the yield stress and ductility of NiAl is shown in Fig.5.43 [70, 155]. Fig.5.43a illustrates the yield strength of NiAl is different for different slip planes. The yield strength in the [110] plane is

extremely high, but in the [100] slip plane, as well as for polycrystalline NiAl, the yield strength is comparatively low. The effect of NiAl as a strengthening phase is therefore dependent upon the orientation of the phase, which is random in the C1, EP1 and EP3 coatings.

Fig.5.43b demonstrates how the ductility of NiAl alloys increases significantly above the DBTT. The ductility of polycrystalline NiAl can range from 0-2 % depending upon the stoichiometry [70], and can also be affected by the addition of a second phase or processing method, as shown in Fig.5.43b. In Fig.5.43b the ductility increases significantly at 1000 K which allows the DBTT to be identified, but the DBTT of NiAl is also sensitive to composition and may range from 400-900 °C [4, 70]. Hence, it is difficult to quantitatively assess the yield strength and DBTT of a NiAl alloy from data concerning NiAl alloys of different compositions. However, NiAl alloys do typically exhibit a decrease in yield strength and an increase in the strain to failure across the DBTT. These general characteristics can be used to evaluate the SPT test behaviour of the MCrAlY alloys.

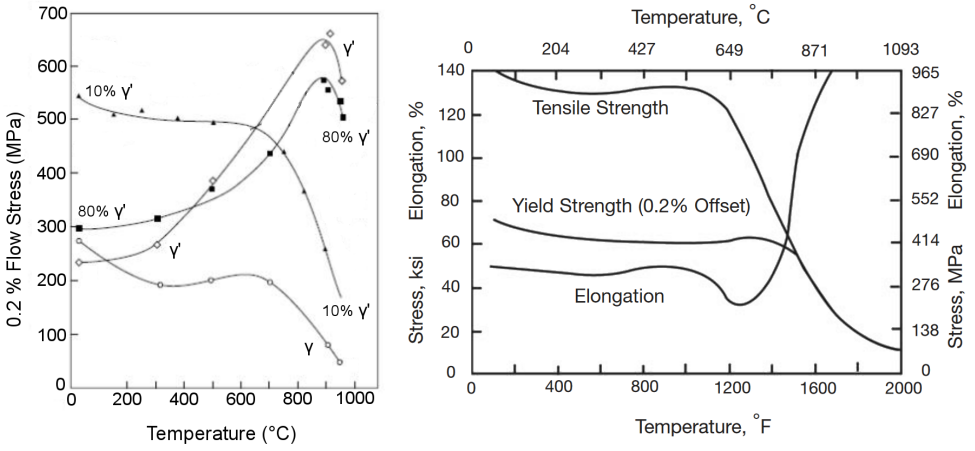

(a) (b)

FIGURE 5.42: a) Yield strength as a function of temperature for a Ni-Cr-Al alloy with varying phase fractions of γ'-Ni_3Al phase. Figure reproduced from [6]. b) tensile properties of an IN625 alloy annealed bar, reproduced from special metals IN625 data sheet [154].

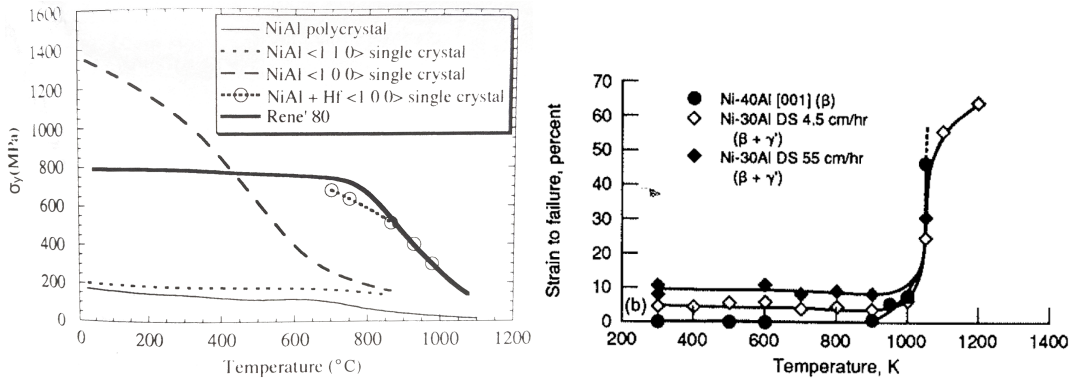

(a) (b)

FIGURE 5.43: a) Temperature dependence of the tensile yield strength of binary, polycrystalline NiAl and binary NiAl single crystals tested along [110] and [100] planes. Figure reproduced from [70]. b) ductility as a function of temperature for a single phase, single crystal nickel aluminide and directionally solidified (DS) two phase Ni-30Al alloys. Figure reproduced from [155].

5.9.2 Temperature Dependent Properties of the Alloys Determined by SPT Tests

5.9.2.1 Ductile to Brittle Transition Temperature

The strain at first cracking as a function of temperature for the C1, EP1 and EP3 coatings is shown in Fig.5.44. The ductile to brittle transition temperatures of the C1, EP1 and EP3 coatings, as summarised in table 5.5, are 500-700 °C, 600-700 °C and 650-750 °C respectively.

A recent study by Subramanian et al. [71] found a coating manufactured from the C1 alloy exhibited a DBTT of around 600 °C, and a coating of similar composition was reported to show ductile behaviour above 677 °C by Wereszczak et al. [72], which is in good agreement with the current work.

There is little data available on the DBTT of MCrAlY alloys with compositions similar to the EP1 and EP3 alloys, but Hesbur and Miner [81] did report a Ni-20Co-17Cr-14Al-0.5Y coating exhibited a marked increase in ductility above 500 °C, which is consistent with the current work.

The DBTT is sensitive to a number of factors including composition, phase distribution, microstructure and manufacturing process [4, 64]. In general, the β-phase is considered the phase responsible for the ductile to brittle transition in MCrAlY alloys and increasing the phase fraction of β-NiAl phase is considered to increase the DBTT of MCrAlY alloys [4, 64, 67, 69, 70]. This general trend is consistent with the current findings.

Increasing the phase fraction of β-phase decreases the phase fraction of the ductile γ-phase. As such, the increase in the DBTT of MCrAlY alloys can also be considered in terms of a reduction in the phase fraction of the ductile phases i.e. the γ-Ni and γ'-Ni_3(Al,Ta) phases. This makes sense with the current findings as the EP3 coating exhibits the lowest phase fraction of γ and γ' and exhibits the highest DBTT.

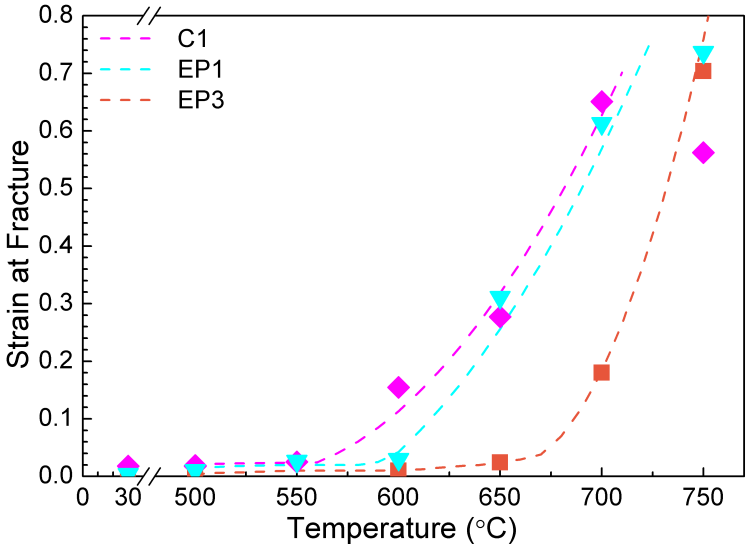

FIGURE 5.44: Stain at fracture as a function of temperature for C1, EP1 and EP3 coatings.

	C1	EP1	EP3
DBTT (°C)	500-700	600-700	650-750

TABLE 5.5: DBTT of the C1, EP1 and EP3 coatings measured from plots of strain to cracking shown in Fig.5.44.

5.9.2.2 Bi-Axial Yield and Fracture Strength

The yield/fracture strength of the C1, EP1 and EP3 coatings as a function of temperature is shown in Fig.5.45. The yield strength of the C1 coating decreases above 550 °C and appears to stabilise at approximately 700 °C.

The yield strength of the C1 coating is constant between 500-550 °C at approximately 1300 MPa but decreases between 550-700 °C to approximately 200 MPa. The yield strength of coatings manufactured from the C1 alloy has been reported as approximately 600 MPa at 500 °C through uni-axial tests for a 1.5 mm thick APS coating (flat tensile strips) [24], and a 0.7 mm thick LPPS coating [71] (flat dog-bone tensile specimen).

The current data was calculated from bi-axial bending whereas the yield strengths reported by Taylor et al. [24] and Subramanian et al. [71] were calculated from uni-axial testing, which could explain the difference in results. It could be that a correctional factor is needed to correlate the SPT test data with the uni-axial test data, as has been demonstrated for steels [99, 100, 102–105]. However, more data is needed before one such factor could be determined.

Despite the difference in absolute values, the yield strength of the C1 coating does show a temperature dependence that is consistent with Taylor et al. [24] and Subramanian et al. [71], as well as the γ-phase alloy, shown in Fig.5.42, and the literature for Ni-based superalloys [4, 6, 24, 68, 156], which indicates the difference between the SPT test results and uni-axial test data is consistent across the temperature range. This allows qualitative comparisons with the EP1 and EP3 coatings to be made.

The EP1 coating did not show a clear transition from elastic to plastic bending below 650 °C which meant the yield strength could not be calculated. As such, the yield strength is shown between 650-750 °C and the brittle fracture strength is shown between RT and 600 °C. The yield strength of the EP1 coating decreases between 650-750 °C and is higher than the C1 coating. The fracture strength increases with temperature between RT and 650 °C.

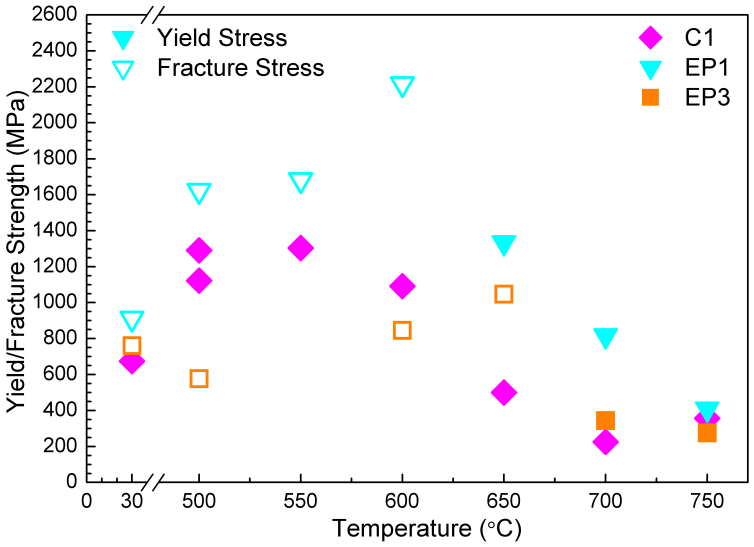

FIGURE 5.45: Yield and fracture strength as a function of temperature for coatings C1, EP1 and EP3. Solid and hollow symbols refer to yield and fracture strength respectively.

The yield strength of the EP1 coating is approximately 1300 MPa at 650 °C and decreases to 408 MPa at 750 °C. There is no data available for coatings which have the same composition as the EP1 coating, but Hesbur and Miner reported the yield strength of a LPPS Ni-20Co-17Cr-14Al-0.5Y to be 560 MPa at 600 °C (3 mm diameter uni-axial specimen) and Eskner et al.[39] reported the yield strength of an APS Ni-23Co-17Cr-12Al-0.5Y coating to be $\sim$ 500 MPa at $\geq$ 500 °C when measured by SPT tests.

The yield strength of the EP3 coating could only be measured at 700 and 750 °C. It shows similar yield strength to the C1 coating at both temperatures and exhibits a lower fracture strength than the EP3 coating between RT and 600 °C.

There is also no data on coatings with composition similar to the EP3 coating, which exhibited a yield strength of 344 and 275 MPa at 700 and 750 °C respectively. Taylor et al. [24] did demonstrate that the addition of Ta could improve the yield strength of MCrAlY coatings but that does not appear to be the case in this work.

The only available data on the fracture strength of MCrAlY coatings was published by Brodin et al. [40] for an APS Ni-23Co-17Cr-12Al-0.5Y coating. The crack initiation stress, determined by SPT tests, was reported as 860 MPa at RT.

It is clear that the absolute values for the yield and fracture strengths of the EP1 and EP3 coatings are not consistent with the literature, as was found for coating C1. However, the temperature dependence of the yield/fracture strength for the EP1 and EP3 coatings is consistent with the data reported by Hesbur and Miner [81] for a NiCoCrAlY coating, and the data for NiAl, shown in Fig.5.43. Therefore, it can be determined that the errors in the yield/fracture strengths are systematic and that the relative strengths of the C1, EP1 and EP3 coatings can be used to evaluate the influence of microstructure on the mechanical properties.

A summary of the calculated tensile properties is shown in table.5.6. The yield strength of the EP1 coating is higher than the C1 coating which suggests an increased phase fraction of β-NiAl phase increases the yield strength at high temperature. The EP3 coating contained γ'-Ni_3(Al,Ta) which can significantly increase the yield strength of γ-Ni alloy, as shown in Fig.5.42, but exhibited a lower yield strength compared to the EP1 coating. This suggests that the increase in yield strength from the γ'-phase was offset by either a reduction in the γ-phase, or an increase in the σ-Cr_2Co phase. Given the high temperature strength of γ/γ'-alloys shown in Fig.5.42, the lower yield strength was probably caused by an increase in the σ-phase.

The EP3 coating also exhibited a lower fracture strength than the EP1 coating between 500-650 °C, which is also probably due to an increase in the σ-Cr_2Co phase.

		Measured Values				**Calculated Values**		
	Temp. (°C)	F_e (N)	δ_e (mm)	F_m (N)	δ_m (mm)	σ_{YS} (MPa)	σ_{FS} (MPa)	ε^*
Coating C1	**RT**	-	-	237	0.181	-	2461	0.018
	500	120	0.06	-	-	1122	-	0.051
	500	108	0.04	-	-	1221	-	0.042
	550	127	0.10	-	-	1303	-	0.246
	600	107	0.07	-	-	1091	-	0.154
	650	50	0.04	-	-	500	-	0.382
	700	22	0.04	-	-	226	-	0.651
	750	35	0.06	-	-	357	-	0.562
Coating EP1	**RT**	-	-	89	0.07	-	912	0.007
	500	-	-	160	0.07	-	1623	0.007
	550	-	-	163	0.13	-	1682	0.013
	600	-	-	216	0.14	-	2216	0.014
	650	130	0.14	-	-	1334	-	0.311
	700	80	0.10	-	-	816	-	0.613
	750	40	0.06	-	-	408	-	0.737
Coating EP3	**RT**	-	-	76	0.03	-	761	0.003
	500	-	-	56	0.04	-	577	0.004
	600	-	-	81	0.11	-	845	0.011
	650	-	-	102	0.21	-	1047	0.024
	700	34	0.04	-	-	344	-	0.406
	750	27	0.09	-	-	275	-	0.704

TABLE 5.6: Material property data for the C1, EP1 and EP3 coatings. Measured values taken from load-displacement curves. Values calculated using equations outlined in section 5.2.

5.9.3 Macroscopic Fracture Patterns and Comparison with FE models

5.9.3.1 Low Temperature Fracture

The macroscopic fracture patterns of the three coatings show distinct characteristics above and below the ductile to brittle transition temperatures. The macroscopic fracture patterns observed for each coating at 500 °C are shown in Fig.5.46, alongside schematics indicating how the macroscopic fracture patterns developed.

At 500 °C, below the DBTT of all three coatings, cracking occurred in the centre of the tensile surface of the specimen. The cracking was indicated by load-drops in the load-displacement curves and for each coating occurred at low displacements. In Fig.5.46, the deformation of each specimen in the schematics is not to scale and is exaggerated in order to highlight that some, albeit very little, deformation occurred before any cracks formed.

For the C1 coating, an initial crack formed in the centre of the specimen. As the crack became larger, it caused the central region of the specimen to fracture into multiple fragments, which then plastically deformed away from the specimen. For the EP1 and EP3 coatings, this plastic deformation was not observed and the central fragments sheared away from the specimens. This is observable in Fig.5.46f for the EP3 coating and presumably also occurred for the EP1 coating.

When the central fragments detached from the EP1 and EP3 specimens, layers of coating also sheared away. This additional shearing probably occurred because the initial radial cracks propagated through the thickness of the specimen to a small distance, indicated by the dotted lines in Figs.5.46c and 5.46e for the EP1 and EP3 coatings respectively. This presumably caused lines of stress concentration along the radial crack paths. As the central fragments deformed normal to the specimen under the movement of the punch head, the stress concentration probably caused sub-surface cracks to spread through the horizontal plane of the specimen. Hence,

the depth of shearing i.e. the thickness of the central fragment, corresponds to the depth of the initial crack.

For the EP3 coating, the initial cracks propagated to the edge of the specimen. This is evidence that the magnitude of cracking was higher in the EP3 coating. As the γ-Ni phase is known to be a ductile phase, it can be assumed that during the SPT test the γ-phase plastically deforms and dissipates energy, whereas the β-NiAl phase remains elastic and stores energy. A higher phase fraction of β-phase results in a higher amount of stored energy during tensile loading and a larger release of energy during crack propagation. This is reflected in the macroscopic fracture patterns of the EP1 and EP3 coatings.

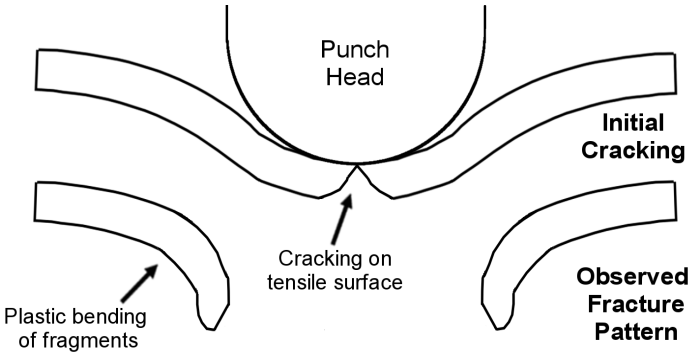

(a) Coating C1 (500 °C)

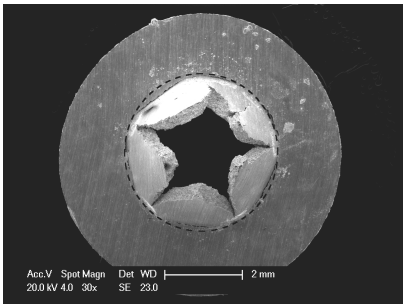

(b) Coating C1 (500 °C)

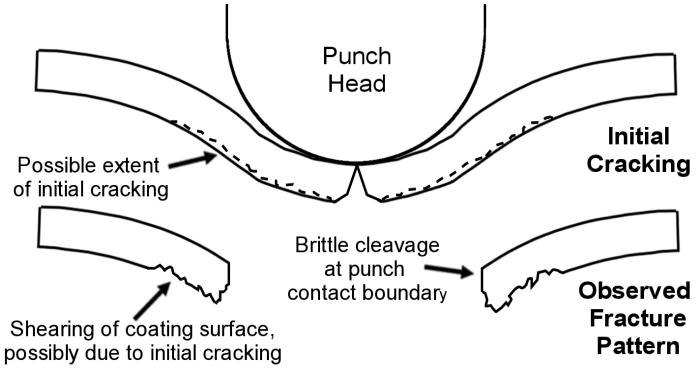

(c) Coating EP1 (500 °C)

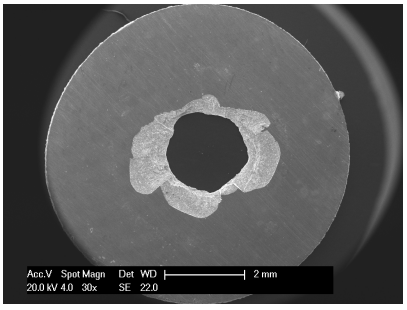

(d) Coating EP1 (500 °C)

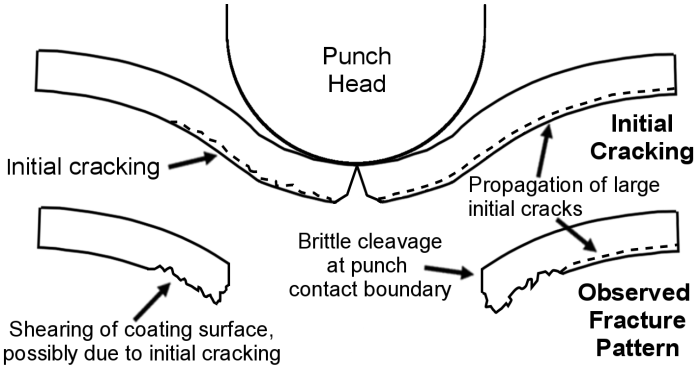

(e) Coating EP3 (500 °C)

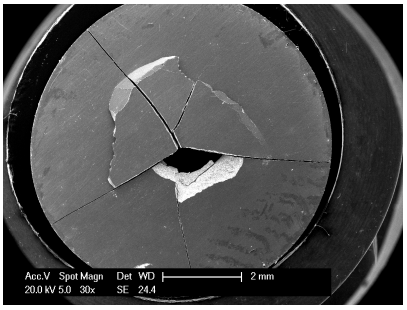

(f) Coating EP3 (500 °C)

FIGURE 5.46: Schematics showing the macroscopic fracture pattern development of the C1, EP1 and EP3 coatings during SPT tests at 500 °C (left) and SE images showing the tensile surfaces of corresponding C1, EP1 and EP3 specimens (right).

5.9.3.2 High Temperature Fracture and Comparison with Finite Element Models

The macroscopic fracture patterns observed at 700 °C for the C1 and EP1 coatings, and at 750 °C for the EP3 coating, are shown in Fig.5.47. The temperatures shown correspond to the temperatures at which the coatings exhibit ductile behaviour. The macroscopic fracture patterns of all three coatings are characterised by circumferential cracking at a radial offset in the area of the specimen in contact with the punch head. There are no major differences between the fracture patterns observed for the coatings which indicates the observed macroscopic fracture patterns are a feature of the SPT test rather than material dependent.

Experimental observations and finite element models of the SPT test [109, 113, 123, 124] have demonstrated that for ductile materials, specimen failure occurs in the area of maximum principle stress, which also corresponds to the location of the maximum thinning and plastic strain in the specimen. This area corresponds to the boundary of contact between the punch head and the specimen. Fig.5.47 shows the fracture patterns observed for the C1, EP1 and EP3 specimens at 700 and 750 °C alongside an FE model of a SPT specimen which illustrates the equivalent plastic strain induced in a specimen during a SPT test.

The axisymmetric FE model, developed by Abendroth and Kuna [124], modelled the upper and lower dies and punch head as rigid bodies and set the friction coefficient between the punch head and specimen as $\mu = 0.25$. In order to simulate plasticity, a continuum damage model was employed. The equivalent plastic strain shown in the model is a function of the damage predicted by the model. Areas of high equivalent plastic strain are shown as red and areas of low equivalent plastic strain shown as blue.

The FE model shows that the area of high equivalent plastic strain corresponds to the area of the specimen underneath the punch contact boundary, which corresponds to the fracture patterns observed for the C1, EP1 and EP3 specimens in Fig.5.47. The high temperature C1, EP1 and EP3 specimens also exhibited

thinning near to location of fracture. Other FE models have shown that thinning generally occurs in the area of high tensile stress [113, 123], which corresponds to the region of high tensile strain, and occurs when the material's strain hardening ability overcomes the reduction in thickness and allows material to sustain load at an increasing rate.

FE models [109] have also shown that at low displacements the punch contact area is limited to the centre of the specimen. As such, there is a region of high stress in the centre of the specimen which is where cracking is observed in the low temperature specimens, as shown in Fig.5.46.

The different FE models [109, 113, 123, 124] show that as the punch displacement increases and the punch contact area increases, the maximum principal tensile stress moves away from the centre into the intermediate region of the specimen. As such, fracture at low displacements is characterised by cracking in the centre of the specimen and fracture at high displacements is characterised by cracking at a radial offset, typically in the region of the specimen underneath the punch contact area. This type of fracture corresponds to the fracture patterns observed for the C1, EP1 and EP3 specimens in Figs.5.46 and 5.47.

5.9.4 Microscopic Fracture Behaviour

The available data on the tensile and fracture behaviour of MCrAlY alloys is limited; studies concerning MCrAlY alloys tend to focus on TBC systems and the spallation of the ceramic top coat or TGO, or fail to study the fracture of the MCrAlY bond coat in detail [8, 12, 149, 157–160].

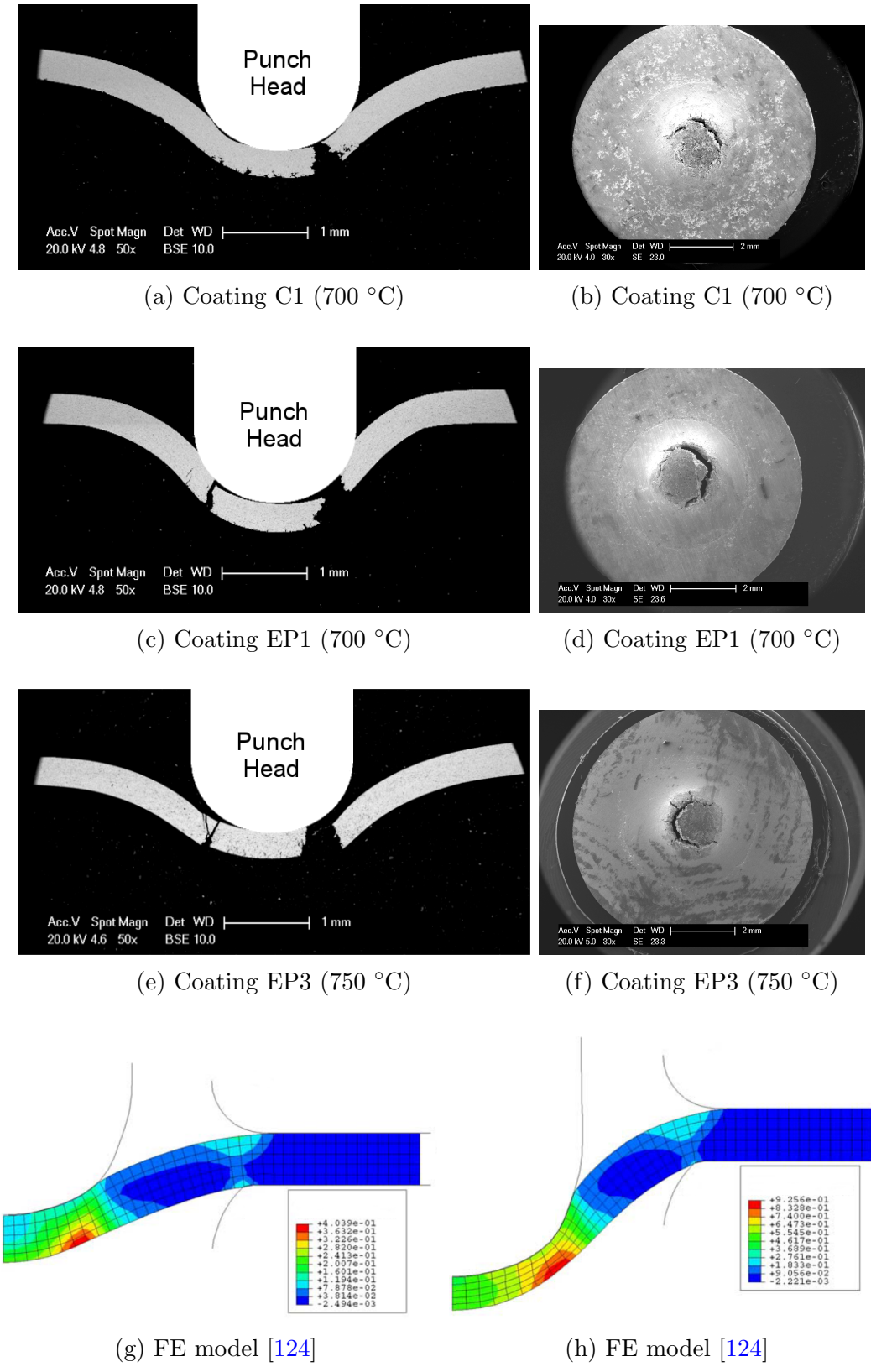

(a) Coating C1 (700 °C) (b) Coating C1 (700 °C)

(c) Coating EP1 (700 °C) (d) Coating EP1 (700 °C)

(e) Coating EP3 (750 °C) (f) Coating EP3 (750 °C)

(g) FE model [124] (h) FE model [124]

FIGURE 5.47: BSE images of cross sections of the C1, EP1 and EP3 coatings during SPT tests at 700 °C (C1 and EP1) and 750 °C (EP3) showing crack development and SE images showing the tensile surfaces of corresponding C1, EP1 and EP3 specimens. g-h) show an FE model showing equivalent plastic strain in a SPT specimen for a) medium displacements and b) at crack initiation. Figure reproduced from [124].

Previous work has attributed the fracture of MCrAlY coatings during tensile testing to oxide dispersions, both for a VPS coating [161] and an APS coating [40]. However, the C1, EP1 and EP3 coatings all exhibit low oxide content so a more detailed explanation is needed.

The C1 coating consists of a ductile matrix with brittle intermetallic precipitates, where as the EP1 and EP3 coatings consist of a brittle matrix and ductile precipitates. In order to simplify the discussion of the microscopic fracture behaviour, the C1 coating is discussed separately to the EP1 and EP3 coatings.

5.9.4.1 MCrAlY Coating With γ-Ni Phase Matrix

For the C1 coating, intergranular fracture along the β/γ phase boundaries was the main mode of crack propagation at both low and high temperature. This type of fracture probably occurred because the interfaces between the BCC β-phase and the FCC γ-phase are incoherent and exhibit low interfacial shear strength.

Shearing at the phase interfaces is a common type of fracture observed for metal matrix composites (MMC's). MMC's, such as dual-phase (DP) steels, typically consist of a ductile matrix phase inter-dispersed with hard precipitates, which can be considered similar to the C1 coating. Thus, a clearer understanding of the fracture mechanisms of the C1 coating can be gained by considering the fracture mechanisms of dual-phase steels.

DP steels typically consist of a soft ferrite phase and hard martensite phase [162–168]. During plastic deformation of a dual phase steel, yielding starts in the soft ferrite phase whereas the hard martensite phase remains elastic. The strain incompatibility at the phase boundaries causes a build up of local stress at the phase interface as well as internal stress in the martensite phase [162–165]. Once the internal stress surpasses the elastic limit of the martensite, it either begins to deform or fractures. The strain incompatibility also causes void formation at the ferrite/martensite interface due to shearing of the phase interface [163, 166–168].

If the γ-Ni and β-NiAl phases are considered to behave in a similar way to the ferrite and martensite, an explanation for the deformation behaviour of the C1 coating can be derived. For simplicity, the deformation is considered under uni-axial tensile loading. The β-phase is considered initially in the [100] slip plane i.e. the β-phase is a 'hard' underformable precipitate with high yield stress and low ductility at low temperature, but at high temperature is a 'soft' precipitate with low yield stress and high ductility.

A schematic showing the deformation of the β and γ-phases is shown in Fig.5.48. Under loading, the γ-Ni phase plastically deforms, which leads to a build up of local stress at the phase boundaries as well as internal stress in the β-phase. At low temperature, the stress at the phase boundary exceeds the interfacial shear stress before it exceeds the yield or fracture stress of the β-phase. In this instance, intergranular fracture occurs along the β/γ phase boundaries. This type of fracture has also been observed for Al metal matrix composites where cracks developed around particles due to debonding between the matrix and the reinforcement phase [110].

At high temperature, the yield strength of the β-phase is lower and the β-phase deforms. Voids and/or cracks still develop at the phase boundaries, but a higher amount of plastic deformation and thinning is achieved before intergranular fracture occurs.

As the orientation of the β-phase in the C1 coating is random, some grains of β-phase may be considered soft at low temperatures i.e. orientated in the [110] slip plane (see Fig.5.43a). In this instance the yield strength of the β-phase may be lower than the interfacial shear strength of the phase boundaries. This may result in deformation of the β-phase and transgranular fracture through the β-phase at low strains, approximately 1-2 % [70], as shown in Fig.5.49. Considering the yield strength of the γ and β-phases are different, and that the orientation of the β-phase is random, a combination of intergranular and transgranular fracture may occur. There was little evidence of transgranular fracture in the C1 coating which

suggests that in general, the yield strength of the β-phase exceeded the interfacial shear strength of the phase boundaries.

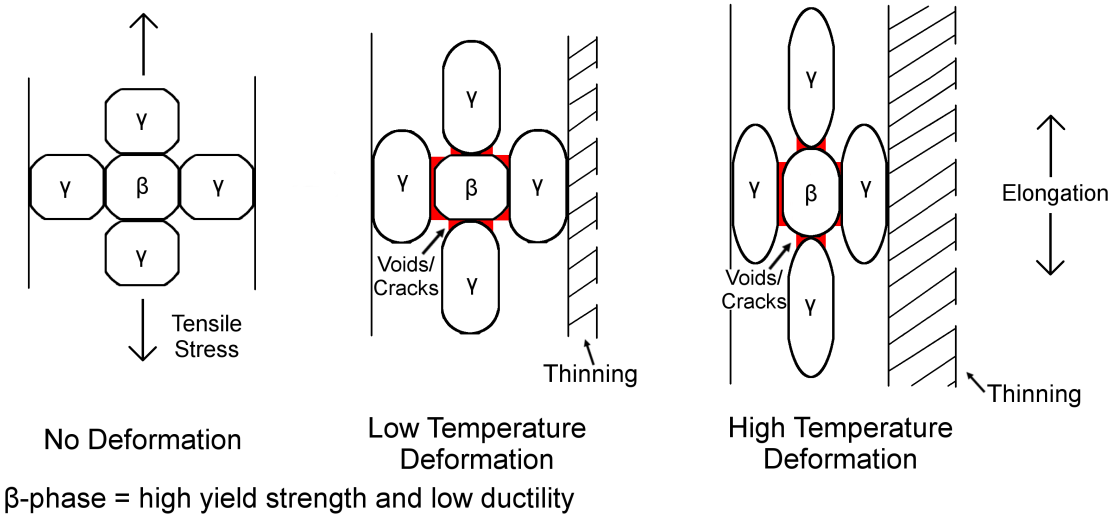

FIGURE 5.48: Schematic of void formation during a SPT test at low and high temperature where the β-NiAl phase can be considered a hard undeformable precipitate with high yield strength and low ductility.

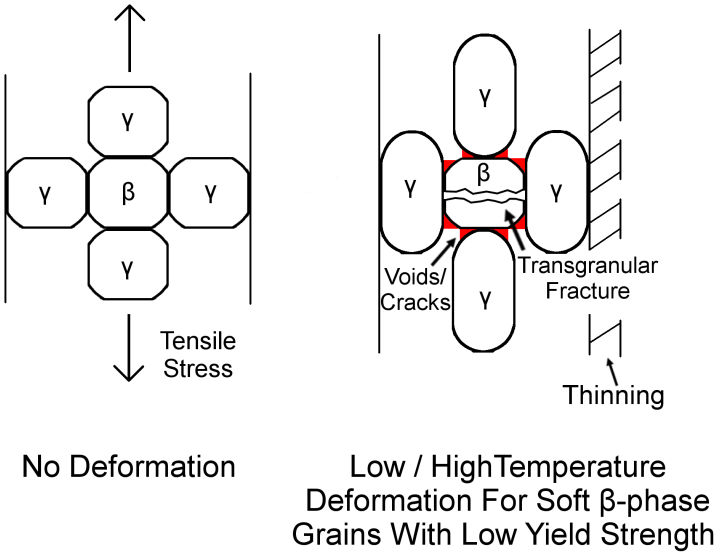

FIGURE 5.49: Schematic of void formation during a SPT test where the β-NiAl phase can be considered a soft phase with low yield strength and low ductility.

5.9.4.2 MCrAlY Coating With β-Phase Matrix

Intergranular fracture along the phase boundaries was the main mode of crack propagation in the EP1 and EP3 coatings. If the EP1 and EP3 coatings are

considered to behave similar to the C1 coating, then the intergranular fracture is also caused by strain incompatability between the phases.

As intergranular fracture is the dominant fracture mechanism, an increase in the number of phase boundaries will increase the density of cracking and decrease the strain to fracture. This is illustrated in Fig.5.50. Intergranular fracture was observed at the β/γ, β/σ and σ/γ phase boundaries for the EP1 and EP3 coatings and both coatings exhibited a lower strain to fracture.

The presence of γ'-phase did not appear to increase the density of crack formation in the EP3 coating, which can be attributed to the coherent interface between the γ and γ'-phases [6].

At high temperature, the increased ductility of the β-NiAl phase will increase the strain to fracture, as illustrated for the C1 coating in Fig.5.48. The σ-phase can be considered to act similar to a hard β-phase precipitate at both low and high temperature, and decreases the strain to fracture.

As the EP1 and EP3 coatings contain a higher phase fraction of β-phase, there is higher possibility of transgranular fracture as more grains of β-phase may be orientated in the [110] plane, which explains why more transgranular fracture was observed in the EP1 and EP3 coatings compared to the C1 coating. There was also transgranular fracture observed through the σ-phase which indicates the σ-phase has a low yield / fracture strength

5.9.5 Interpretation of SPT Test Load Displacement Curves

5.9.5.1 Coating C1

With an understanding of the temperature dependent tensile properties, as well as the macroscopic and microscopic deformation of the SPT test specimens, an interpretation of the load-displacement curves for each coating, as shown in Fig.5.51 can be derived.

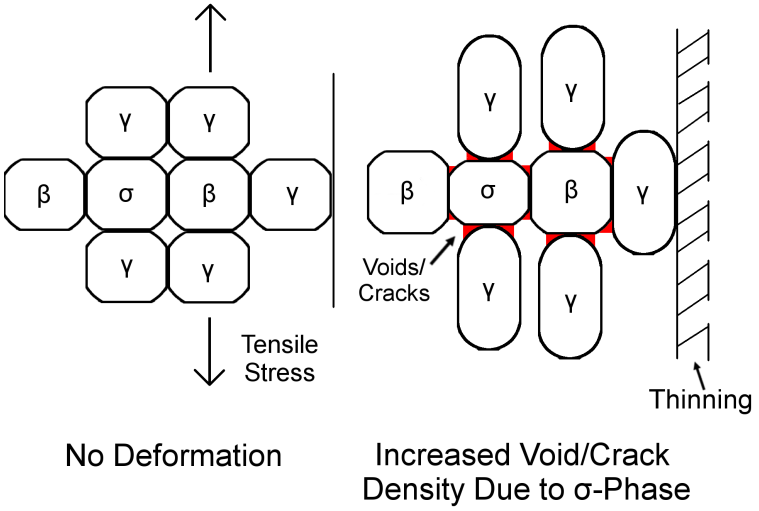

FIGURE 5.50: Schematic of void formation during a SPT test where the β-NiAl and σ-Cr_2Co phases can be considered hard undeformable phases. The increased phase boundaries due to the addition of σ-phase results in a higher density of voids and cracks.

The C1 coating contains 69:31 vol.% γ-Ni:β-NiAl phase and a DBTT of 500-700 °C. Under tensile loading below 500 °C, the γ-Ni phase plastically deformed whilst the β-NiAl remained elastic. This provided the C1 coating with a high resistance to bending and low strain to fracture. Between 500-700 °C, the yield strength of the γ-Ni and β-NiAl phases decreased with temperature, lowering the resistance to bending. The β-NiAl phase also started to exhibit a brittle to ductile transition, which increased the ductility of the β-NiAl phase and presumably reduced the strain incompatibility between the γ-Ni and β-NiAl phases, allowing higher strains to be achieved before specimen failure occurred.

The load at fracture between 500-700 °C for the C1 coating remained approximately constant. This can be attributed to a balance between the increasing strain to fracture and decreasing resistance to bending. The 650 and 700 °C results also exhibited strain hardening in the membrane stretching region which increased the load to fracture. At 750 °C the yield strength of both the γ-Ni and β-NiAl phases decreased further, which resulted in a lower resistance to bending and a lower fracture load.

5.9.5.2 Coating EP1

The EP1 coating contains 60:27:13 vol.% β:γ:σ phase. Below 600 °C the EP1 coating exhibited a high resistance to bending but a very low strain to fracture compared to the C1 coating, which can be attributed to the higher phase fraction of β-NiAl phase, as well as the addition of σ-Cr_2Co phase, which lowered the ductility of the coating.

The EP1 coating also exhibited lower fracture loads than the C1 coating below 600 °C. This is can also be attributed to the high phase fraction of β and σ-phase, which caused a high density of cracking at low strains, resulting in a low fracture load. The increased ductility of the β-NiAl phase between RT and 650 °C allowed higher fracture strains to be achieved, but only caused a small decrease in the resistance to bending, resulting in higher fracture loads.

5.9.5.3 Coating EP3

The EP3 coating contained 56:14:9:21 vol.% β:γ:γ':σ phase. The EP3 coating exhibited much lower fracture loads and fracture strains than the EP1 coating below 700 °C, probably because of the lower phase fraction of γ-phase and higher phase fraction of σ-Cr_2Co phase.

The fracture load of the EP3 coating increased with temperature between 650-750 °C, which can be attributed to the increased ductility of the β-NiAl phase.

It can be concluded that a high phase fraction of β-NiAl phase increases the resistance to bending and SPT test fracture load of an MCrAlY coating at 650 °C and above, but lowers the fracture strain and fracture load below 650 °C.

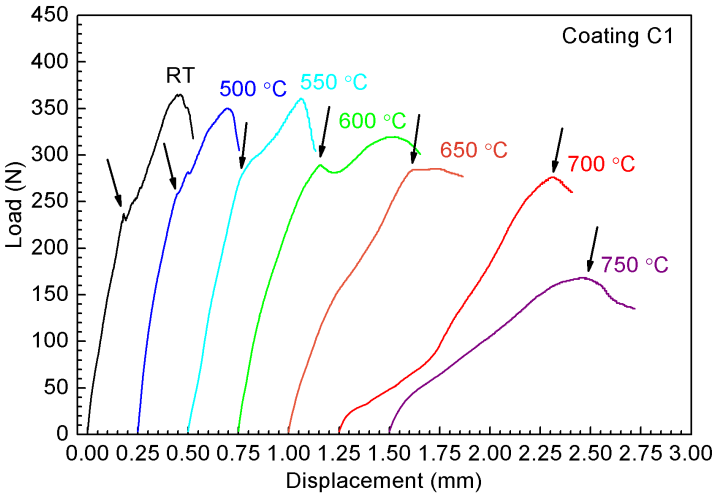

(a)

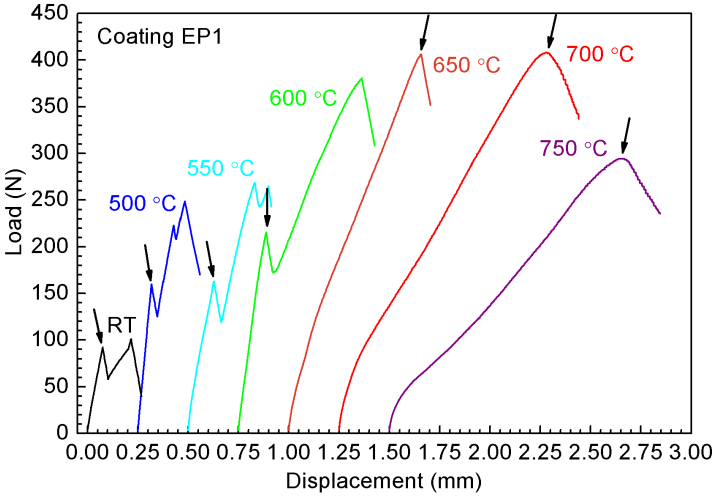

(b)

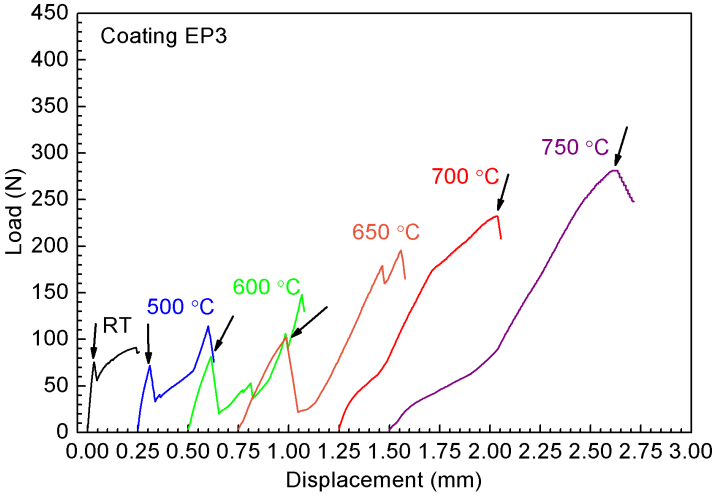

(c)

FIGURE 5.51: Representative load-displacement curves obtained for heat treated C1, EP1 and EP3 coatings at a constant displacement rate of 1 µm s^{-1} between RT and 750 °C. Curves are shifted on the x axis to avoid overlapping of the curves.

Chapter 6

Small Punch Creep Testing of MCrAlY Bond Coats

6.1 Introduction

The high temperature creep behaviour of free-standing coatings manufactured from the C1, EP1 and EP3 alloys was investigated by small punch creep (SPC) testing. The SPC tests were conducted on two different small punch rigs. A full description of each rig is provided in chapter 3, but the main difference between the rigs is that rig 1 uses static weights to apply a constant load to the SPC specimen, whereas rig 2 is installed on a Tinius Olsen single column testing machine and uses a 2.5 kN load cell. SPC tests were conducted on rig 1 and rig 2 at 750 °C for the C1, EP1 and EP3 coatings and on rig 2 at 850 °C for the C1 and EP1 coatings. No tests were conducted on coating EP3 at 850 °C due to the time limitation of the current work.

The creep behaviour of each alloy was quantified with respect to the Norton power law, Monkman-Grant relationship and the creep rupture power law. The microstructure of each coating following SPC testing was investigated by SEM with EDX analysis.

6.2 Data Analysis

In a SPC test, the load and displacement are recorded and can be used to calculate values for the equivalent uni-axial stress and equivalent uni-axial strain. The load was converted to equivalent uni-axial stress (σ_e) using the following equation provided by the CEN workshop agreement[101]:

$$\frac{F}{\sigma_e} = 3.33 K_{sp}\, a_p^{-0.2}\, R_s^{1.2}\, t_0 \tag{6.1}$$

where a_p, R_s and t_0 are the radius of the receiving hole, punch head radius and specimen thickness (m). F is the load (N) and K_sp is a non-dimensional correction factor used to correlate SPC work with traditional uni-axial testing. K_sp is reported in the CEN workshop agreement [101] to be between 1.2∼1.3 but has also been reported as 0.6-0.8 for single crystal CMSX-4 [169]. K_sp is taken to be 1 in this work in line with the CEN workshop recommendations for materials where uni-axial test data does not exist.

The displacement δ was converted to equivalent uni-axial strain (ε) using the solution provided by Li et al. [130]:

$$\varepsilon = 0.20465\delta + 0.12026\delta^2 + 0.00950\delta^3 \tag{6.2}$$

The minimum steady-state strain rate ($\dot{\varepsilon}_{min}$) was calculated by dividing the SPC test time by 5 and calculating the average strain-rate over 1/5th of the SPC displacement-time curve. The upper and lower bounds of the 1/5th time interval were incrementally increased by 300 s (0.08 hours) and the lowest average strain-rate over all time periods taken as $\dot{\varepsilon}_{min}$. This method, referred to as a 1/5th moving average, reduces the influence of fluctuations in the SPC curve on the minimum steady-state strain rate.

6.2.1 Power Law Relationships

The SPC behaviour observed in the displacement-time curves can be characterised with respect to the minimum steady-state strain rate ($\dot{\varepsilon}_{min}$), the time to failure (t_f) and the equivalent uni-axial stress (σ_e).

Linear relationships between the equivalent uni-axial stress, the equivalent uni-axial minimum steady-state strain rate and the time to failure can be used to obtain material property parameters for the Norton power law, Monkman-Grant strain relationship and the creep rupture power law. These parameters are used to describe the material creep behaviour at 750 and 850 °C.

Norton power law:

$$\dot{\varepsilon}_{min} = B\,{\sigma_e}^n \tag{6.3}$$

Monkman-Grant strain relationship:

$$t_f = K_1\,{\dot{\varepsilon}_{min}}^{-m} \tag{6.4}$$

Creep rupture power law:

$$t_f = \frac{1}{M\,{\sigma_e}^{\chi}} \tag{6.5}$$

where B ($s^{-1}MPa^{-n}$), n, K_1 (h s^m), m, χ and M ($h^{-1}MPa^{-\chi}$) are temperature dependent constants.

6.3 Results of SPC Tests at 750 °C

6.3.1 Displacement-Time Curves

SPC tests were carried out on the C1, EP1 and EP3 coatings at 750 °C under equivalent uni-axial stresses between 46-80 MPa. Tests on rig 1 were conducted at 750 °C for the C1, EP1 and EP3 coatings. Tests on rig 2 were conducted at 750 °C for the C1 and EP1 coatings. No tests were conducted on rig 2 for the EP3 coating. Rig 2 was designed as part of this project, as described in appendix A, whereas rig 1 has been used in previous work [63, 132]

The displacement-time curves obtained for the C1, EP1 and EP3 coatings at 750 °C are shown in Figs.6.1 and 6.2 respectively. Breaks have been applied to some axis in order to accommodate the extended loading time of some tests.

The displacement-time curves obtained for all three coatings exhibit a primary region consisting of a large initial deformation followed by a reduction in the displacement rate, a secondary steady-state region where the displacement rate is approximately constant, and a tertiary region where the displacement rate accelerates leading to failure. Some curves do not show a tertiary region because the test was terminated before the tertiary stage was reached.

The displacement-time curves of all three coatings show a general trend where increasing the load increases the slope of the secondary steady-state region and decreases the time to failure. This is in agreement with previous studies concerning SPC testing of the C1 alloy [29, 63]. There are some exceptions to this behaviour. The C1 specimen tested at 58 MPa test, shown in Fig.6.1d, has a lower displacement rate than the C1 specimen tested at 55 MPa, and the EP1 specimen tested at 59 MPa, shown in Fig.6.2a, has a higher displacement rate than the EP1 specimen tested at 65 MPa. Although these examples do not correspond exactly to the general trend, they are still within the acceptable band of error, as is shown in section 6.3.2.

Overall the displacement-time curves show that the C1, EP1 and EP3 coatings all exhibit typical creep behaviour at 750 °C on both rig 1 and rig 2.

The SPC displacement-time curves exhibit a similar shape to conventional uni-axial creep curves. However, the secondary steady-state region in the SPC curves does not represent steady-state creep as it does in uni-axial creep tests [90]. After the large initial displacement, the SPC specimen undergoes stiffening effects due to the reducing cone angle at the center of the specimen and the increasing contact area between the specimen and the punch head. At the same time the specimen also undergoes accelerating effects due to thinning of the specimen in the punch contact region as well as the material entering the tertiary creep region. The result of this is that the minimum steady-state displacement rate is typically found just prior to the tertiary creep region.

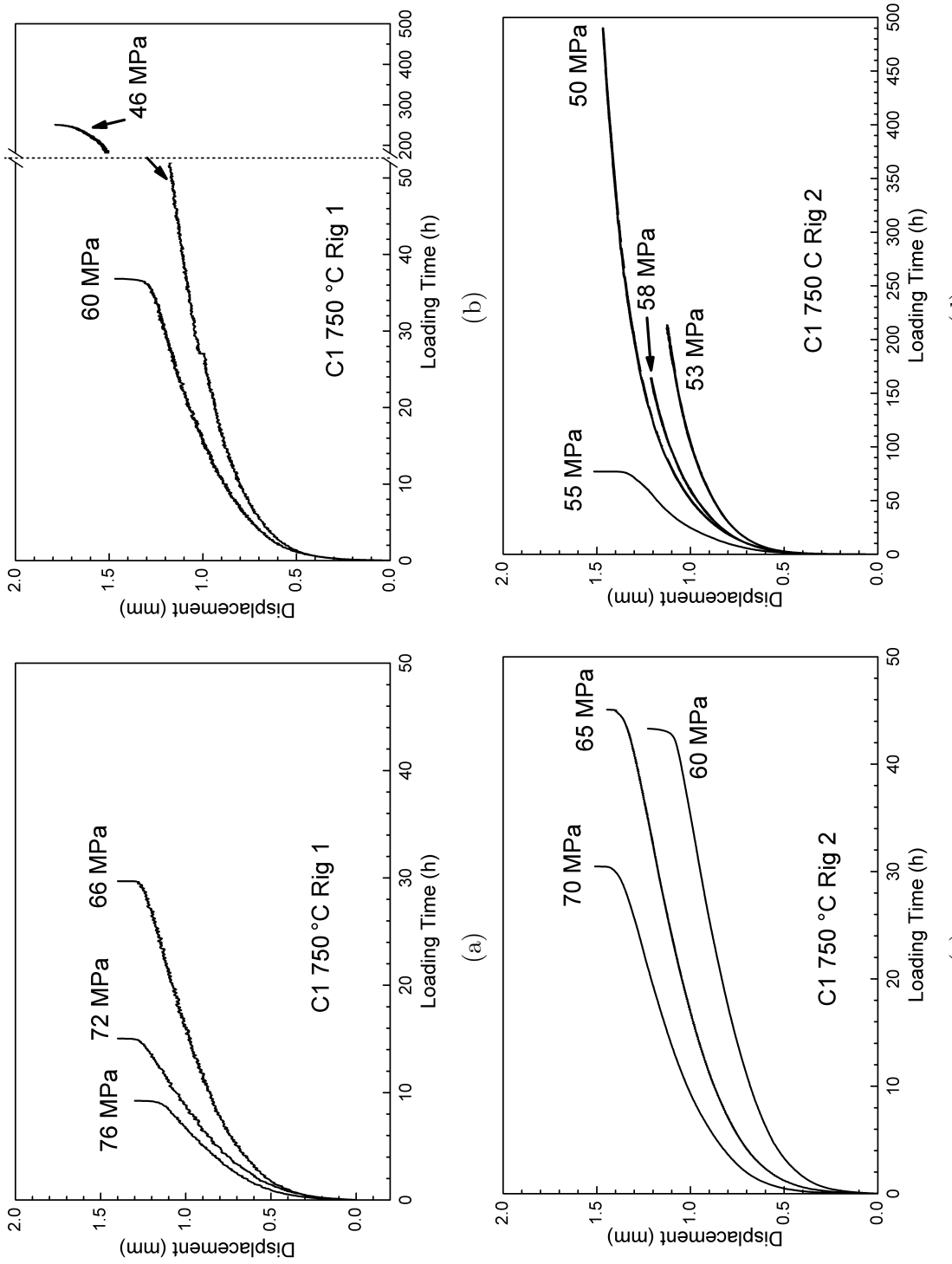

FIGURE 6.1: Displacement-time curves of coating C1 obtained through small punch creep testing at 750 °C on rig 1 and rig 2. The C1 coating shows typical creep behaviour on both rigs at 750 °C. In general, increasing the load increases the displacement rate and decreases the time to failure.

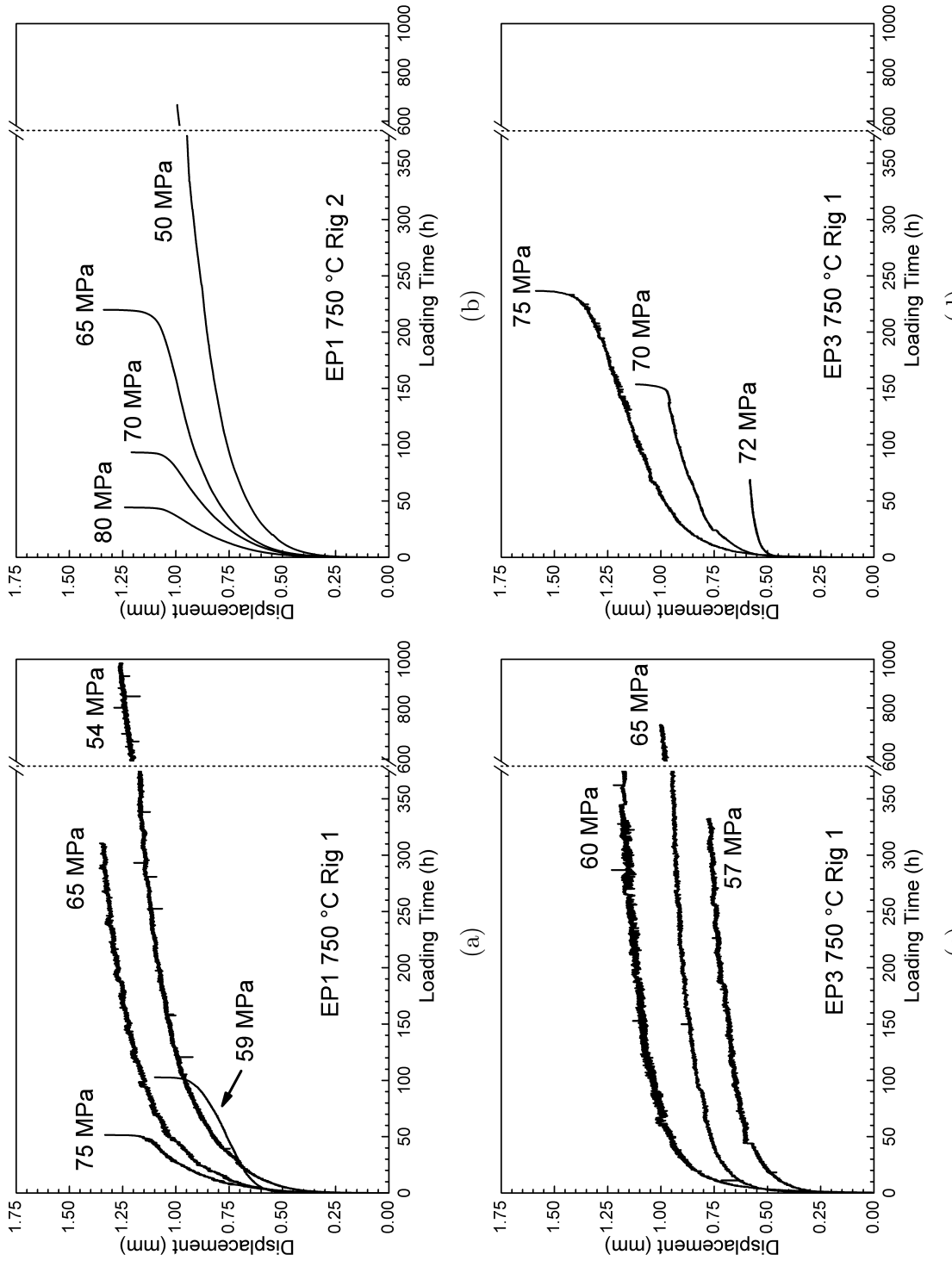

FIGURE 6.2: Displacement-time curves of coating EP1 (a-b) and coating EP3 (c-d) obtained through small punch creep testing at 750 °C on rig 1 and rig 2 for coating EP1 and rig 1 for coating EP3. The EP1 coating shows typical creep behaviour on both rigs at 750 °C and coating EP3 also shows typical creep behaviour on rig 1. In general, increasing the load increases the displacement rate and decreases the time to failure.

6.3.2 Material Creep Parameters and Power Law Relationships

The SPC behaviour observed in the displacement-time curves can be characterised with respect to the minimum steady-state strain rate ($\dot{\varepsilon}_{min}$) (s^{-1}), the time to failure (t_f)(h) and the equivalent uni-axial stress (σ_e)(MPa). Plots of minimum steady-state strain rate vs equivalent uni-axial stress, minimum steady-state strain rate vs time to failure, and equivalent uni-axial stress vs time to failure are shown in Figs.6.3, 6.4 and 6.5 respectively. Where applicable, the results obtained on rig 1 and rig 2 are plotted as separate data sets with a single trend line drawn between them. A value of R^2 (the correlation coefficient) is provided for each trend line where the single most outlying data point was removed from the calculation.

The trend lines are used to calculate parameters for the Norton steady-state power law (Eq.6.3), the Monkman-Grant relationship (Eq.6.4) and the creep rupture power law (Eq.6.5) respectively. The calculated material parameters are summarised in table 6.1.

An asterisk is used to indicate tests which were terminated prior to failure. As the minimum steady-state strain rate is found just before the tertiary creep region, the terminated tests possibly give an artificially high minimum steady-state strain rate. However, in this study it was found that the change in the minimum steady-state strain rate throughout the secondary steady-state region was small, approximately 2×10^{-1} s^{-1}. Therefore, the terminated tests exhibit a strain rate which is a good approximation to the minimum steady-state strain rate.

6.3.2.1 Coating C1

Fig.6.3a shows a plot of minimum steady-state strain rate as a function of equivalent uni-axial stress for the C1 coating at 750 °C. Higher values of $\dot{\varepsilon}_{min}$ are observed at higher stresses. There is also good consistency across rigs 1 and 2 ($R^2 = 0.93$). The Norton power law parameters for the C1 coating at 750 °C are $B = 5.2 \times 10^{-20}$ $s^{-1}MPa^{-n}$ and $n = 7.5$.

Fig.6.3b shows plots of $\dot{\varepsilon}_{min}$ vs time to failure. The time to failure increases as $\dot{\varepsilon}_{min}$ decreases. The data sets for both rigs are highly consistent and there is also a high consistency between the two rigs. The Monkman-Grant relationship parameters are $K_1 = 0.0002$ hs^m and m = 0.92 for the C1 coating at 750 °C.

The time to failure is shown as a function of equivalent uni-axial stress in Fig.6.3c. The time to failure increases as the stress decreases. There is good consistency between the data sets but less so than in Fig.6.3b. The creep rupture power law parameters are $M = 9.4 \times 10^{-13}$ h^{-1}MPa$^{-\chi}$ and $\chi = 5.9$ for the C1 coating at 750 °C.

6.3.2.2 Coating EP1

The creep behaviour of the EP1 coating at 750 °C, shown in Fig.6.4, exhibited similar characteristics to the C1 coating: $\dot{\varepsilon}_{min}$ increases as the stress is increased; the time to failure increases as $\dot{\varepsilon}_{min}$ decreases; and the time to failure increases as the stress is increased. There is good consistency between the data sets obtained on rigs 1 and 2.

The Norton power law parameters for the EP1 coating at 750 °C are $B = 2.2 \times 10^{-21}$ s^{-1}MPa^{-n} and n = 7.8, the Monkman-Grant relationship parameters are and $K_1 = 0.0003$ hs^m and m = 0.87 and the creep rupture power law parameters are $M = 2.6 \times 10^{-17}$ h^{-1}MPa$^{-\chi}$ and $\chi = 7.9$.

6.3.2.3 Coating EP3

The creep behaviour of the EP3 coating is shown in Fig.6.5. The minimum steady-state strain rate increases as the equivalent uni-axial stress increases. The EP3 coating exhibited low strain rates and only two specimens were tested to failure. The failed specimens were tested at 70 and 75 MPa, at higher stresses the EP3 specimens failed very suddenly and cracking was observed on the surface of some specimens. At lower stresses no failure was observed. Estimated times to failure were calculated by extrapolating the EP1 data and the times to failure

were in excess of 1000 hours for each test, which was not feasible in the time frame of this study.

The Norton power law parameters for the EP3 coating at 750 °C are B = 1.7×10^{-24} $s^{-1}MPa^{-n}$ and n = 9.1. No parameters were calculated for the Monkman-Grant relationship or creep rupture power law.

	Norton Power Law		Rupture Power Law		Monkman-Grant Relationship	
	B *	n	M $^\diamond$	χ	K_1 $^\triangleleft$	m
C1	5.2×10^{-20}	7.5	9.4×10^{-13}	5.9	0.0002	0.92
EP1	2.2×10^{-21}	7.8	2.6×10^{-17}	7.9	0.0003	0.87
EP3	1.7×10^{-24}	9.1	-	-	-	-

TABLE 6.1: Parameters for the Norton power law, creep rupture power law and modified Monkman-Grant relationship for the C1, EP1 and EP3 coatings at 750 °C as determined by small punch creep testing. Symbols refer to units where $\star = s^{-1}MPa^{-n}$, $\diamond = h^{-1}MPa^{-\chi}$ and $\triangleleft = h\ s^m$.

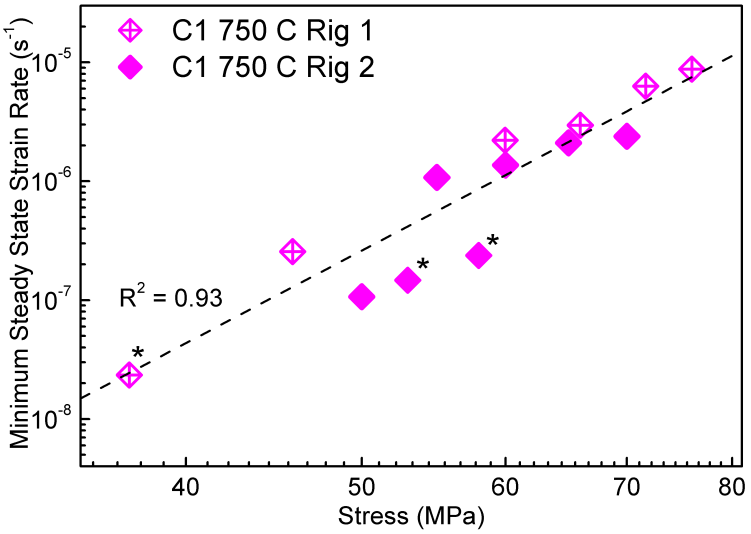

(a)

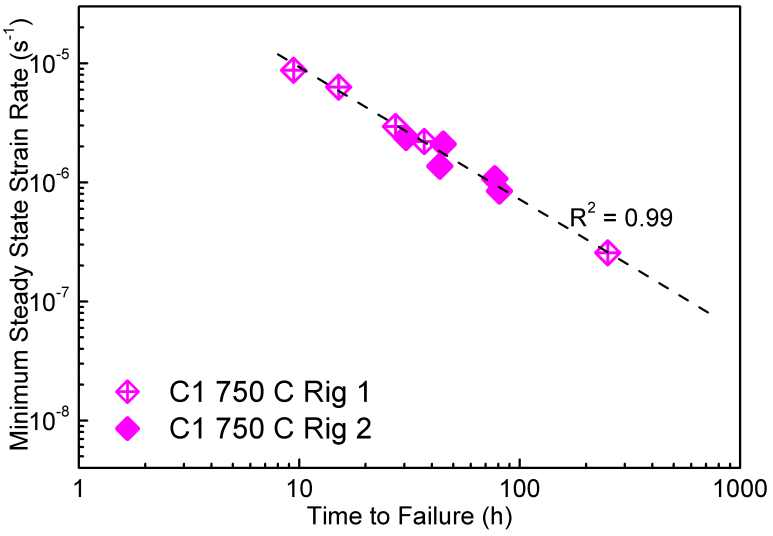

(b)

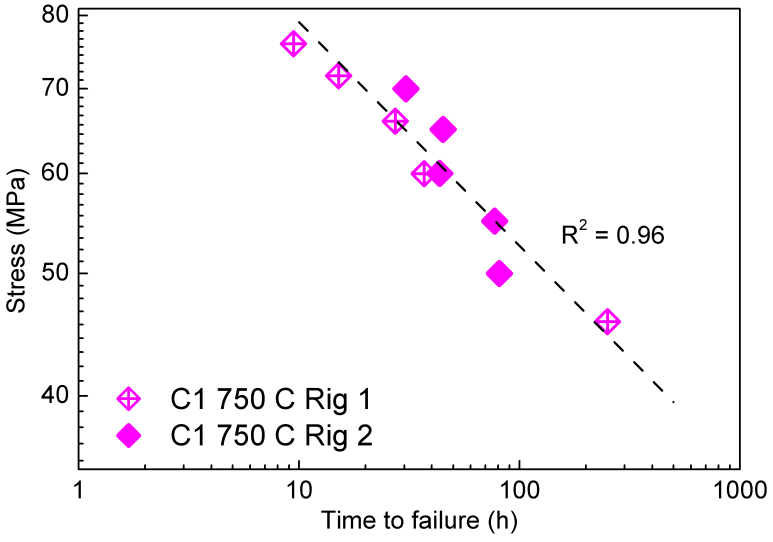

(c)

FIGURE 6.3: Creep behaviour of coating C1 at 750 °C where a) shows minimum steady-state strain rate vs equivalent uni-axial stress, b) shows minimum steady-state strain rate vs time to failure and c) shows equivalent uni-axial stress vs time to failure where all graphs are plotted logarithmic scales. Asterisks indicate tests which were terminated prior to failure.

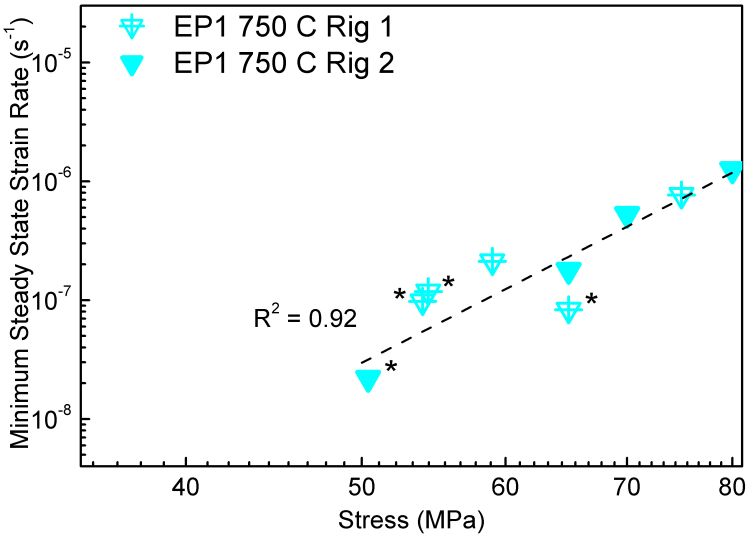

(a)

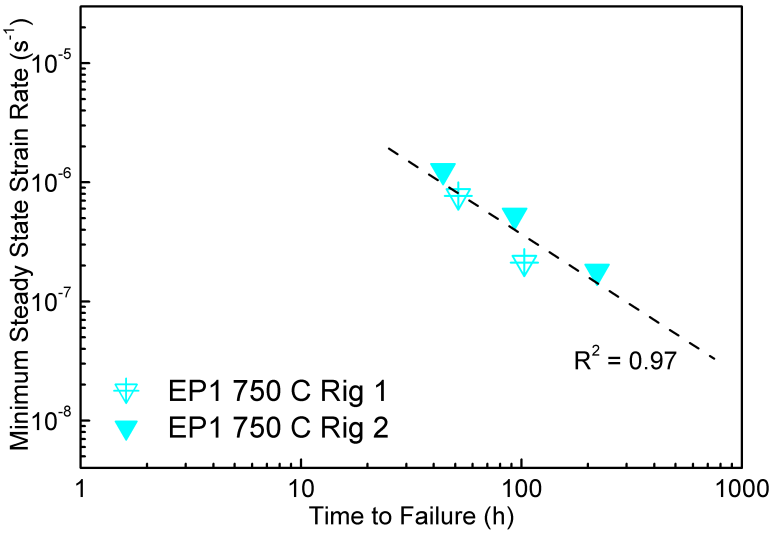

(b)

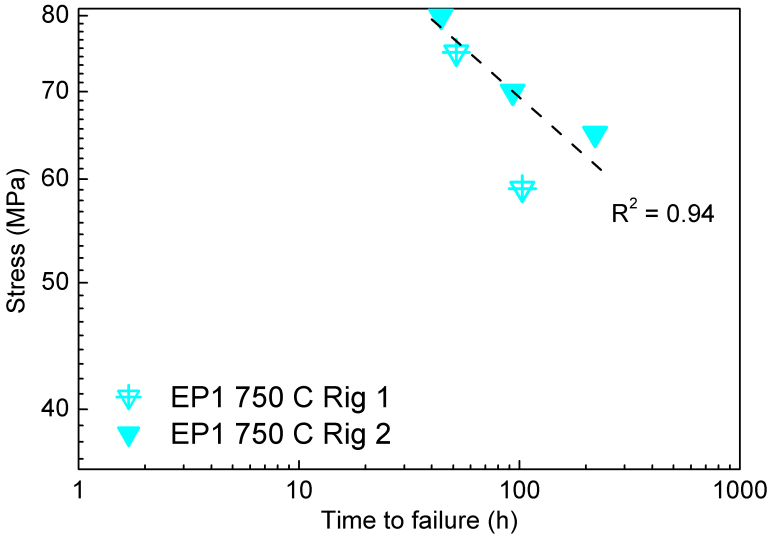

(c)

FIGURE 6.4: Creep behaviour of coating EP1 at 750 °C where a) shows minimum steady-state strain rate vs equivalent uni-axial stress, b) shows minimum steady-state strain rate vs time to failure and c) shows equivalent uni-axial stress vs time to failure where all graphs are plotted logarithmic scales. Asterisks indicate tests which were terminated prior to failure.

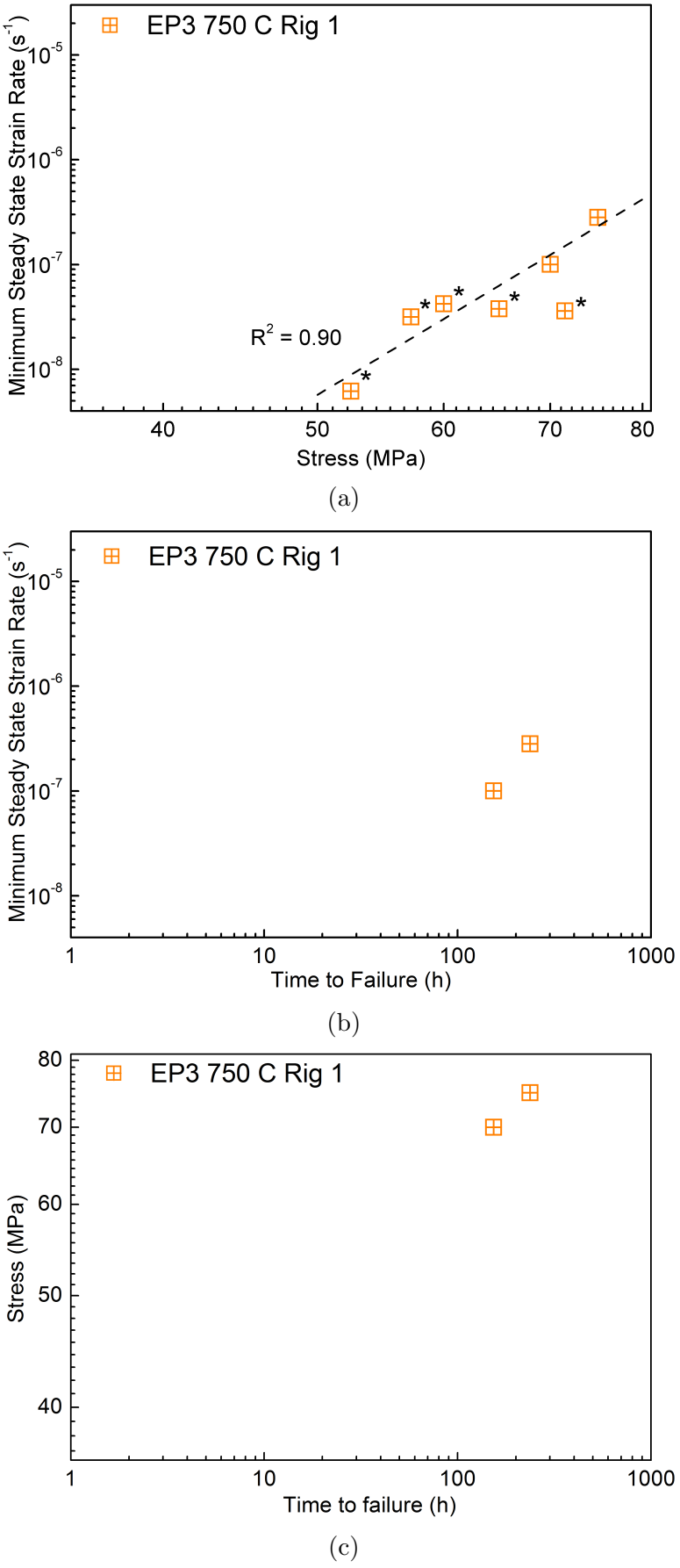

FIGURE 6.5: Creep behaviour of coating EP3 at 750 °C where a) shows minimum steady-state strain rate vs equivalent uni-axial stress, b) shows minimum steady-state strain rate vs time to failure and c) shows equivalent uni-axial stress vs time to failure where all graphs are plotted logarithmic scales. Asterisks indicate tests which were terminated prior to failure.

6.4 SPC Specimen Deformation at 750 °C

In this section the SPC deformation behaviour of the C1, EP1 and EP3 coatings at 750 °C is presented. Two examples are provided for each coating; a low minimum steady-state strain rate specimen which was terminated prior to failure, and a high minimum steady-state strain rate specimen which failed. BSE images of each sample are presented. For each specimen the clamping boundary is indicated by the letter A.

6.4.1 Coating C1

As reported in section 4.3 coating C1 is a dual phase material with 69 vol.% FCC γ-Ni phase and 31 vol.% BCC β-NiAl phase.

6.4.1.1 Low Minimum Steady-State Strain Rate

The C1 specimen tested at 50 MPa and 750 °C was tested for 500 hours but did not fail. A cross section of the specimen is shown in Fig.6.7 where the boxes indicate the area shown at higher magnification in the subsequent image. The shape of the tested specimen is similar to that previously reported for SPC specimens [63, 87–89, 135] and corresponds to the centre of the specimen deforming into a conical shape by stretching around the hemispherical punch head.

Fig.6.7b shows an area of the specimen near to the contact boundary between the punch and the specimen (referred to as the punch contact boundary), which exhibits thinning and a high density of black features. This area corresponds to the region of high tensile stress in a SPC specimen during a SPC test [92, 131–134]. The black features accumulate in bands along the direction of the tensile stress, as indicated by B, and normal to the direction of the tensile stress (through the thickness of the specimen), as indicated by C. The through-thickness black features are more clearly identified by D in Fig.6.7c.

The black features are shown at higher magnification in Fig.6.7d. An EDX chemical map of the same area is shown in Fig.6.6. The EDX map shows that the black feature indicated by E is an Al_2O_3 oxide. The oxide probably formed because of the diffusion of O through the interlinked voids which form under creep deformation. A small amount of oxide is also detected in the region indicated by F, where the black features are thinner. The black features in this region are probably thinner oxides which have developed within smaller voids. Therefore, the black features can be regarded as oxides, which indicate where voids formed under creep.

The black oxide band, indicated by the letter E, formed at the phase boundary between the γ-Ni and β-NiAl phases, which indicates void formation at the phase boundaries. This type of void formation is also apparent in the region indicated by F, as regions of dark contrast β-NiAl phase can be identified within the thin black features. There are small areas of grey contrast phase surrounding the regions β-phase, which is probably where small amounts of β-phase depletion occurred due to a flux of Al towards the voids. The letter G indicates void formation within a region of γ-Ni phase, which is also apparent in the region indicated by F. The letter H indicates a very small black feature, which is probably a finely dispersed oxide stringer that was retained in the coating after HVOF thermal spraying.

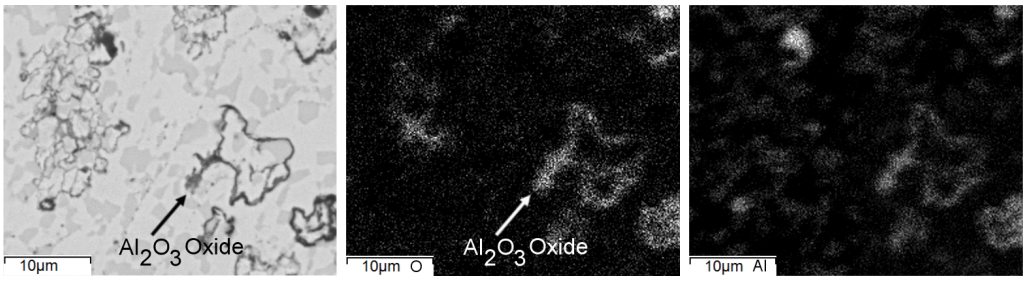

(a) (b) (c)

FIGURE 6.6: BSE image and EDX maps of the cross section of the C1 coating following SPC testing at 750 °C showing the formation of Al_2O_3 oxide in the vicinity of voids.

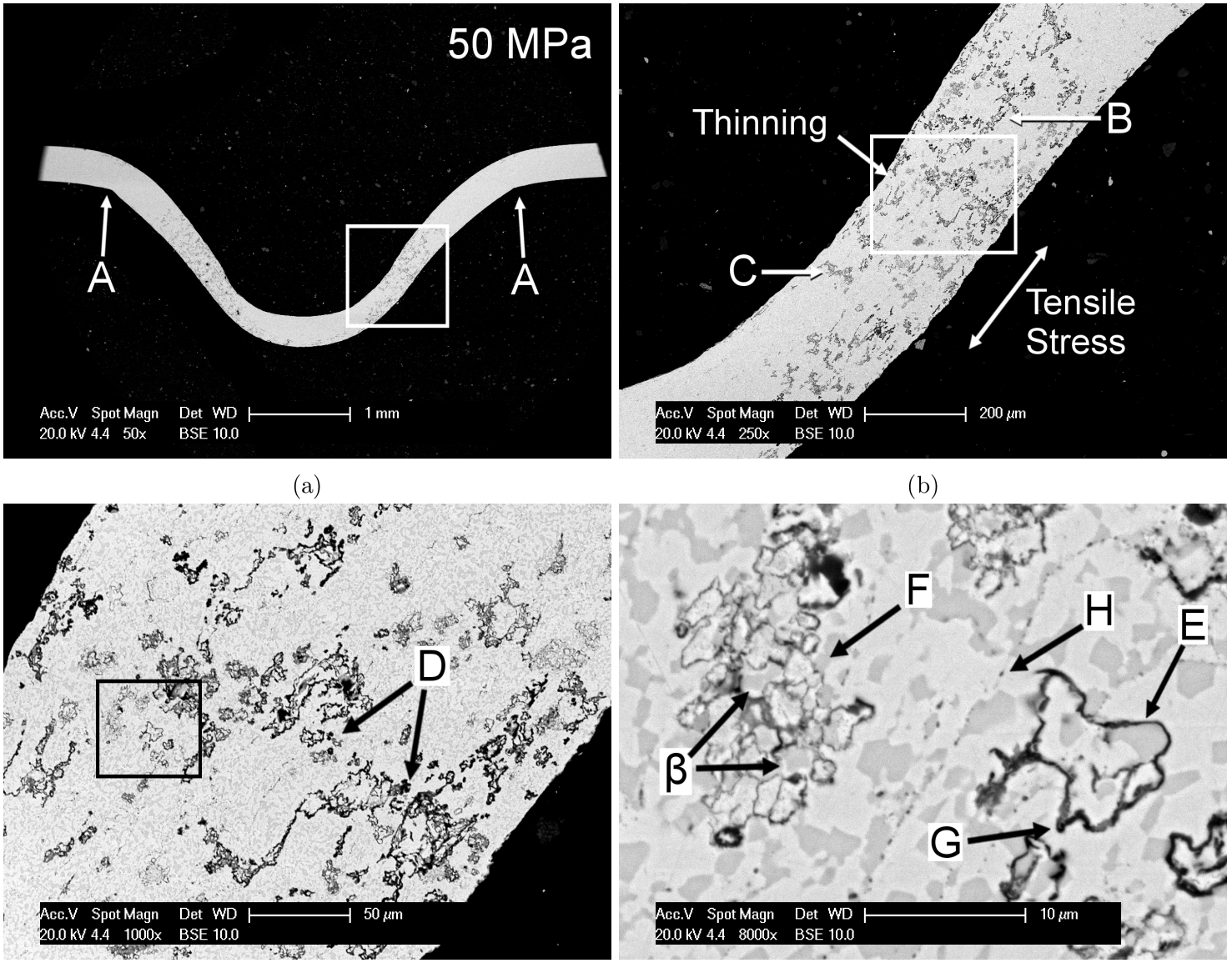

FIGURE 6.7: BSE images of a cross section of the C1 coating following SPC testing at 750 °C and 50 MPa. The specimen was tested for 500 hours but did not fail.

6.4.1.2 High Minimum Steady-State Strain Rate

Fig.6.8 shows a cross section of the C1 specimen tested at 72 MPa and 750 °C where the boxes indicate the area shown at higher magnification in the subsequent image. The specimen failed after 15 hours. The centre of the specimen detached during the SPC test due to a through-thickness circumferential crack which propagated at a radial offset from the centre of the specimen in the area of high tensile stress. The straight edges of the specimen near to B are the result of the punch head plastically deforming the specimen as it continued to move through the specimen after failure had occurred.

Near to the point of fracture there is a large amount of thinning and a higher density of oxides and cracks compared to the rest of the specimen. There are long thin cracks which have formed parallel to the direction of tensile stress, as indicated by C in Fig.6.8b, as well as larger, more rounded cracks, indicated by D, and cracks growing through the thickness of the specimen, as indicated by E.

Fig.6.8d shows the specimen at high magnification. The oxides indicated by F appear to have formed within the β-phase regions. The oxides probably grew in the place of the β-phase regions when the β-phase depleted because of the flux of Al to the Al_2O_3 oxide. The cracks presumably then developed at the interface between the brittle Al_2O_3 oxide and ductile γ-Ni phase during creep.

The letter G indicates where an oxide has grown at the γ/β phase boundary, which indicates void formation at the phase boundaries, similar to the low strain-rate specimen. There are also small oxides that were retained in the coating after HVOF spraying, such as the one indicated by H. It is possible that voids formed at the interface of these small oxides during creep, which then lead to additional oxide growth and cracking within the coating.

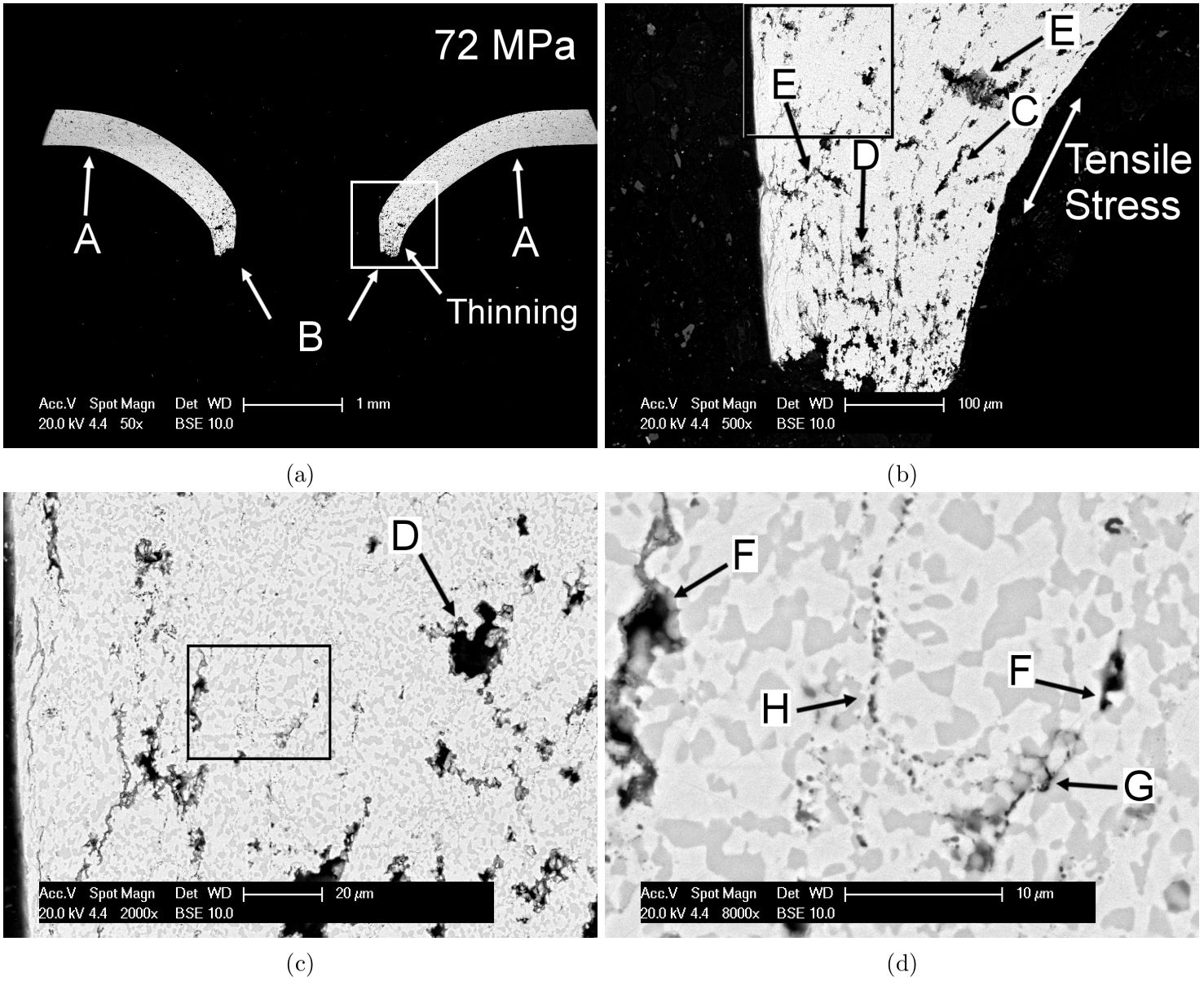

FIGURE 6.8: Cross section of the C1 coating following SPC testing at 750 °C and 72 MPa. The specimen failed after 15 hours.

6.4.2 Coating EP1

Coating EP1 is a three phase coating with approximately 27 vol.% FCC γ-Ni phase, 60 vol.% BCC β-NiAl phase and 13 vol.% TCP σ-Cr_2Co phase.

6.4.2.1 Low Minimum Steady-State Strain Rate

The EP1 specimen tested at 65 MPa and 750 °C was tested for 310 hours but did not fail. A cross section of the specimen is shown in Fig.6.9 where the boxes indicate the area shown at higher magnification in the subsequent image. The overall shape of the tested specimen is similar to that observed for the C1 coating.

The area of the specimen near to the punch contact boundary exhibits thinning and a high density of black features, as shown in Fig.6.9b. The smaller black features are probably oxides, which indicate where void formation occurred during the SPC test, and the larger black features are probably cracks. The oxides mainly accumulate in bands parallel to the direction of the tensile stress, as indicated by B. The letter C indicates where the oxides appear to have formed in a band normal to the direction of the tensile stress, but there is only a few examples of this. There is a large crack which has developed on the compressive surface of the specimen, indicated by D, as well as large cracks which have developed within the specimen, as indicated by E.

The oxides are shown at higher magnification in Fig.6.9d. EDX maps of the same area are shown in Fig.6.10. In the EDX chemical maps, the β-NiAl phase can be identified by high levels of Ni and Al, and low levels of Cr. The σ-Cr_2Co phase can be identified by high levels of Cr and low levels of Ni, and the γ-Ni phase identified by medium levels of Cr and Co and low levels of Al.

The EDX maps show that the oxides are mainly Al_2O_3, but do not detect large amounts of O in the thinner black features. This is probably because the EDX measurements are the average composition of an interaction volume and are influenced by the beam spreading effect, meaning the resolution of the measurement was not high enough to measure a high concentration of O in the

thinner black features. Nevertheless, the thinner black features can be regarded as oxides which have started to grow where void formation has occurred. The letter F indicates void formation at the β/σ phase boundaries which appears to be the most common type of void formation in the EP1 coating.

There are multiple regions of light contrast phase, such as the ones indicated by G, which contain a high level of Ni and low level of Cr, which separates them from the γ and σ-phases which contain medium and high levels of Cr respectively. These light contrast regions could be areas of β-NiAl phase with lower levels of Al due to the flux of Al towards the Al_2O_3 oxides. The lower level of Al would raise the mean atomic number of the phase, making it appear brighter in the BSE image. Conversely, these could be regions of γ-Ni phase with lower levels of Cr which formed as β-phase depletion occurred. Therefore, the oxides which have developed at boundaries of the regions indicated by G could be evidence of void formation at the γ/σ or β/σ phase boundaries.

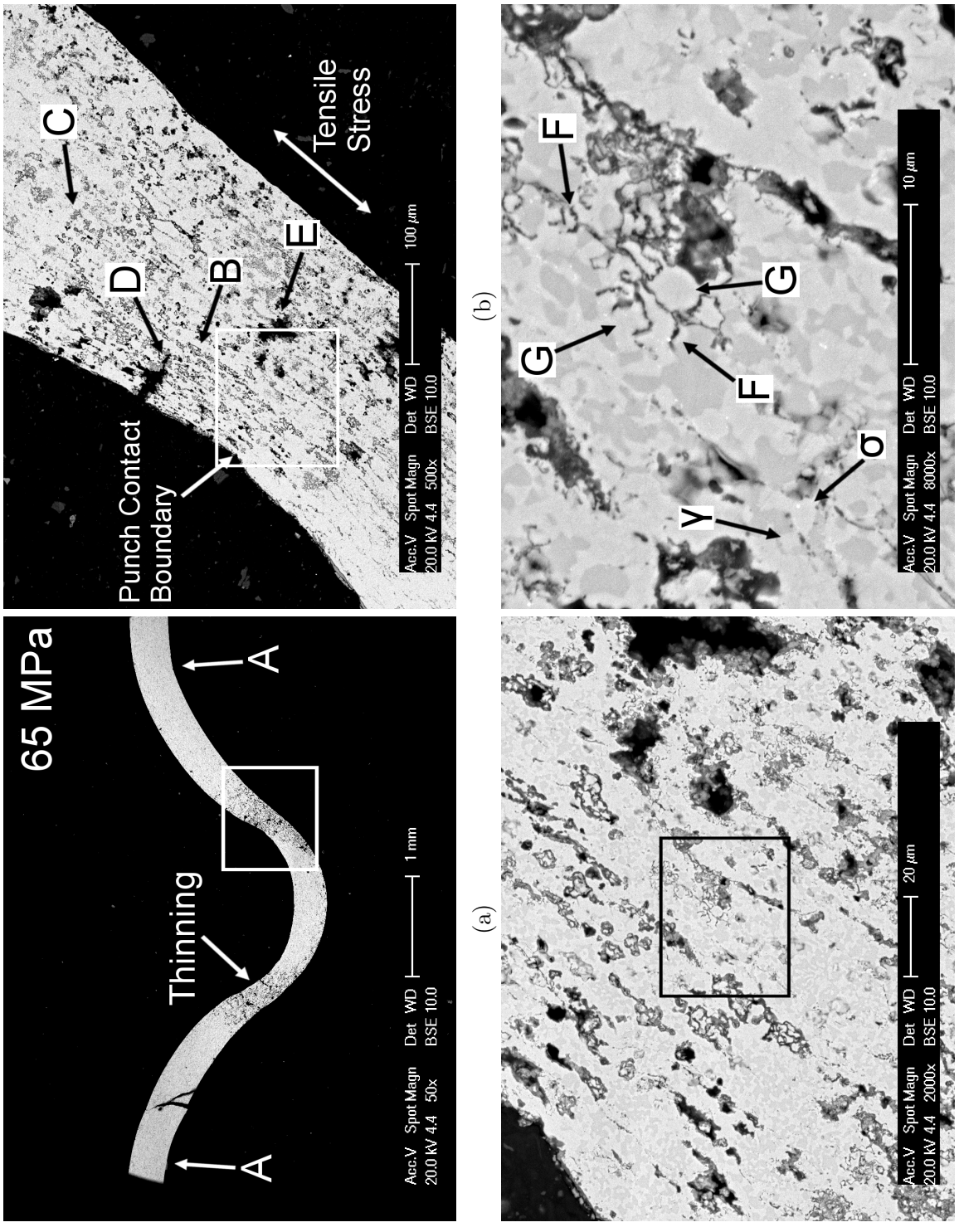

FIGURE 6.9: Cross section of the EP1 coating following SPC testing at 750 °C and 65 MPa. The specimen was tested for 310 hours.

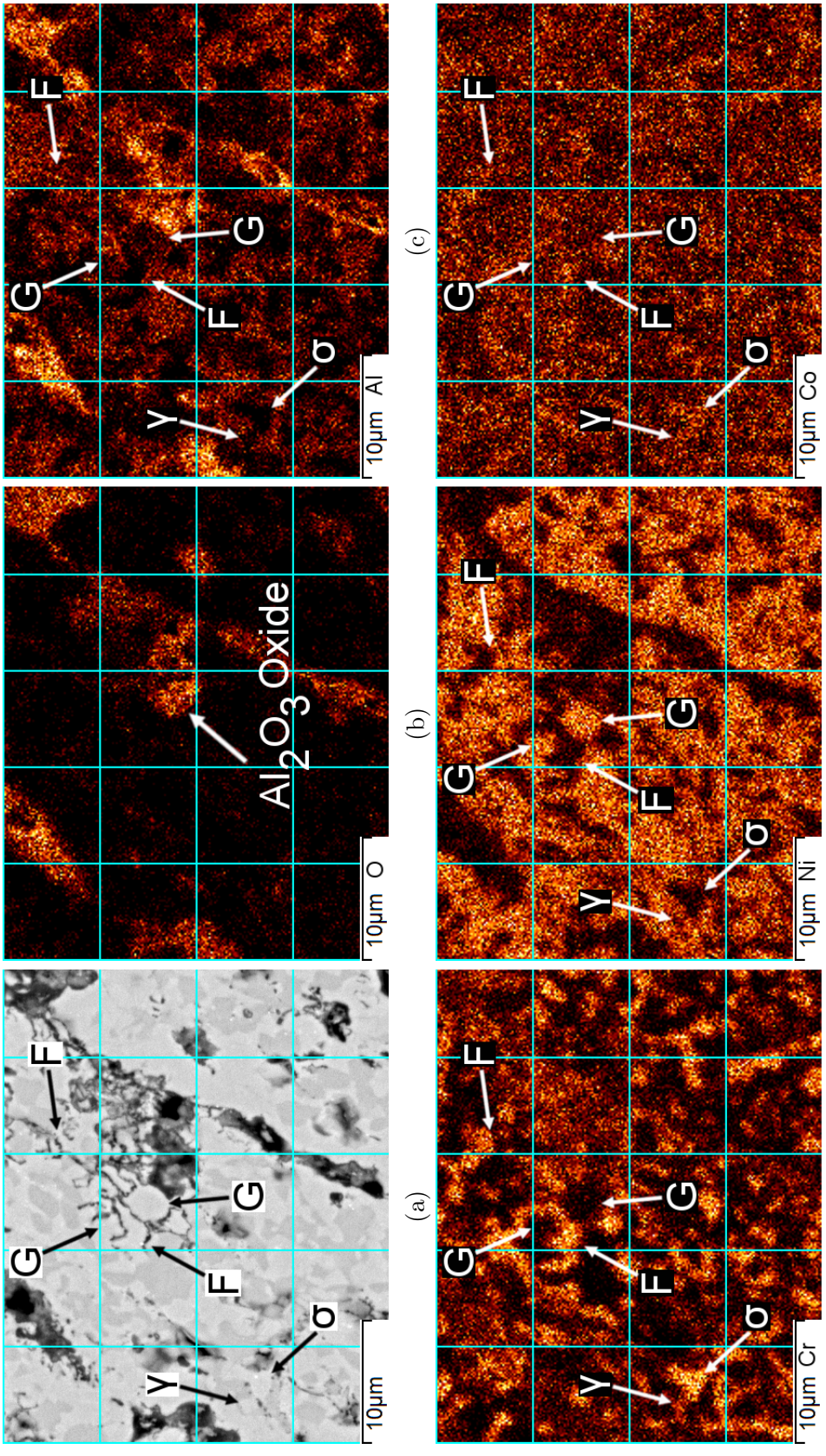

FIGURE 6.10: BSE image and EDX maps of the cross section of the EP1 coating following SPC testing at 750 °C and 65 MPa. The β-phase can be identified by high levels of Ni and Al, and low levels of Cr. The σ-phase can be identified by high levels of Cr and low levels of Ni, and the γ-phase identified by medium levels of Cr and Co and low levels of Al.

6.4.2.2 High Minimum Steady-State Strain Rate

Fig.6.11 shows a cross section of the EP1 specimen tested at 80 MPa and 750 °C. The specimen failed after 45 hours.

The 80 MPa specimen failed due to a through-thickness crack which propagated at a radial offset from the centre of the specimen, as indicated by B. On the left side of the specimen there is thinning near to the point of fracture but there is no observable thinning on the right side. It is presumed that the left side of the specimen is representative of specimen failure whereas the right side of the specimen is the result of shearing as the through-thickness crack spread through the specimen.

Fig.6.11b shows the high density of oxides and cracks near to where the specimen failed. A high number of oxides accumulate in bands along the direction of the tensile stress, as indicated by C, but some form in bands normal to the tensile stress and through the thickness of the specimen, as indicated by D. A large through-thickness crack is indicated by E.

An area of the specimen near to a large crack is shown in Fig.6.11d. EDX maps of the same area are shown in Fig.6.12. The letter F indicates evidence of void formation at the β/σ phase boundaries, discernible by the thin black oxides. There is also evidence of void formation at the γ/β phase boundaries as indicated by G.

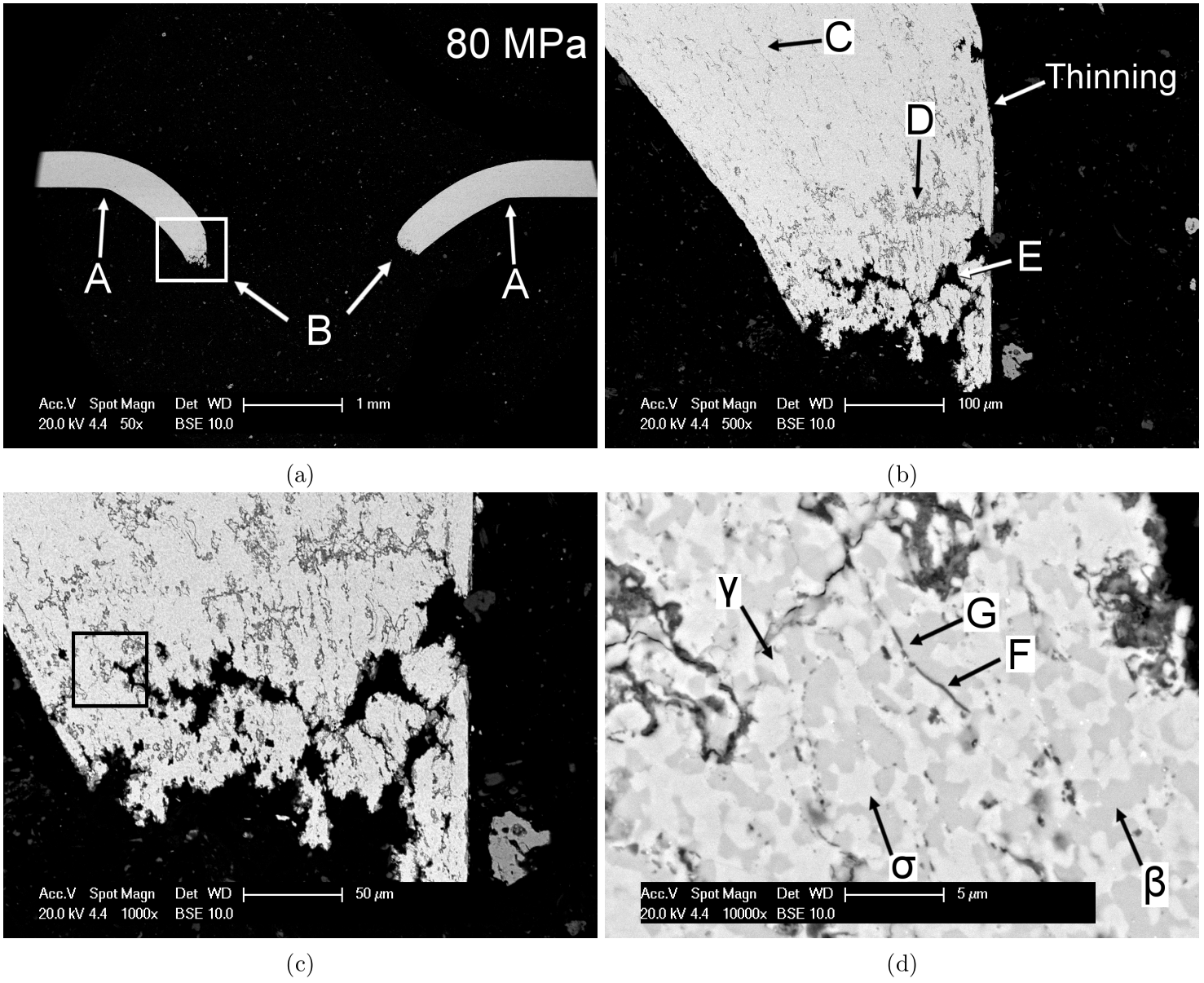

FIGURE 6.11: Cross section of the EP1 coating following SPC testing at 750 °C and 80 MPa. The specimen failed after 45 hours.

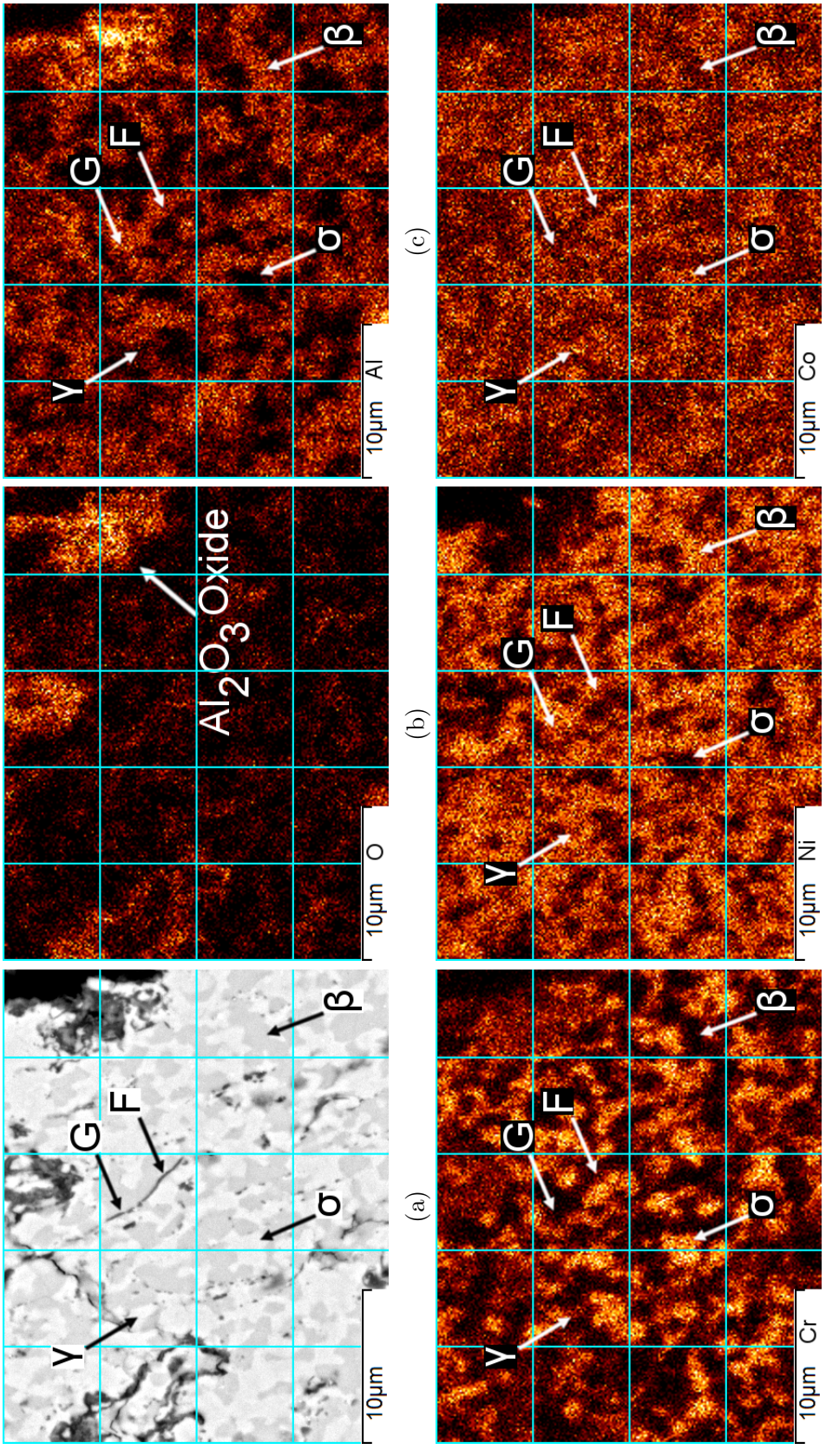

FIGURE 6.12: BSE image and EDX maps of the cross section of the EP1 coating following SPC testing at 750 °Cand 80 MPa. The β-phase can be identified by high levels of Ni and Al, and low levels of Cr. The σ-phase can be identified by high levels of Cr and low levels of Ni, and the γ-phase identified by medium levels of Cr and Co and low levels of Al.

6.4.3 Coating EP3

Coating EP3 is a four phase coating with a β:σ:γ:γ' ratio of 62:18:13:7 vol.%. The microstructure is detailed in full in section 4.6.

6.4.3.1 Low Minimum Steady-State Strain Rate

A cross section of the EP3 specimen tested at 72 MPa and 750 °C is shown in Fig.6.13, where the boxes indicate the area shown at higher magnification in the subsequent image. The specimen was tested for 69 hours but did not fail.

The inflection point normally associated with the clamping boundary is less defined in the EP3 72 MPa specimen than in the C1 and EP1 specimens. This is probably because the specimen was not fully clamped during the SPC test. A lower clamping load was used to avoid pre-cracking in the EP3 coating specimens. It appears that in this instance, the clamping load was too low and the specimen was able to deflect upwards slightly in the clamping region.

On the tensile surface of the specimen, there are two large cracks, indicated by B, as well as a through-thickness crack which has developed in the centre of the specimen. The through-thickness crack did not cause specimen failure and probably developed as the specimen was unloaded from the SPC rig after the test had finished.

Ahead of the cracks which formed on the tensile surface of the specimen, there is a very high density of oxides, as indicated by C in Fig.6.13b, which makes it difficult to discern how the oxides formed in those areas. The area outlined by the white box in Fig.6.13a corresponds to an area near to the punch contact boundary, which is shown at higher magnification in Fig.6.13c. The lower density of oxides in this area makes it easier to discern how the oxides formed. There is evidence of oxides accumulating in bands parallel to the direction of the tensile stress, as indicated by D.

Fig.6.13d shows the oxides at higher magnification. EDX maps of the same area are shown in Fig.6.14. The β-phase can be identified by high levels of Ni and Al, and low levels of Cr. The σ-phase can be identified by high levels of Cr and low levels of Ni, and the γ'-phase can be identified as the very bright regions in the SEM image which have high levels of Ni and low levels of Cr. It is difficult to identify the γ-phase in the EDX maps as it has medium levels of Ni, Co and Cr, which makes it difficult to distinguish from the other phases.

The letter E indicates evidence of oxides forming at β /σ phase boundaries. The letter F indicates evidence of oxides developing at the σ/γ' phase boundaries, which could also be evidence of oxide growth at the γ/γ' phase boundaries as it is difficult to discern the γ and σ-phases in the EDX maps. The oxide growth is probably at the σ/γ' phase boundary as the FCC γ-phase and FCC γ'-phase share a coherent interface [6].

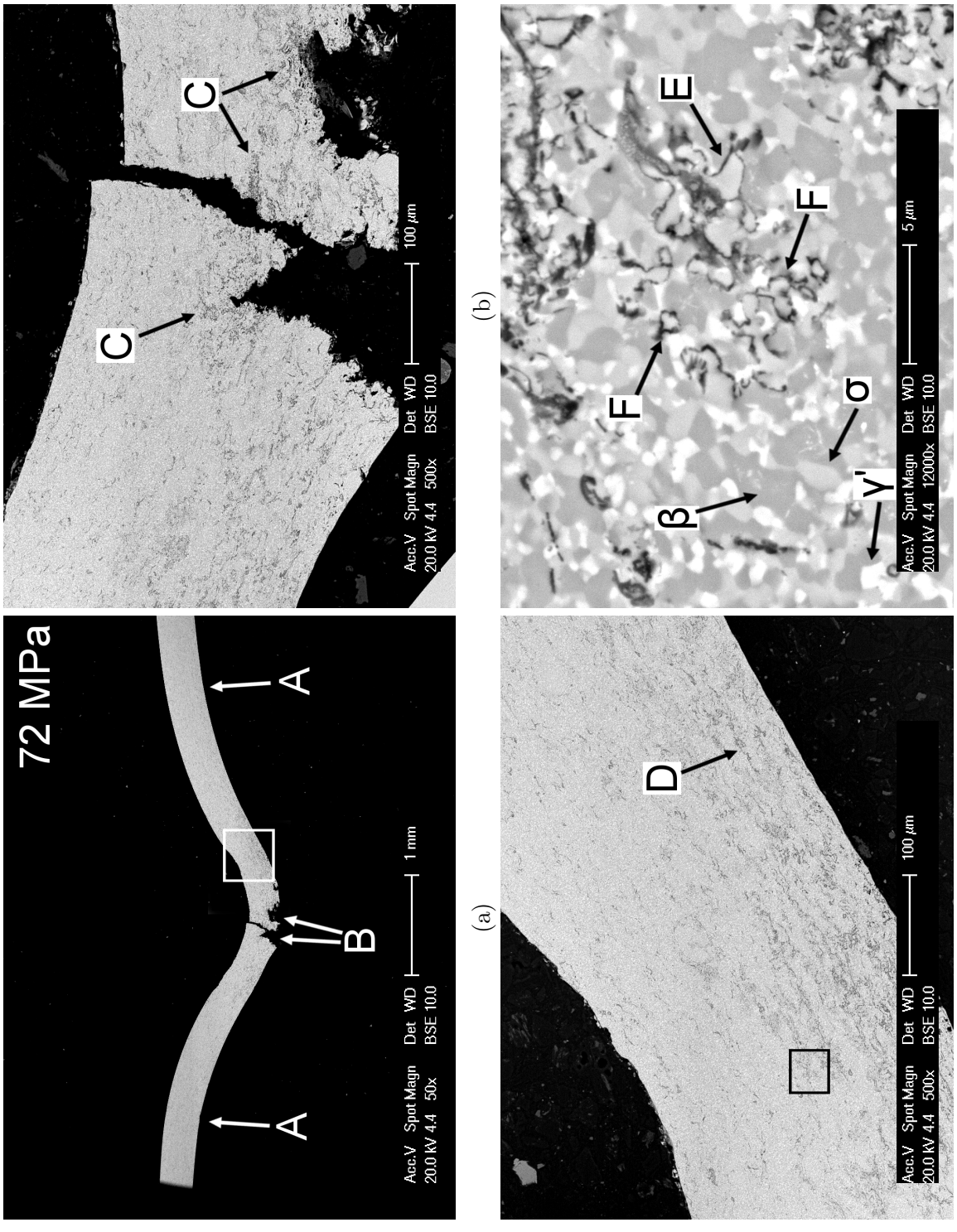

FIGURE 6.13: Cross section of the EP3 coating following SPC testing at 750 °C and 72 MPa. The specimen was tested for 69 hours but did not fail.

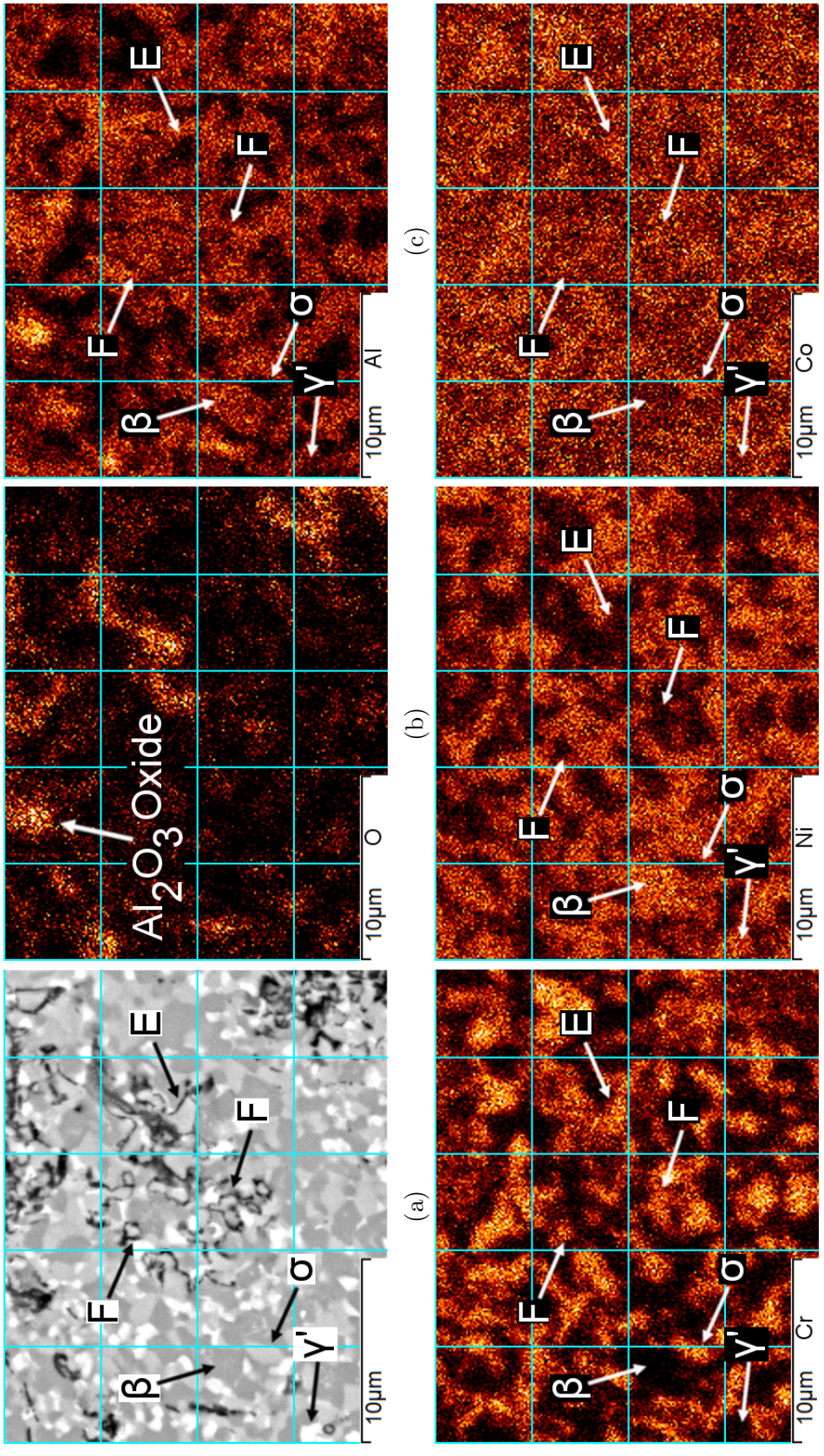

FIGURE 6.14: BSE image and EDX maps of the cross section of the EP3 coating following SPC testing at 750 °C and 72 MPa. The β-phase can be identified by high levels of Ni and Al, and low levels of Cr. The σ-phase can be identified by high levels of Cr and low levels of Ni, and the γ'-phase can be identified as the very bright regions in the SEM image which have high levels of Ni and low levels of Cr. It was not possible to identify the γ-phase in the EDX maps.

6.4.3.2 High Minimum Steady-State Strain Rate

Fig.6.15 shows a cross section of the EP3 specimen tested at 75 MPa and 750 °C. The specimen failed after 47 hours due to a through-thickness circumferential crack, as was observed for the C1 and EP1 coatings. The location of fracture is indicated by B. There is no significant thinning of the specimen and it is unclear why the location of fracture is different on either side of the specimen. The most probable explanation is that the punch head was not correctly aligned to the centre of the specimen, which caused an asymmetrical stress distribution within the specimen.

Fig.6.15b shows the high density of oxides and cracks near to the point of fracture. The letters C and D indicate evidence of oxides accumulating in bands parallel to the tensile stress and normal to the tensile stress respectively. There are large cracks spreading through the thickness of the specimen, as indicated by E, as well as a crack which has developed on the compressive surface of the specimen, indicated by F.

Fig.6.15d shows examples of oxide growth in the area just ahead of a crack tip. The oxides indicate where voids have formed. EDX chemical maps of the same area are shown in Fig.6.16. The letter G indicates evidence of void formation at the σ/β phase boundaries, which appears to be the main type of void formation. This could also include some evidence of void formation at the γ/β phase boundaries, as it is difficult to accurately distinguish the γ-phase, but it is likely that most of the void formation is at the σ/β phase boundaries as there is a higher phase fraction of σ-phase in the EP3 coating. The letter H indicates possible evidence of void formation at the σ/γ' phase boundary.

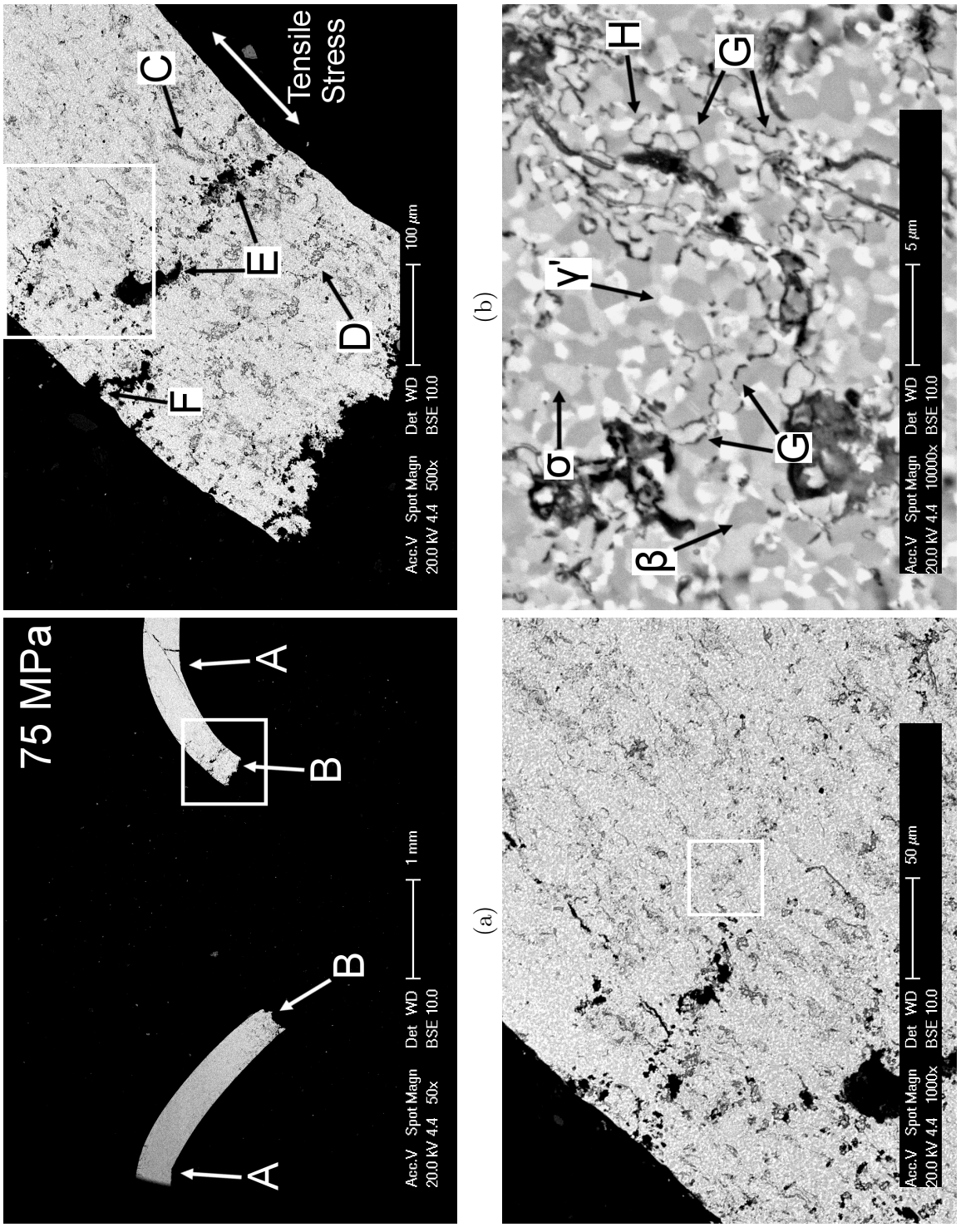

FIGURE 6.15: Cross section of the EP3 coating following SPC testing at 750 °C and 75 MPa. The specimen failed after 47 hours.

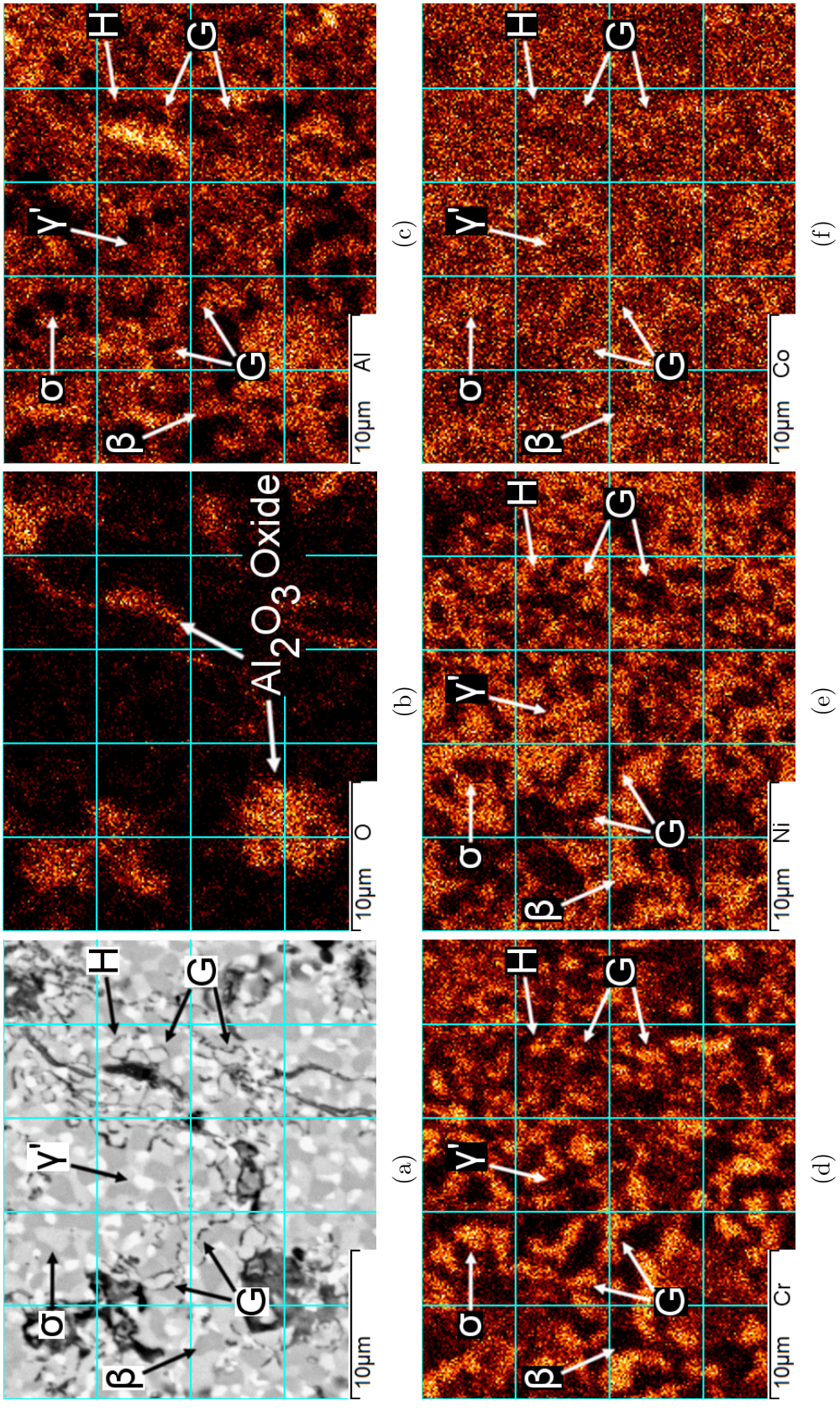

FIGURE 6.16: BSE image and EDX maps of the cross section of the EP3 coating following SPC testing at 750 °C and 75 MPa. The β-phase can be identified by high levels of Ni and Al, and low levels of Cr. The σ-phase can be identified by high levels of Cr and low levels of Ni, and the γ'-phase can be identified as the very bright regions in the SEM image which have high levels of Ni and low levels of Cr.

6.5 Results of SPC Tests at 850 °C

6.5.1 Displacement-Time Curves

SPC tests at 850 °C were conducted for the C1 and EP1 coatings on rig 2 only. The tests were conducted between equivalent uni-axial stresses of 30-50 MPa for the C1 coating and between 50-70 MPa for the EP1 coating. No tests were conducted on coating EP3 at 850 °C due to the time limitation of the current work.

The SPC displacement-time curves obtained for the C1 and EP1 coatings at 850 °C are shown in Fig.6.17. Breaks have been applied to some axis in order to accommodate the extended loading time of some tests.

The displacement-time curves obtained for the C1 and EP1 coatings exhibit a primary region, a secondary steady-state region and a tertiary region, as was observed for both coatings at 750 °C. A number of curves do not show a tertiary region because the tests were terminated prior to failure.

The shapes of displacement-time curves are similar to conventional uni-axial creep curves with primary, secondary and tertiary regions. However, as explained in section 6.3.1, the secondary steady-state region in a SPC curve is not directly comparable to secondary steady-state region in a uni-axial creep curve. The minimum steady-state strain rate is typically found just before the tertiary creep region.

The displacement-time curves of the C1 and EP1 coatings show a general trend where increasing the load increases the slope of the steady-state region, as well as decreases the time to failure. This is similar to the behaviour observed at 750 °C for both coatings.

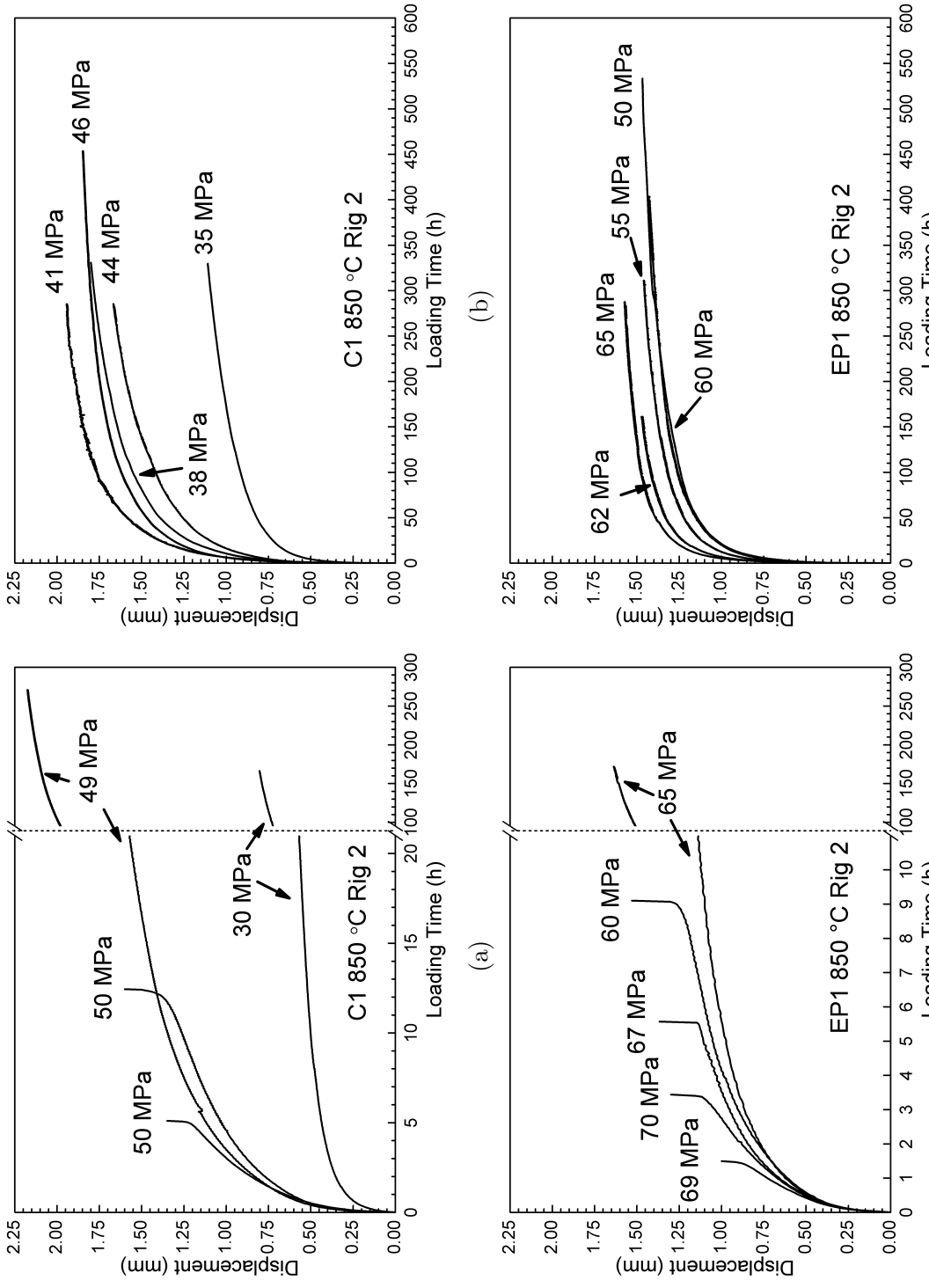

FIGURE 6.17: Displacement-time curves of coatings C1 and EP1 obtained through small punch creep testing at 850 °C on rig 2. Both coatings exhibit typical creep behaviour at 850 ° with primary, secondary and tertiary regions.

6.5.2 Material Creep Parameters and Power Law Relationships

Plots of minimum steady-state strain rate vs equivalent uni-axial stress, minimum steady-state strain rate vs time to failure and equivalent uni-axial stress vs time to failure are shown in Figs.6.18 and 6.19 for the C1 and EP1 coatings respectively. An asterisk is used to indicate tests which were terminated prior to failure. As stated in section 6.3.1, the minimum steady-state strain rate of the terminated specimens is artificially high but is still within the acceptable band of error.

The plots were used to calculate parameters for the Norton steady-state power law, the Monkman-Grant relationship and the creep rupture power law. The parameters for the C1 and EP1 coatings at 850 °C are summarised in table 6.2.

6.5.2.1 Coating C1

The SPC behaviour of coating C1 at 850 °C can be divided into two distinct regions, as shown in Fig.6.18a. Between 30-49 MPa, the C1 coating exhibits a very low increase in the minimum steady-state strain rate with respect to equivalent uni-axial stress, whereas between 49-50 MPa the minimum steady-state strain rate is significantly higher. The change behaviour occurs at a strain rate of approximately 2×10^{-7} s^{-1}.

The Norton power law parameters for the C1 coating at 850 °C are B = 6.7×10^{-10} $s^{-1}MPa^{-n}$ and n = 1.43 between 30-49 MPa, and B = 4.0×10^{-303} $s^{-1}MPa^{-n}$ and n = 175 between 49-50 MPa.

The minimum steady-state strain rate vs time to failure, and equivalent uni-axial stress vs time to failure are shown in Figs.6.18b and 6.18c respectively. Only the two specimens tested at 50 MPa failed. Between 30-49 MPa, the strain rate was so low that the predicted times to failure, based on an extrapolation of the SPC data obtained at 750 °C, were in excess of 1000 hours for each test. Such long test times were not feasible in this work. Above 49 MPa, the minimum steady-state strain

rate increased to approximately 1 $\times 10^{-5}$ s^{-1} and the time to failure decreased to less than 10 hours. The large discrepancy between the creep behaviour at 49 and 50 MPa meant it was not possible in the current work to establish a load where the time to failure for the C1 coating was greater than 10 hours but less than 1000 hours.

No parameters were calculated for the Monkman-Grant relationship or creep rupture power law for the C1 coating at 850 °C.

6.5.2.2 Coating EP1

The SPC behaviour of coating EP1 at 850 °C can also be divided into two distinct regions, as shown in Fig.6.19a. Between approximately 50-65 MPa, there is a gradual increase in $\dot{\varepsilon}_{min}$ with stress, but between 65-70 MPa the strain rate significantly increases. The change in behaviour corresponds to a strain rate of approximately 2 $\times$ 10^{-7} s^{-1}.

The Norton power law parameters for the EP1 coating at 850 °C are B = 1.37 $\times$ 10^{-21} $s^{-1}MPa^{-n}$ and n = 7.9 between 50-65 MPa, and B = 2.0 $\times$ 10^{-86} $s^{-1}MPa^{-n}$ and n = 44.1 between 65-70 MPa.

Between 65-70 MPa, the minimum strain rate was greater than 1$\times 10^{-5}$ s^{-1} and the EP1 specimens failed at less than 10 hours, but no specimens were tested to failure between 50-65 MPa. Figs.6.19b and 6.19c show that between 65-70 MPa, the time to failure decreased as $\dot{\varepsilon}_{min}$ and σ_e increased.

The Monkman-Grant relationship parameters for the EP1 coating at 850 °C are K_1 = 0.0002 hs^m and m = 0.92. The creep rupture power law parameters are M = 7.7 $\times$ 10^{-17} $h^{-1}MPa^{-\chi}$ and χ = 8.5.

	Range	Norton Power Law		Rupture Power Law		Monkman-Grant Relationship	
	MPa	B *	n	M $^\diamond$	χ	K_1 $^\triangleleft$	m
C1	30-49	6.7×10^{-10}	1.43	-	-	-	-
	49-50	4.0×10^{-303}	175	-	-	-	-
EP1	50-65	1.37×10^{-21}	7.9				
	65-70	2.0×10^{-118}	62	7.74×10^{-17}	8.5	0.0002	0.92

TABLE 6.2: Parameters for the Norton power law, creep rupture power law and Monkman-Grant relationship for the C1 and EP1 coating at 850 °C as determined by small punch creep testing. Symbols refer to units where $\star = s^{-1}MPa^{-n}$, $\diamond = h^{-1}MPa^{-\chi}$ and $\triangleleft = hs^{m}$.

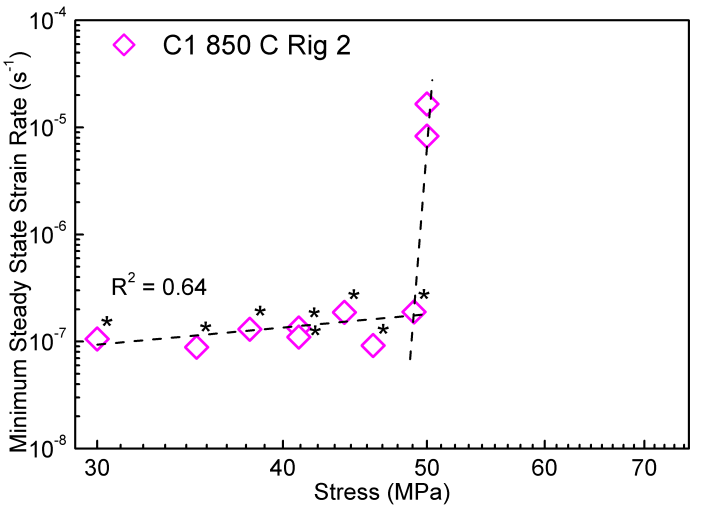

(a)

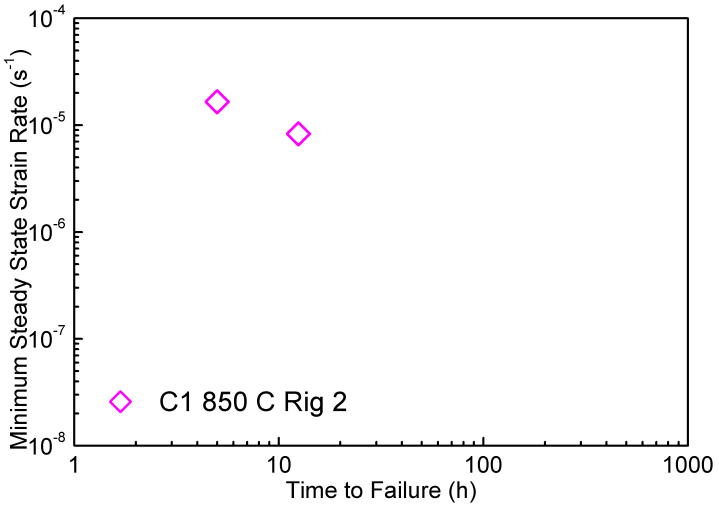

(b)

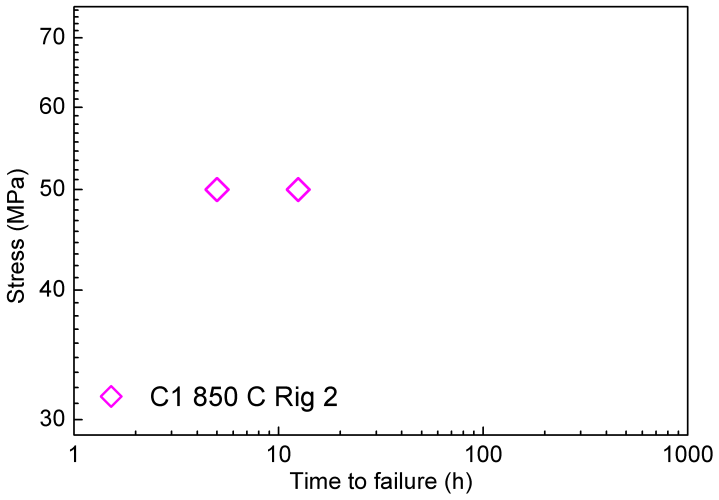

(c)

FIGURE 6.18: Creep behaviour of coating C1 at 850 °C where a) shows minimum steady-state strain rate vs equivalent uni-axial stress, b) shows minimum steady-state strain rate vs time to failure and c) shows equivalent uni-axial stress vs time to failure where all graphs are plotted logarithmic scales. Asterisks indicate tests which were terminated prior to failure.

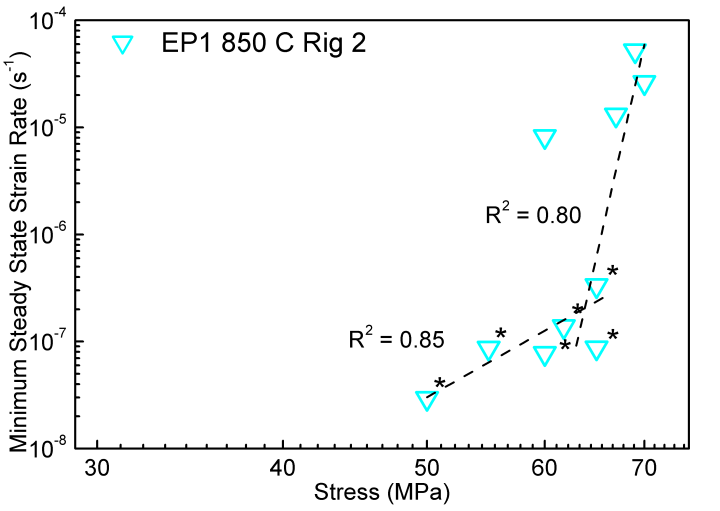

(a)

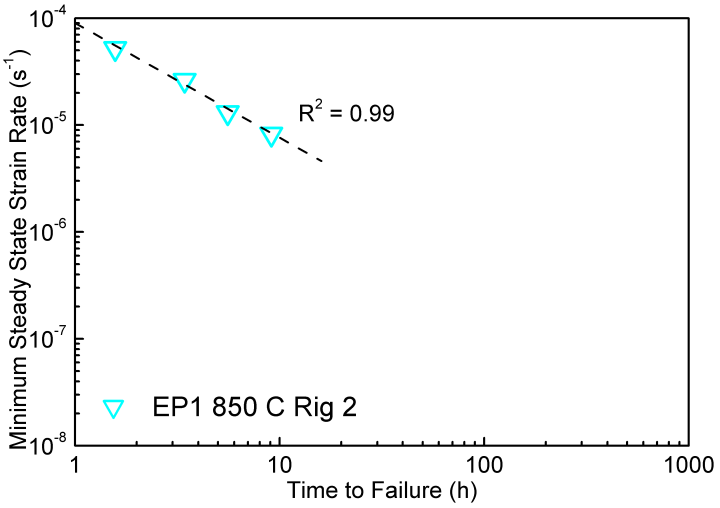

(b)

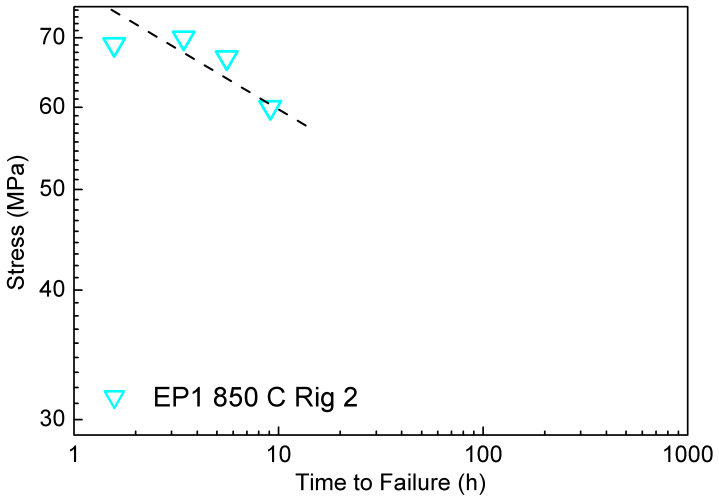

(c)

FIGURE 6.19: Creep behaviour of coating EP1 at 850 °C where a) shows minimum steady-state strain rate vs equivalent uni-axial stress, b) shows minimum steady-state strain rate vs time to failure and c) shows equivalent uni-axial stress vs time to failure where all graphs are plotted logarithmic scales. Asterisks indicate tests which were terminated prior to failure.

6.6 SPC Specimen Deformation at 850 °C

In this section the SPC deformation behaviour of the C1 and EP1 coatings at 850 °C is presented. Two examples are provided for each coating; a low minimum steady-state strain rate specimen which was terminated prior to failure, and a high minimum steady-state strain rate specimen which failed. BSE images of each sample are presented. For each specimen the clamping boundary is indicated by the letter A.

6.6.1 Coating C1

6.6.1.1 Low Minimum Steady-State Strain Rate

The C1 coating specimen tested at 49 MPa and 850 °C was tested for 270 hours but did not fail. A cross section is shown in Fig.6.20 where the white box denoted 1 indicates the areas shown at higher magnification in Figs.6.20b and 6.20c, and the white box denoted 2 indicates the area shown in 6.20d.

The centre of the specimen deformed into a conical shape. The punch contact boundary, which also corresponds to the point of maximum thinning, is indicated by B. The thickness of the specimen decreases gradually between the clamping boundary (A) and the punch contact boundary, before increasing again towards the centre of the specimen.

Fig.6.20b shows the high density of oxides and cracks in the area of the specimen near to the punch contact boundary. There is evidence of oxides accumulating in bands parallel to, and normal to, the direction of the tensile stress, as indicated by C and D respectively. There are also cracks forming within the thickness of the specimen and on the tensile surface of the specimen, as indicated by E and F respectively.

Fig.6.20c shows the oxides at high magnification. The letter G indicates oxides which appear to be the same shape as the β-phase regions, and the letter H

indicates an oxide which appears to be growing through a β-phase region. The evidence suggests the oxides grow within regions of β-phase, as was observed at 750 °C. The letter I indicates a region where extensive β-phase depletion has occurred.

Fig.6.20d shows an area with a lower density of oxide growth. The letter J indicates small oxides which were retained in the C1 coating after HVOF thermal spraying. The letter K indicates examples of where these oxides have grown, largely at the γ/β phase boundaries. The internal oxide growth must be supported by the development of voids, which provide the diffusion path for O. Therefore, the oxides demonstrate that voids formed at the γ/β phase boundaries.

6.6.1.2 High Minimum Steady-State Strain Rate

Fig.6.21 shows a cross section of the C1 specimen tested at 50 MPa and 850 °C, where the white boxes indicate the area shown at higher magnification in the subsequent image. The specimen failed after 5 hours due to circumferential cracking at B.

The area of the specimen near to the point of fracture exhibits a large amount of deformation and there is significant thinning of the specimen. There is also a high density of oxides and cracks. The oxides form in bands parallel to the direction of the tensile stress, as indicated by C. There are circular, and elongated, cracks which have developed in the thickness of the specimen, as indicated by D and E respectively.

Fig.6.21d shows the oxides and cracks form within regions of β-phase, as indicated by F. The large cracks presumably develop either at the interface of the brittle Al_2O_3 oxide and the more ductile γ-phase, when the oxide fractures, or because of significant void growth. The letter G indicates where β-phase depletion has occurred.

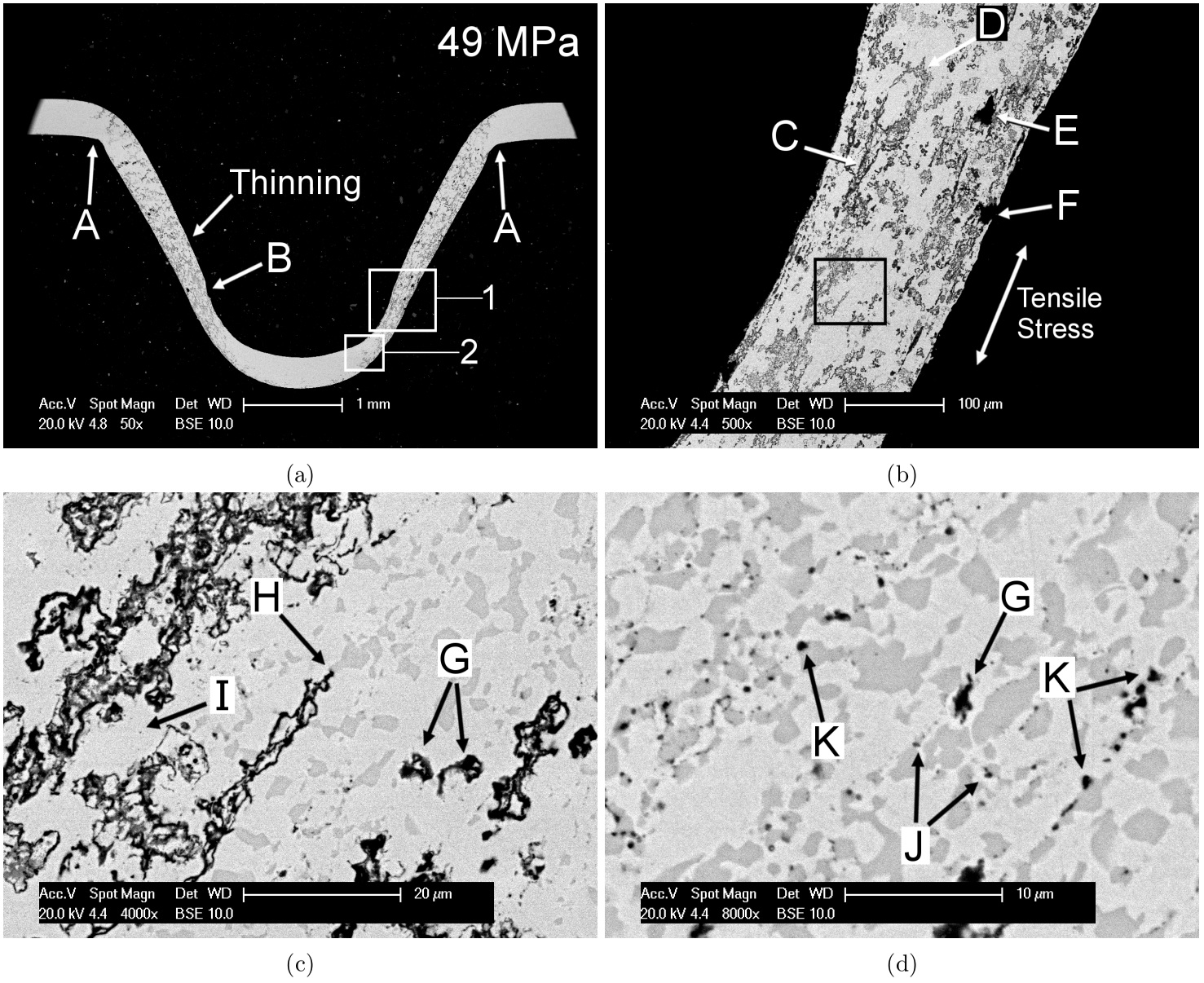

FIGURE 6.20: Cross section of the C1 coating following SPC testing at 850 °C and 49 MPa. The specimen was tested for 270 hours but did not fail.

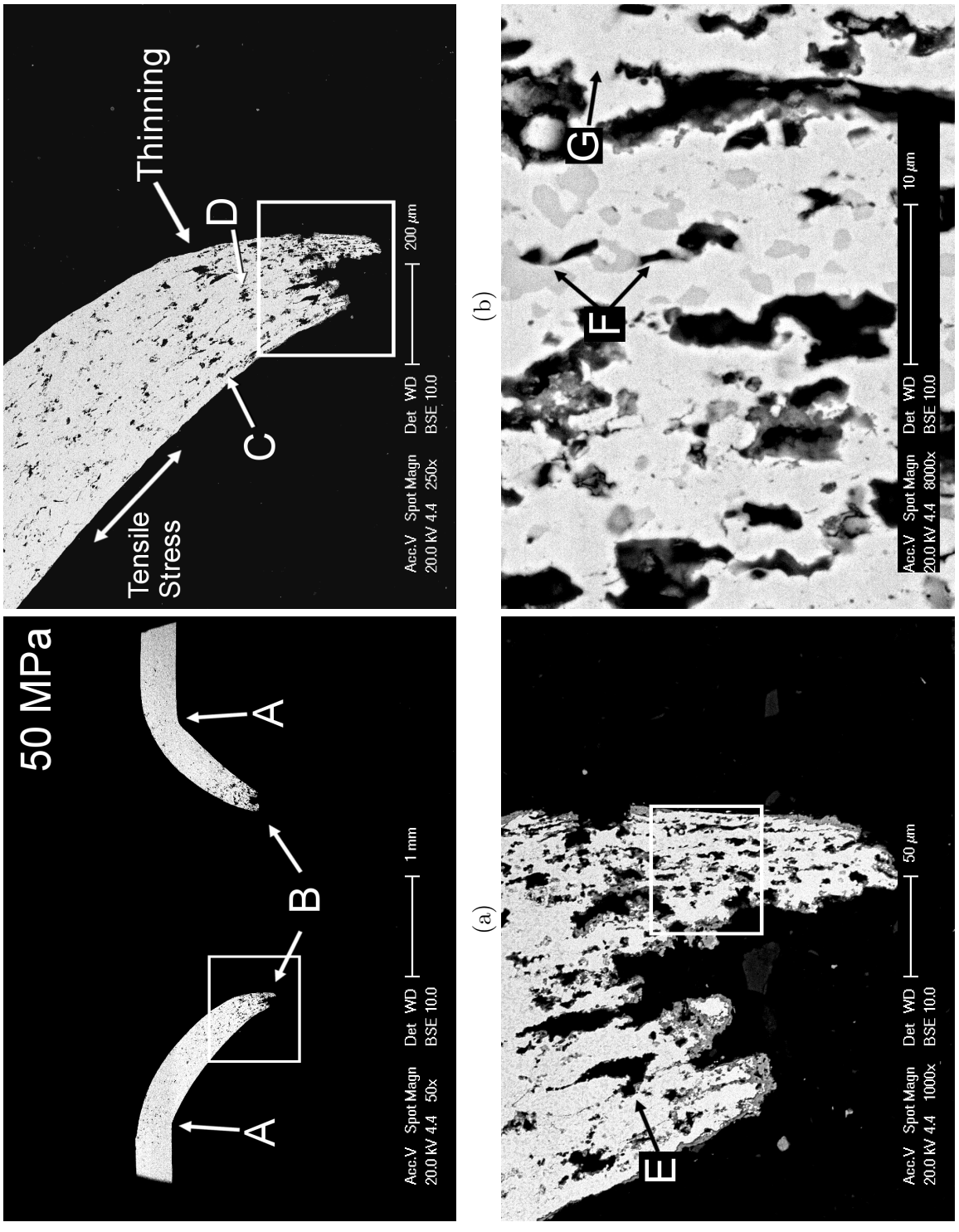

FIGURE 6.21: Cross section of the C1 coating following SPC testing at 850 °C and 50 MPa. The specimen failed after 5 hours.

6.6.2 Coating EP1

6.6.2.1 Low Minimum Steady-State Strain Rate

The EP1 coating specimen tested at 50 MPa and 850 °C is shown in Fig.6.22. The specimen was tested for 530 hours but did not fail. There is an area of thinning at the punch contact boundary, indicated by B. There is also high density of oxides and cracks throughout the the sides of the specimen. The oxides accumulate in bands parallel to the direction of the tensile stress, as indicated by C. There are also through-thickness cracks, as indicated by D.

Fig.6.22c shows examples of where the oxides form, which can be used as an indication of where void formation occurs. EDX maps of the same area are shown in Fig.6.23. The β-phase can be identified by high levels of Ni and Al, and low levels of Cr. The σ-phase can be identified by high levels of Cr and low levels of Ni, and the γ-phase identified by medium levels of Cr and Co and low levels of Al.

The letter E indicates void formation at the β/σ phase boundaries, which appears to be the most common type of void formation. The letter F indicates void formation at the γ/β phase boundaries and G indicates void formation at the σ/γ phase boundaries.

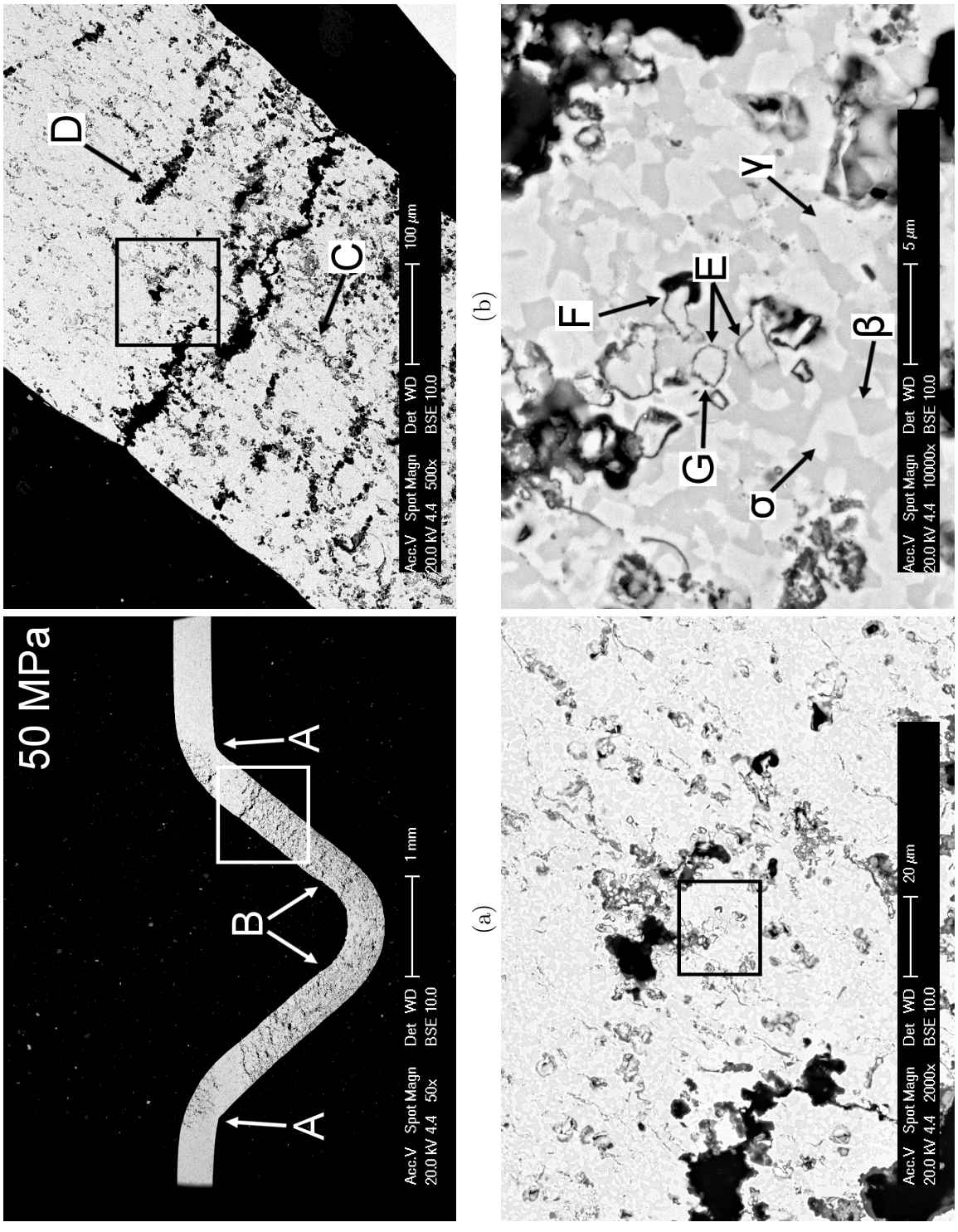

FIGURE 6.22: Cross section of the EP1 coating following SPC testing at 850 °C and 50 MPa. The specimen was tested for 530 hours but did not fail.

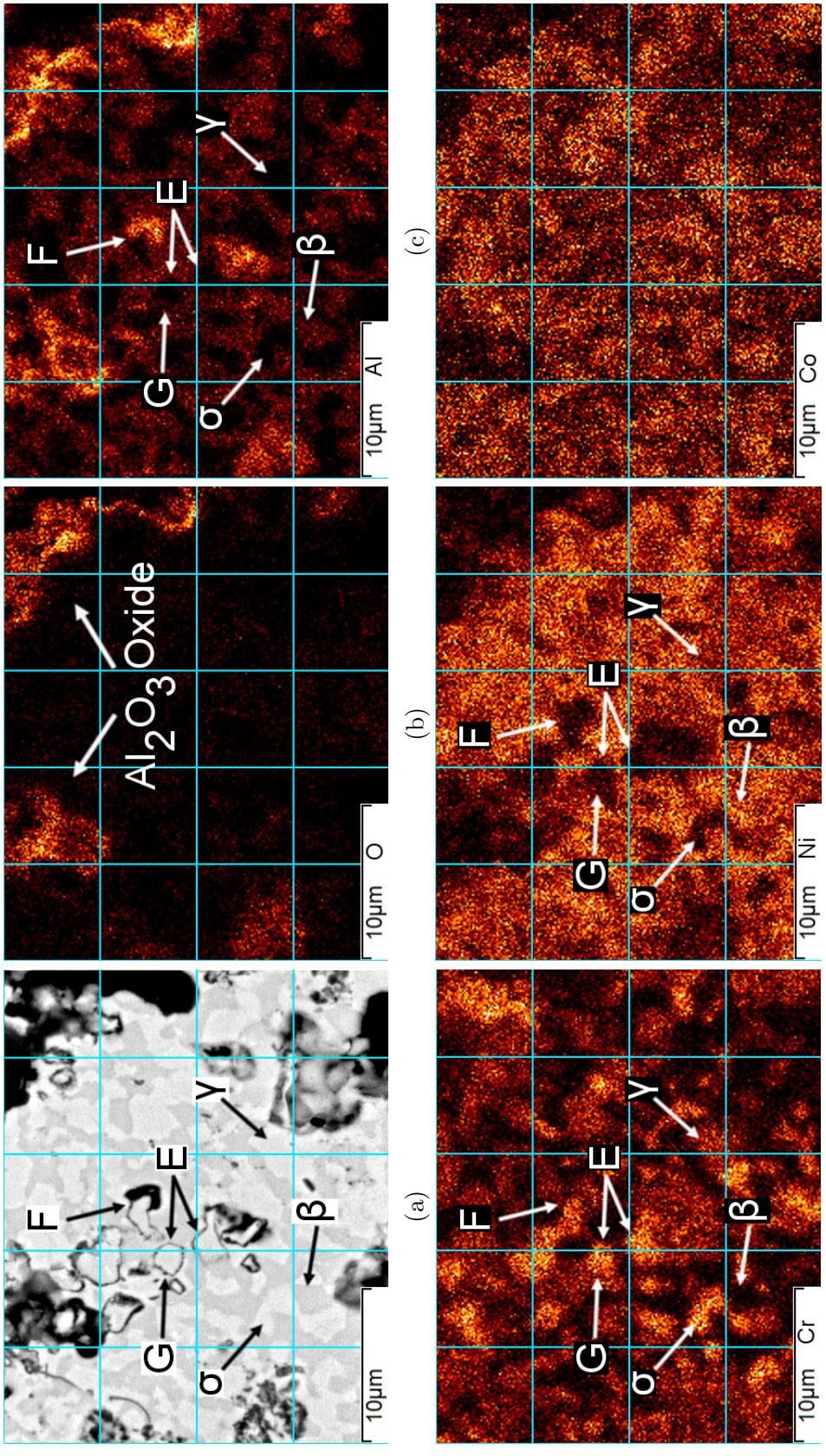

FIGURE 6.23: BSE image and EDX maps of the cross section of the EP1 coating following SPC testing at 850 °C and 50 MPa. The β-phase can be identified by high levels of Ni and Al, and low levels of Cr. The σ-phase can be identified by high levels of Cr and low levels of Ni, and the γ-phase identified by medium levels of Cr and Co and low levels of Al.

6.6.2.2 High Minimum Steady-State Strain Rate

The EP1 specimen tested at 60 MPa and 850 °C is shown in Fig.6.24. The specimen failed after 9 hours due to circumferential cracking at B.

Fig.6.24b shows the high density of oxides and cracks near to the point of fracture. The oxides accumulate in bands parallel to the direction of the tensile stress, as indicated by C, and in bands normal to the tensile stress, as indicated by D. There are large cracks which have formed in the specimen parallel to the tensile stress, as indicated by E, and normal to the tensile stress, as indicated by F.

Fig.6.24d shows an example of the oxide growth at higher magnification. EDX maps of the same area are shown in Fig.6.25. There is evidence of oxide growth, and therefore void formation, at the β/σ phase boundaries, as indicated by G, void formation at the γ/β phase boundaries, as indicated by H and void formation at the γ/σ phase boundaries, as indicated by I.

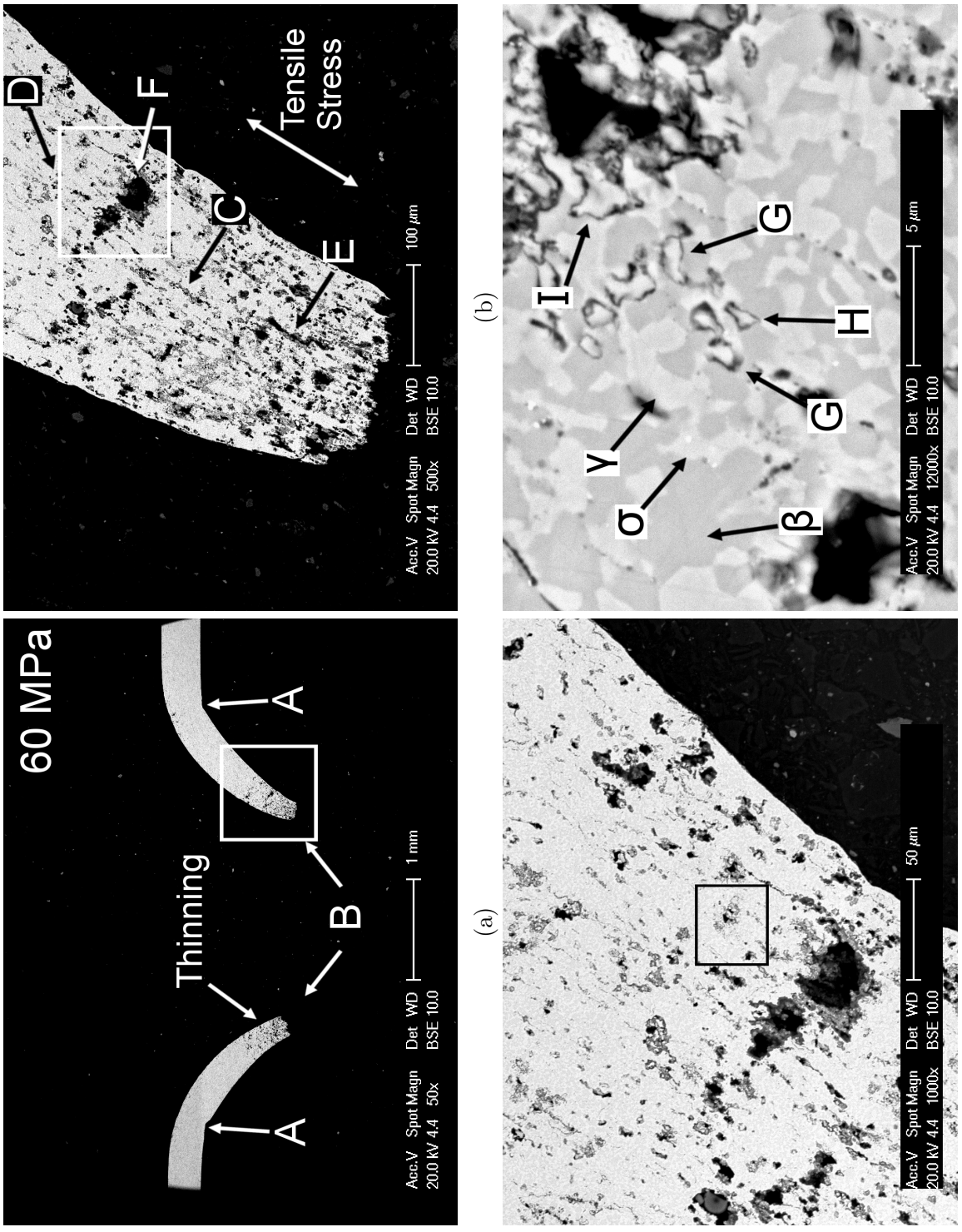

FIGURE 6.24: Cross section of the EP1 coating following SPC testing at 850 °C.

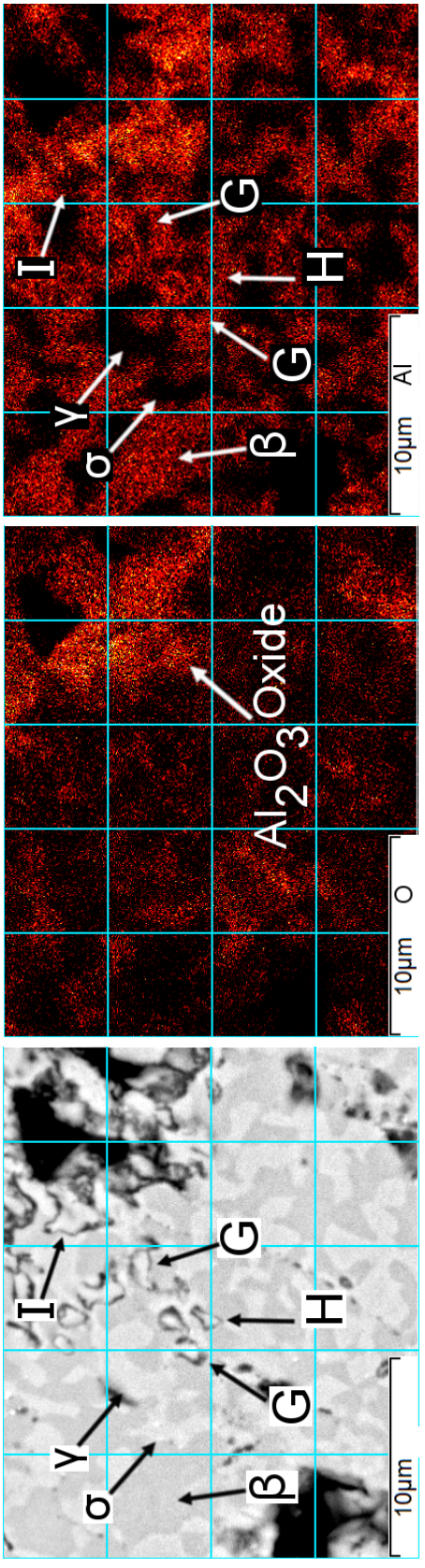

FIGURE 6.25: EDX maps of the cross section of the EP1 coating following SPC testing at 850 °C.

6.7 Discussion

The purpose of this section is to consider the SPC test behaviour exhibited by the MCrAlY coatings at 750 and 850 °C. First, the microstructure of each coating is discussed with reference to any phase evolution which may take place during the SPC test. Secondly, the SPC behaviour of coating C1 is discussed with reference to the literature and previous uni-axial creep and SPC testing of coatings manufactured from the C1 alloy. Thirdly, the creep properties of the coatings at 750 and 850 °C are discussed with reference to the role of the different constituent phases. The SPC deformation of the coatings at 750 and 850 °C is then discussed and compared to current FE models. Finally, the possible mechanisms for void formation under creep will be examined for all three coatings.

6.7.1 Alloy Constitution

A summary of the phase fractions for each coating is shown in table 6.3. As the coatings are held at 750 and 850 °C for extended time periods during the SPC tests, phase evolution may take place within the coatings. The phase fractions of each coating during SPC testing may range between the phase fractions observed in the heat treated coatings and the phase fractions predicted to exist under thermodynamic equilibrium using the CALPHAD method.

For the C1 coating, the CALPHAD calculations predict much higher phase fractions of β-NiAl phase than was observed in the heat treated coatings but it is unlikely that such significant phase evolution will take place at 750 or 850 °C. For all the SPC tests, the C1 coating can be considered to have a γ- Ni phase matrix with a β-NiAl phase fraction of 30-40 vol.%.

For the EP1 coating, the CALPHAD calculations predict higher amounts of β-phase and significantly less γ-phase. There may be a large decrease in the phase fraction of γ-phase and a small increase in the phase fraction of β-NiAl and σ-Cr_2Co phases during the SPC tests. In general, the EP1 coating will exhibit a

β-phase matrix with approximately 15-25 vol.% γ-phase and 13-18 vol.% σ-phase during all the SPC tests.

For the EP3 coating, the measured phase fractions show good agreement with the CALPHAD calculations, with the exception of the predicted phase fraction of γ'-Ni_3(Al,Ta) phase, which was addressed in chapter 4. For all the SPC tests, the EP3 coating can be regarded as having a β-NiAl matrix with 10-16 vol.% γ-Ni phase, 18-23 vol.% σ-Cr_2Co phase and 4-7 vol.% γ'-Ni_3(Al,Ta) phase.

Phase Fraction		Coating C1			Coating EP1			Coating EP3			
		β	γ	σ	β	γ	σ	β	γ	σ	γ'
Measured (vol.%)		31	69	0	60	27	13	62	13	18	7
CALPHAD Method (vol.%)	750 °C	45	47	8	67	15	18	63	10	23	4
	850 °C	43	57	0	67	18	15	65	16	19	0

TABLE 6.3: Phase fractions of the C1, EP1 and EP3 heat treated coatings measured from BSE images and EBSD phase maps, as well as predicted phase fractions calculated from CALPHAD calculations using ThermoCalc and the TTNi7 database. Measured values are approximate and have a standard deviation of ±2-3 vol.%.

6.7.2 Creep Behaviour of Coating C1

The creep behaviour of coatings manufactured from the C1 alloy have been previously studied using both the SPC test and the uni-axial creep test. As such, the creep behaviour of the C1 coating is discussed first so that the current results may be evaluated with reference to previous work.

At 750 °C the C1 coating exhibits a Norton power parameter of 7.5, which agrees well with the value of 7.7 reported by Chen [63] for SPC specimens manufactured from the C1 alloy. However, other studies have reported that n≈3 for the C1 alloy when determined through uni-axial testing [72, 80].

The discrepancy between the different studies could mainly be because the C1 alloy experiences different equivalent uni-axial stress ranges during uni-axial testing and SPC testing, due to the relative strain rates achieved for the different test

methods. Brindley and Whittenberger [79] reported that the stress exponent of Ni-18Cr-12Al-0.3Y alloy increased from approximately 2.7 at strain rates of 10^{-4} s^{-1} to 7.1 at strain rates below 10^{-5} s^{-1}. Given the strain rates experienced in SPC tests are between 10^{-6} and 10^{-7} s^{-1} it is possible that the stress exponent calculated in this work and by Chen [63] are accurate, despite not agreeing with previous work by Thompson et al. [80] and Wereszczak et al. [72].

Despite the difference between the SPC test and uni-axial test results, the SPC creep behaviour of the C1 coating is consistent with previous SPC testing at 750 °C [63]. As such, the SPC results for the C1 coating can be compared to the SPC results of the EP1 and EP3 coatings in order to evaluate the effect of microstructure on the creep behaviour of the MCrAlY coatings.

6.7.3 Effect of Microstructure on the Creep Properties of MCrAlY Coatings Determined by SPC Tests

As discussed in the literature review, the creep properties of MCrAlY coatings are not well established. In particular, the role of each constituent phase has not been widely studied. A general observation from the literature is that MCrAlY alloys with higher Ni and Al content tend to exhibit higher stress exponents, but there is little data concerning the relative creep rates of different MCrAlY alloys or how the microstructure influences creep behaviour. This is mostly due to an inconsistency between test methods and sample preparation. The purpose of this section is to compare the SPC creep behaviour of the C1, EP1 and EP3 coatings with reference to the coating microstructures. The SPC results are summarised in Fig.6.26 and the creep parameters are summarised in table 6.4. The creep behaviour at 750 and 850 °C are discussed separately.

6.7.3.1 750 °C

At 750 °C the C1 coating exhibited the lowest resistance to creep and the EP3 coating exhibited the highest, indicating that higher phase fractions of BCC NiAl-β

phase increases a MCrAlY coatings resistance to creep. The increased creep resistance of the EP3 coating can also be attributed to the γ'-Ni_3(Al,Ta) phase, which is known to improve the creep resistance of γ-Ni superalloys [6] and was reported by Taylor et al. [170] to improve the creep resistance of a β-NiAl matrix Pt-aluminide coating.

The C1 and EP1 coating exhibit similar stress exponents; n = 7.5 for coating C1 and n = 7.8 for coating EP1. The stress exponent for the EP3 coating is 9.1. Theoretically the EP3 coating would exhibit the lowest creep resistance at high loads, but practically such loads could not be achieved as the time to failure would approach zero. As such, the EP3 coating can be regarded as exhibiting the highest resistance to creep during SPC tests below 80 MPa.

Evans and Wilshire [15] reported that when the stress exponent is greater than 5, creep is controlled by dislocation climb and grain boundary sliding. However, as already discussed, the stress exponent calculated for the coatings may be artificially high due to the difference between the SPC test and the uni-axial test. Therefore, dislocation climb and grain boundary sliding may may be the main creep mechanism for the C1, EP1 and EP3 coatings at 750 °C but no conclusion can be made at this time.

The Monkman-Grant relationship parameters for the C1 and EP1 coatings are similar but the C1 coating exhibits slightly higher time to failure for any given strain rate. This indicates increasing the phase fraction of β-NiAl phase decreases the strain to fracture, which is in agreement with the lower strain to fracture observed for the EP1 and EP3 coatings during SPT tests, as described in chapter 5. No comments can be made on the EP3 coating as only two EP3 specimens failed during SPC testing.

The EP1 coating exhibits a higher creep lifetime compared to the C1 coating, which indicates that a higher phase fraction of β-phase increases the overall creep lifetime. This agrees with Thompson et al. [80] who reported a Ni-22Cr-10Al-1Y coating exhibited a lower creep rate than a coating manufactured from the C1

alloy. The NiCrAlY presumably contained a higher phase fraction of β-NiAl phase although no phase fractions were reported.

The EP3 coating appears to exhibit higher creep lifetimes than the EP1 coating. The data points indicated by an asterisk in Fig.6.26e indicate EP3 specimens which were stopped prior to failure. The tests have clearly exceeded the time to failure of the EP1 coating before being terminated, which demonstrates the EP3 coating exhibits a higher creep lifetime than the C1 and EP1 coatings. The higher creep lifetime can be attributed to the high phase fraction of β-NiAl and the addition of γ'-Ni_3(Al,Ta) phase.

It is unclear what effect the σ-Cr_2Co phase has on the creep behaviour of the coatings as there is not enough data to compare the EP1 and EP3 coatings to determine the effect of σ-phase.

Overall, the evidence indicates that higher phase fractions of β-NiAl, as well as the addition of γ'-Ni_3(Al,Ta) phase, improves the creep resistance and lifetime of the MCrAlY coatings at 750 °C.

	Temp.	Range	Norton Power Law		Rupture Power Law		Monkman-Grant Relationship	
	°C	MPa	B *	n	M $^\diamond$	χ	K_1 $^\triangleleft$	m
C1	750	38-80	5.2×10^{-20}	7.5	9.4×10^{-13}	5.9	0.0002	0.92
	850	30-49	6.7×10^{-10}	1.43	-	-	-	-
	850	49-50	4.0×10^{-303}	175	-	-	-	-
EP1	750	50-80	2.2×10^{-21}	7.8	2.6×10^{-17}	7.9	0.0003	0.87
	850	50-65	1.37×10^{-21}	7.9	-	-	-	-
	850	65-70	2.0×10^{-118}	62	7.74×10^{-17}	8.5	0.0002	0.92
EP3	750	50-75	1.7×10^{-24}	9.1	-	-	-	-

TABLE 6.4: Material parameters for the C1 and EP1 coatings at 750 and 850 °C and for the EP3 coating at 750 °C. Symbols refer to units where $\star = s^{-1}MPa^{-n}$, $\diamond = h^{-1}MPa^{-\chi}$ and $\triangleleft = hs^m$.

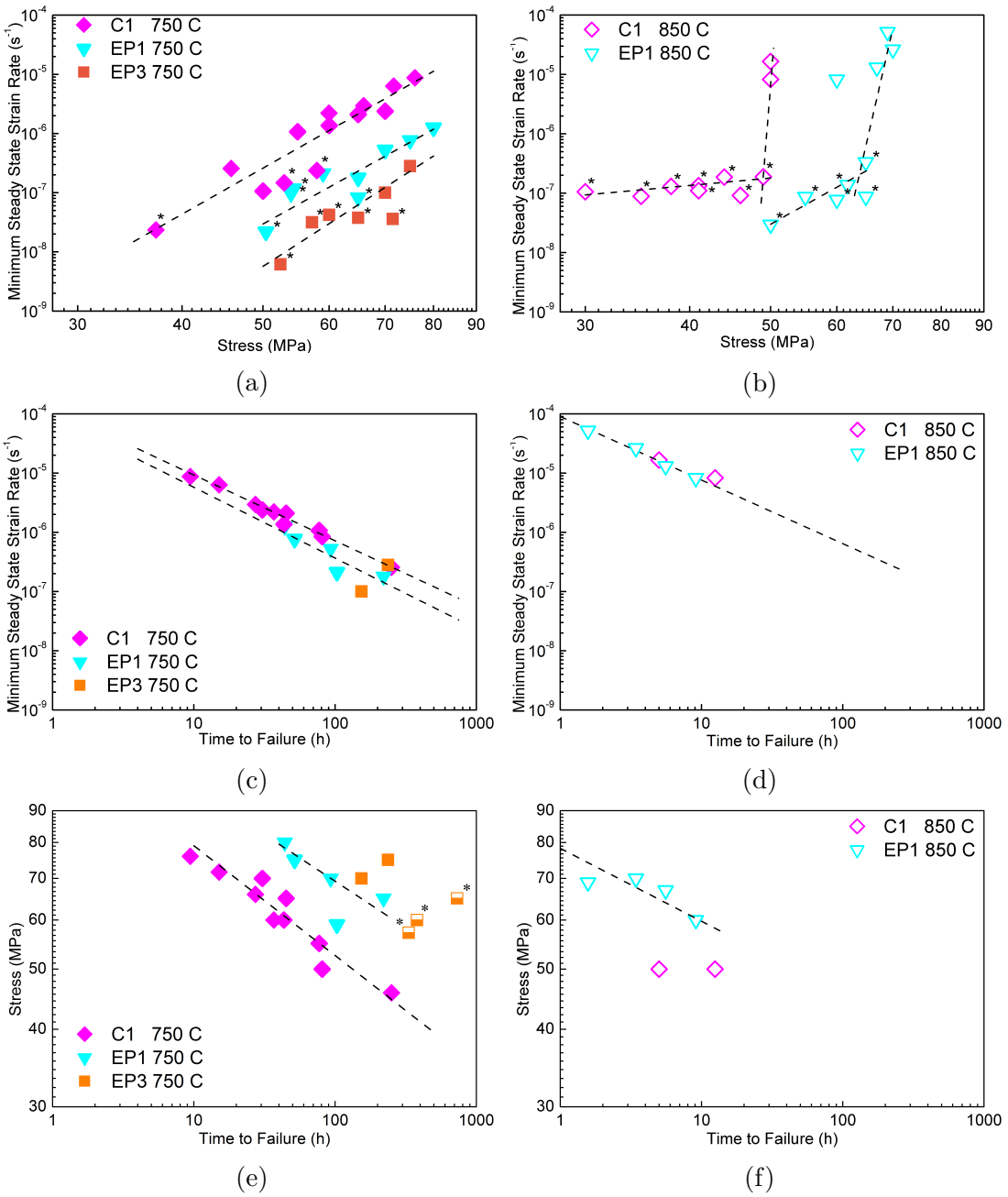

FIGURE 6.26: Comparison of creep behaviour of all coatings at 750 °C (left) and 850 °C (right) where (a-b) shows minimum steady-state strain rate vs equivalent uni-axial stress, (c-d) shows minimum steady-state strain rate vs time to failure and (e-f) shows equivalent uni-axial stress vs time to failure. Asterisks indicate tests which were terminated prior to failure.

6.7.3.2 850 °C

At 850 °C, the SPC behaviour of the C1 and EP1 coatings at 850 °C can be divided into two distinct regions; a low minimum steady-state strain rate region, which occurs between 30-49 MPa for the C1 coating and between 50-65 MPa for EP1

coating, and a high minimum steady-state strain rate region which occurs between 49-50 MPa for the C1 coating and between 65-70 MPa for the EP1 coating. For both coatings the upper limit of the low strain-rate region coincides with a strain rate of approximately 2×10^{-7} s^{-1}.

Considering the high strain rate regions first, the EP1 coating exhibits a higher resistance to creep than the C1 coating. The difference between the creep resistance of the two coatings is similar at 750 and 850 °C; the strain rate observed for the C1 coating at 50 MPa is similar to that observed for the EP1 coating at 65 MPa at both temperatures. Therefore, the effect of microstructure on the creep behaviour of the coatings at 850 °C, in the high strain-rate regions, appears to be similar to that observed at 750 °C, which has already been discussed.

The stress exponents calculated in the high strain rate regions at 850 °C are 175 and 62 for the C1 and EP1 coatings respectively. This is much higher than the stress exponents reported in the literature for any MCrAlY coatings [72, 79–83]. It is not clear why the stress exponents are so high. It is possible that the coatings are exhibiting a step change in behaviour and that the stress exponents calculated are for the transition region, but higher load tests would be needed to confirm this.

The C1 and EP1 coatings exhibit similar Monkman-Grant relationship behaviour at 850 °C, no parameters were calculated for the C1 coating as there are only two data points, but the C1 data points fit within the EP1 trend line. This indicates that neither the β-NiAl phase or σ-Cr_2Co phase decrease the strain to fracture at 850 °C.

The C1 coating exhibits a much lower creep lifetime than the EP1 coating. The time to failure of the C1 coating at 50 MPa is similar to the time to failure of the EP1 coating at 60-67 MPa. The increased creep lifetime can be attributed to the increased phase fraction of β-NiAl phase, as was observed at 750 °C.

Considering the SPC behaviour at 750 °C and the SPC behaviour observed in the high strain-rate regions at 850 °C, the creep resistance of the C1 and EP1 coatings

is significantly reduced at 850 °C, which leads to a marked decrease in creep lifetime of each coating. The decrease in creep resistance with temperature is to be expected and has been observed previously for MCrAlY coatings [72, 79, 80, 82].

The overall strain to fracture for the EP1 coating increases between 750-850 °C, which can be attributed to increased ductility of the β-NiAl phase at 850 °C. Interestingly, the Monkman-Grant relationship behaviour for the C1 and EP1 coatings is similar at 850 °C, which indicates there is little difference between the ductility of the two coatings at 850 °C.

Considering the low minimum steady-state strain rate regions, the EP1 coating exhibits a higher resistance to creep than the C1 coating. It is not possible to comment on the creep lifetimes in the low strain-rate regions as no specimens failed, but presumably the EP1 coating would have exhibited a higher creep lifetime due to the higher resistance to creep.

In the low strain-rate regions at 850 °C, neither coatings appear to exhibit typical creep behaviour. The Norton power law parameters for the EP1 coating in the low strain-rate region at 850 °C, shown in table 6.4, are similar to the parameters calculated at 750 °C. The increase in temperature does not appear to influence the creep resistance which is not typical creep behaviour.

For the C1 coating, below 49 MPa, $\dot{\varepsilon}_{min}$ is higher at 850 °C than at 750 °C, but the stress exponent is very low at 1.43. The stress exponent is probably artificially low; $\dot{\varepsilon}_{min}$ is typically found just before the tertiary region but all the low strain-rate tests were terminated before the tertiary stage was reached. This means the values of $\dot{\varepsilon}_{min}$ are artificially high, particularly at the lower stresses. This probably caused the stress exponent to be artificially low. Considering that the values of $\dot{\varepsilon}_{min}$ are artificially high in the low strain-rate region, there appears to be only a small decrease in the creep resistance at 850 °C compared to the decrease observed in the high strain-rate region.

None of the low strain-rate specimens failed at 850 °C, but the specimens did reach strains of 1-1.6 before the tests were terminated, compared to the fracture strains

of 0.5-0.85 for the high strain rate specimens for both coatings. This demonstrates there is clearly a step change in the ductility of the C1 and EP1 coatings. As the step change occurs at approximately 2×10^{-7} s^{-1} for both coatings, the change in behaviour appears to be strain rate dependent.

The change in creep behaviour is probably because of the onset of superplasticity in the coatings, which has been shown to occur between 850-1150 °C for MCrAlY coatings during uni-axial tensile tests [81] and compression strain-rate jump tests [81]. The onset of superplasticity drastically increased the strain to fracture of the tested MCrAlY alloys in both studies, which resembles the change in behaviour observed for the C1 and EP1 coatings, but no data was provided in either study on how the onset of superplasticity affected the creep behaviour of the MCrAlY coatings. The effect of superplasticity can be more readily observed in the deformation of the SPC specimens, which is described in the next section.

6.7.4 SPC Deformation and Comparison With FE Models

6.7.4.1 SPC Deformation at 750 °C

At 750 °C, with the exception of the EP3 specimen tested at 72 MPa, all three coatings exhibited SPC deformation similar to that previously reported for SPC specimens [63, 87–89, 135]. The central region of each specimen deformed into a conical shape and thinning occurred in the area near to the punch contact boundary, which is also where a high density of voids and cracks were observed and where circumferential cracking occurred. The area of thinning corresponds to the region of high tensile stress and high creep strain at large displacements during SPC tests [92, 131–134]. Fig.6.27 [131] is an FE model illustrating the equivalent creep strain in a SPC specimen based on the elastic-plastic steady-state creep of a Gr91 steel SPC specimen. The model illustrates how the area of high creep strain corresponds to the location of circumferential cracking observed in the C1 and EP1 SPC specimens. Further details of this model are presented in section 2.9.

In the 72 MPa EP3 specimen, cracks developed in the centre of the tensile surface. This is because the area of high tensile stress in a SPC specimen is in the centre of the specimen at low displacements [92, 131, 132, 134, 136]. The 72 MPa EP3 specimen exhibited little initial deformation and a very low creep-rate, which meant the region of high tensile stress remained in the centre of the specimen throughout the SPC test. Hence, void formation and cracking occurred in the centre of the specimen. This type of fracture is not widely reported for SPC specimens because most SPC studies are concerned with ductile materials which exhibit large deformations in the primary creep region. However, similar behaviour has been reported for a γ-TiAl alloy [136] and a 316LN stainless steel [137] during SPC testing.

The microstructure of the coatings does not significantly influence the macroscopic deformation observed during the SPC tests, which is determined by the geometry of the test and the displacement of the specimen.

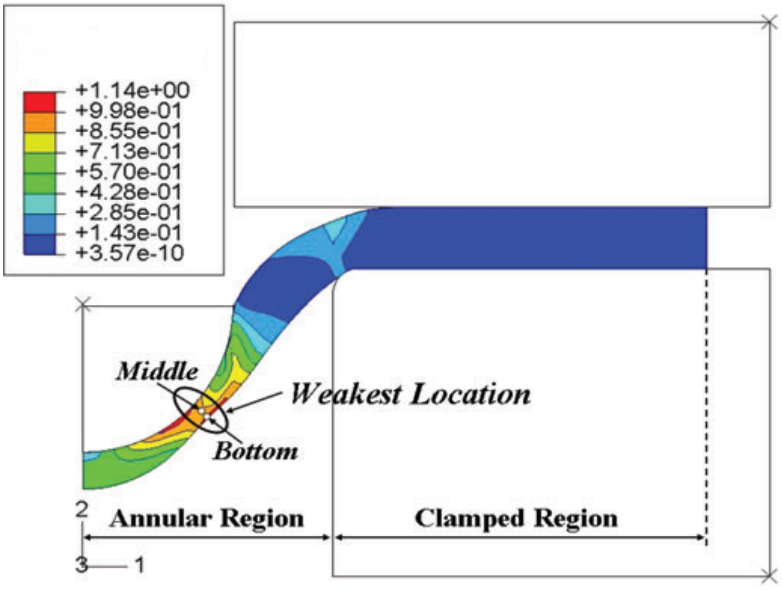

FIGURE 6.27: Finite element model showing the equivalent creep strain distribution within a SPC specimen. Figure reproduced from [131].

6.7.4.2 Comparison of SPC Deformation at 750 and 850 °C

The SPC behaviour of the C1 and EP1 coatings at 850 °C can be divided into two distinct regions, as has been discussed. For both coatings, the deformation

behaviour at 850 °C in the high strain-rate region was similar to the deformation behaviour at 750 °C. As such, the high strain-rate specimens are used to discuss the effect of temperature on the SPC behaviour of coatings C1 and EP1 when superplasticity is not observed.

Fig.6.28 shows BSE images of cross sections of the C1 and EP1 coatings after SPC testing at 750 and 850 °C. At both 750 and 850 °C, failure occurred due a circumferential crack. In the 850 °C specimens, there appears to be more gradual thinning which extends from the point of fracture up to the clamping boundary (indicated by A), whereas in the 750 °C specimens, thinning is limited to near the point of fracture.

There is also more creep damage near to the point of fracture in the 850 °C specimens, particularly for the EP1 coating. This is evidence that both coatings were able to accommodate more creep damage at 850 °C.

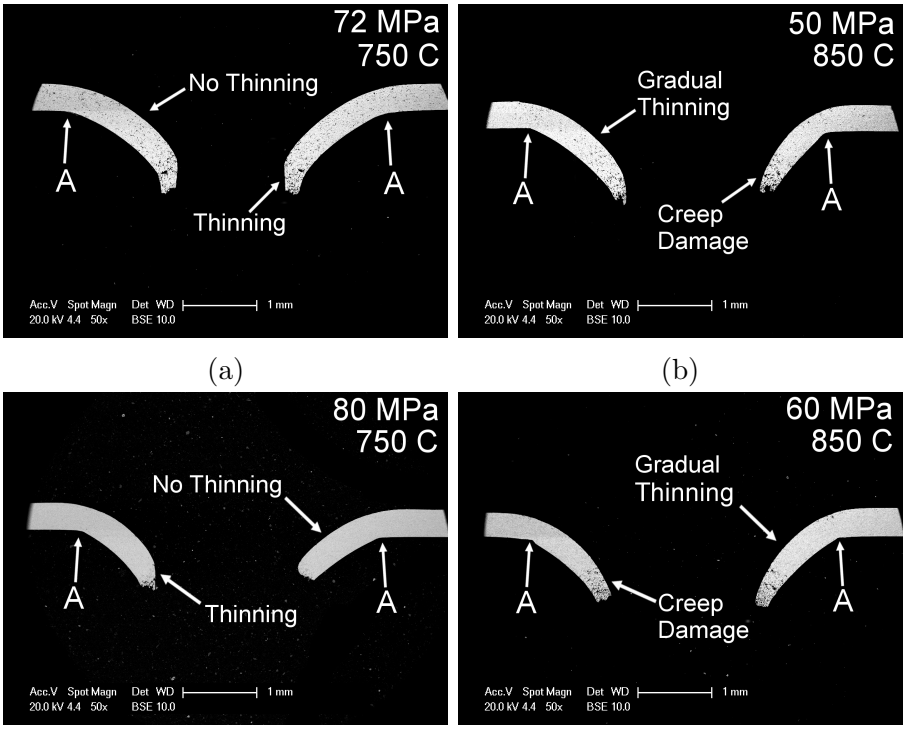

FIGURE 6.28: BSE images of the C1 coating (a-b) and EP1 coating (c-d) after SPC testing at 750 °C (left) and 850 °C (right).

6.7.4.3 Effect of Superplasticity on the SPC Deformation at 850 °C

As discussed in section 6.7.3, the C1 and EP1 coatings appear to exhibit superplasticity at 850 °C at strains below approximately 2×10^{-7} s^{-1}. Fig.6.29 shows the cross sections of the C1 and EP1 coatings after testing at 750 and 850 °C, for specimens which exhibited minimum steady-state strain rates below 2×10^{-7} s^{-1}.

It is clear that the 850 °C low strain-rate specimens do not exhibit similar deformation behaviour to the 750 °C specimens. The main differences between the 750 and 850 °C specimens are: the increased deformation at 850 °C; and more creep damage and thinning throughout larger areas of the specimen at 850 °C.

The low strain-rate specimens at 850 °C were terminated at strains of 1-1.6, compared to the fracture strains of 0.5-0.85 for the 750 °C specimens and high strain-rate 850 °C specimens. The increased strain in both coatings appears to have been accommodated by a higher degree of thinning, which is distributed throughout more of the specimen at 850 °C than at 750 °C. This is clearly observable for the C1 coating in Fig.6.29b, but less so for the EP1 coating in Fig.6.29d which does exhibit thinning but less significantly compared to the C1 specimen.

Hesbur and Miner [81] commented that superplasticity is most likely governed by grain boundary sliding, probably with diffusional accommodation, which may be the mechanism allowing the C1 and EP1 coatings to accommodate higher strains at 850 °C.

The creep damage in the specimens exhibiting superplasticity is more widespread in the 850 °C specimens. For the 750 °C specimens, as well as the FE model shown in Fig.**??**, creep damage, as well as thinning, occurs in the region of high tensile stress. If the stress evolution in all the SPC specimens is considered to be similar, since it is a feature of the test geometry, then the onset of superplasticity causes creep damage and thinning to occur outside the region of high tensile

stress. Because of this, current FE models do not appear to represent the SPC deformation observed for the C1 and EP1 coatings when exhibiting superplasticity.

A possible explanation for why the onset of superplasticity increases the creep resistance of the C1 and EP1 coatings can be gained by considering the steady-state region of the SPC test. A typical SPC specimen undergoes stiffening effects, observed due to the reducing cone angle at the center of the specimen and the increasing contact area between the specimen and the punch head, whilst at the same time experiences accelerating effects, due to thinning of the specimen [90]. For a typical SPC specimen, the combination of the stiffening and accelerating effects produces an approximately steady-state creep region. When the C1 and EP1 coatings exhibit superplasticity, there is less significant thinning of the specimen as the thinning is distributed through more of the specimen. This presumably reduces the accelerating effects and lowers the creep rate, thus increasing the creep resistance of the coatings, although it is not possible to validate this explanation in the current study.

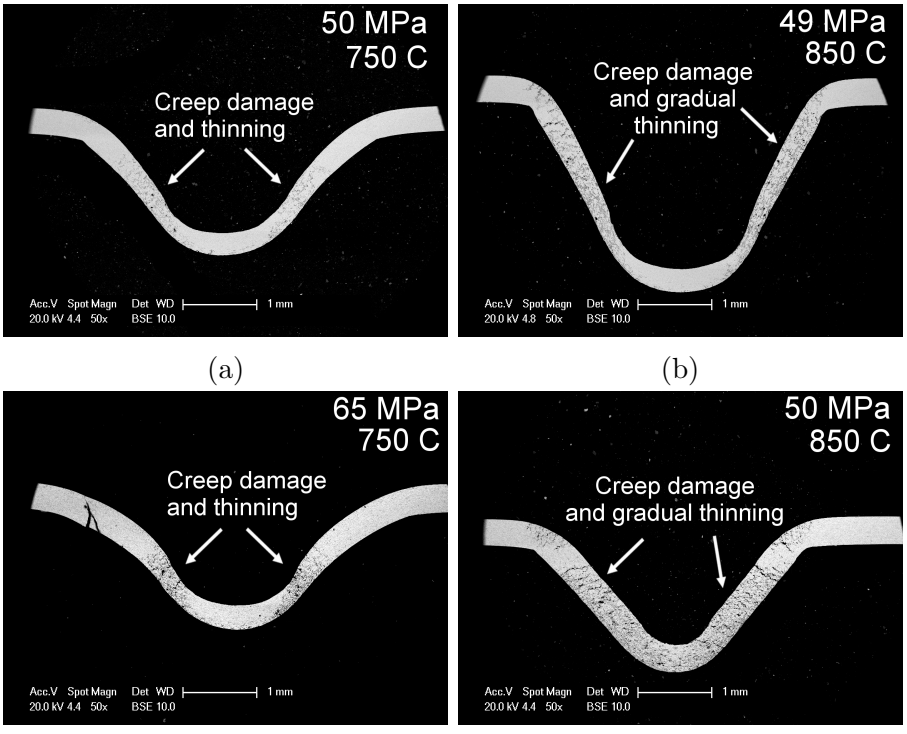

FIGURE 6.29: BSE images of the C1 coating (a-b) and EP1 coating (c-d) after SPC testing at 750 °C (left) and 850 °C (right) showing the effect of superplasticity on the SPC deformation of the coatings at 850 °C.

6.7.5 Microscopic Void Formation During SPC Tests

For the specimens which failed at 750 and 850 °C, the locations of fracture corresponded to the areas which exhibit a high density of oxides and cracks. This has been reported previously for SPC specimens [63, 87–89, 135].

The oxides appeared to develop in the voids created during creep. The oxides then grew in the β-phase regions as β-phase depletion occurred. The brittle Al_2O_3 oxides then presumably caused cracks to develop in the coating during creep. Therefore, the creep failure of the coatings was linked to the rate of oxide growth, which in turn was dependent upon the formation of voids. For all three coatings, including the 850 °C specimens exhibiting superplasticity, voids appeared to form at the phase boundaries. Void formation at the phase boundaries was observed during the SPT tests, as described in chapter 5.

The formation of voids during the SPT tests was described with reference to dual-phase steels, and attributed to the strain incompatibility between the phases. The creep strain in a SPC test is not the same as the plastic strain in a SPT test, but if the different phases are considered to exhibit different creep rates during a SPC test, then strain incompatibility does exist between the phases, and the SPT test strain incompatibility model can be considered applicable to the SPC specimens. Given that the EP1 and EP3 coatings exhibited slower rates of creep, probably due to higher phase fractions of β-NiAl phase, it can be assumed that the different phases do indeed exhibit different creep rates.

Considering coating C1 first, which exhibited the lowest resistance to creep, the γ-Ni phase can be considered the ductile phase and the β-NiAl phase a harder strengthening phase. Hence, during the SPC test, the ductile γ-phase exhibits significant creep strain which causes void formation at the γ/β phase boundaries. As the coating continues to creep, voids coalesce and link to form cracks, which grow and eventually cause specimen failure. This development of voids was shown schematically in Fig.5.48 in section 5.9.4 for the SPT specimens. Similar void damage has been observed for dual-phase materials undergoing creep [171, 172]

which further demonstrates that the strain incompatibility model is applicable to the SPC specimens.

The EP1 and EP3 specimens also contained σ-Cr_2Co phase, which can be considered a non-ductile phase that exhibits different creep rates to the γ-Ni and β-NiAl phases. The additional phase boundaries caused by the σ-phase resulted in a higher density of void formation in the EP1 and EP3 coatings compared to the C1 coating, resulting in a lower strain to fracture, as illustrated in Fig.5.50 in section 5.9.4 for the SPT test specimens. Therefore, it can be concluded the σ-Cr_2Co phase lowers the overall strain to fracture, which was not clear from the SPC creep properties discusses in section 6.7.3.

No void formation was observed at the phase boundaries of the γ-Ni and γ'-Ni_3(Al,Ta) phases in the EP3 coating, which demonstrates the γ'-phase does not reduce the strain to fracture.

Chapter 7

Conclusions

The overall aim of this study was to investigate how the mechanical properties of thin ($\sim$ 400 μm) MCrAlY bond coats produced by HVOF thermal spraying were influenced by the coating microstructure. The research is novel in that there is no systematic study of how the microstructure of thin bond coats influences the strength and ductility of the coatings. Three experimental alloys were studied for the first time and the small punch test method was applied to investigate both the creep and tensile properties of the alloys. The main conclusions from the study are listed below.

7.1 Phase Evolution and Microstructure

- The C1 alloy powder exhibits a γ-Ni matrix and β-NiAl as a secondary phase. The EP2 alloy powder contains a β-NiAl primary phase with γ-Ni as a secondary phase. The EP1 and EP3 alloy powders contain only heavily segregated β-NiAl phase. This demonstrates the high cooling rate of the atomisation process suppressed the formation of the second phase, which was not necessarily to be expected. The EP1, EP2 and EP3 powders exhibit a dendritic microstructure with evidence of solute segregation (known

as 'coring') which occurred during the rapid solidification in atomisation process.

- The heat-treated (1100 °C for 2 h) C1 coating exhibits a γ-Ni matrix with β-NiAl as a secondary phase. The heat treated EP1, EP2 and EP3 coatings all exhibit a β-NiAl matrix phase with γ-Ni as a secondary phase. σ-Cr_2Co phase was also observed in the EP1, EP2 and EP3 coatings, as well as γ'-Ni_3(Al,Ta) phase in the EP2 and EP3 coatings. σ-Cr_2Co phase and γ'-Ni_3(Al,Ta) phase have only been reported in a limited number of studies and no study has investigated, in-depth, MCrAlY coatings that contain all four phases.

- CALPHAD calculations, using ThermoCalc and the TTNi7 database, provide a reasonably accurate description of the phase formation in both the commercial and the experimental alloys following vacuum heat treatment followed by cooling to room temperature. This is the first experimental evidence that the TTNi7 database can be applied to alloys in the composition range of the experimental alloys.

- Under accelerated oxidation conditions at 1100 °C, the EP1, EP2 and EP3 coatings exhibit greater aluminium oxide scale growth compared to the C1 coating. The oxide scale thickness of the EP1, EP2 and EP3 after 96 hours at 1100 °C were 5.0, 6.8 and 7.5 μm respectively.

7.2 Small Punch Tensile Properties and Fracture Behaviour

- For the first time, the SPT test has been used to evaluate mechanical properties of these experimental alloys over a wide range of temperatures. Because of low temperature brittle behaviour, the bi-axial yield strengths of the EP1 and EP3 coatings could only be calculated between 650-750 °C and 700-750 °C respectively. The EP1 coating exhibits the highest bi-axial yield

strength between 650-750 °C and a higher fracture strength than the EP3 coating between RT and 650 °C. The yield strength of the EP3 coating is similar to the C1 coating between 700-750 °C, which was surprising given the different microstructures of those coatings. The fracture strengths of coatings EP1 and EP3 increase between RT-600 °C and RT-650 °C respectively. The results demonstrate that above 650 °C, higher fractions of β-NiAl phase increase the yield strength of a MCrAlY coating and that below 650 °C, lower fractions of γ-Ni phase and higher fractions of σ-Cr_2Co phase embrittle a MCrAlY coating. They also demonstrate that the fracture strength of the EP1 and EP3 coatings increases between RT and 650°C which may be due to increasing ductility of the β-NiAl phase. This is the first time the tensile properties of thin MCrAlY bond coats have been correlated with reference to the detailed coating microstructure.

- The DBTT's of the C1, EP1 and EP3 coatings are 500-700, 600-700 and 650-750 °C respectively. This is the first time the DBTT's of these alloys has been determined from SPT testing. Higher fractions of β-NiAl phase were shown to increase the DBTT and decrease the ductility of a MCrAlY coating. Decreasing the fraction of γ-Ni phase or increasing the fraction of σ-Cr_2Co phase was also shown to reduce the ductility.

- Intergranular fracture was the main mode of fracture in the C1, EP1 and EP3 coatings. Voids and cracks generally developed at the phase boundaries due to strain incompatibility between the phases. The presence of σ-Cr_2Co phase in the EP1 and EP3 coatings reduced the ductility. The presence of γ'-Ni_3(Al,Ta) did not appear to significantly reduce the ductility of the EP3 coating. Transgranular fracture could also be observed in the EP1 and EP3 coatings, This correlation between fracture mechanisms of the MCrAlY coatings and coating microstructures provides important insight into how the constituent phases influence the tensile properties and fracture mechanisms.

7.3 Small Punch Creep Properties and Creep Behaviour

- For the first time, the SPC test has been employed to evaluate the creep properties of the EP1 and EP3 coatings. It is also the first time SPC tests have been conducted on the C1 coating at 850 °C. Coating EP3 exhibits a highest creep resistance at 750 °C whilst coating C1 exhibits the lowest. At 850 °C the EP1 coating exhibits a higher creep resistance than the C1 coating. The results show that higher fractions of β-NiAl increase the creep resistance and creep lifetime of a MCrAlY coating but also reduce the creep strain to fracture. The addition of γ'-Ni_3(Al,Ta) phase also appears to improve the creep resistance and creep lifetime of MCrAlY coatings. σ-Cr_2Co phase reduces the creep strain to fracture, as does reducing the fraction of γ-Ni phase. The influence of the constituent phases on the creep properties of MCrAlY coatings provides useful insight for the development of new TBC systems with improved creep resistance.

- At 850 °C coatings C1 and EP1 exhibit time dependent deformation behaviour at strain rates below 2×10^{-7} s^{-1} where the creep resistance and creep strain to fracture of the coatings significantly increases. The coatings also exhibit atypical SPC test deformation behaviour where thinning, void formation and crack growth are more evenly distributed throughout the SPC test specimen and do not tend to occur in the region of high tensile stress in a SPC specimen as predicted by FE modelling. The change in behaviour is possibly caused by the onset of superplasticity, which has been reported for MCrAlY coatings in a limited number of studies using uniaxial testing of bulk alloys.

- Void formation in the C1, EP1 and EP3 coatings during SPC tests at 750 and 850 °C occurs primarily at the phase boundaries. The presence of σ-Cr_2Co increases the number of phase boundaries in the EP1 and EP3 coatings, which increases the density of void formation and reduces the creep strain

to fracture. γ'-Ni_3(Al,Ta) also increases the number of phase boundaries but does not reduce the creep strain to fracture in the EP3 coating. These findings provide useful insight in to the creep failure mechanisms of MCrAlY bond coats which will be useful in the design of new TBC systems with improved creep lifetimes.

Chapter 8

Future Work

1. Repeat SPT and SPC tests on all three coatings would help to validate the current work. This would involve manufacturing a second batch of HVOF coatings. The results could then also be used to compare similar HVOF coatings manufactured in different spray batches.

2. Interrupted SPT and SPC tests would provide a clearer understanding of the tensile and creep plastic strain evolution within the coatings.

3. SPT tests at 850 and 950 °C would provide clearer understanding of how the coating microstructure influences the tensile properties of MCrAlY coatings above 750 °C.

4. EBSD analysis could be used to evaluate the microstructures of the tested SPC specimens in the clamped regions of the specimens. This would determine if any phase evolution took place during the SPC tests and allow a more detailed evaluation of the CALPHAD calculations made using ThermoCalc and the TTNi7 database.

5. Transmission electron microscopy (TEM) could be employed to investigate the presence of dislocations in individual grains of the SPC specimens. This would help to identify whether the coatings creep via diffusional or dislocation creep mechanisms.

6. Long term SPC tests on the C1 and EP1 coatings at 850 °C could be conducted to evaluate the effect of superplasticity on the SPC creep fracture strain and SPC creep lifetime of the coatings.

7. SPC tests could be conducted at 850 °C on coating EP3 to evaluate the influence of γ'-Ni_3(Al,Ta) phase on the creep properties of MCrAlY coatings at 850 °C. This would also evaluate if coating EP3 exhibits superplasticity at 850 °C.

8. The SPT test and SPC test could be used to determine the time-independent and time-dependent properties of the EP2 coating. This would allow a clearer understanding of how the γ'-Ni_3(Al,Ta) and σ-Cr_2Co phases influence the mechanical properties of MCrAlY coatings, by providing a comparison between a $\gamma/\beta/\gamma'$ coating and a $\gamma/\beta/\sigma$ coating.

9. SPC tests could be conducted at 950 °C to allow Larson-Miller parameters to be determined for the MCrAlY coatings. This would provide useful creep property data for the coatings which could be easily compared to the creep property data of other materials.

Bibliography

[1] B. Gunston. *Development of Jet and Turbine Aero Engines.* Patrick Stephens, 3rd edition, 2002.

[2] T. Giampaolo. *Gas Turbine Handbook: Principles and Practice.* The Fairmont Press, 5th edition, 2013.

[3] J.E. Watson. *Materials Science and Technologies : Superalloys : Production, Properties and Applications.* Nova Science, 2011.

[4] S. Bose. *High Temperature Coatings.* Butterworth-Heinemann, 2007.

[5] Y. Tamarin. *Protective Coatings for Turbine Blades.* ASM International, 2002.

[6] R.C. Reed. *Superalloys - Fundamentals and Applications.* Cambridge University Press, 2006.

[7] R. Sivakumar. High temperature coatings for gas turbine blades: A review. *Surface and Coatings Technology*, 37(2):139–160, 1989.

[8] A.G. Evans, D.R. Mumm, J.W. Hutchinson, G.H. Meier, and F.S. Pettit. Mechanism controlling the durability of thermal barrier coatings. *Progress in Materials Science*, 46, 2001.

[9] Y.H. Sohn, J.H. Kim, E.H. Jordan, and M. Gell. Thermal cycling of EB-PVD/MCrAlY thermal barrier coatings. i. microstructural development and spallation mechanisms. *Surface and Coatings Technology*, 146-147:70–78, 2001.

[10] M.J. Stiger, N.M. Yanar, M.G. Topping, F.S. Pettit, and G.H. Meier. Thermal barrier coatings for the 21st century. *Zeitschrift fuer Metallkunde*, 90(12): 1069–1078, 1999.

[11] R.A. Miller. Ceramic thermal barrier coatings for electric utility gas turbine engines. Technical report, National Aeronautics and Space Administration, 1986.

[12] M. Gell, J. Eric, V. Krishnakumar, B. McCarron, K.and Barber, Y.H. Sohn, and V.K. Tolpygo. Bond strength, bond stress and spallation mechanisms of thermal barrier coatings. *Surface and Coatings Technology*, 120–121:53 – 60, 1999. ISSN 0257-8972.

[13] W.D. Callister and D.G. Rethwisch. *Materials Science and Engineering.* John Wiley and Sons, 8th edition, 2011.

[14] M.F. Ashby and D.R.H. Jones. *Engineering Materials 1: An introduction to properties, application and design.* Butterworth-Heinemann, 3rd edition, 2005.

[15] R.W. Evans and B. Wilshire. *Introduction to Creep.* Maney Publishing, 1993.

[16] J. Weertman. Theory of steady-state creep based on dislocation climb. *Journal of Applied Physics*, 26(10), 1955.

[17] B. Gleeson. *Corrosion and Environmental Degradation*, volume 2 of *Materials Science and Technology*, chapter High-Temperature Corrosion of Metallic Alloys and Coatings, pages 173–228. Wiley-VCH, 2000.

[18] M. J. Prescott, R.and Graham. The formation of aluminum oxide scales on high-temperature alloys. *Oxidation of Metals*, 38(3):233–254, Oct 1992. ISSN 1573-4889.

[19] I.M. Allam, D.P. Whittle, and J. Stringer. The oxidation behaviour of CoCrAl systems containing active element additions. *Oxidation of Metals*, 12(1), 1978.

[20] W.J. Quadakkers. Growth mechanisms of oxide scales on ODS alloys in the temperature range 1000-1100 c. *Werkstoffe und Korrosion*, 41:659–668, 1990.

[21] C.W. Price, G. Wright, and G.Z. Wallwork. Examination of oxide scales in the SEM using backscattered electron images. *Metallurgical and Materials Transactions B: Process Metallurgy and Materials Processing Science*, 4(10): 2423–2427, 1973.

[22] J.G. Smeggil, A.W. Funkenbusch, and N.S. Bornstein. A relationship between indigenous impurity elements and protective oxide scale adherence characteristics. *Metallurgical and Materials Transactions A: Physical Metallurgy and Materials Science*, 17(6):923–932, 1986.

[23] K.L. Luthra and C.L. Briant. Mechanism of adhesion of alumina on MCrAlY alloys. *Oxidation of Metals*, 26(5-6):397–416, 1986.

[24] T.A. Taylor and D.F. Bettridge. Development of alloyed and dispersion-strengthened MCrAlY coatings. *Surface and Coatings Technology*, 86-87:9–14, 1996.

[25] B. Zeumer and G. Sauthoff. Intermetallic NiAl-Ta alloys with strenghening laves phase for high-temperature applications. i. basic properties. *Intermetallics*, 5(6): 563–577, 1997.

[26] D.R.G. Achar, R. Munoz-Arroyo, L. Singheiser, and W.J. Quadakkers. Modelling of phase equilibria in MCrAlY coating systems. *Surface and Coatings Technology*, 187:272–283, 2004.

[27] J. Toscano, A. Gil, T. Huttel, E. Wessel, D. Naumenko, L. Singheiser, and W.J. Quadakkers. Temperature dependence of phase relationships in different types of MCrAlY - coatings. *Surface and Coatings Technology*, 202:603–607, 2007.

[28] C. Costa, E. Barbareschi, P. Guarnone, and G. Borzone. Phase evolution in an MCrAlY coating during high temperature exposure. *Journal of Mining and Metallurgy, Section B: Metallurgy*, 48(3):359–365, 2012.

[29] H. Chen, T.H. Hyde, Voisey K.T., and D.G. McCartney. Application of small punch creep testing to a thermally sprayed CoNiCrAlY bond coat. *Materials Science and Engineering: A*, 585:205–213, 2013.

[30] T. Mori, S. Kuroda, M. Hideyuki, H. Katanoda, Y. Sakamoto, and S. Newman. Effect of initial oxidation on beta phase depletion and oxidation of CoNiCrAlY bond coat coatings fabricated by warm spray and HVOF processes. *Surface and Coatings Technology*, 221:59–69, 2013.

[31] S. Saeidi, Voisey K.T., and D.G. McCartney. The effect of heat treatment and the oxidation behaviour of HVOF and VPS CoNiCrAlY coatings. *J. Thermal Spray Tech.*, 18:209–216, 2009.

[32] R.D. Jackson. *The Effect of Bond Coat Oxidation on the Microstructure and Endurance of Two Thermal Barrier Coating Systems*. PhD thesis, University of Birmingham, 2009.

[33] P. Richer, M. Yandouzi, L. Beauvais, and B. Jodoin. Oxidation behavior of CoNiCrAlY bond coats produced by plasma, HVOF and cold gas dynamic spraying. *Surface and Coatings Technology*, 204:3962–3974, 2010.

[34] P. Poza and P.S. Grant. Microstructure evolution of vacuum plasma sprayed CoNiCrAlY coatings after heat treatment and isothermal oxidation. *Surface and Coatings Technology*, 201(6):2887–2896, 2006.

[35] Y. Itoh, M. Saitoh, and M. Tamura. Characteristics of mcraly coatings sprayed by high velocity oxygen-fuel spraying system. *Journal of Engineering for Gas Turbines and Power*, 122:43–49, 2000.

[36] P. Song, D. Naumenko, R. Vassen, L. Singheiser, and W.J. Quadakkers. Effect of oxygen content in NiCoCrAlY bondcoat on the lifetimes of EB-PVD and APS thermal barrier coatings. *Surface and Coatings Technology*, 221:207–213, 2013.

[37] A. Gil, D. Naumenko, R. Vassen, J. Toscano, M. Subanovic, L. Singheiser, and W.J. Quadakkers. Y-rich oxide distribution in plasma sprayed MCrAlY- coatings studied by SEM with a cathodoluminescence detector and raman spectroscopy. *Surface and Coatings Technology*, 204:531–538, 2009.

[38] D. Texier, D. Monceau, F. Crabos, and E. Andrieu. Tensile properties of a non-line-of-sight processed β-γ-γ' MCrAlY coating at high temperature. *Surface and Coatings Technology*, 326(A):28–36, 2017.

[39] M. Eskner and R. Sandstrom. Mechanical properties and temperature dependence of an air plasma-sprayed NiCoCrAlY bondcoat. *Surface and Coatings Technology*, 200(8):2695 – 2703, 2006. ISSN 0257-8972.

[40] H. Brodin and M. Eskner. The influence of oxidation on mechanical and fracture behaviour of an air plasma-sprayed NiCoCrAlY bondcoat. *Surface and Coatings Technology*, 187:113–121, 2004.

[41] K.J. Hemker, B.G. Mendis, and C. Eberl. Characterizing the microstructure and mechanical behaviour of a two-phase NiCoCrAlY bond coat for thermal barrier systems. *Materials Science and Engineering A*, 483-484:77–730, 2008.

[42] J. Toscano. *Influence and Composition and Processing on the Oxidation Behaviour of MCrAlY-Coatings for TBC Applicatiions*. PhD thesis, Energy and Environment, Research Centre Julich, 2009.

[43] E. Lugscheider, C. Herbst, and L. Zhao. Parameter studies on high-velocity oxy-fuel spraying of MCrAlY coatings. *Surface and Coatings Technology*, 108-109: 16–23, 1998.

[44] P. Niranatlumpong, C.B. Ponton, and H.E. Evans. The failure of protective oxides on plasma-sprayed NiCrAlY overlay coatings. *Oxidation of Metals*, 53(3/4), 2000.

[45] D. Naumenko, V. Shemet, L. Singheiser, and W.J. Quadakkers. Failure mechanisms of thermal barrier coatings on MCrAlY-type bondcoats associated with the formation of the thermally grown oxide. *Journal of Materials Science*, 44(7):1687–1703, Apr 2009. ISSN 1573-4803.

[46] H. Chen, G.A. Jackson, Voisey K.T., and D.G. McCartney. Modelling and experimental study on β-phase depletion behaviour of HVOF sprayed free-standing conicraly coatings during oxidation. *Surface and Coatings Technology*, 291:34–42, 2016.

[47] Y. Itoh and M. Saitoh. Mechanical properties of overaluminized MCrAlY coatings at room temperature. *Journal of Engineering for Gas Turbines and Power*, 127: 807–813, 2005.

[48] W. Brandl, H.J. Grabke, D. Toma, and J. Kruger. The oxidation behaviour of sprayed mcraly coatings. *Surface and Coatings Technology*, 86-87(1):41–47, 1996.

[49] D.J. Wortman, E.C. Duderstadt, and W.A. Nelson. Bond coat development for thermal barrier coatings. *Journal of Engineering for Gas Turbines and Power*, 112:527–530, 1990.

[50] A. Feuerstein, J. Knapp, T. Taylor, A. Ashary, A. Bolcavage, and N. Hitchman. Technical and economical aspects of current thermal barrier coating systems for gas turbine engines by thermal spray and EBPVD: A review. *Journal of Thermal Spray Technology*, 17(2):199–213, 2008.

[51] V. Higuera, F.J. Belzunce, and J. Riba. Influence of the thermal-spray procedure on the properties of a CoNiCrAlY coating. *Surface and Coatings Technology*, 200: 5550–5556, 2006.

[52] M.L. Thorpe and H.J. Richter. A pragmatic analysis and comparison of hvof processes. *Journal of Thermal Spray Technology*, 1(2):161–170, 1992.

[53] W. Saechua. *Optimisation of HVOF sprayed MCrAlY coatings for gas turbine.* PhD thesis, University of Nottingham, 2014.

[54] B. Rajasekaran, G. Mauer, and R. VaBen. Enhanced characteristics of HVOF-sprayed MCrAlY bond ccoat for TBC applications. *Thermal Spray Technology*, 20(6):1209–1216, 2011.

[55] T. Marrocco. *Development of Improved Cold Spray and HVOF Deposited Coatings.* PhD thesis, Faculty of Engineering, 2008.

[56] S. Saeidi. *Microstructure, Oxidation and Mechanical Properties of As-sprayed and ACoatingsHVOF and VPS CoNiCrAlY Coatings.* PhD thesis, University of Nottingham, 2010.

[57] L. Zhao, M. Parco, and E. Lugsheider. High velocity oxy-fuel thermal sprspray of a NiCoCrAlY alloy. *Surface and Coatings Technology*, 179:272–278, 2004.

[58] S. Saeidi, Voisey K.T., and D.G. McCartney. Mechanical properties and microstructure of VPS and HVOF CoNiCrAlY coatings. *Thermal Spray Technology*, 20(6):1231–1243, 2011.

[59] D. Zhang, S.J. Harris, and D.G. McCartney. Microstructure formation and corrosion behaviour in hvof-sprayed inconel 625 coatings. *Materials Science & Engineering, A*, 344:45–56, 2003.

[60] S. Gu, C.N. Eastwick, K.A. Simmons, and D.G. McCartney. Computational fluid dynamic modeling of gas flow characteristics in a high-velocity oxy-fuel thermal spray system. *Journal of Thermal Spray Technology*, 10(3):461–469, 2001.

[61] R. L. Chang, C. H.and Moore. Numerical simulation of gas and particle flow in a high-velocity oxygen-fuel (hvof) torch. *Journal of Thermal Spray Technology*, 4 (4):358, Dec 1995. ISSN 1544-1016.

[62] R.T. Kiepura, H.F. Lampman, P. Thomas, and N.D. Wheaton, editors. *ASM Handbook Volume 4, Heat Treating.* ASM International, 1991.

[63] H. Chen. *Mechanical and Chemical Behaviour of Thermall Sprayed CoNiCrAlY Bond Coats.* PhD thesis, University of Nottingham, 2014.

[64] C. Duret-Thual, R. Morbioli, and P. Steinmetz. A guide to the control of high temperature corrosion and protection of gas turbine materials. Technical report, Commission of European Communities, 1986.

[65] G.W. Goward. Progress in coatings for gas turbine airfoils. *Surface and Coatings Technology*, 108-109:73–79, 1998.

[66] G.W. Meetham. Use of protective coatings in aero gas turbine engines. *Materials Science and Technology*, 2(3):290–294, 1986.

[67] M. Eskner and R. Sandstrom. Measurement of the ductile-to-brittle transition temperature in a nickel aluminide coating by a miniaturised disc bending test technique. *Surface and Coatings Technology*, 165(1):71 – 80, 2003. ISSN 0257-8972.

[68] G. Sauthoff. *Mechanical Properties of Complex Intermetallics*, chapter Deformation of Intermetallic Alloys at High Temperature, pages 125–159. World Scientific Publishing Company, 2010.

[69] W.F. Hosford. *Mechanical Behavior of Materials*. 2010.

[70] D.B. Miracle and R. Darolia. *Structural Applications of Intermetallic Compounds*, chapter NiAl and it's alloys, pages 55–74. John Wiley and Sons, 2000.

[71] R. Subramanian, Y. Mori, S. Yamagishi, and M. Okazaki. Thermo-mechanical fatigue failure of thermal barrier coated superalloy specimen. *Metallurgical and Materials Transactions A*, 46(9):3999–4012, Sep 2015. ISSN 1543-1940.

[72] A.A. Wereszczak, J.G. Hemrick, T.P. Kirkland, J.A. Haynes, T.J. Fitzgerald, and J.E. Junkin. Stress relaxation of MCrAlY bond coat alloys as a function of temperature and strain. In *Manufacturing Materials and Metallurgy; Ceramics; Structures and Dynamics; Controls, Diagnostics and Instrumentation; Education*, volume 5, 1998.

[73] M.Z. Alam, D. Chatterjee, S.V. Kamat, V. Jayaram, and Das. D.K. Evaluation of ductile-brittle transition temperature (dbtt) of aluminide bond coats by micro-tensile test method. *Materials Science & Engineering, A: Structural Materials: Properties, Microstructure and Processing*, 527:7147–7150, 2010.

[74] A.K. Ray, N. Roy, A. Kar, A.K. Ray, S.C. Bose, G. Das, J. K. Sahu, D. K. Das, B. Venkataraman, and S. V. Joshi. Mechanical property and characterization of a NiCoCrAlY type metallic bond coat used in turbine blade. *Materials Science and Engineering: A*, 505(1–2):96 – 104, 2009. ISSN 0921-5093.

[75] H. Waki, T. Kitamura, and A. Kobayashi. Effect of thermal treatment on high-temperature mechanical properties enhancement in LPPS, HVOF, and APS CoNiCrAlY coatings. *Journal of Thermal Spray Technology*, 18(4):500–509, 2009. ISSN 1544-1016.

[76] M.I. Wood. The mechanical properties of coatings and coated systems. *Materials Science and Engineering*, A121:633–643, 1989.

[77] J. Alcala, F. Gaudette, S. Suresh, and S. Sampath. Instrumented spherical micro-indentation of plasma-sprayed coatings. *Materials Science and Engineering: A*, 316(1–2):1 – 10, 2001. ISSN 0921-5093.

[78] R. Webler, M. Ziener, S. Neumeier, P.J. Terberger, R. VaBen, and M. Goken. Evolution of microstructure and mechanical properties of coated Co-base superalloys during heat treatment and thermal exposure. *Materials Science and Engineering A*, 628:374–381, 2015.

[79] W.J. Brindley and J.D. Whittenberger. Stress relaxation of plasma sprayed NiCoCrAlY alloys. *Materials Science & Engineering, A: Structural Materials: Properties, Microstructure and Processing*, 163:33–41, 1993.

[80] J.A. Thompson, Y.C. Tsui, R.C. Reed, D.S. Rickerby, and T.W. Clyne. Creep of plasma spspray CoNiCrAlY and NiCrAlY bond coats and it's effect on residual stresses during thermal cycling of thermal barrier coating systems. In J. Nicholls, editor, *High Temperature Surface Engineering*, pages 199–212. IOM, Maney, 2000.

[81] M.G. Hesbur and R.V. Miner. High temperature tensile and creep behaviour of low pressure plasma-sprayed NiCoCrAlY coating alloy. *Materials Science and Engineering*, 83:239–245, 1986.

[82] J. Schwarzer and O. Vohringer. High-temperature deformation behavior of the bond coat alloy pwa 1370. *Advanced Engineering Materials*, 5(7):490–493, 2003. ISSN 1527-2648.

[83] X.C. Zhang, C.J. Liu, F.Z. Xuan, Z.D. Wang, and S.T. Tu. Effect of nicr and nicral coatings on the creep resistance of a ni alloy. *Materials Science and Engineering: A*, 528(6):2282 – 2287, 2011.

[84] L. Ajdelsztajn, D. Hulbert, A. Mukherjee, and J.M. Schoenung. Creep deformation mechanism of cryomilled NiCrAlY bond coat material. *Surface and Coatings Technology*, 201(24):9462 – 9467, 2007. ISSN 0257-8972.

[85] M.P. Taylor, H.E. Evans, C.B. Ponton, and J.R. Nicholls. A method for evaluating the creep properties of overlay coatings. *Surface and Coatings Technology*, 124: 13–18, 2000.

[86] Y. Itoh, M. Saitoh, and Y. Ishiwata. Influence of high-temperature protective coatings on the mechanical properties of nickel-based superalloys. *Journal of Materials Science*, 34(16):3957–3966, Aug 1999. ISSN 1573-4803.

[87] Naveena and S. Komazaki. Evaluation of creep rupture strength of high nitrogen ferritic heat-resistant steels using small punch creep testing technique. *Materials Science and Engineering: A*, 676:100 – 108, 2016. ISSN 0921-5093.

[88] M.F. Moreno. Application of small punch testing on the mechanical and microstructural characterizations of p91 steel at room temperature. *International Journal of Pressure Vessels and Piping*, 142:1 – 9, 2016. ISSN 0308-0161.

[89] Zhixiang Zhou, Yangyan Zheng, Xiang Ling, Ruomei Hu, and Jianqiu Zhou. A study on influence factors of small punch creep test by experimental investigation and finite element analysis. *Materials Science and Engineering: A*, 527(10):2784 – 2789, 2010. ISSN 0921-5093.

[90] T. Hyde, H. Stoyanov, W. Sun, and C.J. Hyde. On the interpretation of results from small punch creep tests. *Journal of Strain Analysis for Engineering Design*, 45:141–164, 2010.

[91] M. Evans and D. Wang. The small punch creep test: some results from a numerical model. *Journal of Materials Science*, 43(6):1825–1835, Mar 2008. ISSN 1573-4803.

[92] J. Chen, Y.W. Ma, and K.B. Yoon. Finite element study for determination of material's creep parameters from small punch test. *Journal of Mechanical Science and Technology*, 24(6):1195–1201, Jun 2010. ISSN 1976-3824.

[93] F.M. Huang and G.L. Hamilton, M.L. ad Wire. Bend testing for miniature disks. *Nuclear Technology*, 57(2):234–242, 1982.

[94] J.M. Baik and J. Kameda. Small punch test evaluation of intergranular embrittlement of an alloy steel. *Scripta Metallurgica*, 17(12):1443–1447, 1983.

[95] J. Kameda. A kinectic model for ductile-brittle fracture mode transition behaviour. *Acta Metallurgica*, 34(12):2391–2398, 1986.

[96] M.P. Manahan, A.S. Argon, and O.K. Harling. The development of a miniaturized disk bend test for the determination of postirradiation mechanical properties. *Journal of Nuclear Materials*, 104:1545–1550, 1981.

[97] A. Okada and M. Hamilton. Microbulge testing applied to neutron irradiated materials. *Journal of Nuclear Materials*, 179:445–448, 1991.

[98] X. Mao, T. Shoji, and H. Takahashi. Characterization of fracture behaviour in small punch test by combined recrystallization-etch method and rigid plastic analysis. *Journal of Testing and Evaluation*, 15(1):30–37, 1987.

[99] X. Mao and H. Takahashi. Development if a further-miniaturised specimen of 3mm diameter for tem disk. *Journal of Nuclear Materials*, 150(1):42–52, 1987.

[100] H. Li, F.C. Chen, and A.J. Ardell. A simple versatile disk-bend test apparatus for quantatative yield-stress measurements. *Metallurgical and Materials Transactions A: Physical Metallurgy and Materials Science*, 22(9):2061–2068, 1991.

[101] *CEN CWA 15627 Workshop Agreement: Small punch test method for metallic materials*. European Committee for Standardization, Brussels, December 2006.

[102] G. Lucas and A. Okada. Parametric analysis of the disc bend test. *Journal of Nuclear Materials*, 141:532–535, 1986.

[103] R. Hurst and K. Matocha. Experiences with the european code of practice for small punch testing for creep, tensile and fracture behaviour. In *Determination of Mechanical Properties of Materials by Small Punch and Other Miniature Testing Techniques*, pages 1–26, September 2014.

[104] T.E. Garcia, C. Rodriguez, F.J. Belzunce, and C. Suarez. Estimation of the mechanical properties of metallic materials by means of the small punch test. *Journal of Alloys and*, 582:708–717, 2014.

[105] E. Altstadt, H.E. Ge, V. Kuksenko, M. Serrano, M. Houska, M. Lasan, M. Bruchhausen, J.M. Lapetite, and Y. Dai. Critical evaluation of the small punch test as a screening procedure for mechanical properties. *Journal of Nuclear Materials*, 472:186–195, 2016.

[106] J. Kameda and O. Buck. Evaluation of the ductile-to-brittle transition temperature shift due to temper embrittlement and neutron irradiation by means of a small-punch test. *Materials Science and Engineering*, 83(1):29–38, 1986.

[107] E. Fluery and J.S. Ha. Small punch tests to estimate the mechanical properties of steels for steam power plant: I. mechanical strength. *International Journal of Pressure Vessels and Piping*, 75:699–706, 1998.

[108] S. Soltysiak, M. Selent, S. Roth, M. Abendroth, M. Hoffman, H. Biermann, and M. Kuna. High-temperature small punch test for mechanical characterization of a nickel-base super alloy. *Materials Science & Engineering, A: Structural Materials: Properties, Microstructure and Processing*, 613:259–263, 2014.

[109] R.J. Lancaster, H.W. Illsley, G.R. Davies, S.P. Jeffs, and G.J. Baxter. Modelling the small punch tensile behaviour of an aerospace alloy. *Materials Science and Technology*, 0(0):1–9, 2016.

[110] J.C.K. Mak. *Small Punch Testing of Advanced Metal Matrix Composites*. PhD thesis, Faculty of Science, University of Technology Sydney, 2011.

[111] M.P. Manahan. A new postirradiation mechanical behaviour test - the miniaturized disk bend test. *Nuclear Technology*, 1983.

[112] V. Vorlicek, L.F. Exworthy, and P.E.J. Flewitt. Evaluation of a miniaturized disc test for establishing the mechanical properties of low-alloy ferritic steels. *Journal of Materials Science*, 30(11):2936–2943, 1995.

[113] M. Coleman, H. Alsherhri, R. Banik, W. Harrison, and S. Birosca. Deformation mechanisms of in713c nickel based superalloy during small punch testing. *Materials Science & Engineering, A: Structural Materials: Properties, Microstructure and Processing*, 650:422–431, 2016.

[114] S. Rasche and M. Kuna. Improved small punch testing and parameter identification of ductile to brittle materials. *International Journal of Pressure Vessels and Piping*, 125:23–34, 2015.

[115] R. Lacalle, J.A. Alvarez, and F. Gutierrez-Solana. Analysis of key factors for the interpretation of small punch test results. *Fatigue and Fracture of Engineering Materials and Structures*, 31(10):841–928, 2008.

[116] J. Siegl, P. Hausild, A. Janca, and R. Kopriva. Fractographic aspects of small punch test results. *Procedia Materials Science 3*, pages 912–917, 2014.

[117] J. Kameda and X. Mao. Small-punch and TEM-disc testing technique and their application to characterization of radiation damage. *Journal of Materials Science*, 27(4):983–989, 1992.

[118] X. Mao. Small punch test to predict ductile fracture toughness J_{IC} and brittle fracture toughness K_{IC}. *Scripta Metallurgica et Materialia*, 25:2481–2485, 1991.

[119] J. Isselin and T. Shoji. Yield strength evaluation by small-punch test. *Journal of Testing and Evaluation*, 37(6):531–537, 2009.

[120] J.S. Cheon and I.S. Kim. Initial deformation during small punch testing. *Journal of Testing and Evaluation*, 24(4):255–262, 1996.

[121] R.J. Roark and W.C. Young. *Formula's for Stress and Strain.* McGraw-Hill, New York, 1975. pg 366.

[122] D.T. Blagoeva and R.C. Hurst. Application of the cen (european committee for standardization) small punch creep testing code of practice to a representative repair welded p91 pipe. *Materials Science and Engineering: A*, 510:219 – 223, 2009. ISSN 0921-5093. 11th International Conference of Creep and Fracture of Engineering Materials and Structures, CREEP 2008.

[123] Y.S. Chang, J.M. Kim, J.B. Cho, Y.J. Kim, M.C. Kim, and B.S. Lee. Derivation of ductile fracture resistance by use of small punch specimens. *Engineering Fracture Mechanics*, 75:3413–3427, 2008.

[124] M. Abendroth and M. Kuna. Identification of ductile damage and fracture parameters from the small punch test using neural network. *Engineering Fracture Mechanics*, 73:710–725, 2006.

[125] J.D. Parker and J.D. James. Disc-bend creep deformation behaviour of 1/2Cr1/2Mo1/4V low alloy steel. In *Creep and fracture of engineering materials and structures*, pages 651–660, 1993.

[126] K.I. Kobayashi, I. Kajihara, H. Koyama, and G.C Stratford. Deformation and fracture mode during small punch creep tests. *Journal of Solid Mechanics and Materials Engineering*, 4(1):75–86, 2010.

[127] J.P. Rouse, F. Cortellino, W. Sun, T.H. Hyde, and J. Shingledecker. Small punch creep testing: review on modelling and data interpretation. *Materials Science and Technology*, 29(11):1328–1345, 2013.

[128] J. Chakrabarty. A theory of stretch forming over hemispherical punch heads. *International Journal of Mechanical Sciences*, 12:315–325, 1970.

[129] Z. Yang and Z. Wang. Relationship between strain and central deflection in small punch creep specimens. *International Journal of Pressure Vessels and Piping*, 80: 397–404, 2003.

[130] Y. Li, M. Sun, and C. Zhang. Practical approach to determine creep properties from small punch test. In M. Karel, R. Hurst, and W. Sun, editors, *2nd International Conference SSTT Determination of Mechanical Properties of Materials by Small Punch and Other Minature Testing Techniques*, pages 47–63. Ocelot, 2012.

[131] Y. W. Ma, K., S. Shim, and K. B. Yoon. Assessment of power law creep constants of gr91 steel using small punch creep tests. *Fatigue & Fracture of Engineering Materials & Structures*, 32(12):951–960, 2009. ISSN 1460-2695.

[132] B. Cacciapuoti, W. Sun, and D.G. McCartney. A study on the evolution of the contact angle of small punch creep test of ductile materials. *International Journal of Pressure Vessels and Piping*, 145:60–74, 2016.

[133] L. Zhao, H. Jing, L. Xu, Y. Han, J. Xiu, and Y. Qiao. Evaluating of creep property of distinct zones in p92 steel welded joint by small punch creep test. *Materials & Design*, 47:677 – 686, 2013. ISSN 0261-3069.

[134] P. Dymacek and K. Milicka. Creep small-punch testing and its numerical simulations. *Materials Science and Engineering: A*, 510:444 – 449, 2009. ISSN 0921-5093. 11th International Conference of Creep and Fracture of Engineering Materials and Structures, CREEP 2008.

[135] M. Saucedo-Munoz, S.I. Komazaki, Hashida T., and V. Lopez-Hirata. Small punch creep test in a 316 austenitic stainless steel. *Revista de Metalurgia*, 51(1), 2015.

[136] R.J. Lancaster, W.J. Harrison, and G. Norton. An analysis of small punch creep behaviour in the gamma-titanium aluminide ti-45al-2mn-2nb. *Materials Science and Engineering: A*, 626:263 – 274, 2015. ISSN 0921-5093.

[137] J. Ganesh Kumar, V. Ganesan, and K. Laha. Analyses of transient and tertiary small punch creep deformation of 316ln stainless steel. *Metallurgical and Materials Transactions A*, 47(9):4484–4493, Sep 2016. ISSN 1543-1940.

[138] S. Zhang, L. Li, and A. Kumar. *Materials Characterization Techniques*. CRC Press, 2009.

[139] M.D. Ball and D.G. McCartney. The measurement of atomic number and composition in an sem using backscattered detectors. *Journal of Microscopy*, 124 (1):57–68, 1981.

[140] A.J. Schwartz, M. Kumar, B.L. Adams, and D.P. Field. *Electron backscatter diffraction in materials science*. Springer Verlag, 2009.

[141] B.D. Cullity. *Elements of X-Ray Diffraction*. Prentice Hall, 3rd edition, 2001.

[142] X.J. Yan. *microstructural evolution of MCrAlY coated Ni-based superalloy systems*. PhD thesis, Loughborough University, 2014. Closed Access.

[143] C.J. Kong. *Microstructural evolution in AISn-based gas atomised powder and thermally sprayed coatings*. PhD thesis, University of Nottingham, 2004.

[144] D.A. Porter and K.E. Easterling. *Phase Transformations in Metals and Alloys*. Chapman & Hall, 2nd edition, 1992.

[145] B. Baufeld and M. Schmucker. Microstructural evolution of a nicocraly coating on an in100 substrate. *Surface and Coatings Technology*, 199(1):49 – 56, 2005. ISSN 0257-8972.

[146] W. Brandl, D. Toma, J. Kruger, H. Grabke, and G. Matthaus. The oxidation behaviour of HVOF ththermal-spray MCrAlY coatings. *Surface and Coatings Technology*, 94-95:21–26, 1997.

[147] R. Goti, M. Betaille-Francoual, E. Hourcastagne, B. Viguier, and F. Crabos. Isothermal oxidation behaviour of nicocralyta coatings produced by hvof spraying and tribomet process. *Oxidation of Metals*, 81:105–113, 2014.

[148] B.G. Mendis, B. Tryon, T.M. Pollock, and K.J. Hemker. Microstructural observations of as-prepared and thermal cycled nicocraly bond coats. *Surface and Coatings Technology*, 201(7):3918 – 3925, 2006. ISSN 0257-8972. Proceedings of the 33rd International Conference on Metallurgical Coatings and Thin Films.

[149] A. Rabiei and A.G. Evans. Failure mechanisms associated with thermally grown oxide in plasma sprayed thermal barrier coatings. *Acta Metallurgica*, 48:3963–3976, 2000.

[150] J.J. Liang, K. Matsumoto, K. Kawagishi, and H. Harada. Morphological evolution of thermal barrier coatings with equilibrium (eq) and nicocraly bond coats during thermal cycling. *Surface and Coatings Technology*, 207:413 – 420, 2012. ISSN 0257-8972.

[151] K. Yuan, R. Eriksson, R.L. Peng, X.H. Li, S. Johansson, and Y.D. Wang. MCrAlY coating design based on oxidation-diffusion modelling. part i: Microstructural evolution. *Surface and Coatings Technology*, 254:79–96, 2014.

[152] Y.J. Xie, D. Wang, M.S. Wang, and W. Ye. Evaluation of three kinds of mcraly coatings produced by electrospark deposition. *Transactions of Nonferrous Metals Society of China*, 26(6):1647 – 1654, 2016. ISSN 1003-6326.

[153] C. Kaplin and M. Brochu. The effect of grain size on the oxidation of NiCoCrAlY. *Applied Surface Science*, 301:258–263, 2014.

[154] Special Metals. In625 alloy data sheet. Technical report. URL www.specialmetalswiggins.co.uk/products/inconel-alloy-625.

[155] R.D. Noebe, A. Misra, and R. Gibala. Plastic flow and fracture of b2 nial-based intermetallic alloys containing a ductile second phase. *ISIJ International*, 31(10): 1172–1185, 1991.

[156] M. Durand-Charre. *The Microstructure of Superalloys*. Gordon and Breach Science, 1997.

[157] A.K. Ray. Failure mode of thermal barrier coatings for gas turbine vanes under bending. *International journal of turbo and jet-engines*, 17(1):1–24, 2000.

[158] Y.H. Zhang, P.J. Withers, M.D. Fox, and D.M. Knowles. Damage mechanisms of coated systems under thermomechanical fatigue. *Materials Science and Technology*, 15(9):1031–1036, 1999.

[159] M. Funk, K. Ma, C. Eberl, J. M. Schoenung, M. Göken, and K. J. Hemker. High-temperature mechanical behavior of end-of-life cryomilled nicraly bond coat materials. *Metallurgical and Materials Transactions A*, 42(8):2233, Mar 2011. ISSN 1543-1940.

[160] Z.B. Chen, Z.G. Wang, and S.J. Zhu. Tensile fracture behavior of thermal barrier coatings on superalloy. *Surface and Coatings Technology*, 205(15):3931 – 3938, 2011. ISSN 0257-8972.

[161] I. Vougiouklakis, P. Hahner, F. De Haan, V. Kostopoulos, and S. Petevs. Damage mode analysis of mcraly overlay coatings subjected to isothermal stepwise tensile testing by using in situ video imaging and acoustic emission monitoring. *Fatigue & Fracture of Engineering Materials & Structures*, 27(3):219–230, 2004. ISSN 1460-2695.

[162] M. Calcagnotto, Y. Adachi, D. Ponge, and D. Raabe. Deformation and fracture mechanisms in fine- and ultrafine-grained ferrite/martensite dual-phase steels and the effect of aging. *Acta Materialia*, 59:658–670, 2011.

[163] J. Kadkhodapour, A. Butz, and S. Ziaei Rad. Mechanisms of void formation during tensile testing in a commercial, dual-phase steel. *Acta Materialia*, 59(7): 2575 – 2588, 2011. ISSN 1359-6454.

[164] K. Park, M. Nishiyama, N. Nakada, T. Tsuchiyama, and S. Takaki. Effect of the martensite distribution on the strain hardening and ductile fracture behaviors in dual-phase steel. *Materials Science and Engineering: A*, 604:135 – 141, 2014. ISSN 0921-5093.

[165] M. Azuma, S. Goutianos, N. Hansen, G. Winther, and X. Huang. Effect of hardness of martensite and ferrite on void formation in dual phase steel. *Materials Science and Technology*, 28(9-10):1092–1100, 2012.

[166] H. Ghadbeigi, C. Pinna, S. Celotto, and J.R. Yates. Local plastic strain evolution in a high strength dual-phase steel. *Materials Science and Engineering: A*, 527 (18):5026 – 5032, 2010. ISSN 0921-5093.

[167] C.C. Tasan, J.P.M. Hoefnagels, and M.G.D. Geers. Microstructural banding effects clarified through micrographic digital image correlation. *Scripta Materialia*, 62 (11):835 – 838, 2010. ISSN 1359-6462.

[168] H.P. Shen, T.C. Lei, and J.Z. Liu. Microscopic deformation behaviour of martensitic–ferritic dual-phase steels. *Materials Science and Technology*, 2(1): 28–33, 1986.

[169] S.P. Jeffs and R.J. Lancaster. Elevated temperature creep deformation of a single crystal superalloy through the small punch creep method. *Materials Science & Engineering, A: Structural Materials: Properties, Microstructure and Processing*, 626:330–337, 2015.

[170] M.P. Taylor, H.E. Evans, E.P. Busso, and Z.Q. Qian. Creep properties of a pt-aluminide coating. *Acta Materialia*, 54:3241–3252, 2006.

[171] C.H. Shek, D.J. Li, K.W. Wong, and J.K.L. Lai. Creep properties of aged duplex stainless steels containing σ-phase. *Materials Science & Engineering, A*, 266(1-2): 30–36, 1999.

[172] D.C. Dunand, B.Q. Han, and A.M. Jansen. Monkman-grant analysis of creep fracture in dispersion strengthened and particle reinforced aluminum. *Metallurgical and Materials Transactions A*, 30A:829–838, 1999.

[173] Z. Jianxin, L. Xiang, and Z. Yang. Mechanical properties of surface plastic deformation layer of Q345R steel measured by small punch test. In K. Matocha, R. Hurst, and W. Sun, editors, *2nd International Conference SSTT Determination of Mechanincal Properties of Materials by Small Punch and Other Miniature Testing Techniques*, pages 110–114. OCELOT, 2012.

[174] Y. Zheng, J. Zhou, X. Ling, Z. Yang, S. Yang, and Y. Wang. Creep property assessment of type 304 by small punch creep test. In K. Matocha, R. Hurst, and W. Sun, editors, *2nd International Conference SSTT Determination of Mechanincal Properties of Materials by Small Punch and Other Miniature Testing Techniques*, pages 127–131. OCELOT, 2012.

Appendix A

Design of Custom Small Punch Rig

In this work, two custom-built small punch rigs were used to evaluate the mechanical properties of MCrAlY coatings. Rig 1 had previously been used for small punch creep testing at the University of Nottingham [63] but was unsuitable for small punch tensile testing as it was a constant load system. In order to carry out SPT tests a new custom rig, referred to as rig 2, was designed and built as part of this work. The design process is outlined below.

A.1 Previous Designs of Small Punch Rigs

The CEN workshop agreement [101] concerning small punch testing provides some guidance on the geometry of SP rigs. A standard geometry provided by [101] is shown in Fig.A.1. The agreement suggests the rig should support an 8 mm diameter disc specimen, have a receiving hole diameter of 4 mm with a 45 ° chamfered lip, and a hemispherical punch head with a radius between 1-1.25 mm.

The method of clamping the specimen is not specified, some designs use screws to clamp the specimen [173], where as for other designs, the upper die is screwed onto the lower die [174]. An example of each is shown in Figs.A.3 and A.2.

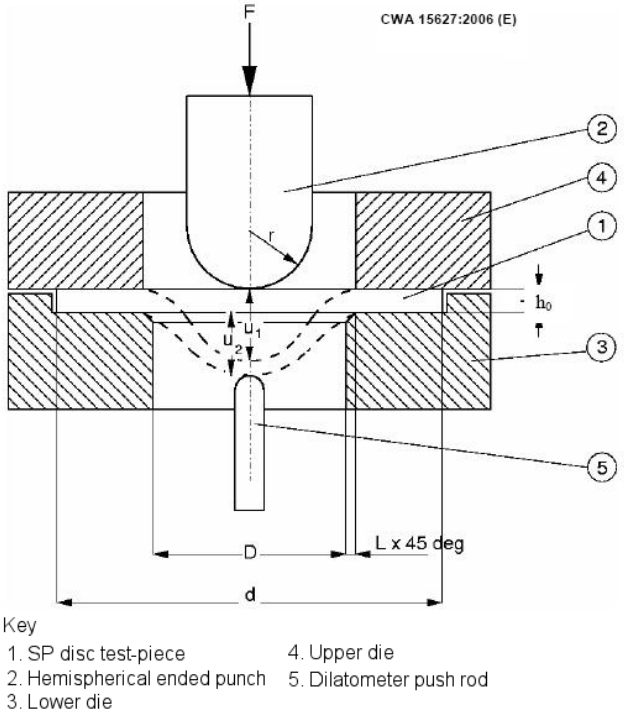

FIGURE A.1: Geometry of small punch creep test installation according to CEN workshop agreement.

The method of applying the load to the specimen is also not specified in the workshop agreement. The designs shown in Figs.A.3 and A.2 use ceramic balls as the punch heads where as rig 1, shown in Fig.A.4, uses a rod with a hemispherical head.

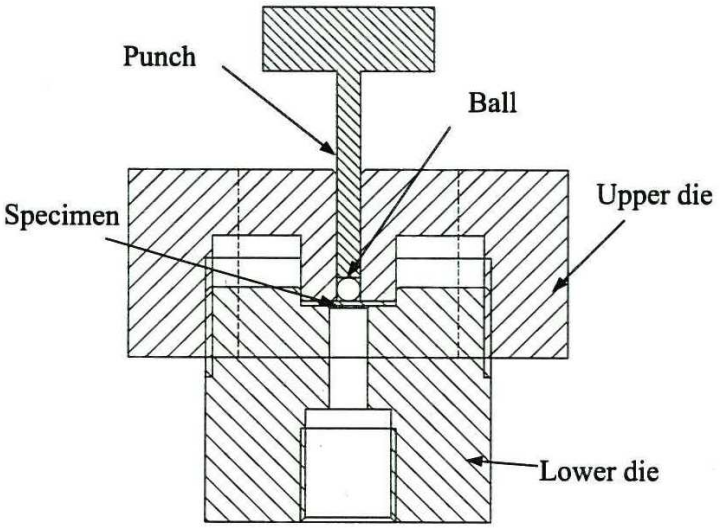

FIGURE A.2: Schematic of SP rig taken from Jianxin et al. [173].

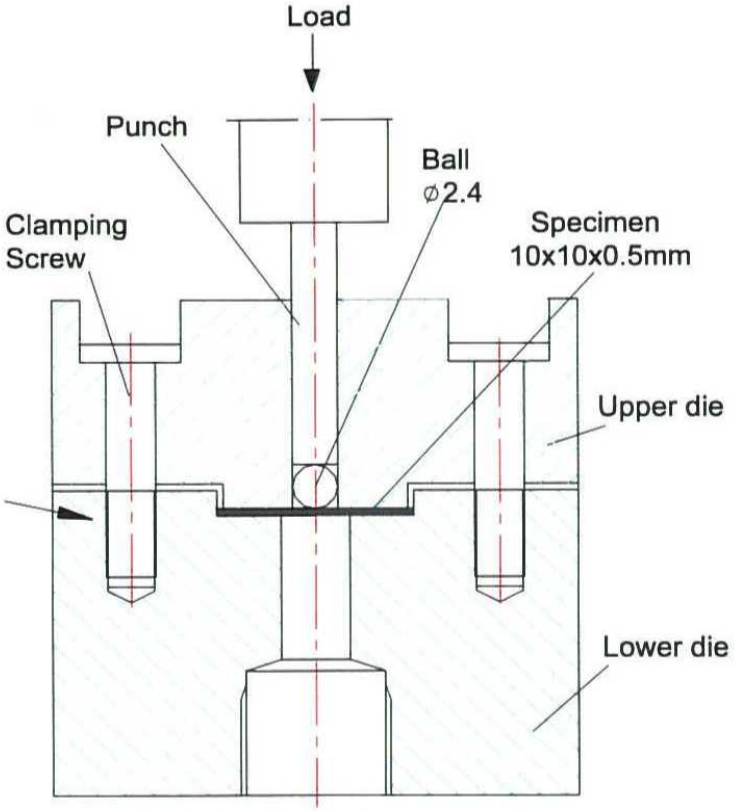

FIGURE A.3: Schematic of SPC rig taken from Zheng et al. [174]

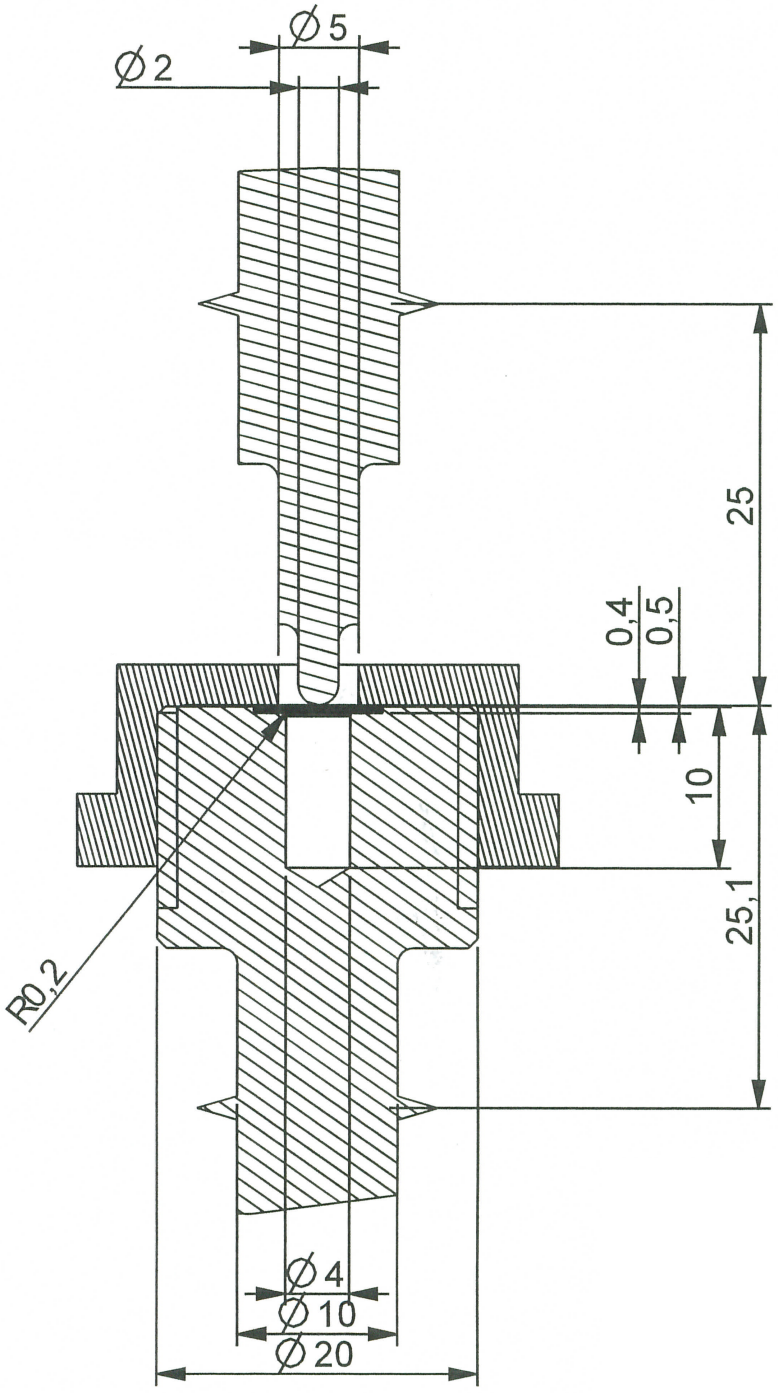

FIGURE A.4: Detailed drawing of E.ON SPC test rig

A.2 Design Limitations of Rig 1

As both rig 1 and rig 2 were used in this work for SP testing, the design of rig 2 was based around rig 1. This was an attempt to ensure consistency between the SP data obtained on both rigs. Rig 2 was also designed to improve on some of the design limitations of rig 1.

The main design limitation of rig 1 is that the load is applied as static weights. This means rig 1 is only suitable for SPC testing and cannot be used for SPT testing. To accommodate SPT testing, rig 2 was designed to be installed on a Tinius Olsen H5KS single column materials testing machine. The load could then be applied through a load cell and constant displacement rates could be applied to the specimen.

Another design limitation of rig 1 is that the load is transmitted to the punch head via a vertical rod. A small misalignment of the rod results in the load being applied off-centre of the specimen. Rig 1 uses alignment bushes but misalignment could still occur when these are removed or when additional loads are applied to the punch head. The single column testing machine reduced alignment issues as the punch head could be moved in the z axis without altering the position in the x and y axis.

Another design limitation of rig 1 is that when the specimen was clamped by the die, a rotational frictional force was applied to the surface of the specimen. The effect of this has not been quantified but is something which should ideally be avoided. To avoid friction on the surface of the specimen, rig 2 was designed to use a clamping disc which is held in place by two pins.

A.3 Design Specification

The selected design specification of rig 2, based on the guidance provided by the CEN workshop agreement [101] and the design limitations of rig 1, is detailed below.

The following specifications were chosen:

- Punch head radius of 1 mm
- Receiving hole of diameter 4 mm
- 45 ° chamfer on the lip of receiving hole
- Hold and clamp an 8 mm diameter disc specimen of 0.5 mm thickness
- Compatible with a Tinius Olsen H5KS single column materials testing machine

A detailed drawing of the final design of rig 2 is shown in Fig.A.5. The specimen is held by the lower die which has a receiving hole diameter of 4 mm. The specimen is clamped by screwing the upper die onto the lower die. A clamping disc, which cannot rotate due to the locating pins, sits on top of the specimen and prevents any rotational friction on the surface of the specimen. An alignment bush centres the 1 mm radius hemispherical punch head onto the specimen. The displacement of the punch head is recorded by two LDVTs connected to the knife edges and the temperature is measured by a thermocouple located at 3.

A.4 Material Selection

Rig 2 was manufactured from Nimonic 115 which is suitable for testing at temperatures up to 1010°C. The chemical composition is given in table A.1.

Chemical Composition (wt.%)								
Ni	**Cr**	**Co**	**Al**	**Mo**	**Ti**	**Mn**	**S**	**B**
Balance	14.4	13.2	5.02	3.29	3.77	0.09	<0.001	0.016
Cu	**Fe**	**Nb**	**C**	**Si**	**V**	**W**	**Zr**	
0.02	0.45	0.02	0.15	0.17	0.01	<0.05	0.045	

TABLE A.1: Composition of Nimonic 115 as measured by X-ray fluorescence analysis. Data provided by supplier IncoTest

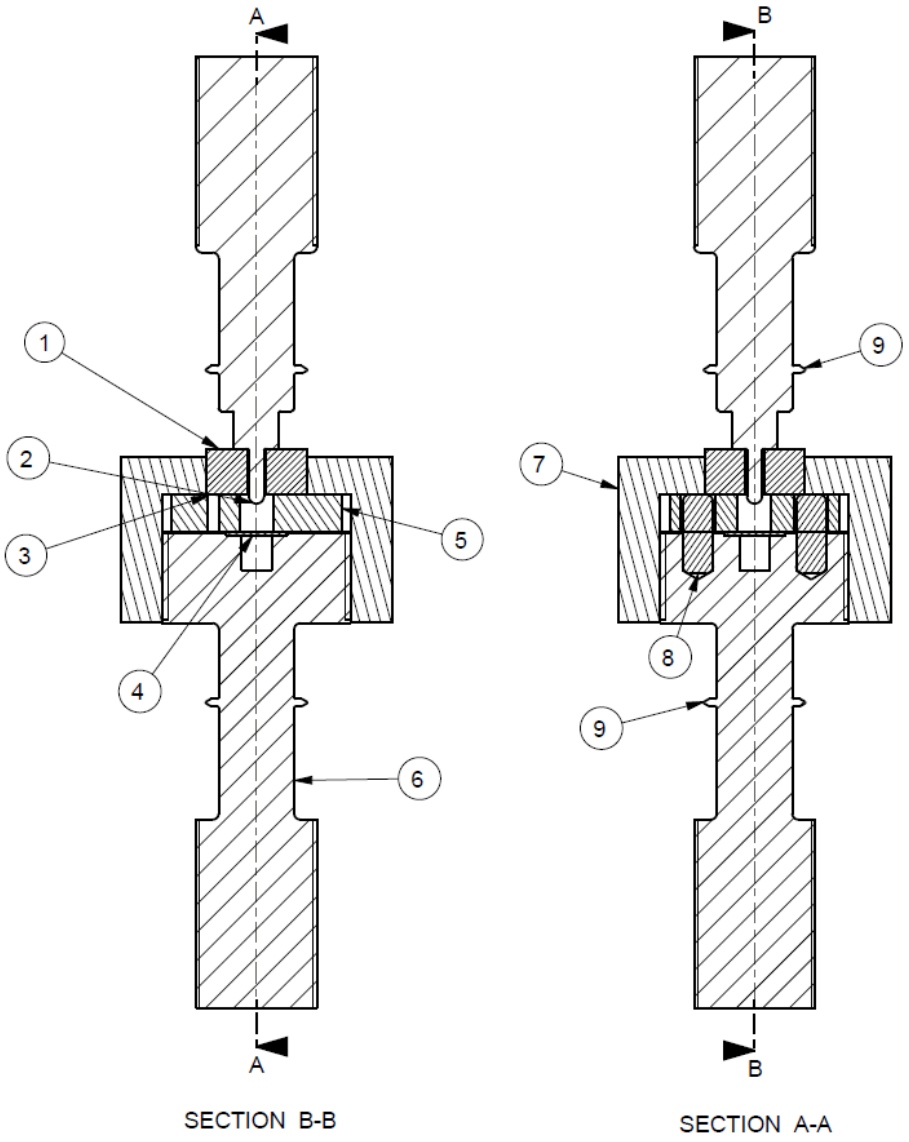

FIGURE A.5: Detailed drawing of rig 2. The part numbers are as follows: 1. Alignment bush 2. Hemispherical punch head R = 1.0mm 3. Thermocouple location 4. Specimen 5. Clamping disc 6. Lower die 7. Upper die 8. Locating pin 9. Knife edge for LDVT

A.5 Validation of Rig 2

The results of the SPC tests conducted for the C1 alloy on rig 1 and rig 2 at 750 °C were presented in chapter 6. They are presented here with reference to results obtained for coatings manufactured from the C1 alloy in a previous study [63].

The data sets obtained from SPC tests conducted on rig 1 and rig 2 at 750 °C in this work are referred to as C1 Rig 1 and C1 Rig 2. The data set obtained on rig

1 at 750 °C by Chen [63] is referred to as Chen Rig 1.

The different data sets are shown in Fig.A.6. The C1 Rig 1 data set and Chen Rig 1 data set show good agreement, which demonstrates consistency between this study and the results obtained by Chen [63]. The data obtained on rig 2 at 750 °C shows good consistency with the data obtained on rig 1 in both studies. This demonstrates rig 2 produces SPC data at 750 °C that is consistent with rig 1 at 750 °C. Therefore, rig 2 can be used with confidence for SPC creep testing.

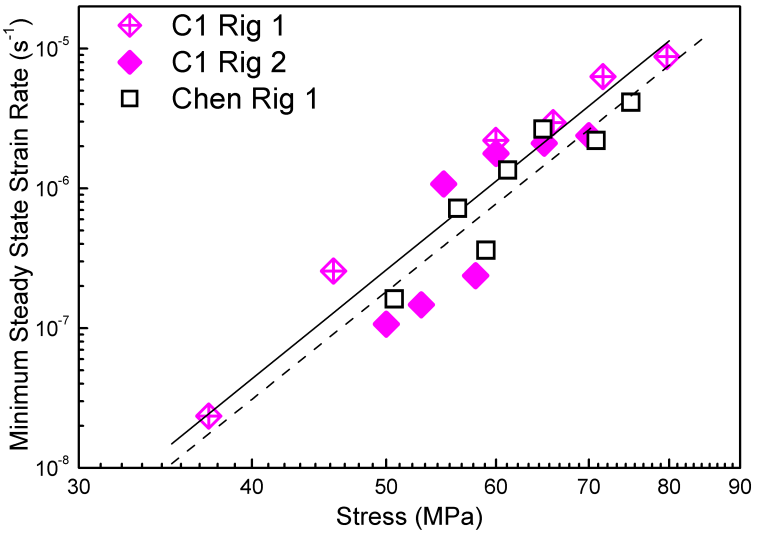

FIGURE A.6: Minimum steady-state strain rate as a function of stress for the C1 coating at 750 °C on rig 1 and rig 2. Data is compared with SPC data obtained by Chen [63] on rig 1 at 750 °C for a coating manufactured from the same powder as coating C1 (Praxair CO-210-24).

Appendix B

Mass fraction to Volume Fraction Conversion

In order to convert the mass fraction of a phase to volume fraction the following method was used.

$$\text{Density} = \frac{\text{Mass}}{\text{Volume}} \longrightarrow V = \frac{M}{\rho} \tag{B.1}$$

where V = volume, M = mass and ρ = density.

Considering a single phase with respect to the overall alloy:

$$\frac{V_{phase}}{V_{alloy}} = \frac{M_{phase}}{M_{alloy}} \div \frac{\rho_{phase}}{\rho_{alloy}} \tag{B.2}$$

Rearranging Eq.B.2:

$$\frac{V_{phase}}{V_{alloy}} = \frac{M_{phase}}{M_{alloy}} \times \frac{\rho_{alloy}}{\rho_{phase}} \tag{B.3}$$

Therefore the volume fraction of a single phase can be calculated as:

$$Vol.\% = Mass.\% \times \frac{\rho_{alloy}}{\rho_{phase}} \tag{B.4}$$

where ρ_{alloy} can be experimentally measured by measuring the density of the MCrAlY powders.

The density of a single phase can be calculated as:

$$\rho_p = \frac{\sum(atm_E \times Am_E)}{(N_A/4x)\ \alpha_p^3 \times 10^6} \tag{B.5}$$

where:

- atm = Atomic fraction
- Am = Atomic mass
- α = Lattice parameter
- N_A = Avagadro's constant
- x = Atoms per unit cell (4 for fcc, 2 for bcc)
- subscript p = Phase
- subscript E = Element